Novel iron ore direct reduction process using biomass

Tao Wang

To cite this version:

Tao Wang. Novel iron ore direct reduction process using biomass. Materials Science [cond-mat.mtrl-sci]. Université de Lorraine, 2022. English. NNT : 2022LORR0297 . tel-04128333

HAL Id: tel-04128333
https://hal.univ-lorraine.fr/tel-04128333

Submitted on 14 Jun 2023

UNIVERSITÉ
DE LORRAINE

École Doctorale C2MP
Laboratoire IJL

<u>Thèse</u>

Présentée et soutenue publiquement pour l'obtention du titre de

DOCTEUR DE l'UNIVERSITÉ DE LORRAINE

Mention : Science des Matériaux

par **Tao WANG**

sous la direction de Fabrice PATISSON et Olivier MIRGAUX

Novel iron ore direct reduction process using biomass

Nouveau procédé de réduction directe du minerai de fer utilisant de la biomasse

présentée et soutenue publiquement le 12 décembre 2022

Membres du jury :

Rapporteurs :	**Loïc FAVERGEON**	**Maître de Recherche, École des Mines de Saint-Étienne, Saint-Étienne**
	Frédéric MARIAS	**Professeur, Université de Pau et des Pays de l'Adour, Pau**
Examinateur et président	**Hervé COMBEAU**	**Professeur, IJL, Université de Lorraine, Nancy**
Examinatrice :	**Muriel MARCHAND**	**Chercheuse, CEA, Grenoble**
Directeur de thèse :	**Fabrice PATISSON**	**Professeur, IJL, Université de Lorraine, Nancy**
Co-directeur de thèse :	**Olivier MIRGAUX**	**Maître de Conférences, IJL, Université de Lorraine, Nancy**
Membre invité :	**Thibault QUATRAVAUX**	**Professeur associé, IJL, Université de Lorraine, Nancy**

Remerciements

Ces travaux ont été réalisés au laboratoire Institut Jean Lamour (IJL) de l'Université de Lorraine (UL). La thèse a été financé par le Labex Damas auquel je tiens à exprimer ma gratitude.

Je remercie tout d'abord, M. Thierry Belmonte directeur du Laboratoire, Sabine Denis et Hervé Combeau, respectivement ancienne et actuel chefs du département Science et Ingénierie des Matériaux et Métallurgie, ainsi que Alain Jardy, chef de l'équipe Procédés d'Élaboration pour m'avoir accueilli et m'avoir permis d'effectuer cette thèse.

Je tiens à remercier M. Fabrice Patisson, qui a dirigé cette recherche. Je le remercie pour la confiance qu'il m'a accordée et pour l'aide et les conseils qu'il m'a donnés. C'est grâce à sa grande compétence que ma formation de chercheur a progressé. J'ai toujours apprécié de travailler avec lui et avec une relation rigoureuse et amicale.

Je tiens à remercier M. Olivier Mirgaux, qui a codirigé cette recherche. Je le remercie pour le suivi et l'évaluation de mes travaux en continu, son aide pour la réalisation de l'analyse du cycle de vie et, ces derniers temps, ses efforts constants pour corriger mon manuscrit de thèse.

Je tiens à exprimer ma gratitude à nouveau à Hervé Combeau, qui était chef du département pendant mes études aux Mines Nancy, d'avoir accepté d'examiner ce travail lors des comités de suivi et aujourd'hui en étant membre de ce jury. De même, je suis très reconnaissant à M. Guillain Mauviel d'avoir accepté d'être membre du comité de suivi de ma thèse.

Je remercie M. Fréderic Marias et M. Loïc Favergeon d'avoir accepté d'examiner ce travail et d'en être les rapporteurs.

Je remercie Mme Muriel Marchand d'avoir accepté de revoir ce travail et d'en être l'examinatrice.

Je suis très reconnaissant à M. Jean-Baptiste Letz, ingénieur de recherche, pour son aide lors des expériences tout au long de la thèse. Je remercie à M. Pascal Boulet pour les analyses par diffraction des rayons X.

Enfin, je tiens à exprimer ma gratitude à ceux qui m'ont aidé : les équipes administratives et financières pour toutes les démarches ; tous les membres de l'équipe 301 pour leur avis et aides ; les doctorants et les post-doctorants dans le département qui apportent les moments conviviaux.

Summary

Notations	**Unity**	**Significations**
$\Delta_r H$	J/mol	Enthalpy changes of reactions
ρ_{app}	kg/m^3	Apparent density
ρ_{true}	kg/m^3	True density
$\Delta G^o_{(n)}$	J/mol	Standard Gibbs energy changes of reactions
$\Delta G_{(n)}$	J/mol	Gibbs energy changes of reactions
μ	Pa s	viscosity
A	s^{-1} or min^{-1}	pre-exponential factor
$a_{sp,Fe}$	m^2/kg	specific surface of the final reduced iron
c	-	Mass fraction
c	-	empirical constant(MRPM)
C_p	J/kg/K	heat capacity
D	m^2/s	Diffusion coefficients
d	m	diameter
E	kJ/mol	activation energy
E_t	kJ/mol	intrinsic activation energy
$f(X)$	-	Reactivity function
$g(P)$	-	Function of pressure
k	s^{-1} or min^{-1}	Rate constant
K	-	Equilibrium constant
m	g	Mass
n	-	Total number of reactions
P	Pascal or bar	Pressure
p	-	empirical constant(MRPM)
P_i	Pascal or bar	Pressure of gases
r	s^{-1} or min^{-}	Reaction rate
R	kJ/mol	universal gas constant
R	-	reactivity
R^2	-	Correlation coefficients
T	K	Temperature
t	s or min	time
X	-	Conversion
x or y	-	Concentration of gas
$x_{i,\infty}$	mol/m^3	molar concentration of gas species i in the gas
$x_{i,s}$	mol/m^3	molar concentration of the gaseous species i at the external surface of the solid

β	K/min	Heating rate
Γ	-	tortuosity
τ	s	characteristic time
φ	-	pore structure constant (RPM)
ϵ	-	Porosity

Other notations for the modelling of the reactor are explained in the part V.2.2 with governing equations.

Subscripts	**Significations**
0	initial
f	Final or active site
i	The number of reactions
exp	experimental
calc	calculated
(g)	gas
(s)	solid
eq	Equivalent or equilibrium
t	At any instant
a	activation
1-3	Number of reactions
reac	reaction
intrag	intragranulary
interg	intergranulary
cryst	crystallite
eff	effective
stat	static
dyn	dynamic
kn	Knudsen diffusion
im	gaseous species (i) in the mixture
ext	External
diff	diffusion
chim	chemical

Acronyms	**Signification**
AAEM	Alkali and Alkaline Earth Metals
BECCS	Bioenergy with Carbon Capture And Storage
BET	Brunauer-Emmett-Teller
BF	Blast Furnace
BOF	Basic Oxygen Furnace
CCUS	Carbon Capture, Utilization, and Storage
CFB	Circulating Fluidised Bed
CFD	Computational Fluid Dynamics
CML	Centrum voor Milieuwetenschappen Leiden
COG	Coke Oven Gas
CPI	Charcoal Powder Injection
DAEM	Distributed Activation Energy Model
DEM	Discrete Element Method
DRI	Direct Reduced Iron
DTG	Derivative of the Thermogravimetry
EAF	Electric Arc Furnace
FBB	Fluidised Bubbling Bed
Fior	Fluidised Iron Ore Reduction
FU	Functional Unit
FWO	Flynn-Wall-Ozawa
GHG	Greenhouse Gas
GIEC	Groupe d'experts intergouvernemental sur l'évolution du climat
HBI	Hot Briquetted Iron
HC	Hydrocarbons
HRC	Hot Rolled Coiled
ICM	Integrated Core Model
IEA	International Energy Agency
IPCC	Intergovernmental Panel on Climate Change
KAS	Kissinger-Akahira-Sunose
LCA	Life Cycle Assessment
LCIA	Life Cycle Impact Assessment
LHV	Low Heating Value
L-H equation	Langmuir-Hinshelwood Equation
MRPM	Modified Random Pore Model
PCI	Pulverized Coal Injection

PSS	Pseudo Steady State
PWHR	Pressurized Wire-Heating Reactor
RPM	Random Pore Model
SCM	Shrinking Core Model
TG	Thermogravimetry
TGR	Top Gas Recycling
TRF	Trust Region Reflective
TRL	Technology Readiness Levels
VM	Volatile Matter
ULCOS	Ultra Low CO_2 Steelmaking
USCM	Unreacted Shrinking Core Model
USS	Unsteady State
VRM	Volume Reaction Model
ZR	Zero Reforming

Résumé en français

Contexte et concept

De 1900 à 2000, la température moyenne de la terre a augmenté d'environ 0,75 degré et elle augmentera encore de 1,4 à 5,8 degrés d'ici 2100 selon différents scénarios.[1] Le réchauffement climatique est connu comme la conséquence de l'augmentation des émissions de gaz à effet de serre (GES), en particulier le dioxyde de carbone dans l'atmosphère. Le monde a conclu des accords afin de réduire les émissions de GES, dont le premier est le protocole de Kyoto signé en 1997. Plus tard en 2015, l'accord de Paris a fixé comme objectif de limiter le réchauffement de la planète bien en dessous de 2°C et de poursuivre les efforts pour le limiter à 1,5°C d'ici 2100. Pour atteindre cet objectif, l'Union européenne doit réduire ses émissions d'au moins 55% d'ici à 2030 par rapport aux niveaux de 1990 pour finalement atteindre la neutralité en 2050-2060.[2]

La motivation de cette thèse est la nécessité de lutter contre le réchauffement climatique en réduisant partout où c'est possible les émissions de CO_2, en particulier celles des industries les plus émettrices comme la sidérurgie. Celle-ci représente au niveau mondial 19 % des émissions industrielles de CO_2.[1]

La production d'acier par la filière haut fourneau-convertisseur (BF-BOF, Blast Furnace-Basic Oxygen Furnace) domine dans ce secteur et représente 71,9% de la production mondiale.[4] Dans le haut fourneau, le coke et le charbon utilisés (500 kg par tonne de fonte) produisent l'essentiel du CO_2 émis par la filière. En modifiant les procédés, ce carbone fossile pourrait être remplacé par du carbone biogénique (issu de la photosynthèse) fourni par de la biomasse. La biomasse, si elle est exploitée de manière durable, est considérée comme renouvelable et neutre en carbone car l'émission de CO_2 dégagée par sa combustion peut être absorbée par la photosynthèse pour produire une nouvelle biomasse.[5] Il s'agit d'une réserve d'énergie renouvelable à fort potentiel: chaque année en France, les arbres produisent naturellement 81 millions de mètres cubes de bois.[6] L'un des moyens d'utiliser la biomasse pour ce type d'application est de la gazéifier à la vapeur ou au CO_2. Le gaz de synthèse H_2-CO produit est un réducteur gazeux parfaitement adapté à la réduction des minerais de fer.

Du point de vue des émissions de CO_2, deux principales améliorations ont été réalisées dans l'industrie sidérurgique. L'une est la production d'acier par la filière électrique, à partir de ferraille dans un four électrique (EAF, Electric Arc Furnace), mais elle ne concerne que le recyclage. L'autre est la fabrication d'acier à partir de minerai par la filière de réduction dite directe suivie d'une fusion au four électrique.

La réduction directe (Direct Reduction) est une approche alternative au haut fourneau pour produire du fer, même si les produits ne sont pas équivalents : fer solide à 2% de carbone dit préréduit ou éponge de fer ou DRI (Direct Reduced Iron) dans la réduction directe. Aujourd'hui, les procédés au gaz produisent la majorité des DRI (79%) : le procédé MIDREX, qui est le leader du marché et le procédé HYL/ENERGIRON, tandis que les 21% restants sont issus de procédés à base de charbon.[7]

L'objectif de la thèse est de développer une nouvelle approche de la fabrication du fer à partir de minerai et de biomasse, en utilisant la biomasse et le minerai de fer le moins transformés possible dans un réacteur le plus simple possible. La simulation numérique est l'outil pour déterminer les conditions opératoires favorables et l'expérimentation est l'outil d'obtention des données pour la cinétique des réactions et de vérification du concept. Le réacteur envisagé a priori est un four à cuve comme ceux employés par les procédés MIDREX et HYL.

Le réacteur est un système à contre-courant (Voir Figure 0-1). Les minerais de fer et la source de carbone (biomasse) sont introduits en haut à température ambiante puis chauffés par le gaz entrant en bas à haute température (1100 °C). Les oxydes de fer sont réduits par CO mais le monoxyde de carbone utilisé pour cette réduction ne provient pas directement du mélange gazeux. En effet, le gaz circulant dans l'ensemble du réacteur est recyclé, éventuellement traité en fonction de sa composition et sa température, et injecté en bas à nouveau. Ainsi, le gaz réducteur CO consommé par la réduction provient principalement de la gazéification du carbone de la biomasse par CO_2, par la réaction appelée réaction de Boudouard, $C + CO_2 \rightleftarrows 2CO$.

Le minerai de fer utilisé dans le procédé pourra être soit des boulettes (un produit standard fabriqué par boulettage de fines de minerai et cuisson, sphéroïdes de 10 à 15 mm de diamètre contenant 95% de Fe_2O_3) soit du minerai de fer en morceaux. Nous avons considéré ici un four alimenté par des boulettes comme dans les procédés de réduction directe actuels.

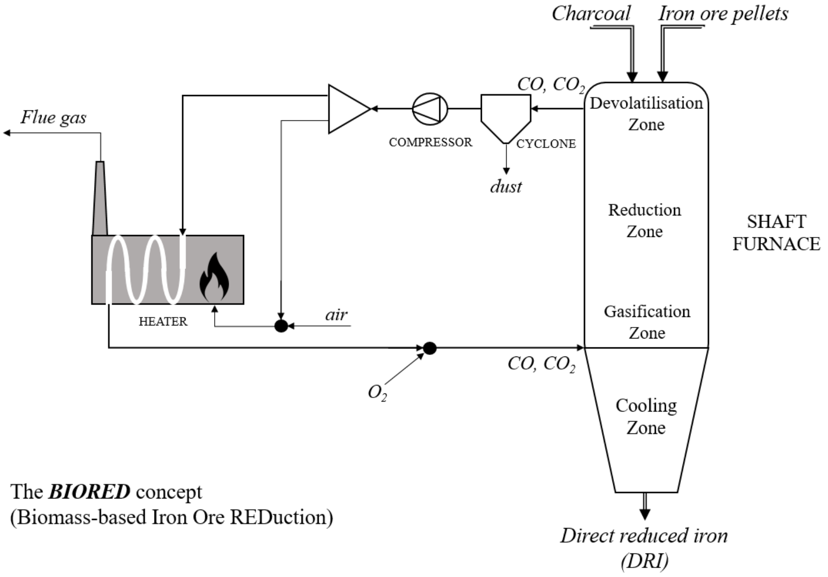

Figure 0-1. Schéma du four à cuve avec biomasse et recyclage

Quant à la biomasse, après avoir considéré dans un premier temps par simplification qu'il s'agissait de carbone pur, nous avons ensuite considéré du charbon de bois, solide à teneur en carbone élevée et présentant une bonne résistance mécanique, a priori plus facile d'utilisation que le bois.

Expériences de dévolatilisation

Le charbon de bois contient du carbone dit fixe, des matières volatiles et de la matière inorganique, les cendres. Après son entrée dans le four à cuve, le charbon de bois va très vite sécher, s'il était humide, puis perdre ses matières volatiles pour n'être plus composé que de carbone et de cendres. Les gaz émis lors de la dévolatilisation (CO, CO_2, H_2, H_2O, CH_4...) sont susceptibles d'interagir avec les oxydes de fer. Il est donc nécessaire de décrire la dévolatilisation dans le modèle. C'est ce qui nous a conduit à étudier expérimentalement la dévolatilisation d'un charbon de bois, pour en tirer une loi cinétique de la dévolatilisation à introduire dans le modèle. Les expériences ont été réalisées par thermogravimétrie.

Le charbon de bois employé dans cette étude est du charbon de bois de chêne. Ce charbon a été préparé par pyrolyse lente à une température de 390°C. Sa composition (sur sec) est de 24,45% de matières volatiles et de 74,5% de carbone fixe. Il se présente sous forme de morceaux bruts de tailles vairées. La thermobalance SETARAM TAG 24 à fours symétriques a été utilisée pour étudier la décomposition non-isotherme des échantillons lors de la dévolatilisation. La masse d'échantillon était d'environ 50 mg sous forme d'un petit morceau.

Nous avons appliqué la méthode des réactions indépendantes en parallèle. Pantoleontos et al. ont utilisé cette méthode pour la loi cinétique de la dévolatilisation de noyaux d'olives et de résidus forestiers.[11] Le charbon de bois est supposé se dévolatiliser par des réactions multiples, parallèles et de premier ordre, qui se déroulent indépendamment. Chacune de ces réactions est exprimée par l'équation différentielle du premier ordre :

$$\frac{dX_i}{dt} = A_i \exp\left(-\frac{E_i}{RT}\right) * (1 - X_i)$$

Nous avons écrit un code Python pour déterminer les paramètres cinétiques par ajustement. Le principe est de minimiser l'écart quadratique entre points mesurés et calculés. On peut faire intervenir un nombre quelconque de réactions. Les paramètres obtenus pour un modèle à deux réactions sont listés dans Tableau 0-1, et Figure 0-2 montre l'ajustement obtenu.

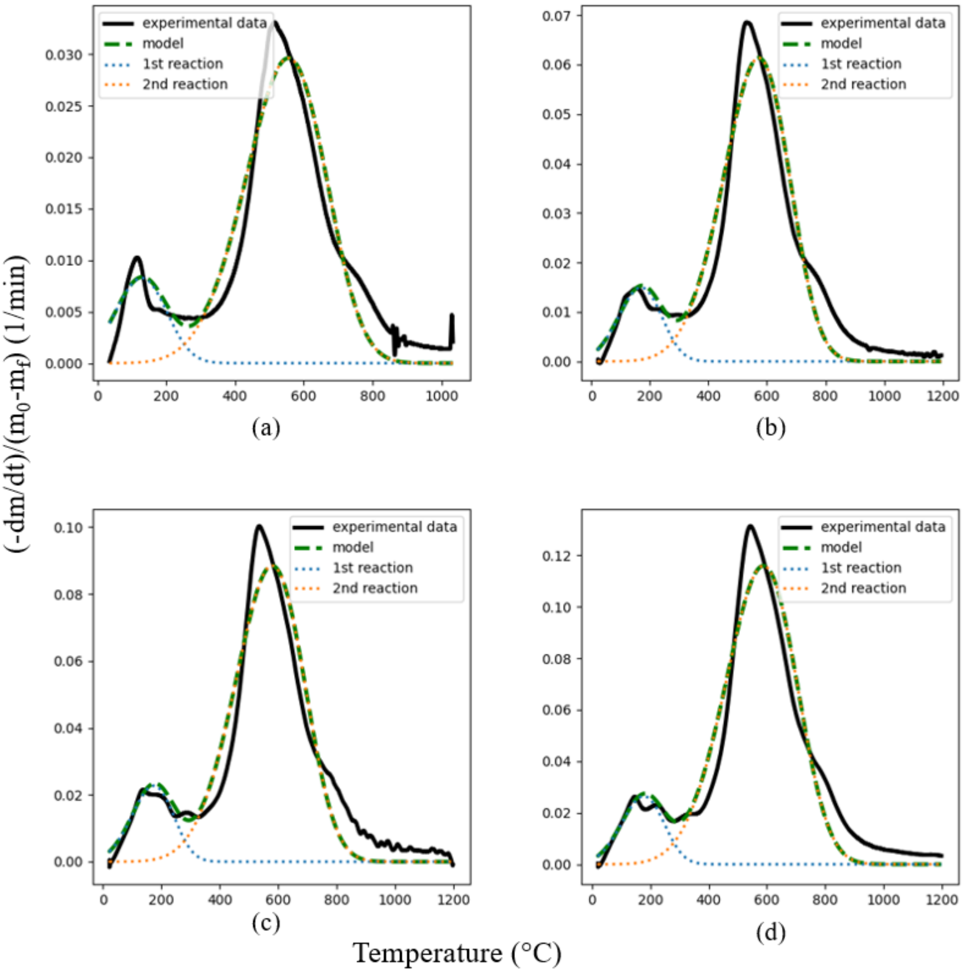

Figure 0-2 : Modélisation de la dévolatilisation du charbon de bois chauffé à 10, 20, 30 et 40 K/min avec deux pseudo-réactions en parallèle

La deuxième réaction domine la dévolatilisation globale en représentant 86,7 % en masse des matières volatiles. Il s'agit probablement de la décomposition thermique de la lignine. En effet, les travaux de Skodras et Pantoleontos ont situé l'énergie apparente d'activation de la décomposition de la lignine entre 32,8[11] et 46,1[12] kJ/mol, ce qui correspond à notre valeur.

De plus, le charbon de bois que nous utilisons a été carbonisé à la température de 390 °C qui n'est pas suffisamment élevé pour la décomposition totale de la lignine.[13]

Heating rates (K/min)	**Pseudocomponent 1**			**Pseudocomponent 2**			**Correlation coefficient (R^2)**
	E_1 (J/mol)	A_1 (1/min)	C_1	E_2 (J/mol)	A_2 (1/min)	C_2	
10	15029	10	0.136	42465	35	0.864	0.922
20	18711	37	0.133	46024	109	0.867	0.933
30	19861	75	0.131	44675	121	0.869	0.931
40	19794	92	0.116	43787	129	0.884	0.935

Tableau 0-1. Paramètres cinétiques de premier ordre des deux réactions parallèles

Expériences de gazéification

La gazéification du carbone par CO_2 (la réaction de Boudouard) est la base du procédé envisagé puisqu'on souhaite produire la quantité de monoxyde de carbone nécessaire à la réduction du minerai de fer par la gazéification complète de la biomasse introduite. L'analyse bibliographique de la gazéification du charbon de bois, et en particulier de la gazéification par CO_2, réalisée a montré une grande variabilité des cinétiques de gazéification, selon les conditions de gazéification, les échantillons étudiés, et les auteurs. Nous avons donc décidé de réaliser nos propres expériences de gazéification, toujours par thermogravimétrie avec cette fois la thermobalance SETARAM TG 96, en utilisant des échantillons d'environ 1g du même charbon de bois de chêne, à des températures entre 850 et 1100°C, et pour différentes compositions d'un mélange CO-CO_2 (rappelons qu'on prévoit dans le réacteur la recirculation d'un gaz avec environ 50% de CO et 50% de CO_2).

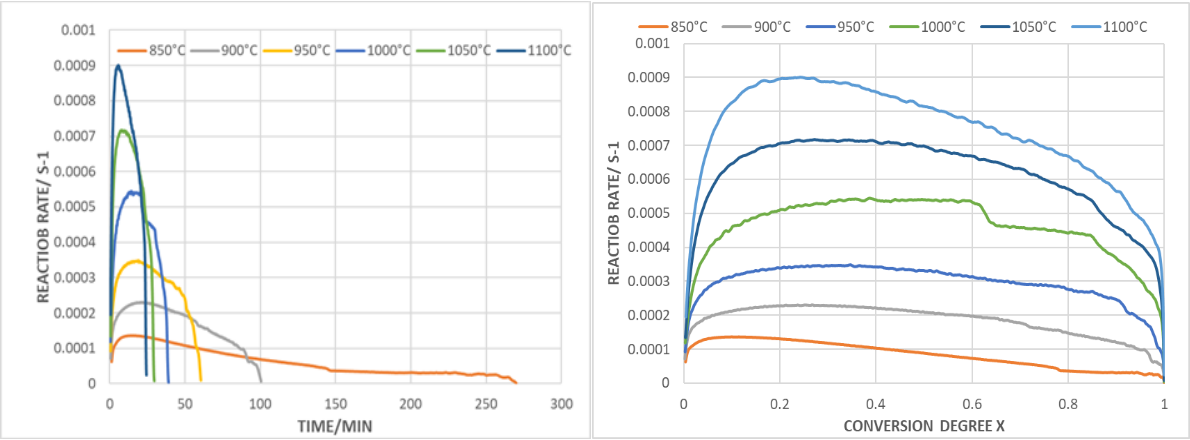

Figure 0-3 : Evolution de la vitesse de gazéification avec (a) le temps et (b) la conversion à 850-1100°C sous CO_2 pur

La Figure 0-3 illustre le grand effet de la température sur la cinétique de gazéification du charbon de bois sous CO_2. L'augmentation de la température contribue à une vitesse de gazéification plus rapide et à un temps de réaction plus court, surtout à des températures relativement basses. Par exemple, le temps de gazéification diminue de 270 minutes à 40 minutes lorsque la température passe de 850°C à 1000°C. Ce phénomène est cohérent avec la loi de Le Chatelier puisque la réaction de Boudouard est fortement endothermique avec un changement d'enthalpie de 172 kJ/mol. De plus, l'augmentation de la température favorise la réactivité des molécules de biomasse et la quantité de sites de gazéification actifs pour la réaction avec le CO_2, deux facteurs qui améliorent la réactivité globale.[14]

Le modèle de Langmuir-Hinshelwood (L-H) permet de déterminer la vitesse de gazéification en tenant compte de la présence de CO dans le mélange de gaz, donc nous avons modélisé la réaction par cette méthode. Pour obtenir les paramètres cinétiques du modèle de L-H, différentes températures (850°C-1100°C) et compositions gazeuses (CO_2-CO/50-50, 75-25, 100-0) ont été utilisées dans un ensemble d'expériences. Un programme de curve-fitting en Python avec la méthode TRF pour l'optimisation d'un moindre carré non linéaire a permis d'estimer les paramètres cinétiques. Figure 0-4 montre que les valeurs modélisées et expérimentales correspondent bien. La formule de la vitesse de gazéification sous forme de L-H est:

$$k(T,P_i) = \frac{k_1 P_{CO_2}}{1+\frac{k_1}{k_3}P_{CO_2}+\frac{k_2}{k_3}P_{CO}} = \frac{328 * \exp\left(-\frac{130,795}{RT}\right)P_{CO_2}}{1+\frac{328 * \exp\left(-\frac{130,795}{RT}\right)}{0.128 * \exp\left(-\frac{57,176}{RT}\right)}P_{CO_2}+\frac{5340 * \exp\left(-\frac{172,316}{RT}\right)}{0.128 * \exp\left(-\frac{57,176}{RT}\right)}P_{CO}}$$

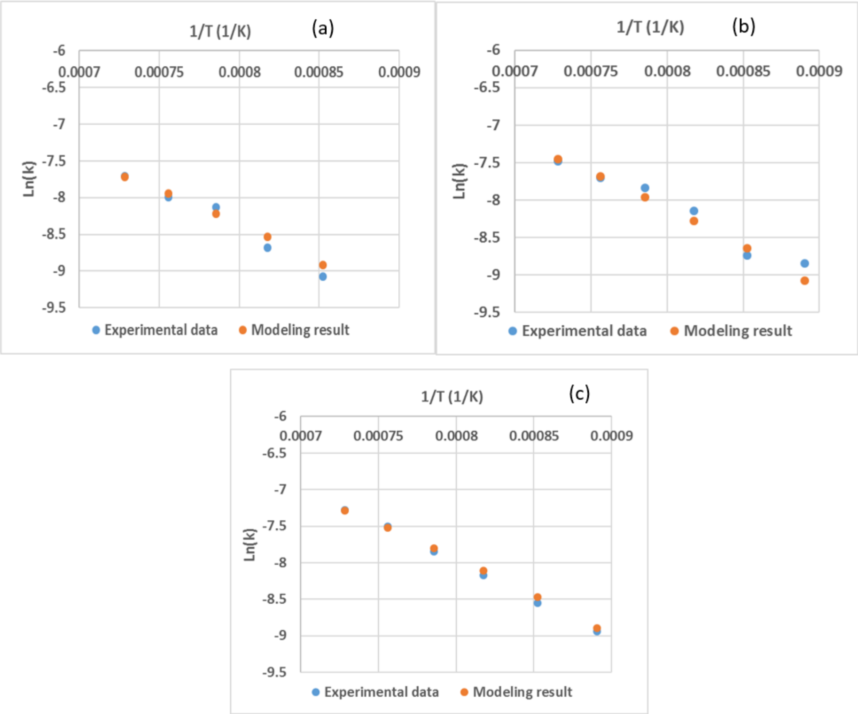

Figure 0-4. Comparaison du modèle L-H et de la vitesse de réaction expérimentale dans différentes conditions de CO_2-CO (a) 50-50 ; (b) 75-25 ; (c) 100-0

Modélisation et simulation du four à cuve

Le modèle cinétique pour simuler la réduction d'un lit mixte de boulettes de minerai de fer et de biomasse est une extension de ceux précédemment développés à l'IJL par Ranzani da Costa et Hamadeh.[15] [16]

Rappelons que dans le réacteur envisagé la charge solide est chargée par le haut du réacteur en un lit mobile de particules solides (les boulettes de minerai de fer et les morceaux de charbon de bois) qui descendent par gravité. Elles sont réduites par le mélange de CO-CO_2 à contrecourant dans la zone de réduction.

Le modèle original est en deux dimensions (*r* et *z*) et le four comporte une partie cylindrique et une partie conique. Puisque la partie conique a pour but de refroidir le DRI produit et afin de simplifier la simulation, on a considéré pour notre étude un simple cylindre alimenté uniformément en solide en haut et en gaz en bas, ce qui a pour effet de rendre les résultats monodimensionnels (selon *z*). On calcule les écoulements du gaz et du solide, mais ceux-ci sont uniformes du type piston. Le modèle est basé sur la résolution numérique des équations de conservation locales de masse, énergie et quantité de mouvement en utilisant la méthode des volumes finis. Les composants solides sont Fe_2O_3, Fe_3O_4, $Fe_{0,95}O$, Fe, C et inerte. Les constituants du gaz sont principalement CO et CO_2, mais aussi H_2, H_2O, CH_4, N_2.

Le gaz réducteur est alimenté en bas du réacteur et se déplace vers le haut à contre-courant du solide, mais une autre source de gaz réducteur est générée par la gazéification de carbone in situ, ainsi que dans une moindre mesure par le gaz de pyrolyse produit par la dévolatilisation de matières volatiles. L'objectif du réacteur idéalement est de réduire totalement le minerai de fer et de gazéifier totalement le carbone. Le gaz circulant est recyclé au maximum (la partie excédentaire du gaz de gueulard est brûlée pour le réchauffage du gaz). Il faut donc que les compositions des gaz haut et bas soient proches.

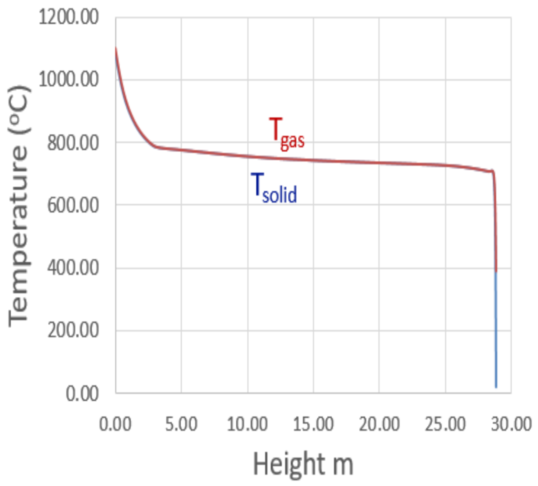

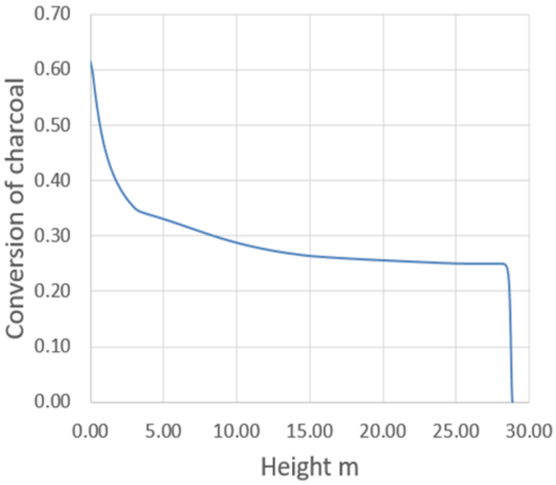

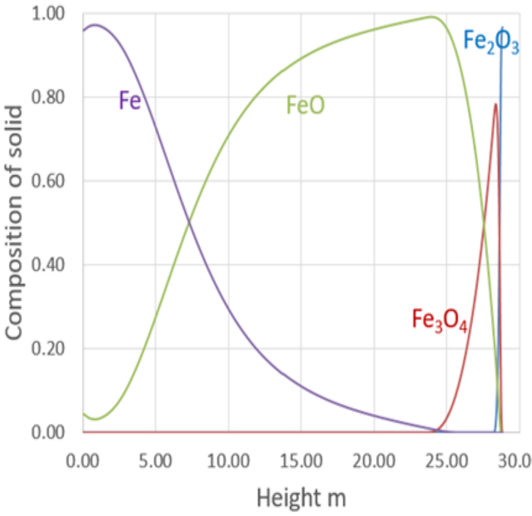

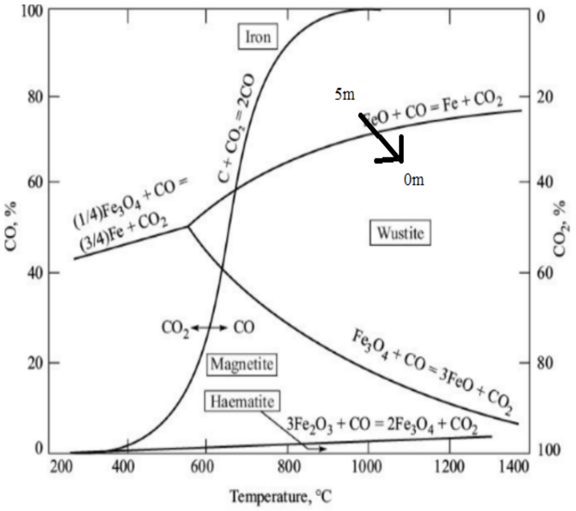

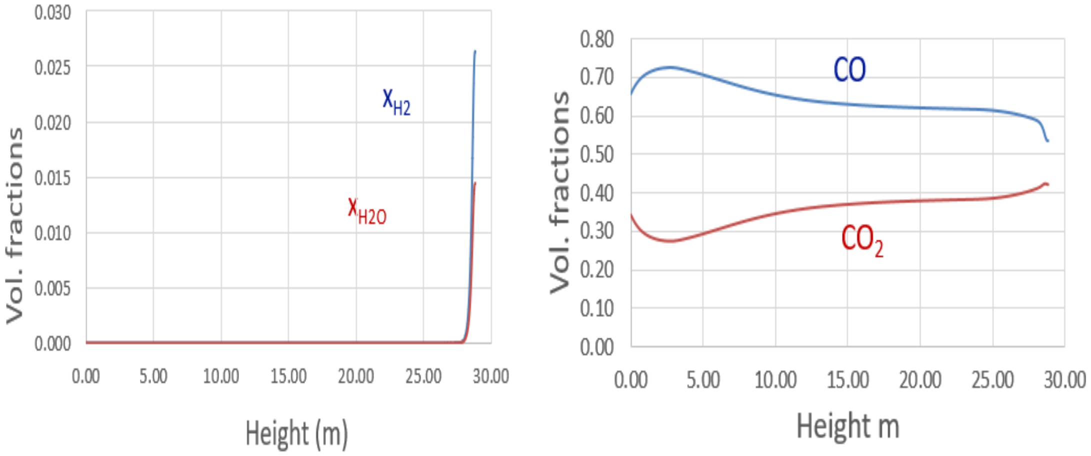

Figure 0-5. Résultats de la simulation du four à cuve et diagramme de Chaudron

Les résultats des calculs révèlent le fonctionnement interne du four et montrent qu'il est effectivement possible, avec un tel réacteur, d'obtenir un DRI bien métallisé à partir de minerai de fer et de charbon de bois.

Avantages environnementaux et développement potentiel du four à cuve à base de biomasse

Le développement potentiel de ce nouveau procédé nécessite une ressource abondante de biomasse ou une plantation envisageable à côté des mines. Nous avons vérifié qu'il existait des sites de ce type en différents endroits du monde et nous avons sélectionné pour la suite des calculs le cas de la mine de Kiruna en Suède. Nous avons simulé trois scénarios: vente directe des boulettes des minerai, vente du DRI issu du procédé Midrex et vente du DRI issu du nouveau procédé. Les résultats montrent qu'à cause de l'investissement important des usines, le nouveau procédé ne peut pas générer un bénéfice plus important que la vente directe des boulettes, mais qu'il est plus rentable que le procédé Midrex.

Ensuite une analyse du cycle de vie de la filière DRI(BIORED)-EAF basé sur la biomasse a également été réalisée en considérant à nouveau le cas de la Suède. Le calcul des impacts intermédiaires à l'aide de la méthode ReCiPe 2016 met en évidence les avantages environnementaux du nouveau procédé. En outre, la comparaison à la filière classique avec le haut fourneau montre que la filière DRI-EAF issue de la biomasse est la plus respectueuse de l'environnement avec une émission de 242 $\text{kg}_{CO2\text{-eq}}$ par tonne d'acier et de meilleures scores pour la plupart des impacts. Les faibles émissions de CO_2 s'expliquent par l'utilisation d'un agent réducteur sans carbone et d'une électricité à faible teneur en carbone.

I. General introduction

From 1960 to 2017, global temperature had increased by 0.75 °C and it will continue to increase by 1.5°C according to the modelling of IPCC (Intergovernmental Panel on Climate Change). [17]

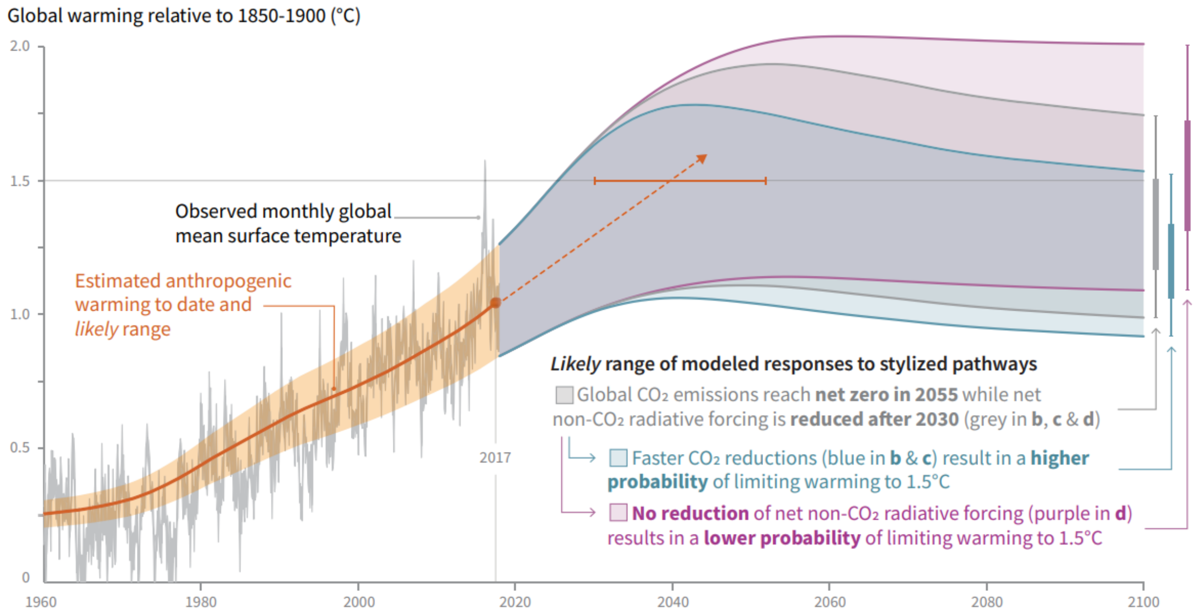

Figure 1. Observed global temperature change and modelled responses to stylized anthropogenic emission and forcing pathways [17]

The global warming is known as the consequence of the increase in greenhouse gas (GHG) emissions, especially carbon dioxide in the atmosphere. The world has been reaching accords in order to cut down the GHG emissions, among which the first was the Kyoto protocol signed in 1997. This protocol called for reducing the emissions of six greenhouse gases (carbon dioxide, methane, nitrous oxide, perfluorocarbons, hydrofluorocarbons, and sulphur hexafluoride) in 41 countries plus the European Union to 5.2 percent below 1990 levels. [18] Later in 2015, the Paris agreement set the limiting global warming to well below 2°C and pursuing efforts to limit it to 1.5°C by 2100. To achieve this goal, the European Union has to cut down its emissions by at least 55% by 2030 from 1990 levels to eventually reach neutrality by 2050-2060. [19]

Many studies have been realized in different fields to transit towards more environmentally friendly processes, especially in industrial and transportation sectors, which play an important role in the anthropogenic GHG emissions. Among industrial sectors, ironmaking and steelmaking is currently responsible for about 8% of global final energy demand and 7% of CO_2 emissions (including process emissions). [20]

Steel is an alloy made from iron, carbon (up to 2%) and other alloying materials. Several routes are currently used to produce steel from iron ore (primary steel) or scrap (secondary steel).

The conventional route relies on the blast furnace (BF) to produce pig iron and on the basic oxygen furnace (BOF) to convert it into steel. In a blast furnace, coke and iron ore (in the form of sinter or pellets) are alternatively loaded. Sinter is a small, irregular nodule of iron mixed with small amounts of other minerals, also called gangue. Pellets are larger (10-15 mm) particles, of spherical shape. Coke is produced from fossil coal heated at high temperature without oxygen in coke ovens. In a blast furnace, coke is the source of carbon for the reduction of the iron oxides, either directly or after its combustion into CO. In both cases, CO_2 is formed. This is the main source of CO_2 emissions in the steel industry. Indeed, this massive use of fossil carbon for steelmaking leads to the release of 1.8 $t_{CO2\text{-}eq}$ in the atmosphere to produce one tonne of hot rolled coiled (HRC). Many research and development programs have been launched to improve the performance of blast furnaces, especially in terms of GHG emissions, and we will discuss them thoroughly in Section II.4.4.

Another route, called direct reduction, turns iron ore pellets into "direct reduced iron (DRI)", at solid state, into a shaft reactor (90% of the DRI produced) or a rotary kiln. The reducing agent is a syngas produced from methane, in the case of a shaft reactor, or coal, in the case of a rotary kiln. The reduction reactions are as follows:

$$3Fe_2O_{3(s)} + H_{2(g)} \rightarrow 2Fe_3O_{4(s)} + H_2O_{(g)} \qquad \text{R1}$$

$$Fe_3O_{4(s)} + H_{2(g)} \rightarrow 3FeO_{(s)} + H_2O_{(g)} \qquad \text{R2}$$

$$FeO_{(s)} + H_{2(g)} \rightarrow Fe_{(s)} + H_2O_{(g)} \qquad \text{R3}$$

$$3Fe_2O_{3(s)} + CO_{(g)} \rightarrow 2Fe_3O_{4(s)} + CO_{2(g)} \qquad \text{R4}$$

$$Fe_3O_{4(s)} + CO_{(g)} \rightarrow 3FeO_{(s)} + CO_{2(g)} \qquad \text{R5}$$

$$FeO_{(s)} + CO_{(g)} \rightarrow Fe_{(s)} + CO_{2(g)} \qquad \text{R6}$$

The DRI produced is next sent to an electric arc furnace (EAF) to produce steel. GHG emissions with the DRI-EAF route are almost halved (around 970 $kg_{CO2\text{-}eq}/t_{HRC}$) in comparison of the BF route. [21]

An important alternative to the primary steelmaking routes is the production of secondary steel from scrap in an electric arc furnace (scrap-EAF route). EAF are smaller and easier to operate than the other processes, which make them good candidates for regions where scrap is more available than ores, especially in developing countries. In addition, the GHG emissions are far lower than the other routes, for instance, 441 $kg_{CO2\text{-}eq}/t_{HRC}$ in EVRAZ, Canada. [21]

Figure 2 shows the share of the different routes in terms of production, energy consumption and CO_2 emissions. [20]

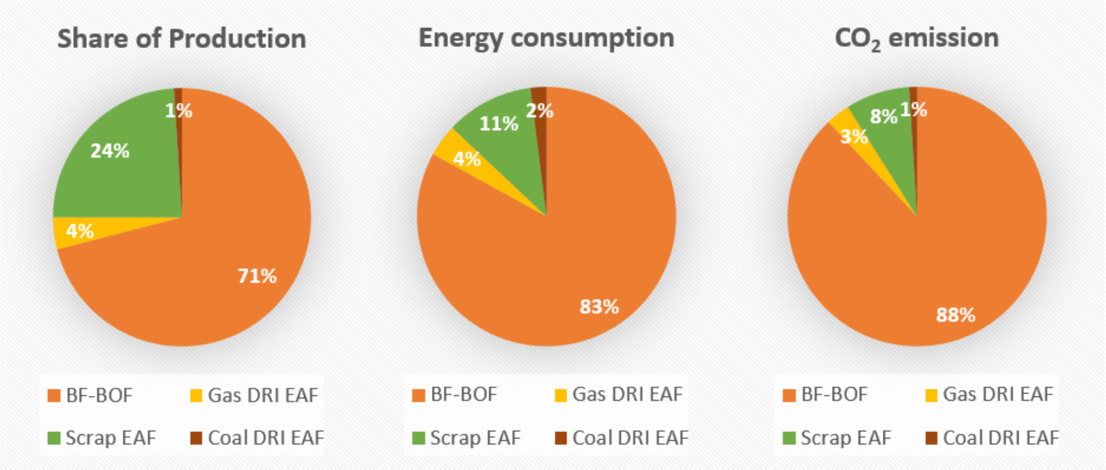

Figure 2. Share of global (a) production, (b) energy consumption, and (c) CO_2 emission [20]

Conventional route with blast furnaces is dominant (71% of iron production) because BF have been commercially used for more than a century. The EAF scrap-based route is developing fast, but represents only 24% of the current production. This means that the BF-BOF and DRI-EAF routes are essential to supply the current demand, and should remain mandatory at least until 2050. [23]

To reach the target of the European Union in terms of CO_2 mitigation, many research and development programs, such as the European project ULCOS (Ultra Low CO_2 Steelmaking), were launched to investigate new breakthrough processes to produce low CO_2 steel. [24] Among the identified breakthrough processes, stands the reduction of iron oxides with hydrogen and biomass.

Hydrogen, as an alternative to fossil carbon reductants, may have a very low impact in terms of GHG emissions for two reasons. First, the reduction reaction of iron oxides with hydrogen releases H_2O, while CO_2 is released when fossil carbon is used as reductant. Secondly, if hydrogen is produced from renewable resources (water electrolysis for instance) and low CO_2 energy, such as electricity from nuclear, hydro or wind power plants, the global CO_2 balance of the whole route is to be very low (less than 200 $kg_{CO2\text{-}eq}/t_{HRC}$). The direct reduction with hydrogen has been studied in our group at IJL for two decades and showed promising results. This route is currently developed at industrial scale by different steel producers in Europe. [25] [26] [27]

The second promising substitution of fossil carbon is the substitution by carbon from biomass (biogenic carbon). The advantage of using carbon from biomass lies in its very low impact on global warming. Indeed, in the natural cycle of carbon, the carbon in biomass comes from the CO_2 taken from the atmosphere and stored by the plant by photosynthesis during its growth. Thus, the CO_2 released while burning the biomass is just a return to atmosphere of the CO_2 previously stored, which results, in a first approximation, in a neutral balance. The biomass is a renewable resource with large stocks in many European countries, like France, Sweden, and Norway. However, bearing the deforestation in mind, a reasonable management of biomass production and harvest is crucial.

An innovative process for direct reduction using biomass as carbon feed is studied in the present thesis. In this process, biomass is loaded in the shaft furnace together with iron ore pellets and the reducing gas is directly produced inside the shaft from the biomass thermal degradation and gasification.

The outline of the manuscript will be as follows. The first chapter will be dedicated to the state of art. The next two ones will focus on the biomass degradation by devolatilisation (Chapter 2) and gasification (Chapter 3). The fourth chapter is devoted to the modelling of the biomass-based direct reduction furnace, effect of the main parameters, and comparison with experiments. Eventually, we will investigate the environmental benefit of the whole process through a life cycle assessment (Chapter 6) before concluding.

II. Background on steelmaking, biomass and their interplay

Since the first industrial revolution, the production of steel has been an essential element for the development of our society. The main processes to produce primary steel are the conventional route (BF-BOF route) and the DRI-EAF route. In this chapter, we will first introduce the basic knowledge of these two processes. Then we will present in detail different configurations of Direct Reduction (DR) reactors, which is the main focus of the present study. The last part of the chapter is dedicated to the utilisation of biomass in the iron and steelmaking industry as means to reduce GHG emissions.

II.1. Context of iron and steelmaking

Figure 3 illustrates briefly principal processes in the field of iron and steelmaking for both from primary steel and secondary steel. [28]

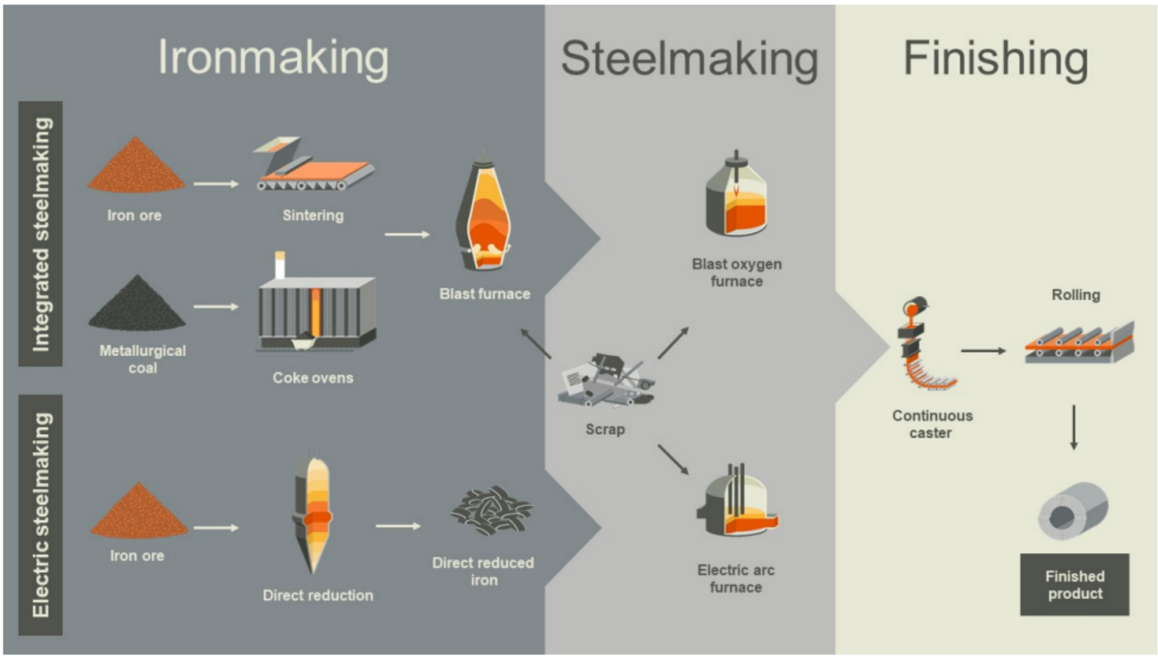

Figure 3. Diagram of iron and steelmaking routes [28]

II.1.1 Conventional route

Despite the growing concern on climate change and high CO_2 emissions of the BF, the conventional BF-BOF route remains the main one to produce primary steel. It accounts for 71% of steel production in 2019. As shown in Figure 3, this route is composed of several units, which are the sintering plant, the coking plant, the blast furnace and the basic oxygen furnace. The first two plants are dedicated to the preparation of the mineral loads (iron ore fines and coal); the blast furnace reduces the iron ore and melt it into pig iron (ironmaking) and the basic oxygen furnace turns it into steel (steelmaking).

The sintering plant consists in converting iron ore fines (mostly hematite Fe_2O_3 and magnetite Fe_3O_4) into sinter: particles with a controlled size (5-50 mm) and a strong mechanical resistance at high temperatures (at least 1000 °C). The sinter usually represents 70-80% of the iron ore burden of the blast furnace. Pellets and iron ore lumps are also used. Recent research and development programs have been focusing on the use of ferrous scrap and DRI in the blast furnace. [29] The sintering plant uses coke, limestone and anthracite mixed with the iron ore fines and natural gas as the heat source. As listed in Table 1 next page, the sintering plant releases about 211 kg $_{\text{CO2-eq}}$/t $_{\text{liquid steel}}$. [30]

The coking plant produces coke in diameter of about 50 mm from raw coal. It has less volatile matter and higher mechanical resistance than coal to meet the requirement of blast furnace. The coal used is usually low-ash and low-sulphur bituminous coal and quite expensive in comparison to other coals. It is heated up to around 1200°C in the absence of air, to perform a pyrolysis. The produced gas is a side product called Coke Oven Gas (COG), which is burned on-site to produce the heat required, or exported to other units of the steel plant as a fuel or a feed gas. Finally, the COG in excess is burned to generate electricity. The coking plant results in large amounts of CO_2 emissions (824 kg $_{\text{CO2-eq}}$/t $_{\text{liquid steel}}$, Table 1).

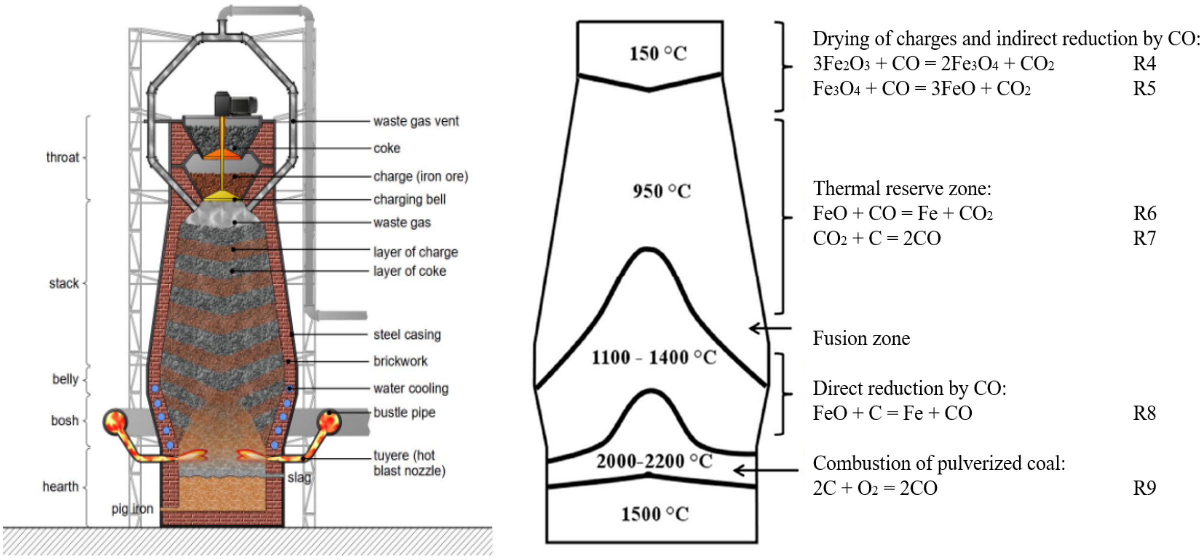

Figure 4. Diagrams of installation (a) and reactions (b) of a blast furnace [87]

The BF has been largely studied technically and theoretically over the last century and its internal behaviour is thoroughly understood. It is composed of five physical zones: throat, stack, belly, bosh and hearth as shown in Figure 4a and five operating zones represented in Figure 4b. The mineral load consists of alternative layers of coke and sinter. This solid is fed at the throat. In the throat and the higher part of the shaft, the sinter is heated from 100°C to 800°C and the hematite (Fe_2O_3) and magnetite (Fe_3O_4) are gradually reduced to wustite (Fe_xO) by the indirect reduction with CO (R4-R5). The reducing agent CO here is produced mainly by the reaction of Boudouard (namely the gasification of the coke by CO_2, R7, Figure 4) in the thermal reserve zone. Then the solid enters into the thermal reserve zone, the temperature increases to about 950°C. The thermal reserve zone extends over several meters due to the equilibrium between the reduction from wustite to iron (R6) and the Boudouard reaction (R7). In the lower part of the shaft, the temperature continues to increase up to 2200°C thanks to the heat provided by the hot blast injected at the tuyeres and the combustion of pulverized coal (R9) injected at the tuyeres as well. The fusion of mineral matters and the direct reduction from wustite to iron (R8) by solid carbon takes place at such a temperature. In the hearth, the remaining iron oxides are reduced to hot metal in liquid phase with some slag. Taking all the fossil carbon into account, the total emission of blast furnace is about 1279 $\text{kg}_{\text{CO2-eq}}/\text{t}_{\text{liquid steel}}$, nearly two thirds of the conventional route.

The BOF is a converter in which oxygen is fed to reduce the carbon content of the pig iron typically 4% to less than 2% (usually 0.1-0.2%) and thus form low-carbon steel. Here “low carbon” refers to the carbon content of the steel, not for the CO_2 emissions of the process. DRI and ferrous scrap may be added to the pig iron. Modern BOFs will take a charge of iron of up to 400 tonnes and convert it into steel in less than 40 minutes. The CO_2 emissions of the BOF are 202 $\text{kg}_{\text{CO2-eq}}/\text{t}_{\text{liquid steel}}$.

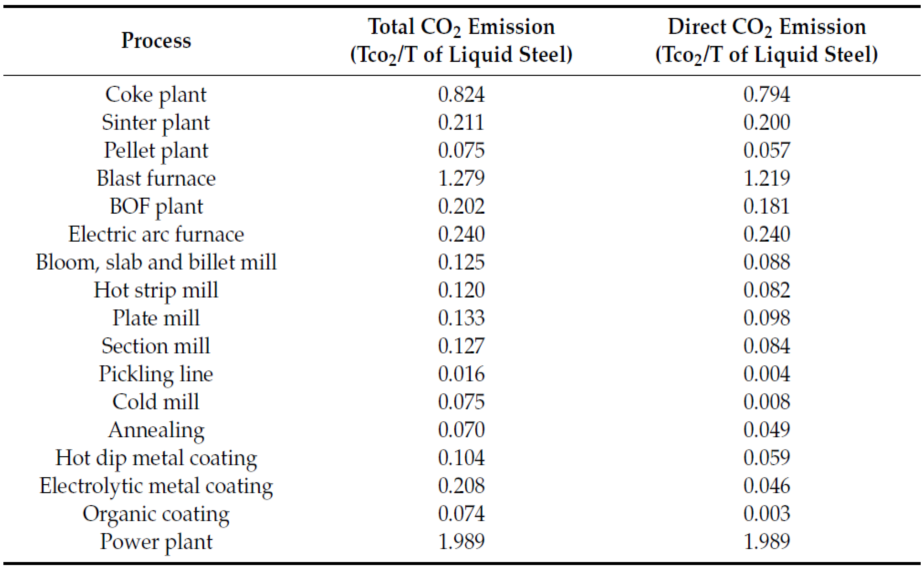

Process	Total CO_2 Emission (Tco_2/T of Liquid Steel)	Direct CO_2 Emission (Tco_2/T of Liquid Steel)
Coke plant	0.824	0.794
Sinter plant	0.211	0.200
Pellet plant	0.075	0.057
Blast furnace	1.279	1.219
BOF plant	0.202	0.181
Electric arc furnace	0.240	0.240
Bloom, slab and billet mill	0.125	0.088
Hot strip mill	0.120	0.082
Plate mill	0.133	0.098
Section mill	0.127	0.084
Pickling line	0.016	0.004
Cold mill	0.075	0.008
Annealing	0.070	0.049
Hot dip metal coating	0.104	0.059
Electrolytic metal coating	0.208	0.046
Organic coating	0.074	0.003
Power plant	1.989	1.989

Table 1. Estimated CO_2 emissions per tonne of product, in European iron and steelmaking industry [30]

The total CO_2 emissions of the conventional route reaches up to 1989 $\text{kg}_{\text{CO2eq}}/\text{t}_{\text{liquid steel}}$, which is huge. Alternative route DRI-EAF was created in 1950s and is much more environmentally friendly. The following studies are dedicated to the presentation of this alternative route.

II.1.2 Direct reduction route (DRI-EAF)

In the DR process, the sintering plant is replaced by a pelleting plant, the BF is replaced by a shaft furnace or rotary kiln, and the coking plant is no longer necessary, which leads to a great cut of 50% in the CO_2 emissions.

In the shaft furnace process, iron ore is loaded in the furnace in the form of pellets or lump ore, mainly composed of hematite and residual inert matters, also known as gangue. The characteristics of pellets or lump ore for gas-based reduction process are listed in Table 2. [31] The pellets or lump ore are reduced at solid state with a reducing gas H_2+CO, so called syngas. The product consists of porous metallic pellets called direct reduced iron (DRI) or sponge iron. DRI can be discharged hot and directly fed into a briquetting machine for the production of Hot Briquetted Iron (HBI). HBI is far more resistant to re-oxidation, so it can be exported by sea to steelmaking plants and rolling mills in other countries.

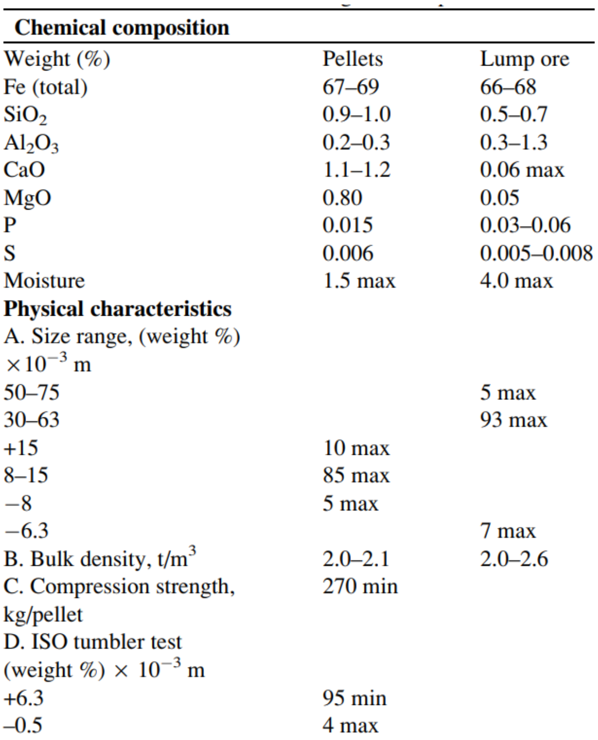

Chemical composition		
Weight (%)	Pellets	Lump ore
Fe (total)	67–69	66–68
SiO_2	0.9–1.0	0.5–0.7
Al_2O_3	0.2–0.3	0.3–1.3
CaO	1.1–1.2	0.06 max
MgO	0.80	0.05
P	0.015	0.03–0.06
S	0.006	0.005–0.008
Moisture	1.5 max	4.0 max
Physical characteristics		
A. Size range, (weight %) $\times 10^{-3}$ m		
50–75		5 max
30–63		93 max
+15	10 max	
8–15	85 max	
−8	5 max	
−6.3		7 max
B. Bulk density, t/m^3	2.0–2.1	2.0–2.6
C. Compression strength, kg/pellet	270 min	
D. ISO tumbler test (weight %) $\times 10^{-3}$ m		
+6.3	95 min	
–0.5	4 max	

Table 2. Characteristics of ore for gas-based process [31]

Compared to scrap, the DRI has less nonferrous impurities, which makes it easier for the steelmaking in EAF. In the EAF, the main heat source is provided by graphite electrodes and the solid is melted into a liquid phase. Different additives elements are added in order to remove the impurities and form a foaming slag at the surface of the liquid steel. The advantages of the DRI-EAF lie in:

- EAF is usually much smaller than the conventional steelmaking reactors, which makes the installation favourable in developing countries and closer to markets,

- EAF has more flexibility, and can be rapidly stopped and restarted, which is not the case for blast furnaces. The share of the DRI in the ferrous charge ranges from small amounts to 100% depending on different plants,
- EAF requires mostly electricity for the energy demand, and the electricity could come from clean sources in terms of CO_2 emissions, for example, nuclear power plants in France. The DRI-EAF route decreases by 50-60% of GHG emissions of the BF-BOF routes.

DR processes are divided into two different types: gas-based and coal-based. The gas-based direct reduction is kinetically faster than coal-based direct reduction, and requires lower operating temperature. As a result, it leads to lower CO_2 emissions, higher yield and less energy consumption in comparison to coal-based direct reduction technologies. [32] Besides, the reducing gas is composed of mainly H_2 and CO and it may be produced from various ways, using natural gas, low-quality coal or biomass as well. This flexibility can largely simplify the installation of direct reduction furnaces in countries with various sources of energy. In addition, the use of gas rather than coal avoids the presence of residual coal ash in the output solid. [33] At present, the gas-based furnaces, which are more convenient and environmentally friendly, are dominant in the market, representing about 90% of the global production of the DRI. The following part presents the evolution of gas-based process since its creation in 1950s.

II.2. Different types of gas-based process

The gas-based process in general consists of a reducing furnace for the reduction of iron ore to metallic iron and a gas reforming section for increasing the reducing potential of raw gases. The gas reforming encompasses the decomposition of methane by CO_2 and H_2O as reaction (10) and (11), also known as dry and steam reforming, respectively.

$$CH_{4(g)} + CO_{2(g)} \rightarrow 2CO_{(g)} + 2H_{2(g)} \qquad \text{R10}$$

$$CH_{4(g)} + H_2O_{(g)} \rightarrow CO_{(g)} + 3H_{2(g)} \qquad \text{R11}$$

Though the reactors are different, all the gas-based furnaces require large amounts of natural gas. According to Chatterjee, the specific consumption is around 300-350 Nm^3 per tonne of DRI. [33] Table 3 reveals that the natural gas is mainly composed of CH_4, CO_2, N_2 and C_2H_6. [31] Different types of reducing furnaces exist: shaft furnaces, fluidized beds, and retorts in most cases. These reactors are presented in the following.

Chemical analysis	Volume (%)
CH_4	75 min
C_2H_6	0–25
C_3H_8	0–4
C_4H_{10}	0–2
+ C_4 hydrocarbons	0–0.5
CO_2	Max 20
N_2	Max 20
S	Max 20 ppm wt

Table 3. Composition of natural gas for gas-based process [31]

II.2.1 Retort reactor (First HYL process)

Based on several retort reactors, the HYL process was first built in 1957 in Monterrey, Mexico. The process had an important role in the early history of gas-based process and is worth to be introduced here even though it is not used any more.

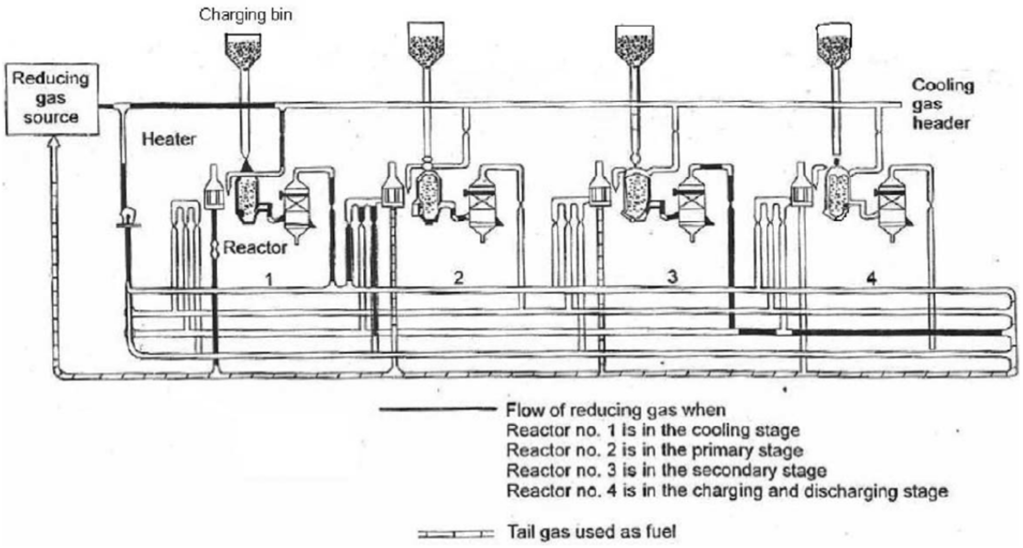

Figure 5. Flow sheet of the HYL I process [31]

The flowsheet of the HYL I (first generation) is shown in Figure 5. [31] The process is composed of one gas reformer and four vertical units (retort reactors) in different stages: cooling stage (unit 1), primary reduction stage (unit 2), secondary reduction stage (unit 3), and charging and discharging stage (unit 4). Each stage needs about three-hour operation. In the first step (unit 4), reactor loading follows reactor discharging. In the second step (unit 3), the gas is the partially depleted reducing gas flowing out of the unit 2. The partially depleted reducing gas is dehumidified and heated up to 1040°C to increase its reducing potential for the secondary reduction, which accounts for about 40% of the oxygen removal. The waste gas after unit 3 becomes fuel gas to heat the whole plant. In the third step of primary reduction (unit 2), fresh reducing gas after unit 1 is dehumidified and heated up to 1040°C and reduces the remaining oxides in the iron ore. In the beginning of the third step, the shift of gas is by means of automatic valve manipulation. In the fourth step (unit 1), the cold, dry reducing gas is introduced for cooling down the reduced iron ore and for carbon deposition.

Regarding the production of reducing gas, the natural gas is reformed in a catalytic steam reformer to produce H_2 and CO. The reformed gas (75% H_2, 14% CO, 7% CO_2 and 4% CH_4) flows into the quench tower to remove the excess water and into the cooling unit. Though the produced DRI has an enough good quality, the number of reactors and the complexity of the system make the process hard to control. Thus, investigations were carried out to the simplify and better control the system. The HYL III that is a great improvement in comparison to HYI I and II will be introduced in the following part.

II.2.2 Shaft furnaces

II.2.2.1 HYL III process

In 1979, the HYL III process was created as the improved process from HYL I. The main difference is the substitution of four reactors by a single shaft furnace at high pressure (6-8 bar) and the reducing gas introduced only once in the lateral side of the shaft furnace. This process accounts for 17-20% of global production of DRI, which represents about 11Mt annually. [33] The details of the HYL III are shown in Figure 6: [33]

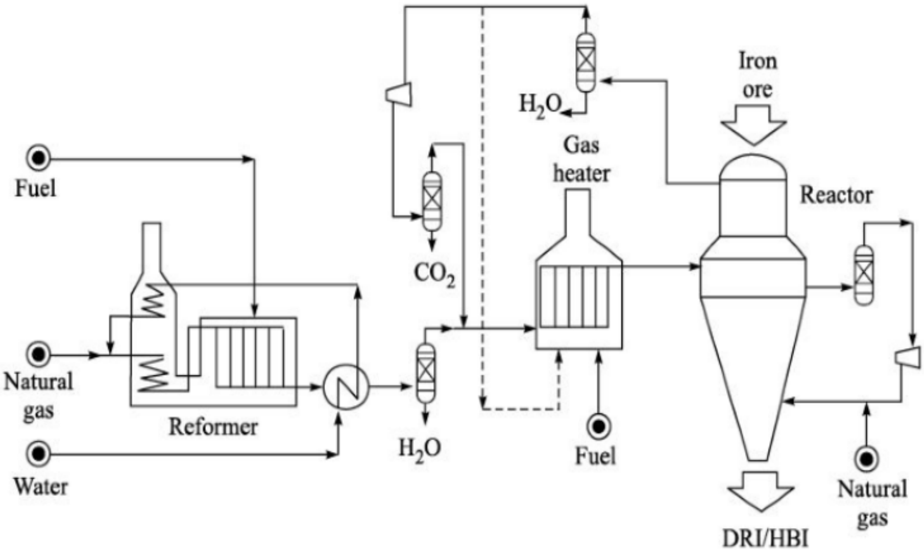

Figure 6. Flow sheet of the HYL III process [33]

The iron ore (pellets or lump ore) is fed through a sealing mechanism. An automated valve system pressurises and depressurises the inlet vessels. The solid charge descends by gravity. The fresh reducing gas produced by the natural gas reformer is mixed with recycled, processed and heated top gas. The mixed gas is then introduced in the top side of the furnace, which is the reducing zone. In the lower zone, the solid is cooled down by the cooling gas, which is recycled by means of a gas compressor. After cooling, the DRI is discharged through a sealing mechanism similar to that of the reactor inlet.

An important feature of the HYL III is the production of high-carbon DRI thanks to the high temperature (930°C) in the shaft and to the sufficient methane concentration in the reducing gas. Due to the endothermicity of the reforming reaction and the carburisation of metallic iron, the shaft furnace requires a combustion chamber for partial combustion of methane to obtain adequate heat. In order to simplify the plant, the fourth generation combines the functions of the reformer and shaft furnace in a single shaft furnace, called self-reforming.

II.2.2.2 HYL IV M with self-reforming (HYL ZR)

The HYL IV M with self-reforming was first developed in 1991 at pilot scale in Venezuela and then at industrial scale at the Monterrey HYL plant in Mexico with a capacity of 675,000 tonnes of DRI. The self-reforming requires three criteria: adequate availability of oxidising components (CO_2 or H_2O), high temperature and presence of a catalyst. All these conditions are fulfilled in the lower zone of the shaft furnace, where the amount of oxidising gas is controlled, the metallic iron acts as catalyst.

In this process, natural gas is sent with the recycled gas into a humidifier as shown in Figure 7. [34] This mix is first preheated in a heat recuperator and then heated in a gas heater to 900°C. In order to promote the reforming reactions, oxygen is added on this hot gas before the shaft furnace, which leads to a very partial combustion of the reducing gas for increasing the temperature up to 1020°C. In the lower part of the reduction zone, reforming reactions take place as soon as the hot gas comes into contact with the metallic iron. In the meantime, the carburisation occurs due to the presence of CH_4, which is beneficial to increase the carbon content. As a result, the amount of water in the humidifier is an operating parameter to adjust the carbon content in the DRI. In the upper part of reduction zone, the gas flows upwards against solids and reduces the iron oxides gradually.

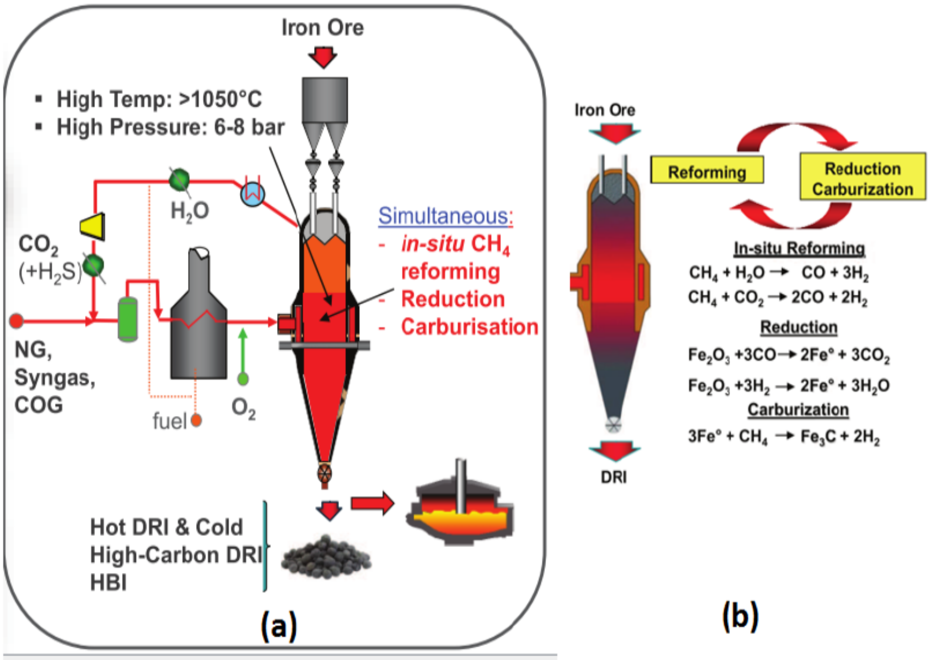

Figure 7. HYL ZR flow sheet and related reactions [34]

Compared with the HYL III process, HYL ZR consumes less energy, less capital cost and has no sensitivity to sulphur. As previously said, HYL process produces about 20% of global DRI; the rest of the production mainly comes from a competitor process, the "Midrex process", which is presented in the following.

II.2.2.3 Midrex process

The Midrex process has built over 70 shaft furnace modules in 21 countries worldwide since 1969 when Midland Ross Corporation of Cleveland, USA first developed it. The production of DRI by the Midrex process accounts for approximately 65% of global production, which represents 47 Mt in 2016. [35] The size of Midrex reactors has gradually increased in diameter, from 4.25 m to 7.15 m since the creation, and the consequent annual production of DRI reaches 2 million tonnes annually for the most recent Midrex plants. [36] The Midrex process is composed of a shaft furnace, a gas reformer section and a cooling section for the reduced iron as shown in Figure 8. [33]

In the shaft furnace, the mineral load consisting of iron ore pellets or lump ore is fed at room temperature under atmospheric pressure. The pellets are mostly used to facilitate the solid flow in the shaft and for their superior physico-chemical properties. The solid descends by gravity and is heated by the hot reducing gas flowing counter-currently. The iron oxides are reduced by steps in the reduction zone, following Fe_2O_3-Fe_3O_4-FeO-Fe. After the reduction, the DRI crosses the transition zone and is then cooled down in the lower part of the shaft by the cooling gas.

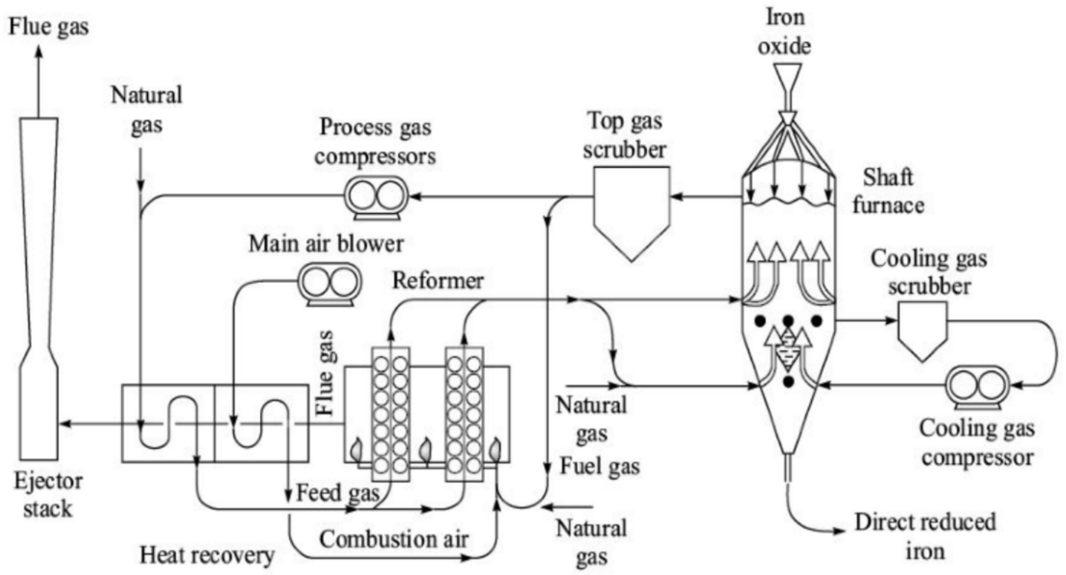

Figure 8. Flow sheet of Midrex process [33]

The syngas is produced in a separated reformer containing mainly CO_2 and H_2O as reactants and nickel as catalyst. Natural gas is mixed with the cleaned and recycled top gas and introduced in the reformer at around 900°C. The reformed gas (50-60% H_2 and 30-40% CO) is then injected into the shaft furnace directly at high temperature (about 950°C) at the bottom of the cylindrical part of the shaft. All the heat required is produced by the combustion of part of the recycled top gas and natural gas.

In the cooling section, a cold gas made of methane and an inert gas is introduced at the bottom of the conical part at a temperature below 100°C to cool down the produced DRI. In this part, the decomposition of the methane leads to the carburization of the DRI and to an additional production of CO-H_2 in the shaft. The cooling gas is collected below the reducing zone and recycled in the cooling loop.

Midrex and HYL processes are the main gas-based technologies for direct reduction. However, for a complete presentation of the gas-based processes, the fluidised bed technology, which works with iron ore fines, is presented next.

II.2.3 Fluidised bed process

This type of process uses directly iron ore fines in suspension in a fluidised bed for reduction. The use of iron ore fines has the advantage to avoid the costly preparation of pellets or lump ore. However, these processes, which work with a series of units (four fluidised beds for the

Finmet process) are more difficult to control and operate. In addition, the fines are easily carried out in the top gas that needs to be processed consequently.

I.2.3.1 Finmet process

Base on Fior process (Fluidised iron ore reduction) developed by Esso Research and Engineering Company in USA, Finmet process was investigated jointly by Fior in Venezeula and Voestalpine in Australia. Two commercial plants were built: Orinoco iron at Puerto Ordaz in Venezeula in 1999 with a capacity of 2 Mtpa and BHP plant at Port Hedland in Australia with a capacity of 2.5 Mtpa.

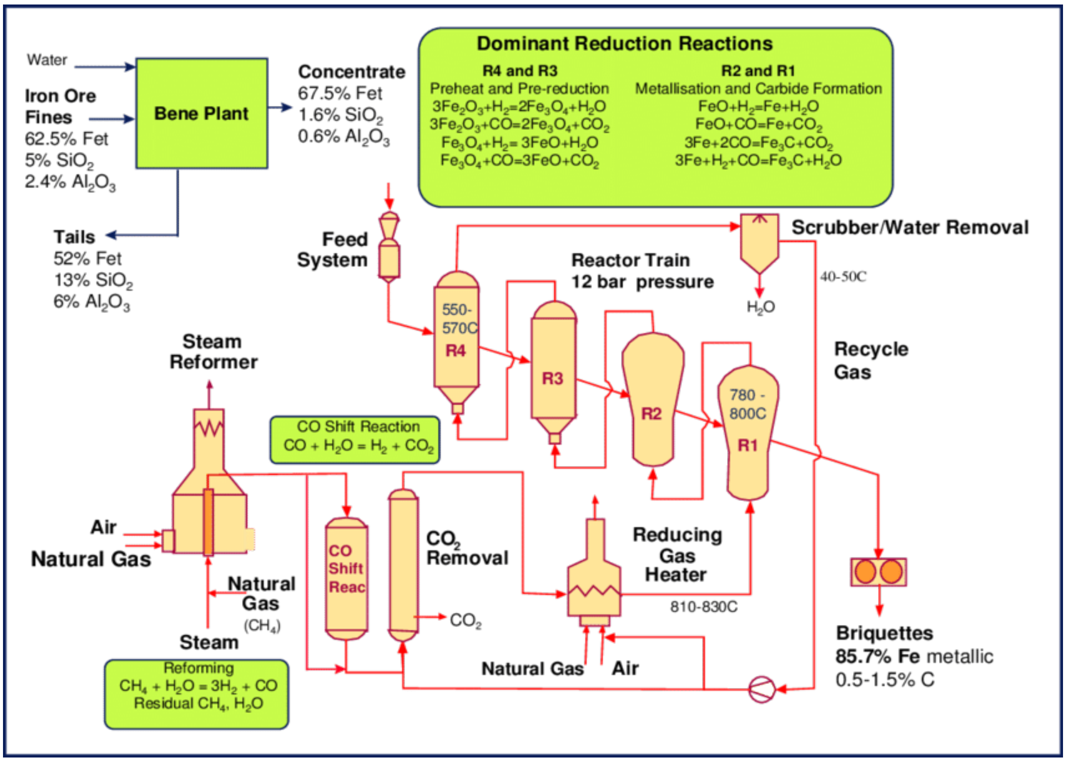

Figure 9. Flow sheet of the Finmet process [37]

The process is constituted of four fluid-bed reactors at 10.8-12.8 atm. in which the iron ore fines and the reducing gas flow counter-currently, like in the shaft furnaces, as shown in Figure 9. [37] The fines in diameter of less than 12 mm are charged in the Reactor 4 by a pressurised lock hopper system and get pre-heated to 550-570°C by the reducing gas leaving from Reactor 3. After gradual reduction in Reactor 3 and Reactor 2, the final stages of reduction take place in Reactor 1 at 780-800°C with fresh reducing gas after CO_2 removal. The reducing gas is composed of the recycled top gas and fresh reformed gas produced by a steam reformer. The hot fines DRI are then briquetted and cooled on a cooling conveyor. Another system of fluidised reactors is the Circored process that is of particular interest nowadays because it only uses hydrogen as the reductant.

II.2.3.2 Circored process

The first Circored process with a capacity of 500,000 tpa was built in Trinidad and Tobago in April 1999. The plant was operated for a few years in the early 2000s but stopped its activities for economic reasons. The flow sheet is shown in Figure 10. [38]

CIRCORED is a process for the reduction of fine ore via two fluidised beds in series at four bars: a CFB (circulating fluidised bed) which reaches a pre-reduction of 50-70% metallisation and a FBB (fluidised bubbling bed), where the reduction is completed to 93-95% metallisation. The iron ore fines (0.1 to 2 mm) are first preheated and calcined at 800ºC before being fed into the first reactor (CFB). A 20-min residence time in the CFB results in 70-80% oxygen removal. The remaining oxygen is removed in the FBB within 4 hours. The reduced product from FBB is then heated to approximately 700ºC before the hot briquetting process.

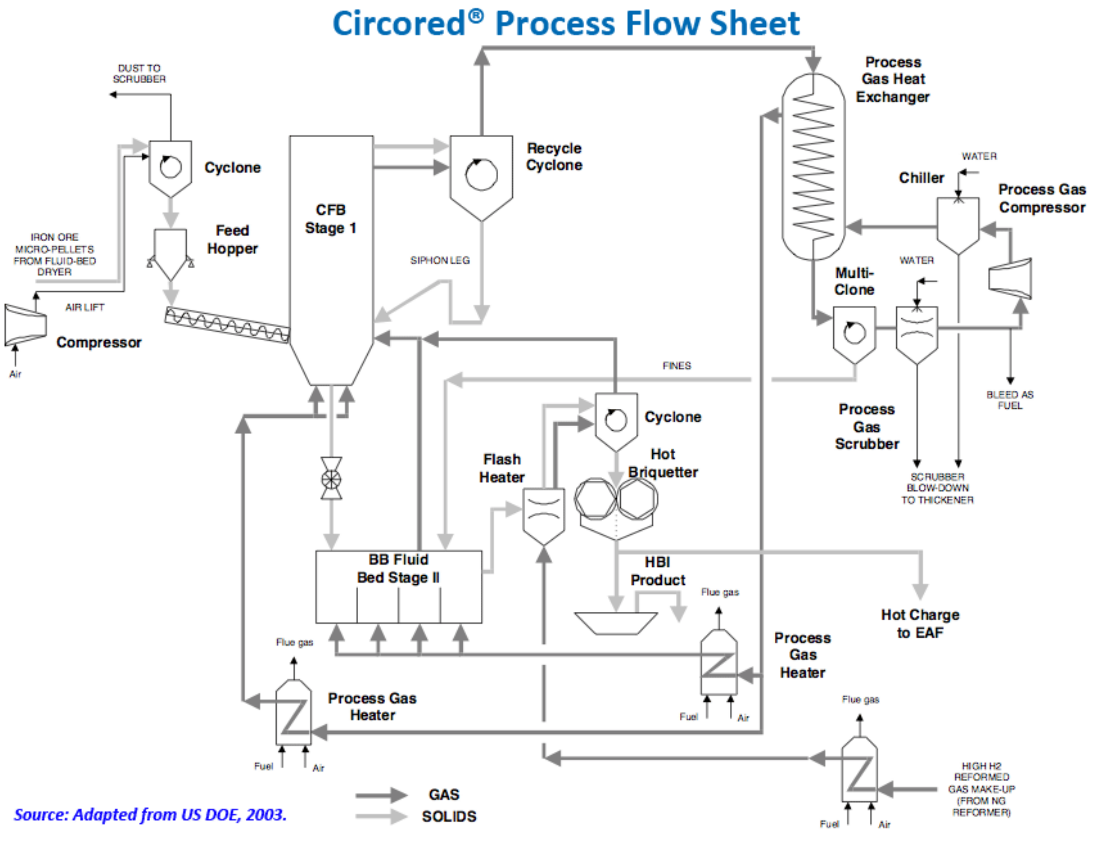

Circored® Process Flow Sheet

Source: Adapted from US DOE, 2003.

Figure 10. Flow sheet of the Circored process [38]

Hydrogen was produced from the reforming of natural gas and the consumption of natural gas was higher than that of the other processes previously mentioned. At low temperature, less than 650°C, the iron ore fines can be reduced without sticking if the operating pressure and the flow rate are sufficiently high.

All the gas-based processes presented here rely on natural gas to produce the reducing gas, which results in consequent GHG emissions, even if those emissions remain significantly lower than the emissions of the BF route. To go further, pure hydrogen could be used instead of the syngas. This is a very topical option, studied in our group at IJL. [3] [39] [40]

One of the most promising proposals is the use of renewable biomass as feedstocks to produce the reducing agents. Biomass could be used both in the BF or the EAF route. Different options are presented in the following.

II.3. Reductions of the iron oxides by CO and H_2

In general, iron is in the form of hematite (Fe_2O_3) or magnetite (Fe_3O_4) in the ores as mentioned in II.1.1. The blast furnace and the shaft furnace make use of CO and H_2 for the reduction of the iron oxides. For this reason, we will present here the thermodynamic mechanisms of R1-6. During the reduction of hematite, two intermediate oxides are successively formed at temperatures above 570°C (below this temperature, wustite does not appear), according to the Fe-O stability diagram (Figure 11).

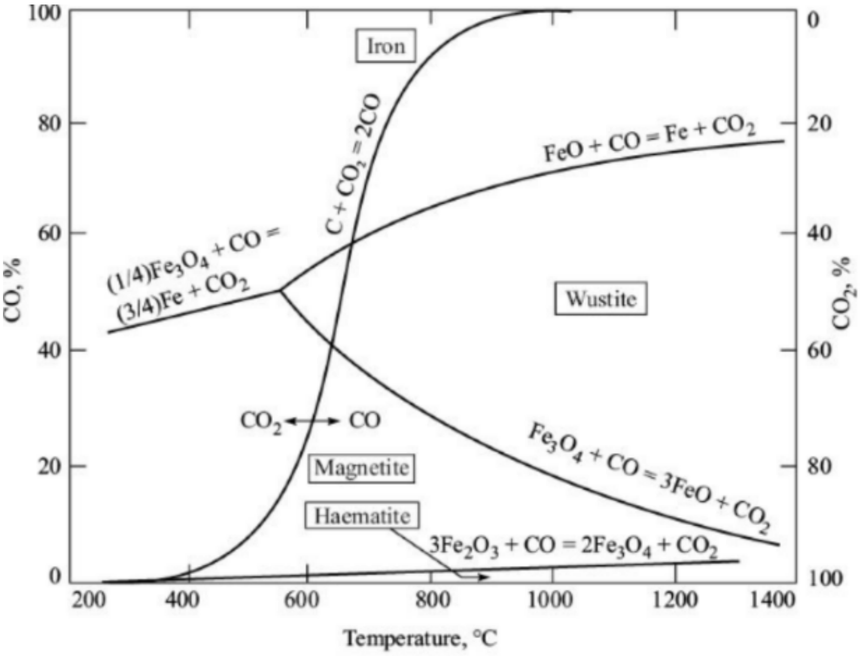

Figure 11. Fe-O stability diagram [33]

The reduction reactions of iron oxides are characterized by the degree of reduction R (oxygen eliminated compared to the total oxygen bound to iron before the reduction) and by the degree of metallization M (iron present as metallic iron Fe compared to the total iron in the final product). The charged iron ore can be graded lump ore or agglomerates such as pellets or micro-pellets. Pellets (10 to 20 mm in diameter) and micro-pellets (1 to 8mm diameter) are produced by pelletizing different fractions of ore fine. Then the agglomerated fines are heated at high temperature to obtain sufficient mechanical resistance for the requirements of reduction reactors. Therefore, there are differences in the physical properties of these various types of ores and agglomerates (granulometry, specific surface and porosity), which affects the reducibility. The mineralogy also has a strong influence since hematite, magnetite or wustite are not reduced in the same way. The constituents of the gangue (silica, alumina, lime, etc.) are also involved in the reaction. Silica, for example, leads to the formation of iron silicate, which modifies the equilibrium. [41]

Hematite, named from its blood red color, is the iron oxide, which has the highest degree of oxidation (Fe^{+3}). Magnetite is a natural magnet and it is a crystal composed of a mixture of iron ions: one mole of Fe^{2+} and two moles of Fe^{+3}. The notation FeO is a simplification to designate the wustite which is a non-stoichiometric oxide, often represented as Fe_xO or $Fe_{1-y}O$, where the letter x denotes the ratio between the number of vacancies present and the total number of positions available for Fe^{2+} ions. The perfect FeO crystal (cubic NaCl type) would contain as many Fe^{2+} ions as O^{2-}. The deviation from stoichiometry results from a lack of Fe^{2+} ions in the crystal lattice, and the corresponding place is taken by neutral vacancies. To respect the electroneutrality, the lack of a Fe^{2+} is compensated by the presence of two Fe^{3+} ions near the gap (See Figure 12). [42] Around 800°C, the stoichiometry of wustite is between $Fe_{0.95}O$ (equilibrium with iron) and $Fe_{0.89}O$ (equilibrium with Fe_3O_4).

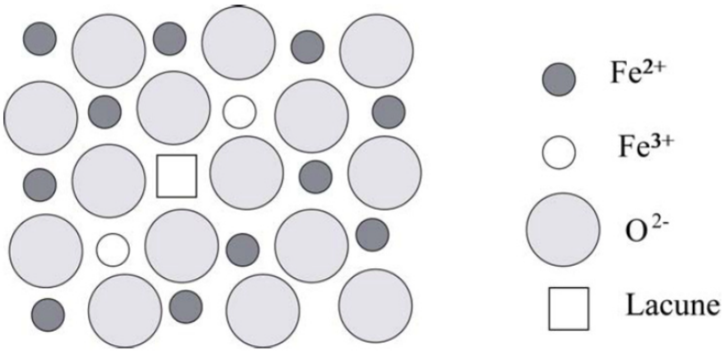

Figure 12. Diagram of the structure of wustite [42]

Regarding stoichiometric try, the reduction of hematite to iron by H_2 is identical to that by CO. Concerning the thermal aspect, one of the main differences is that the reaction by H_2 is globally endothermic, contrary to the reduction by CO, which is rather exothermic. Figure 13a shows the enthalpy change of the reduction reactions of the different iron oxides by H_2 (R1-3, solid lines) and by CO (R4-6, dotted lines) as a function of temperature. The values of $\Delta_r H_{reac}$ values are those obtained from the COACH database (v. 3.4) of the ThermoSuite software by

Thermodata (Grenoble, France), taking $x = 0.95$ for the composition of the wustite. From the figure, it can be seen that, for all the reactions by H_2, only the reduction of hematite to magnetite is slightly exothermic ($\Delta_r H_1$ between 0 and -10 kJ/mol) below 700ºC. In contrast, the reductions of the other two oxides (reactions 2 and 3) are always endothermic between 580 and 1300ºC. It is therefore important to provide enough heat for the reduction of iron oxides by H_2. On the other hand, for all the reactions by CO, only the reduction of magnetite to wustite (reaction 5) is endothermic ($\Delta_r H_5$ between 17 and 22 kJ/mol), while reactions 4 and 6 are always exothermic ($\Delta_r H_4$ between -40 and -25 and $\Delta_r H_6$ between -20 and -15 kJ/mol).

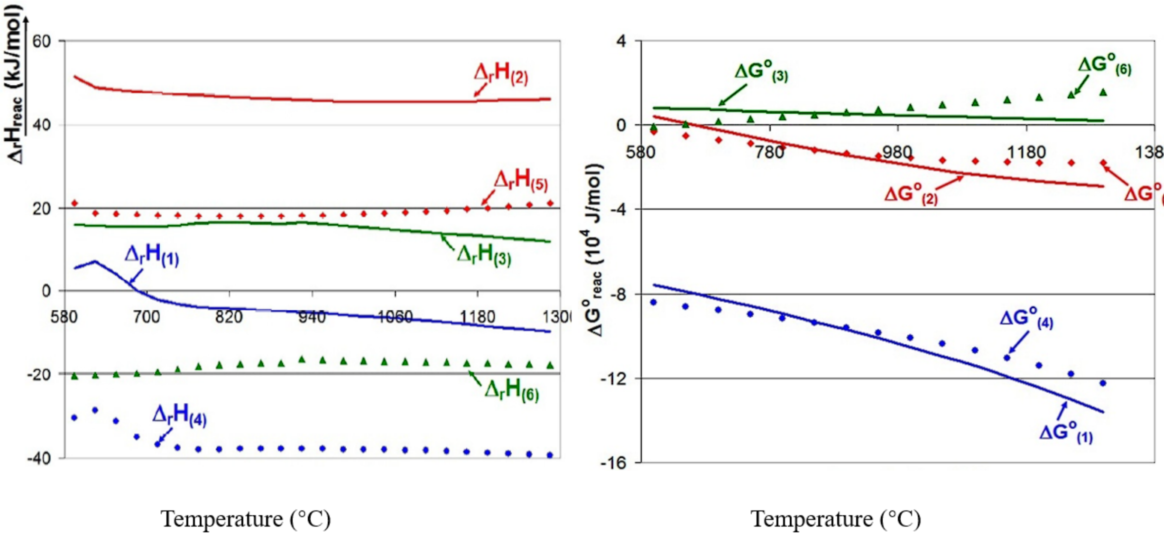

Figure 13. Enthalpy changes and Gibbs energy changes of the reduction reactions [15]

Figure 13b shows the Gibbs energy changes of each reaction ($\Delta G^o_{(n)}$) as a function of temperature. Only the reduction reactions of wustite to iron, by H_2 and by CO, show slightly positive values of the $\Delta G^o_{(n)}$. In contrast, the value of $\Delta G^o_{(3)}$ decreases with increasing temperature in the case of reduction by H_2 and that of $\Delta G^o_{(6)}$ increases in the case of CO. For the other reactions, the values of Gibbs energy changes are always negative and decrease with increasing temperature, especially in the reduction from hematite to magnetite.

However, each of the reactions is a heterogeneous equilibrium which is influenced not only by the temperature, but also by the composition of H_2 and H_2O in the gas (in the reduction by H_2), or CO and CO_2 (in the reduction by CO), according to the following equations of the free enthalpy of reaction:

$$\Delta G_{(n)}(T) = \Delta G^o_{(n)}(T) + RT\ln\left(\frac{p_{H_2O}}{p_{H_2}}\right) \qquad \text{II-1}$$

$$\Delta G_{(n)}(T) = \Delta G^{o}_{(n)}(T) + RT \ln\left(\frac{p_{CO_2}}{p_{CO}}\right) \qquad \text{II-2}$$

Thus, the reduction reactions of a given oxide may or may not take place ($\Delta G_{(n)}(T) < 0$) or ($\Delta G_{(n)}(T) > 0$) after calculating the value of $\Delta G_{(n)}(T)$.

The Chaudron diagrams of reduction by H_2 (Figure 14a) and by CO (Figure 14b) show the stability ranges of the different iron oxides as a function of temperature and oxidising potentials of gases. The lines of the diagram represent, for each temperature and each reaction, the concentration of H_2O and CO_2 in the gas where two solids are in equilibrium. The lines a and a' correspond to the equilibrium of the Fe_3O_4-FeO reaction, while the lines b and b' correspond to the FeO-Fe equilibrium. Finally, the segments c and c' represent the equilibria of the Fe_3O_4-Fe reduction below 570°C, by H_2 and by CO respectively. In practice, the reduction from hematite to magnetite is very favourable, thus not shown in the figure. The arrows shown in the diagrams in Figure 14 represent the values of driving forces of the reduction reactions (by the values of (xH_2-$xH_{2,eq}$) and (xCO-$xCO_{,eq}$)) at 600, 800 and 1200ºC for the reduction from FeO to Fe under 100% H_2 or CO atmosphere. We can clearly see that the reduction by H_2 is thermodynamically more favourable at high temperatures as opposed to CO reduction by the length of blue arrows. In fact, it becomes more favourable by H_2 than by CO from 800°C. The ratio of CO and H_2 to a large degree influences the reduction behaviour.

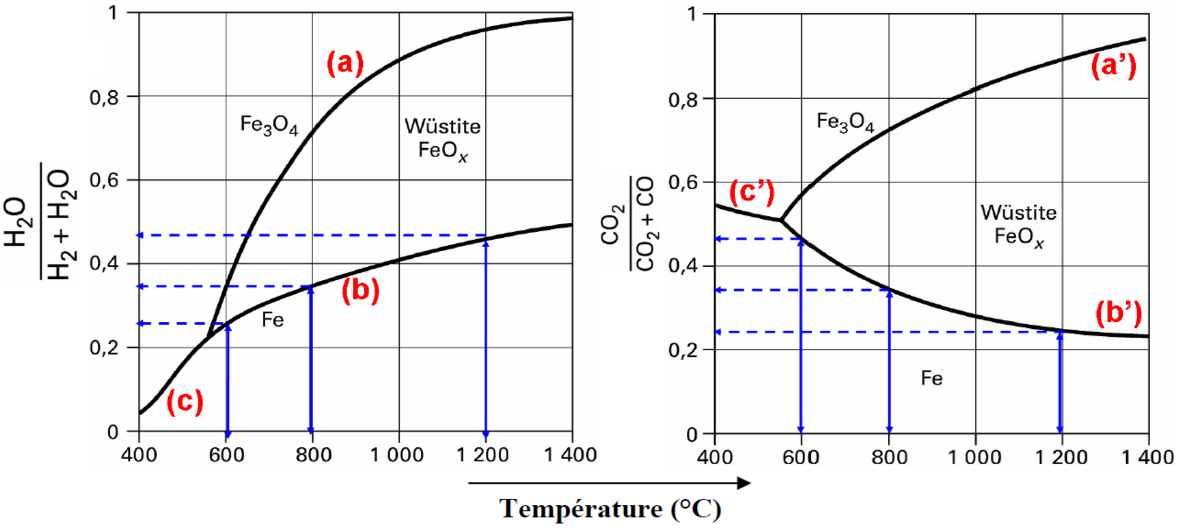

Figure 14. Chaudron diagrams for reduction reaction by H_2 and CO [15]

In the case of reduction by CO, the carbon deposition in the form of atomic carbon and cementite can take place by the Boudouard reaction and the formation of cementite (R12).

$$2CO_{(g)} \leftrightarrow C_{(s)} + CO_{2(g)} \qquad \text{R7}$$

$$3Fe_{(s)} + 2CO_{(g)} \leftrightarrow Fe_3C_{(s)} + CO_{2(g)} \qquad \text{R12}$$

These reactions only occur at relatively low temperatures (below 1000°C) and high CO concentrations. [43]

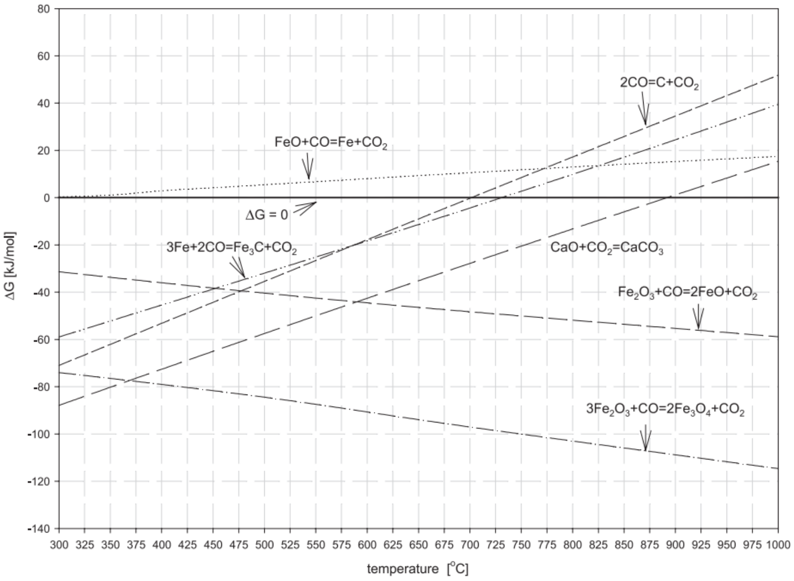

Figure 15. Gibbs free energy as a function of temperature [44]

Figure 15 shows that the standard Gibbs energies change (ΔG^o) with temperature of the reduction of iron oxides to iron by CO are, in principle, favoured by high temperatures, in contrast to the Boudouard reaction and the formation of cementite, which are not thermodynamically favoured at temperatures above 700°C.

II.4. Biomass use in ironmaking

II.4.1. Definition of biomass

In general, biomass can be considered as all the organic matter of plants and animals. The European regulation defines it more precisely as "the biodegradable fraction of products, waste and residues from agriculture, forestry and agriculture, forestry and related industries, as well as the biodegradable fraction of industrial and municipal waste". In order to differentiate them, the Ministry of Ecology, Sustainable development, transport and housing (2010) classified biomass resources into five categories according to their origin: [45]

- Wood: it can be in original form or in pieces;
- Wood by-products: corresponding to all the waste from the forestry (branches, bark, sawdust), sawmills (sawdust, wood chips), wood processing industries (carpentry, furniture, parquet), panel or packaging manufacturers;
- Industrial by-products: for example, sludge from the paper pulp industry (black liquor) and waste from the food industry;

- Products from traditional agriculture: cereals and oilseeds, residues such as straw, bagasse;
- Organic waste such as municipal waste including sewage sludge, garbage, and waste, household waste, and agricultural waste such as agricultural effluents.

II.4.2. Advantages of biomass

The most significant advantage of biomass is its short life cycle of about 1 year for plants and 5-10 years for woody biomass:

- growth of biomass by the photosynthesis ($6CO_2 + 6H_2O + \text{light} = C_6H_{12}O_6 + 6O_2$),
- use of biomass (e.g. for ironmaking) and CO_2 emissions,
- recycle of the emitted CO_2 by growing of new biomass,

which results in an almost zero net CO_2 emissions. The second advantage lies in the fact that biomass is available almost everywhere, it is abundant and cheap. For this reason, biomass (mainly woody biomass) represents more than 3/4 of all renewable energy and 13% of the global energy supply. [46]

Biomass can grow in most places and in particular in the area of ironmaking plants, which avoid long distance of transportation, as it usually is the case with coal. Furthermore, it brings benefit to the local communities economically and provides the steel industry with a better opportunity to control the sustainability of biomass sourcing. [47]

Besides the large amount, the use of biomass-derived materials in the ironmaking plants is rather simple, without much modification or capital expenditure. Compared to coal, biomass is characterized by low sulphur content, low ash, high reactivity, high specific surface area and stable pore structure. On the other hand, it is important to control the content of potassium and chlorine to avoid negative impacts on the refractory materials. [48]

However, the direct use of raw biomass is limited, and most of it needs to be treated prior to injection in existing processes. These treatments will be described in the following part.

II.4.3. Requirements and treatments of biomass

Even though raw biomass has ecological and economic advantages, the direct use of raw biomass is not appropriate due to its high moisture, low density, high volatile content, low carbon content, high bulk volume, low calorific value, low grindability in addition to inconveniency and inefficiency in the transportation and storage. [48] Thus, a pre-treatment of raw biomass is necessary in order to meet the ironmaking requirements.

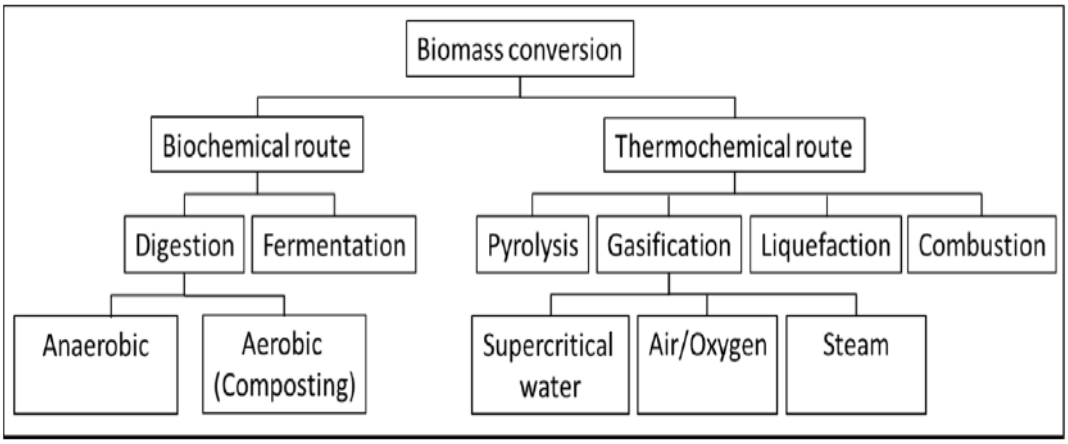

Figure 16. Schematic diagram for different options to convert biomass into bio-fuel [49]

The treatment consists of drying and densification of the biomass in order to reduce its porosity, moisture and bulk volume. The dried biomass can then be converted through a biochemical or thermochemical route as shown in Figure 16. [49] The former is not largely used in the ironmaking field because of the slow conversion rate by bacteria or enzymes, so attention has been paid to the latter. The thermochemical route lies in pyrolysis/torrefaction, gasification, liquefaction and combustion.

II.4.3.1 Pyrolysis

Pyrolysis is an old process for the thermal treatment of biomass. It refers to the thermal decomposition of organic matter in the absence of oxygen, resulting in the creation of three primary products, i.e., char, tar, and gas, in varying proportions.

Pyrolysis can be divided into two stages: primary phase at lower temperature (250°C to 300°C) and secondary phase (above 300°C). [50] The primary phase lies in the decomposition of hemicellulose and then cellulose to form bio-chars, incondensable gases (CO, CO_2, and CH_4) and bio-vapor as shown in Figure 17. [50] In the secondary phase, the bio-vapor continues to decompose and form some gas and bio-oil (tar) that can further produce char in the final stage. Based on different heating rates and residence time, the pyrolysis can be divided into three types: slow pyrolysis, fast pyrolysis and flash pyrolysis.

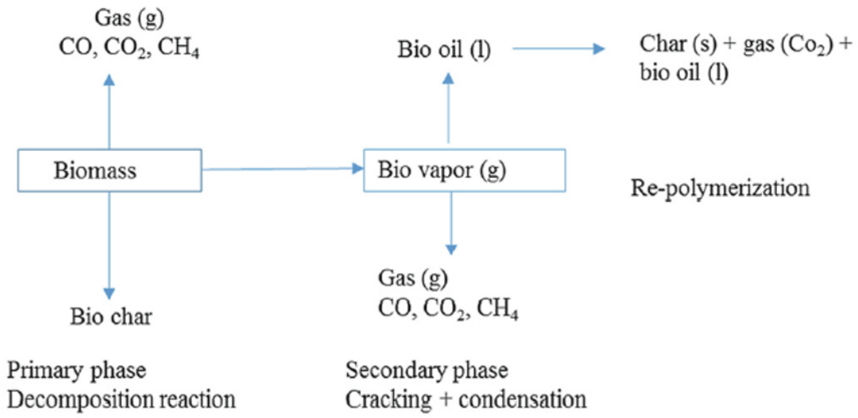

Figure 17. Primary and secondary mechanism of pyrolysis process [50]

Slow pyrolysis

In slow pyrolysis, also known as carbonization, biomass is heated relatively slowly in the absence of oxygen at the minimum heating rates ranging from 5-7°C/min and at the maximum heating rates ranging from 20-100°C/min. [51] [52] It reaches 400-650°C and lasts from 5 minutes to days. During the process, organic compounds are decomposed and rearranged, forming charcoals and bio-oils. The low heating rates, low temperature and long residence time lead to the maximum production of charcoal and the minimum production of bio-oil and gas. [53]

Fast pyrolysis

Fast pyrolysis results in the maximum production (50-70%) of high-quality bio-oil, which can be valorised to industrial fuel and transport fuel applications. [51] [54] The residence time is only of a few seconds or even less: it could range between 0.5-10s, but the most typical residence time for fast pyrolysis is shorter than 2s. In the process, organic compounds are heated to 600-650°C at up to 1000°C/s without oxygen, which causes the organic matter to decompose rapidly, producing mostly vapours and aerosols, with small amounts of gas and charcoal. [55] Another great feature is that it is feasible in various kinds of pyrolysis reactors, such as the vacuum furnace reactor, bubbling fluidised bed reactor, dragged-flow reactor, rotary reactor, and vortex reactor. [52]

Flash pyrolysis

Flash pyrolysis is named by its nature of extremely rapid residence time (<0.5s). It is featured by small particle sizes of less than 200 µm, heating rate of 1000-10000°C/s, and high operating temperature, usually more than 1000°C, contributing to the high production proportion of bio-oils up to 75-80 wt.%. However, flash pyrolysis is more difficult due to higher requirements on the mass transfer and heat transfer. [56]

II.4.3.2 Gasification

To maximize the production of incondensable gas, the process of gasification is prominent. It forms the produced gas (also called syngas, including mainly CO, CO_2, H_2, and CH_4), as well as tar, charcoal, and ash. Figure 18 depicts the potential paths of the gasification. [57] The process starts with drying and pyrolysis of biomass, which releases gas, tar and charcoal. Partial combustion of the released matter with a little amount of oxygen increases the temperature up to 700-1300°C for the following gasification. Gasifying agents include oxygen, air, CO_2 and steam. In the gasification zone, the char reacts with the gasifying agent and is converted into syngas by water gas reaction (R13), Boudouard reaction (R7 in Figure 4), water gas shift reaction (R14), and methane formation (R15).

$C + H_2O \rightarrow CO + H_2$ R13

$CO_2 + H_2 \leftrightarrow CO + 2H_2O$ R14

$C + 2H_2 \leftrightarrow CH_4$ R15

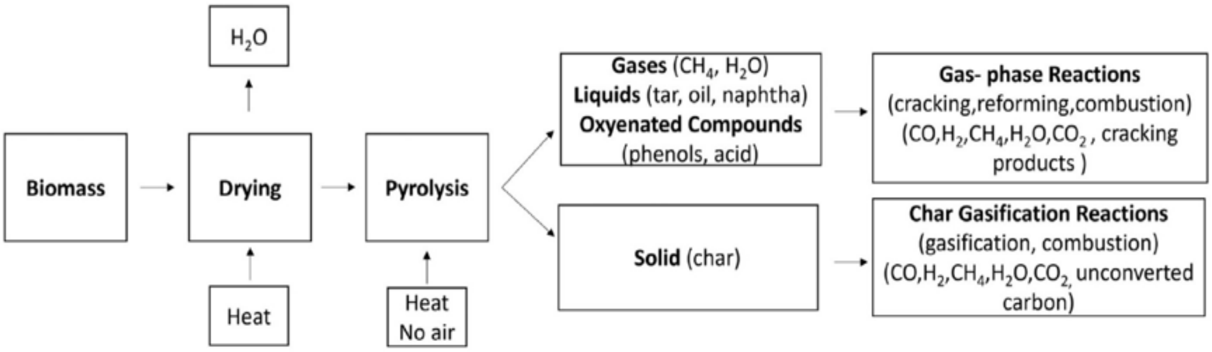

Figure 18. Potential paths of gasification [57]

II.4.3.3 Liquefaction

The hydrothermal liquefaction of biomass, also called direct liquefaction, is a thermochemical process of biomass which produces liquid fuels. The process is carried out in pressurized hot water for a period long enough for the decomposition of biopolymeric structures to form liquid fuels. The typical temperature lies between 523 and 647K and the pressure is in the range of 4 to 22 Mpa. The temperature provides the heat for the degradation of biopolymeric structures and the pressure is to maintain the treatment at liquid water phase. The process aims at valorizing the humid materials without drying. However, the process remained at small scale and the largest set up (Albany Facility) produced 52 barrels of product (approximately 8 m^3) over its life time. [58]

II.4.3.4 Combustion

Combustion is the most common route for using biomass due to its low cost and simplicity to operate. It is also beneficial and important in terms of economy and environment to valorise waste matters by combustion. A controlled biomass combustion needs carful maintenance and surveillance because of the risk of fire and monoxide emission in case of a lack of oxygen. In addition, various types of biomass exist and their chemical and physical properties differ with each other, so adapted measures need to be taken into account. Last but not least, the gas produced by combustion may induce environmental concerns as the release of atmospheric pollutants such as CO, hydrocarbons (HC), oxides of nitrogen and sulphur among others. Reactions among inorganic species may also occur and lead to fouling and slagging. [45] All these factors must be kept in mind for facilities implementation.

We will now focus on the potential use of biomass in the framework of iron and steelmaking. Many breakthrough options have been investigated and these can be divided into three categories: [59] [60]

- Gasification to produce reducing agent or fuel (CO)
- Injection into blast furnace, Corex or electric arc furnace
- Incorporation into coal blend for coking, composites, self-reducing pellets, fuel for sintering etc.

II.4.4. Applications of biomass in the iron and steelmaking

In the following part, we will discuss different uses of biomass in the main processes of the conventional steelmaking route and of the DRI-EAF route. In the conventional route, BF, sintering plant and coking plant are responsible for 90% of CO_2 emission. [36] For this reason, biomass use as substitute for fossil fuels in these units is of particular importance. In the gas-based direct reduction process, the reducing gas comes mainly from the natural gas and could be replaced by syngas coming from biomass. In the coal-based processes, fossil carbon could be replaced by charcoal as well.

II.4.4.1 Conventional route (BF-BOF)

In the conventional route, each of the three plants consumes significant amounts of fossil carbons that could be substituted by biomass, at least partially. This part will be devoted to a presentation of different possible substitutions. It will be divided into three parts: the coking plant, the sinter plant and finally the blast furnace.

Coking blend component for coke

Coke plays three fundamental roles in the BF: physical, chemical and thermal function. Physically, it stabilizes the descending burden thanks to its mechanical strength and provides a good permeability for the reducing gases due to its gradual degradation. Chemically, it reduces the iron ore indirectly (by CO) and directly (by C) and provides carbon in the metallic iron. Thermally, the combustion of carbon represents 80% of total heat supply, the rest being brought by the hot blast. Thus, the coking plant requires coal of high quality to ensure the successful operation of the BF and the addition of biomass into the coal for cokefaction is complex. This option was investigated in [61] to reduce the carbon footprint of the BF route. The study showed that the biomass could be blended in the form of raw, torrefied or pyrolyzed materials. Performances of the obtained coke are better if the biomass used is pre-treated (torrefaction or pyrolysis). In any case, the fraction of biomass in the blend cannot exceed a few percents to maintain a satisfactory coke quality.

Solid fuel for sintering

Sintering plant turns iron ore fines into large, hard and porous particles. Coke breeze, which is the undersize residual coke of coking plants, is used as solid fuel and emits 10% of the total CO_2 emissions in the BF-BOF route. Meanwhile, the sintering produces SO_x, NO_x, dioxins and fine dust. [61] Consequently, the substitution by biomass can reduce the CO_2 emissions, but also decrease the release of the harmful gas above due to a reduced content of S and N in the biomass. The raw biomass cannot be used directly due to its high moisture content and volatile matter, and even the charcoal after pyrolysis requires precise optimization for the following reasons: [62]

- high porosity results in more water feed,
- low bed permeability due to more water content and lower crushing strength leads to slower sintering speed,
- high reactivity generates much CO in the off-gas and lower degree of post-combustion. This decreases the temperature of the combustion zone (from 1390°C to 1240°C) and consequently is unfavourable to the product yield.

Use in the blast furnace

The use of biomass in the BF can be performed in the top charging and by injection at the tuyeres. Top charging includes (bio)-sinter, (bio)-coke, (bio)-pellets and charcoal lumps or torrefied biomass. Pulverized charcoal, grinded charcoal, grinded torrefied material, bio-oil and/or bio-PCI are fit for tuyeres injection. [61] All the components loaded in the top charging should have sufficient mechanical strength to ensure the smooth and efficient operation of the BF under high temperature and pressure. This is the reason why only mini-BFs with reduced height and pressure in Brazil can charge pure charcoal. Charging some higher-reactivity biomass instead of coke can decrease the temperature of the thermal reserve zone (early beginning of the Boudouard reaction), and consequently reduces the carbon and energy demand. Pellets and composites with embedded charcoal are a hot topic for recent research studies, but their lower mechanical strength is still a limiting factor.

Fortunately, the injection of biomass in the tuyeres like Pulverized coal injection (PCI) is much more feasible compared to the top charging as it has no constraint regarding mechanical strength. According to Wang et al., in terms of PCI, it was found that 166.7 kg of charcoal/t Hot Metal is able to fully replace 155 kg of PCI /t HM. The torrefied material and wood pellets could partially replace PCI by 22.80% and 20% respectively. [63] The Charcoal powder injection (CPI) can not only replace the PCI directly, but also lower the feeding rate of coke for heat supply.

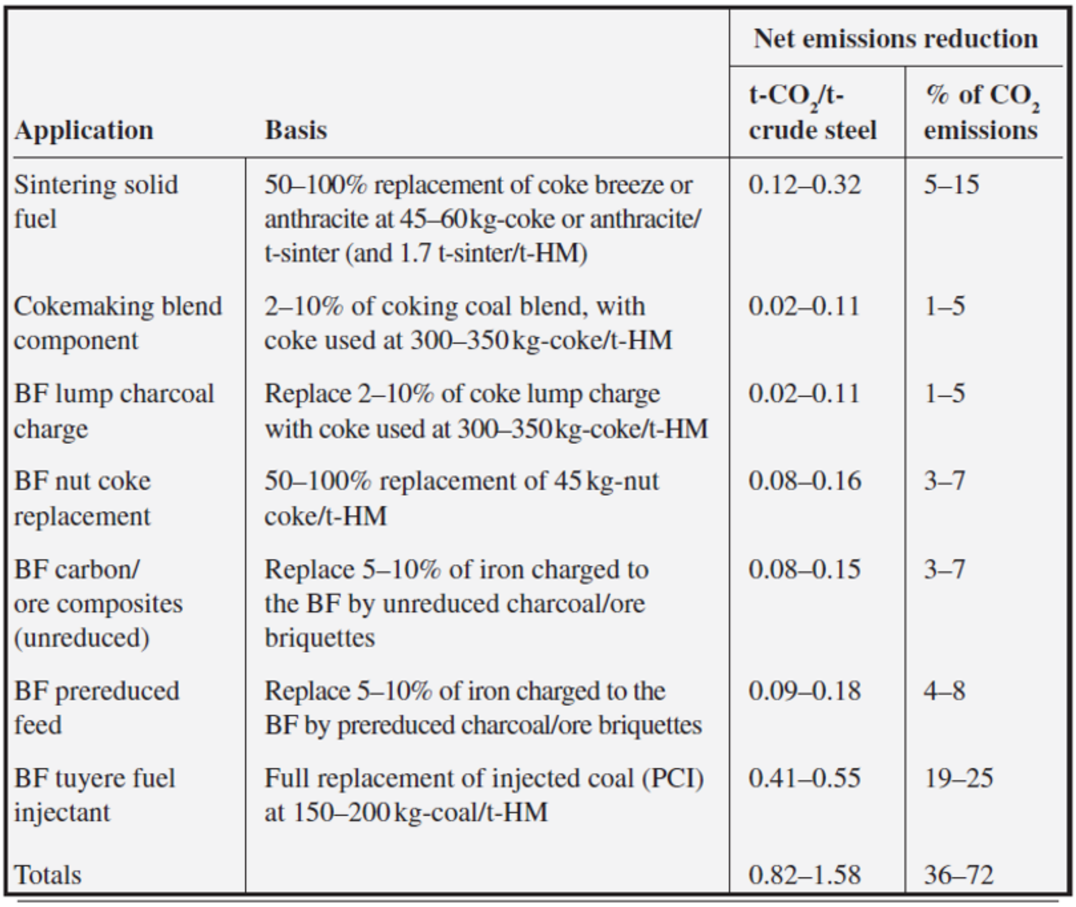

		Net emissions reduction	
Application	**Basis**	**t-CO_2/t-crude steel**	**% of CO_2 emissions**
Sintering solid fuel	50–100% replacement of coke breeze or anthracite at 45–60 kg-coke or anthracite/t-sinter (and 1.7 t-sinter/t-HM)	0.12–0.32	5–15
Cokemaking blend component	2–10% of coking coal blend, with coke used at 300–350 kg-coke/t-HM	0.02–0.11	1–5
BF lump charcoal charge	Replace 2–10% of coke lump charge with coke used at 300–350 kg-coke/t-HM	0.02–0.11	1–5
BF nut coke replacement	50–100% replacement of 45 kg-nut coke/t-HM	0.08–0.16	3–7
BF carbon/ore composites (unreduced)	Replace 5–10% of iron charged to the BF by unreduced charcoal/ore briquettes	0.08–0.15	3–7
BF prereduced feed	Replace 5–10% of iron charged to the BF by prereduced charcoal/ore briquettes	0.09–0.18	4–8
BF tuyere fuel injectant	Full replacement of injected coal (PCI) at 150–200 kg-coal/t-HM	0.41–0.55	19–25
Totals		0.82–1.58	36–72

Table 4. Proposed applications for biomass-derived chars in ironmaking operations and consequent CO_2 emissions reductions [64]

Table 4 illustrates the investigated options of biomass in the BF-BOF route and this potential gain in CO_2 emissions. [64] If all these options were cumulated, we could achieve a cut of CO_2 emissions by 72% at most. This value is promising but would require many adaptations to be reached. The use of biomass in the DRI-EAF route is even more promising as this process in its standard from yet emits 50-60% less CO_2 emissions than the BF route. The following part is dedicated to the use of biomass in this route.

II.4.4.2 Direct reduction route (DRI-EAF)

It is important to note that the use of biomass in the DRI-EAF route is mainly investigated in the laboratory scale and no industrial application has been reported yet. [65] Biomass may be used in the DR route in two ways: biomass-derived gas and use of self-reducing pellets with biomass.

Biomass-derived syngas

This procedure aims of replacing the syngas produced from natural gas with a green syngas rich in H_2 and CO produced from biomass gasification. It is the most reliable and economical choice among the three methods above because it does not require to modify the reduction unit. Organic compounds of various types, like raw woody biomass, garden waste and straw hust, etc. can be collected and gasified to produce the syngas. This gas is heated up and injected into the shaft furnace to reduce iron ore pellets, lumps or concentrate.

For better control of the H_2/CO ratio of the reducing gas, Kaewpanha et al. examined the role of steam co-gasification of brown seaweed and land biomass and the steam content promoted the H_2 content in the produced gas. [66] According to Guo et al., iron ore pellets were successfully reduced to 99.95% at 1323K after 30 minutes by the reducing gas from sawdust steam gasification. [67]

Self-reducing mixture with biomass

The self-reduction process relies on a well-mixed agglomerate of a reducing carbonaceous agent (coal or biomass) and iron ore. The amount of carbon should be sufficient to completely reduce the oxides in the iron ore. The main reactions are the indirect reduction (R1-6) by the reducing gas produced by pyrolysis and the Boudouard reaction (R7) and the direct reduction by solid carbon (R8).

The self-reducing mixture of coal and iron ore has been extensively investigated for decades. [68] [69] In this framework, the replacement of coal with biomass was also studied. According to

Hu et al., 60wt% iron ore-40wt% bio-char composite pellets can be fully reduced to wustite under N_2 atmosphere at 1000°C.[74] Based on the experiments of mixing sugar pine sawdust and iron ore, Strezov et al. concluded that the 30 wt.% of sawdust in the mixture reduced the iron ore to predominately metallic iron and the reduction took place from 670°C to 1200°C. [70] These studies focus on reduction of self-reducing mixture in the form of fines under inert atmosphere. The indirect reduction by reducing gas is able to remove certain amount of oxygen in the oxides, while the direct reduction by solid carbon plays an essential role for the residual reduction. The studies on the reduction behaviour of composite pellets were carried out on the lab scale. The targeted application can be in shaft furnaces, fluidized bed reactors, electric arc furnace and rotary hearth furnaces. [71] [72] To better understand the first use, Guo et al. has studied the kinetics and mechanisms of direct reduction of 96wt% iron ore-2wt% pine sawdust composite pellets with hydrogen gas and they concluded that the addition of biomass not only enhanced the metallization degree of pellets, but also promoted the reduction reaction rate. [73] So far, it does not seem that such composite pellets (with coal or biomass) have been used in industrial ironmaking plants, except for coal composite pellets in rotary hearth furnaces.

II.5. Other emerging technologies to reduce the CO2 emissions of the steelmaking industry

Besides the use of biomass in the BF-BOF route and DRI-EAF route, several other avenues have been proposed to increase the efficiency of energy and material use in the steelmaking industry like CCUS (Carbon Capture, Utilization, and Storage), top gas recycling BF, H_2-based DR and electrolysis).

The main obstacles for the steelmaking industry to reduce its emissions, as announced by the International Energy Agency (IEA), [75] are as follows:

- Carbon-based process: coke is widely used for iron ore reduction. Hydrogen-based solutions are currently being studied, but changing the whole production technique on a global scale remains a technical and economic challenge.
- Long life time of equipment: the equipment has a long life time. Blast furnaces are built to last at least 25 years and many of them are expected to remain in operation for over 40 years. Replacing all the equipment, which is already in place and operational, with a new process is economically difficult in the short term.
- Competitive international market: steel is one of the most traded products in the world and producers compete on the international market. The industry has already invested

heavily in reducing the energy used during steel production in recent decades. This leaves little room for further changes to established production methods.

In the longer term, a solution to massively reduce CO_2 emissions will come from solutions for primary steel production. According to IEA, the key technologies for this reduction are as follows:

- DRI - natural gas (CO and H_2 as reducing agents) equipped with CCUS
- DRI - 100% electrolytic hydrogen (only H_2 as reducing agent)
- Smelting Reactor equipped with CCUS
- BF equipped with CCUS
- Direct electrolysis of iron ore.

Several projects are under development on a global scale, with different Technology Readiness Levels (TRL). The IEA has listed the technologies under development that may have an important role in reducing emissions from the steelmaking industry; these technologies are presented in Table 5. [75]

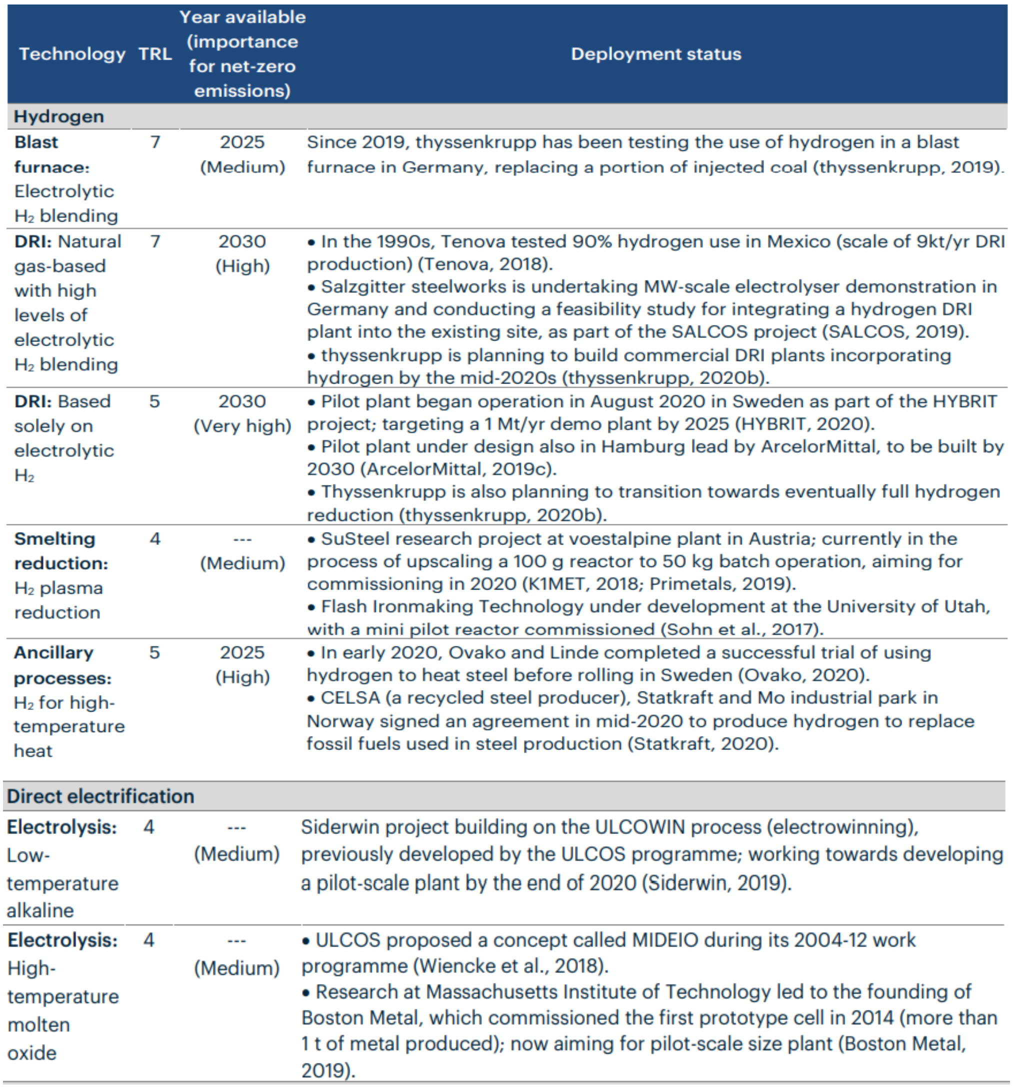

Technology	TRL	Year available (importance for net-zero emissions)	Deployment status
Hydrogen			
Blast furnace: Electrolytic H_2 blending	7	2025 (Medium)	Since 2019, thyssenkrupp has been testing the use of hydrogen in a blast furnace in Germany, replacing a portion of injected coal (thyssenkrupp, 2019).
DRI: Natural gas-based with high levels of electrolytic H_2 blending	7	2030 (High)	• In the 1990s, Tenova tested 90% hydrogen use in Mexico (scale of 9kt/yr DRI production) (Tenova, 2018). • Salzgitter steelworks is undertaking MW-scale electrolyser demonstration in Germany and conducting a feasibility study for integrating a hydrogen DRI plant into the existing site, as part of the SALCOS project (SALCOS, 2019). • thyssenkrupp is planning to build commercial DRI plants incorporating hydrogen by the mid-2020s (thyssenkrupp, 2020b).
DRI: Based solely on electrolytic H_2	5	2030 (Very high)	• Pilot plant began operation in August 2020 in Sweden as part of the HYBRIT project; targeting a 1 Mt/yr demo plant by 2025 (HYBRIT, 2020). • Pilot plant under design also in Hamburg lead by ArcelorMittal, to be built by 2030 (ArcelorMittal, 2019c). • Thyssenkrupp is also planning to transition towards eventually full hydrogen reduction (thyssenkrupp, 2020b).
Smelting reduction: H_2 plasma reduction	4	--- (Medium)	• SuSteel research project at voestalpine plant in Austria; currently in the process of upscaling a 100 g reactor to 50 kg batch operation, aiming for commissioning in 2020 (K1MET, 2018; Primetals, 2019). • Flash Ironmaking Technology under development at the University of Utah, with a mini pilot reactor commissioned (Sohn et al., 2017).
Ancillary processes: H_2 for high-temperature heat	5	2025 (High)	• In early 2020, Ovako and Linde completed a successful trial of using hydrogen to heat steel before rolling in Sweden (Ovako, 2020). • CELSA (a recycled steel producer), Statkraft and Mo industrial park in Norway signed an agreement in mid-2020 to produce hydrogen to replace fossil fuels used in steel production (Statkraft, 2020).
Direct electrification			
Electrolysis: Low-temperature alkaline	4	--- (Medium)	Siderwin project building on the ULCOWIN process (electrowinning), previously developed by the ULCOS programme; working towards developing a pilot-scale plant by the end of 2020 (Siderwin, 2019).
Electrolysis: High-temperature molten oxide	4	--- (Medium)	• ULCOS proposed a concept called MIDEIO during its 2004-12 work programme (Wiencke et al., 2018). • Research at Massachusetts Institute of Technology led to the founding of Boston Metal, which commissioned the first prototype cell in 2014 (more than 1 t of metal produced); now aiming for pilot-scale size plant (Boston Metal, 2019).

Technology	TRL	Year available (importance for net-zero emissions)	Deployment status
Carbon capture, utilisation and storage			
Blast furnace: off-gas hydrogen enrichment and/or CO_2 removal for use or storage	5	2030 (Very high)	• Japan's COURSE 50 project has completed the first experimental testing phase; the second phase aims to reach full commercial scale by 2030; it can be deployed with CCUS (JISF, 2011). • Top gas recycling using vacuum pressure swing absorption proven in an experimental blast furnace under ULCOS (EC, 2014). Concepts being further developed at the ArcelorMittal site in Dunkirk, France. IGAR project testing reforming with plasma torches, with a lab-scale pilot successfully completed in 2017 and an industrial-scale demonstration likely to be completed by 2025-27. The "3D" project launched in mid-2019 by a consortium of 11 stakeholders will test amine-based carbon capture for blast furnace process gases, aiming for pilot scale (4 kt/yr CO_2) by 2021 and industrial scale (1 Mt/yr CO_2) by 2025. Final arrangement would feed plasma torches with recovered CO_2 from process gases. (ArcelorMittal, 2019a; 2019b; 2017). • The ROGESA pilot is testing H_2-rich coke oven gas in a blast furnace in Germany, with implementation in two blast furnaces expected as early as 2020 (Saarstahl, 2019). • The STEPWISE project is piloting a technology in Sweden to decarbonise blast furnace gas for use in power production (14 t/day CO_2 removal) (STEPWISE, 2020).
Blast furnace: Converting off-gases to fuels	8	Today (Medium)	• The first commercial plant began in 2018 in China by Lanza Tech, Shougang Group and TangMing; it produced 30 million litres of ethanol for sale in its first year of operation (Lanzatech, 2018; 2019). A second large-scale plant is under construction in Ghent, Belgium under the Steelanol/Carbalyst project by ArcelorMittal and Lanzatech, to be completed by early 2021 and with a capacity of 80 million litres of ethanol (ArcelorMittal, 2019a). • The FReSMe project, by a consortium of European partners, is piloting steel off-gas conversion to methanol (1 t/day); it builds on research from the STEPWISE project on CO_2 capture and the MefCO2 project on producing methanol from CO_2 (FReSMe, 2020; EC, 2019).
Blast furnace: Converting off-gases to chemicals	7	2025 (Medium)	• The Carbon2Chem pilot plant in Germany initiated by thyssenkrupp in 2018 has produced ammonia and methanol from steel off-gases; it is aiming for an industrial-scale plant by 2025 (thyssenkrupp, 2020a; 2020b). • Carbon4PUR, a project by a consortium of 11 partners across Europe, is piloting converting steel off-gases to polyurethane foams and coatings (20 t/yr) (Carbon4Pur, 2020).
DRI: Natural gas-based with CO_2 capture	9	Today (Very high)	• Operating plant since 2016 in Abu Dhabi with 0.8 Mt/yr of CO_2 capture capacity, with CO_2 used for enhanced oil recovery at nearby oilfield (ADNOC, 2017). • Two plants of Ternium in Mexico operating since 2008 capturing 5% of emissions (0.15-0.20 Mt/yr combined) for use in the beverage industry, with planning underway to upscale capture capacity (Ternium, 2018). • Commercial Finmet plant since 1998 at Orinoco Iron, Venezuela with amine-based CO_2 separation achieving close to 100% CO_2 concentrations as an integral part of the process, but captured CO_2 is not currently used or stored.*
Smelting reduction: with CCUS	7	2028 (Very high)	• Developed by the ULCOS consortium, the HIsarna pilot plant is currently operating at a Tata Steel plant in Ijmuiden, Netherlands (60 kt steel produced, CCS not yet implemented) (Tata Steel, 2017); a demonstration scale (0.5 Mt/yr) plant (TRL8) is expected in 2023-27 in India and an industrial scale (1.5 Mt/yr) plant with CCS (TRL 9) is targeted in the Netherlands in 2027-33. • Initial testing of amine-based CO_2 scrubbing in FINEX plant (Primetals, 2020).

Table 5. Status of main emerging technologies in the iron and steel sector [75]

II.6. Conclusion

In this chapter, we have introduced different routes and processes for making steel. The conventional, predominant route is the BF-BOF one, with a long history, high CAPEX, high quality products, but too high specific CO_2 emissions to continue as it is.

The DRI-EAF route has been a fierce competitor to the BF-BOF route for last decades. The different gas-based processes for the production of DRI were presented here. Among those, the Midrex and HYL processes are dominant in the present market and the shaft furnace shows greater advantages than the retort reactor and fluidized bed reactor. The main advantages of the DRI-EAF route are a smaller number of unit processes and, currently most important, halved CO_2 emissions compared with BF-BOF route.

Biomass, as an abundant renewable energy, has been well investigated in the field of steelmaking. It can be used (partially replacing coke and coal) in the BF to reduce the CO_2 emissions of the conventional route significantly. In parallel, the use of biomass in the DRI-EAF route has been a hot topic in the last three decades.

II.7. The BIORED (Biomass-based Iron Ore REDuction) concept

Following this presentation of the state of the art, it is time to come to the concept of our new process. We looked at how to reduce iron ore to iron using biomass in a large, simple, continuously operating reactor, using common raw materials. For the reactor, the direct reduction shaft furnace is well suited: little charge preparation, solids descending by gravity, counter-current, possible high production. We can thus produce a DRI which will find the same outlets as DRI in general, i.e. to constitute the ferrous burden of an electric arc furnace. The so-called direct reduction is carried out via a reducing gas. To produce this from biomass, gasification is ideal. However, rather than opting for a biomass gasifier upstream of the iron ore reduction furnace, as sometimes mentioned in the literature, we preferred 'a priori' an all-in-one reactor. The biomass is gasified in situ by the Boudouard reaction. The situation is then quite similar to the conditions prevailing in the upper part of a blast furnace but with biomass instead of coke. Which biomass to choose? As we expect to charge iron ore in pellets or lumps, as in the usual direct reduction furnaces, and we do not intend to prepare a specific charge such as composite pellets, the biomass must also be in the form of lumps of similar size (centimetric). As large quantities are needed, it can be wood, torrefied wood, charcoal. For the sake of simplicity, we chose charcoal as a first step. Moreover, charcoal is already used for the reduction of iron ore (see II.4.4 and the small Brazilian blast furnaces).

At this stage, the reactor envisaged could remind us of a bloomery, the ancestor of the blast furnace (Figure 19), but this is not the case considering in our case the much greater height, a truly continuous operation and, above all, gas recycling.

Figure 19. Bloomery for making wrought iron [76]

Indeed, from the operation point of view, the reactor has to produce the CO amount necessary for the reduction from the gasification of the biomass by CO_2. The top gas, containing CO and CO_2, can be recycled, with CO being useful for reduction and CO_2 for gasification. Ideally, the composition of the top gas should be identical to the composition of the gas injected at the bottom, and the charcoal introduced at the top should be entirely consumed in the furnace. Finally, the furnace is heated by the hot gas mixture introduced, as in the conventional direct reduction furnaces. The gas flow rate increases between the gas inlet and outlet due to the heterogeneous reactions, and the excess gas can be burnt to obtain the necessary energy input. Figure 20 summarises this information.

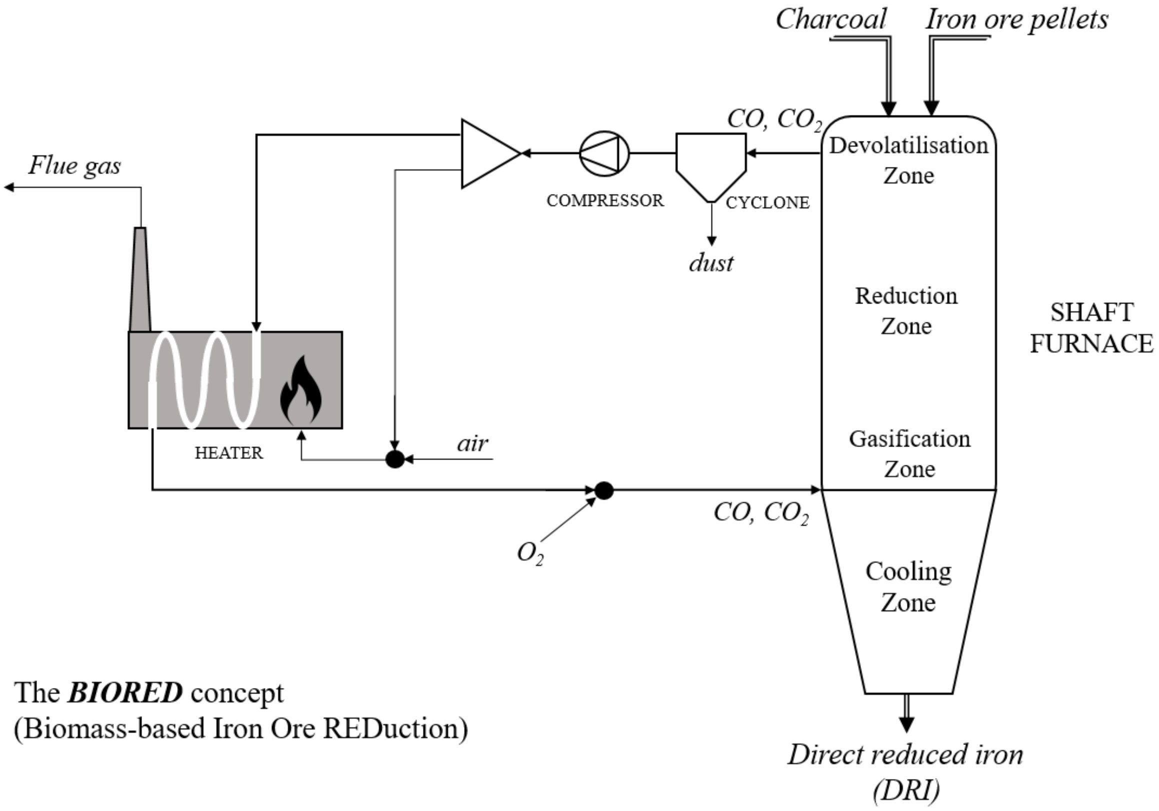

Figure 20. Principle of the BIORED process

To the best of our knowledge, such a process has never been considered in the literature. In the remainder of this manuscript, we will try to assess this novel process, using a modelling and simulation approach. However, before addressing this part, it is necessary to determine the charcoal devolatilisation and gasification kinetics. The next two chapters are devoted to this issue.

III. Devolatilisation

III. 1. Introduction

The biomass product used in the BIORED process will be charcoal, obtained from carbonisation of lignocellulosic biomass. The industrial processes and the physico-chemical mechanisms leading to charcoal are first presented. When loaded in the shaft furnace, charcoal first undergoes devolatilisation, which consists in the release of the remaining volatile matter and the formation of gases like CO, CO_2, H_2 and H_2O. These gases although evolved in small amounts can play a role in the indirect reduction of iron ore pellets (R1-6). For this reason, it was necessary to investigate the kinetics of the devolatilisation process. To do so, we carried out the thermogravimetry (TG) experiments on charcoal samples at different heating rates. Then the independent parallel reactions model was used to build a kinetic model and obtain the kinetic parameters of charcoal devolatilisation.

III. 1.1 Composition of biomass and charcoal

As previously mentioned in section II.4.1, biomass encompasses a variety of sources: wood, wood by-products, industrial by-products, products from traditional agriculture and organic waste. Plant biomass is the most widespread on earth among all the types of biomass. It is a composite material based on organic polymers. It can be separated into several categories according to its composition: lignocellulosic biomass (wood, grass, straw, etc.) cellulose biomass (cereals) and oleaginous biomass (rape, sunflower, etc.). [35] It is mainly composed of carbohydrate polymers and oligomers (cellulose and lignin, representing respectively 65 to 75% and 18 to 35% of the biomass). Cellulose is a carbohydrate formed from a chain of glucose, and it is responsible for the resistance of plant fibres. Hemicellulose is a mixture of different monomers carbohydrates (glucose, mannose, galactose, xylose, and arabinose). Finally, lignin is an amorphous resin with no "fixed" structure, which acts as a binder between the cellulose fibres.

Figure 21 gives typical representations of these three chemical compounds. [77] The mass fraction of these three components is significantly dependent on the nature of the biomass.

In addition to these three compounds, biomass may contain inorganic minerals (ash) and extractable compounds (tannins, oils and gum) between 5 and 30%. [78]

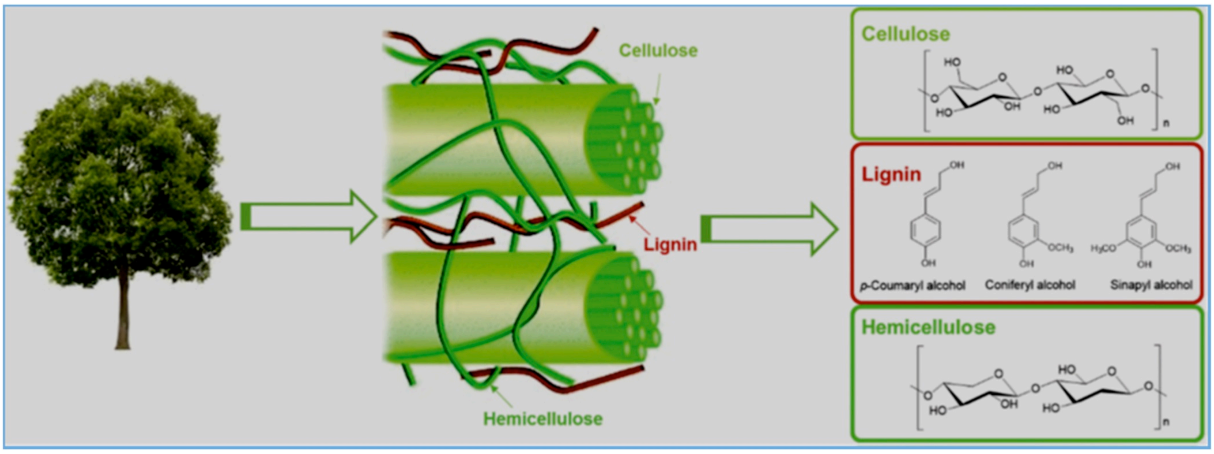

Figure 21. Structure of hemicellulose cellulose and lignin of lignocellulosic biomass [77]

Biomass	Fixed carbon	Volatile matter	Ash
Wheat straw	17.71	75.27	7.02
Switch grass	14.34	76.69	8.97
Willow wood	16.07	82.22	1.71
Rice hulls	16.22	63.52	20.26
Alfalfa stems	15.81	78.92	5.27
Sugar cane bagasse	11.95	85.61	2.44
Rice straw	15.86	65.47	18.67
Almond shells	20.71	76	3.29
Hybrid poplar	12.49	84.81	2.7

Table 6. Proximate analysis of various biomass at dry basis (wt.%) [79]

Biomass	C	H	O	N	S
Hazelnut shell	51	6	42	1	0
Tobacco stack	49	6	43	1	1
Almond shell	49	6	43	1	1
Rice husk	48.86	9	42	0.1	0.04
Lignite	66	8	21	1	4
Corn Stover	49	6.6	43.7	0.6	0.1
Corncob	49	6	44.2	0.8	0
Saw dust	53.9	7	37	2	0.1
Spruce wood	51.4	7.1	41.2	0.3	0

Table 7. Ultimate analysis of various biomass at dry basis (wt.%) [79]

Table 6 and Table 7 show the proximate and ultimate analysis of typical agricultural biomass, respectively. The proximate analysis involves heating the sample under various conditions to determine moisture, volatiles, fixed carbon and ash yield. Moisture is determined by heating the sample to a temperature slightly above the boiling point of water (377-383K) and holding it at this temperature until no further weight loss occurs. The volatiles are measured based on further weight loss by heating the sample to 950°C in an N_2 atmosphere. The remaining residue after full combustion in an O_2 atmosphere is called ash. The fixed carbon is the organic matter contained in the coal, determined by the difference between 100% and the sum of the percentages of volatile matter, ash and moisture.[80] While the ultimate analysis is meant to determine the composition of various elements in a compound.

This composition can be translated in an approximate formula giving biomass composition as that of a molecule e.g. $C_6H_9O_4$ [81] or $CH_{1.44}O_{0.66}$ [82] . It can be noted that there is much less variation in the ultimate analysis among biomass than in the cellulose/hemicellulose/lignin distribution.

III. 1.2 Charcoal and charcoal production

Biomass is converted into charcoal through pyrolysis process, which was briefly mentioned in part II.4.3. In the following part, we will explain the thermal degradation of raw biomass during the pyrolysis at different temperatures. Three types of reactors are then introduced for the production of charcoal and divided by the source of heat: internal heating, external heating and heating by gas recirculation. Finally, the solid, liquid and gaseous products of pyrolysis are characterized.

III. 1.2.1 Chemical processes

In this part, the pyrolysis refers to a slow pyrolysis process, also called carbonisation. The physico-chemical process of pyrolysis involves many mechanisms such as chemical degradation of the primary components of the biomass, transport of gases within the solid and heat exchange. For a lignocellulosic biomass, there are five main steps of decomposition during the pyrolysis with increasing temperature:[83]

- Drying takes place below 100°C.
- Dehydration. It mainly refers to the elimination of cellular and external bound water below 200°C after drying.
- Between 220-315°C, most of the hemicellulose is likely to decompose.
- Between 315-400°C, the decomposition of cellulose and lignin starts.
- Above 450°C, lignin is the last compound that undergoes further degradation because the other two reach full decomposition. The decomposition of lignin forms the solid charcoal.[84]

These five thermal phases are dependent on the heating rate and duration of the pyrolysis, therefore, the nature and the granulometry of the biomass, the type of reactor and the conditions of operation will have an impact on the final yield of charcoals.[85] In general, large biomass particles and slow heating promote the formation of charcoals by increasing the contact time between the charcoal and the volatile matter. The charcoals adsorb the later at higher temperatures on the solid surface and the volatile matter is decomposed to form graphite, water, CO_2 and CH_4. [86]

The evolution of the composition of the biomass during the pyrolysis process can be visualized by the red arrow on a Van Krevelen diagram in Figure 22. [87] At the beginning of the pyrolysis (at low temperature), there is a significant reduction of the oxygen content (evaporation of water, formation of CO, CO_2 and pyrolytic liquid). Then as the temperature increases, a significant release of hydrogen takes place in the form of H_2, CH_4 and tars. Finally, we obtain the charcoal with high carbon content and low hydrogen and oxygen content. In this way, we can distinguish a charcoal produced at high temperature (500°C) from a charcoal produced at 400 °C by its higher fixed carbon content.

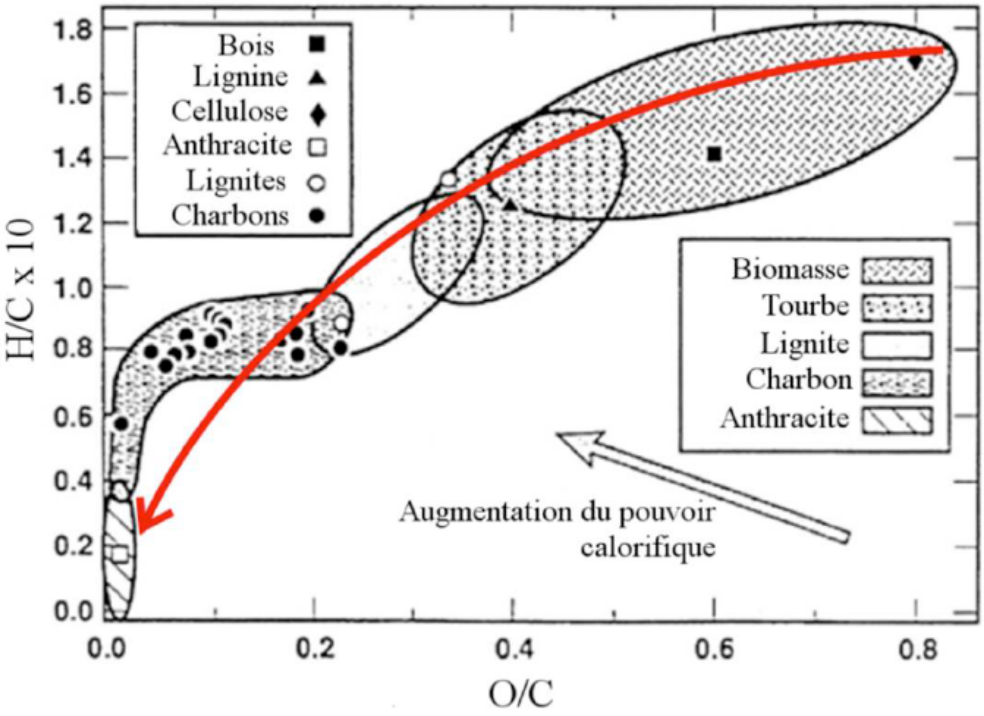

Figure 22. Van Krevelen diagram for different types of fuels [87]

III. 1.2.2 Pyrolysis reactors

There are different kinds of reactors for slow pyrolysis. Depending on the process used, the produced charcoals may retain 30-60% of the LHV of the initial biomass. The by-products: pyrolysis gas or tar may be valorised internally for energy saving if the process is well optimized.

The literature identifies three types of heating used for the production of charcoal: internal heating, external heating and heating by gas recirculation. [85] [88] In internal heating, a portion of the biomass is burned under a controlled airflow for heat supply, so the production of charcoal is relatively low (about 20-35%). This traditional pyrolysis process typically lasts from 20 hours to 7 days, or even longer. Examples like honeycomb kilns and Missouri kilns are shown in Figure 23a and Figure 23b.

Figure 23. (a) Honeycomb kilns and (b) Missouri kilns [87]

In external heating, no oxygen enters in the reactor. The heat comes from the walls by conduction and radiation. The material yield (30-32%) is higher than that with internal heating and the pyrolysis time is much shorter (8-12 hours). The energy is provided by the recovered carbonization flue gas, so it is necessary to have several reactors in this process. An example (Van Marion Retort reactor) is shown in Figure 24.

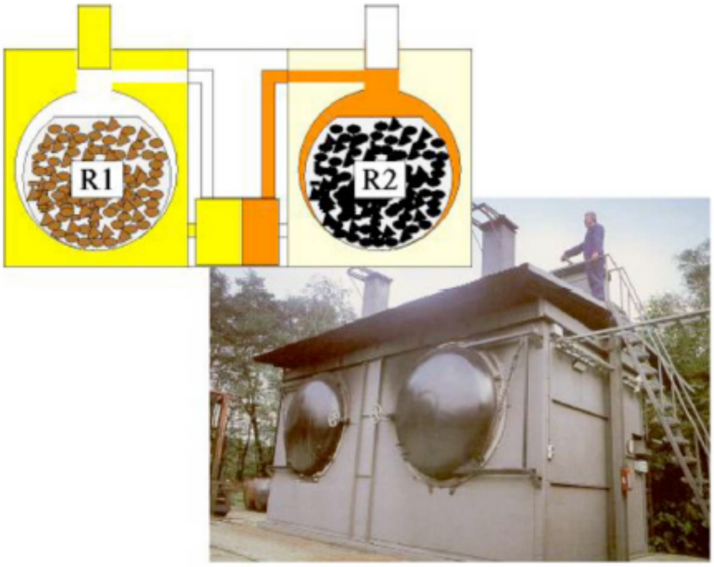

Figure 24. Van Marion Retort reactor [87]

For processes with gas recirculation, part of the pyrolytic bio-vapours and gases produced is burned in an external combustion chamber and then injected back to the reactor. The biomass inside is directly heated by the hot gas by convection. The pyrolysis process lasts from 16 to 35 hours. The carbonization fumes are also burned for energy saving. The existing processes of this type are the Degussa, Lambiotte (Figure 25) and Lurgi.

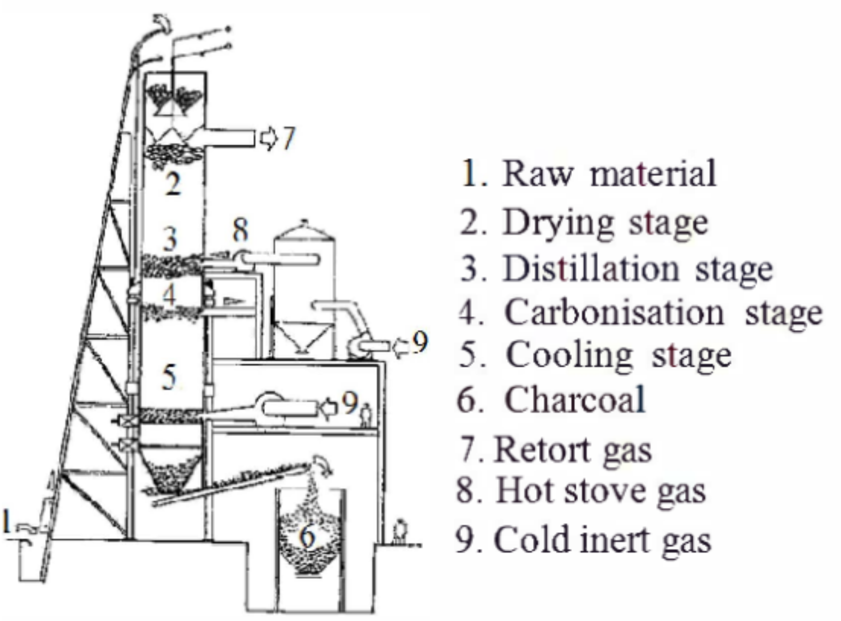

Figure 25. Diagram of the Lambiotte process [89]

III. 1.2.3 Pyrolysis products

Pyrolysis produces three phases, solid, liquid and gas.

Bio-oil

Bio-oil (tar) is the liquid product of pyrolysis. It is a complex mixture of water (15 to 30%) and a large number of organic compounds. The compounds condense to form a microemulsion. Branca et al. found that bio-oils could contain more than 80 different compounds including alcohols, ketones, acids, furfuryl, phenolic compounds, cyclic or aromatic hydrocarbons. [90] Several authors have simplified the composition of bio-oils by using simple formulas such as $CH_{2.5}O$, $CH_{1.9}O_{0.7}$ and $CH_{2.15}O_{0.85}$. [91] [92] [93] Due to the high acid content, bio-oils generally have a low pH, making them corrosive and therefore restrictive for transportation and storage.

Pyrolysis gas

Even more than for bio-oil, the composition of the pyrolysis gas is a function of both the biomass and the pyrolysis conditions, and a prediction of the pyrolysis gas composition is difficult. In general, this composition is determined experimentally. Many studies were devoted to that issue, e.g. [97] [99] [98]

Charcoal

Charcoal is the solid product of pyrolysis. According to Akom et al., one kilo of lignocellulose biomass produces 0.36-0.45kg charcoal. [94] It is composed of about 65-90% fixed carbon. The physical and chemical properties are dependent on both the nature of the biomass and the pyrolysis conditions. Thanks to their micro porous nature, cation exchange capacity and high specific surface, charcoals are able to filter and absorb toxic pollutants and serve as forerunners for mass production of activated carbon by virtue of its physic chemical activation. [95] Besides, as it is mainly composed of fixed carbon, charcoal is a great combustible and reducing agent without concern of global warming. The composition of the charcoal can be characterized by proximate and ultimate analysis (as Table 7 for raw biomass).

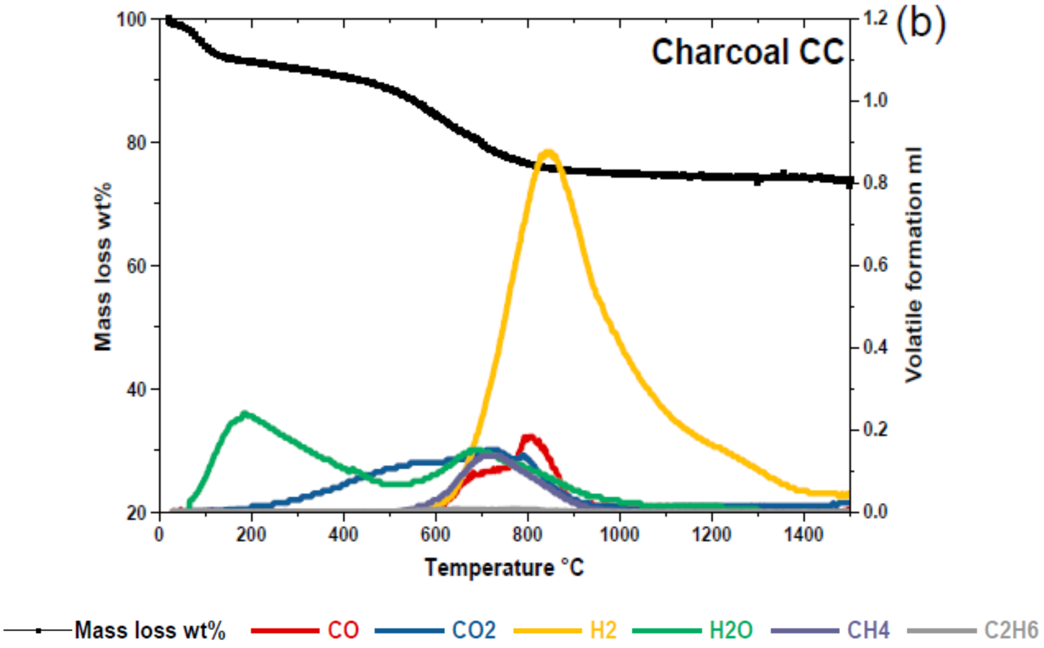

Figure 26. Gas species evolved and solid mass loss during heating of charcoal at 10 °C/min under argon atmosphere [101]

Charcoal devolatilisation, i.e. the release of the 10-30% volatile matter remaining in the charcoal after its production, when charcoal is reheated, can be seen as a special case of pyrolysis. Like for pyrolysis gas, the knowledge of the composition of the devolatilisation gas is important for future modelling. Among the literature work, we will make use of the work of Khasraw et al. They studied the pyrolysis of charcoals by thermogravimetry and used a vertical tube furnace coupled with a quadrupole mass spectrometer for off-gas analysis during the devolatilisation. [101] From their results shown in Figure 26, the formation of gases corresponds well to the mass loss of the charcoal. The prevailing produced gas is the H_2, followed by the release of H_2O, CO, CO_2 and CH_4.

From these results it is possible to obtain a composition of the devolatilised gas. By calculating the area under each curve and after normalisation, we determined the following gas composition: 56% H_2, 23% H_2O, 6% CO, 11% CO_2 and 4% CH_4. The devolatilisation process can therefore be written as reaction (R16):

$$C_{0.21}O_{0.51}H_{1.74} \rightarrow 0.56H_2 + 0.23H_2O + 0.06CO + 0.11CO_2 + 0.04CH_4 \qquad R16$$

(H/C=8.29 and O/C=2.43)

III. 1.3 Kinetic models for pyrolysis and charcoal devolatilisation

Di Blasi, in his review of the pyrolysis modelling, distinguishes three different kinetic models: single-step model, multi-step reaction model (independent parallel reaction schemes) and multi-stage model. [100] Although we are eventually only interested in charcoal devolatilisation, we present the biomass pyrolysis models for sake of generality. Let us first define the conversion and reaction rate, which are used in numerous studies by TGA.

The conversion X is calculated by equation (III-1):

$$X = \frac{m_0 - m_t}{m_0 - m_{ash}} \qquad \text{(III-1)}$$

Where m_0 is the initial weight before the pyrolysis or devolatilisation reaction, m_t is the sample weight at time t and m_{ash} is the weight at the end of the transformation.

The reaction rate is defined as:

$$r_X = \frac{dX}{dt} \qquad \text{(III-2)}$$

III. 1.3.1. Single-step reaction model

The single-step global model is the most frequently used and the simplest. It is based on a set of irreversible reactions and it can be divided into three categories:[87]

- global model which involves only one reaction and three products as shown in Figure 27a,
- two-reaction model in which the tar and gas are produced by the reactions shown in Figure 27b,
- three-reaction model where the char, tar and gas are produced by their own reaction as shown in Figure 27c.

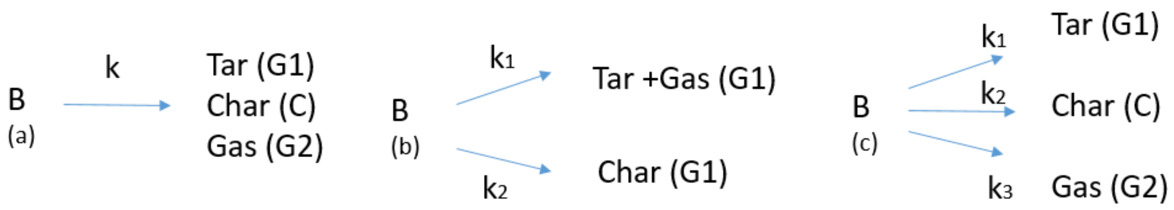

Figure 27. Three examples of kinetic mechanisms of biomass decomposition in one-step with one, two or three reactions in parallel [87]

For the single-step reaction model, the general formula of reaction rate is defined as:

$$r_X = k(T)f(X) = A\exp\left(-\frac{E}{RT}\right)f(X) \qquad \text{(III-3)}$$

where $k(T)$ is the temperature-dependent rate constant in the form of the Arrhenius equation:

- A is the pre-exponential factor or frequency factor [s^{-1}];
- E is the apparent activation energy of the decomposition reaction [J/mol];
- R is the universal gas constant [$8.314 J \cdot K^{-1} \cdot mol^{-1}$];
- T is the absolute temperature [K].

$f(X)$ is the reactivity function, which describes the change in reactivity with conversion. It is important to note that the reactivity function is assumed being only related to the conversion degree regardless of the value of the temperature. [102]

The kinetics of devolatilisation can be determined by the differential (reaction rate vs temperature) and integral methods (conversion vs temperature). The most commonly used differential method is that of Friedman. [103] However, the drawback of differential methods compared to integral methods is that the former is sensitive to inaccuracies in the experimentally determined reaction rate; therefore, integral methods are often preferred. [104] Some of these integral methods include Coats-Redfern, Kissinger, Flynn-Wall-Ozawa (FWO), Starink, and Kissinger-Akahira-Sunose (KAS). [105] [106] [107] [108] [109] These methods, called iso-conversional methods, can be applied for calculating the apparent activation energy without requiring prior knowledge of the reaction model and order. [110] Clearly, the apparent activation energy itself is not able to describe the complete mechanism of the reaction, but it provides further understanding.

III. 1.3.2. Independent parallel reactions modelling

The second type of model is based on the decomposition of the biomass into elementary components or pseudo-components (namely cellulose, hemicellulose and lignin as mentioned above). Each component (C_i) is considered as independent of the others and is then degraded with its own kinetics and products (MV_i).

$$C_i \xrightarrow{k_i} MV_i \qquad \text{with } i \text{ from 1 to } n \qquad \text{R17}$$

The reactions occur in parallel and without interacting with each other. Here again, the decomposition of the components is generally represented by an irreversible first-order reaction with an Arrhenius-type law. However, sometimes the first order is not suitable and higher order reactions are used. [38] The pseudo-component represents a certain percentage of the weight and goes through the decomposition independently, thus each has its own kinetic parameters. The number of pseudo-components is to be identified by the overlapping differential Thermogrametry (DTG) diagram in which the number of peaks is shown.

Orfao et al. have compared several models and concluded that the independent parallel reaction modelling is the most reliable one. [113]

Each of the pseudo-component is decomposed under the following reaction rate:

$$\frac{dX_i}{dt} = A_i exp\left(-\frac{E_i}{RT}\right)(1 - X_i), i = 1,2, \dots n \qquad \text{(III-4)}$$

Eventually, the overall conversion rate, calculated for n reactions is described by:

$$\frac{dX}{dt} = \sum_{i=1}^{n} c_i \frac{dX_i}{dt} \qquad \text{(III-5)}$$

where c_i is the mass fraction of volatiles of the i_{th} reaction.

The objective, which is to obtain the mass fraction, apparent activation energy and frequency factor for each reaction, is reached by minimizing the objective function: the square of the difference between the experimental reaction rate and calculated reaction rate in equation (III-6):

$$OF = \sum_{i=1}^{n}[(\frac{dX}{dt})_{exp} - (\frac{dX}{dt})_{calc}]^2 \qquad \text{(III-6)}$$

III.1.3.3. Multi-stage model

Finally, some authors consider that pyrolysis must be decomposed into several stages, by more complex mechanisms involving consecutive reactions. With three consecutive steps, the products of the first two steps become intermediates that can be further degraded. Figure 28 describes this type of model, where B is the initial biomass and C and D are intermediate products that can also be degraded to form degraded to form new solid or volatile products. [64]

In the same way as shown in Figure 29, other authors consider that some of the heavy volatiles, tars, undergo further degradation leading to the production of lighter char and volatiles. [64] [65] [66] We did not choose to use this model due to the complexity of the kinetic mechanism.

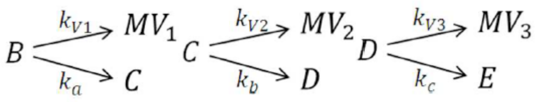

Figure 28. Kinetic mechanism of biomass decomposition into three steps

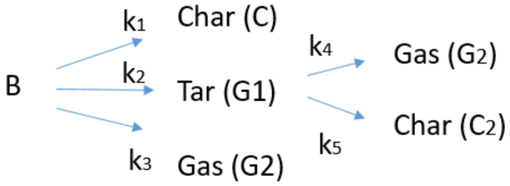

Figure 29. Kinetic mechanism of biomass decomposition into two steps

III.1.3.4. Heat and mass transfer

All of the previous models correspond to reactions kinetically limited by the intrinsic reaction rates. Like all the solid-gas reactions, the devolatilisation is dependent on the intrinsic reaction rate, heat transfer and mass transfer. [115] However, it is very difficult to analyse the kinetics bearing all aspects into consideration. Considering that devolatilisation is of secondary importance for our study (which will be checked a posteriori), we accepted some simplifications in its description. In particular, we assumed that the reaction rate was only determined by the internal reaction. If the kinetic reaction rate is the limiting step, the reaction rate should be almost same at different heating rates. This will be checked.

III. 2. Devolatilisation experiments

The objective of the experiments conducted was to determine the kinetic rate of devolatilisation of a charcoal that could be loaded in a shaft furnace.

Thermogravimetry (or TGA, Thermogravimetry Analysis) is the preferred method for the study of gas-solid reactions: a sample is heated in a tube furnace under a controlled atmosphere. If the sample gains or loses mass, the recorded mass change reflects the overall kinetics. Two types of TG experiments can be performed: isothermal and non-isothermal. The isothermal method is well adapted to gas-solid reactions with a gaseous reactant. It consists in reaching the desired test temperature as fast as possible in an inert atmosphere. Then, the gaseous reactant is introduced and the main reactions take place and are recorded by the signal of mass loss or gain. Non-isothermal method refers to the triggering of main reactions along with the increase in the temperature, so the heating rate is usually much lower than in the isothermal method. This method is well adapted to decomposition reactions, like devolatilisation. The decomposition behaviour during the heating is recorded since the beginning of the experiment. Thus, we have chosen the non-isothermal method.

The SETARAM TAG 24 thermobalance shown in Figure 30 was used to study the non-isothermal decomposition of charcoal samples during devolatilisation. Its main feature is that it has two symmetrical furnaces, one for the sample and the other for the reference. This system makes it possible to avoid the effects of buoyancy and drag forces that disturb the measurements. The two suspension wires, made of platinum, are attached to the arms of the balance, which records the evolution of mass loss as a function of time. The resulting signal is then sent to and processed by a computer.

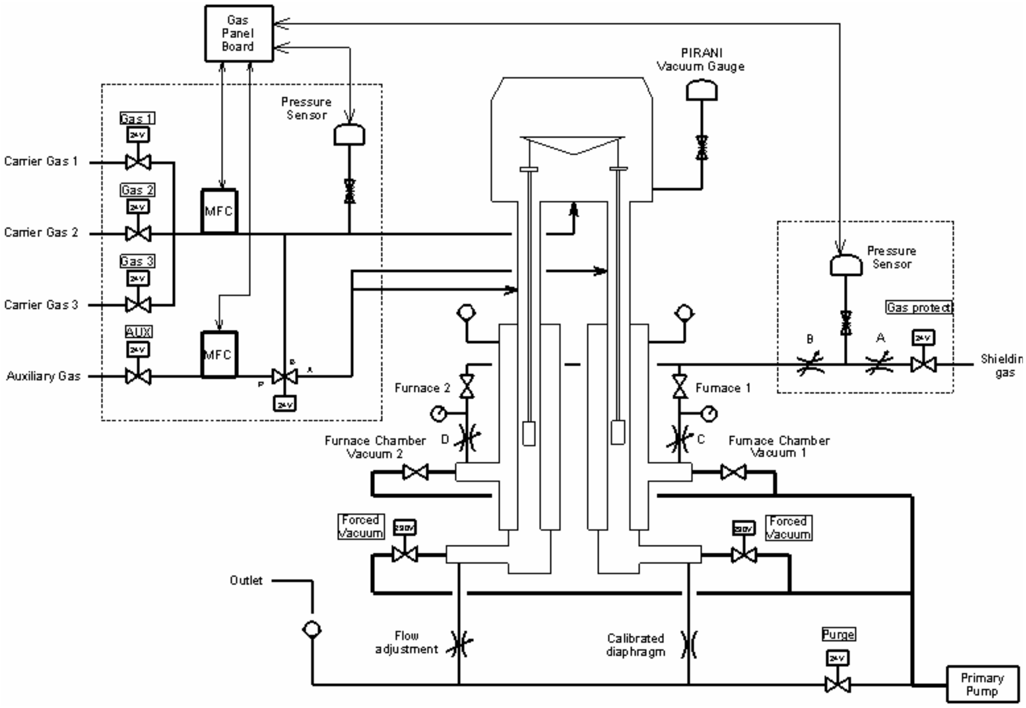

Figure 30. Schematic diagram of SETARAM TAG 24 thermobalance

For each analysis, a sample was loaded into an alumina crucible in one of the furnaces. Pure argon was the inert gas during purge and devolatilisation, with a volumetric flow rate of 100 ml/min. The oven was heated from room temperature to 1200°C with a heating rate of 10, 20, 30 and 40 K/min. Each experiment was repeated twice to verify repeatability, and the comparison at 20 K/min is shown in Figure 31 as an example.

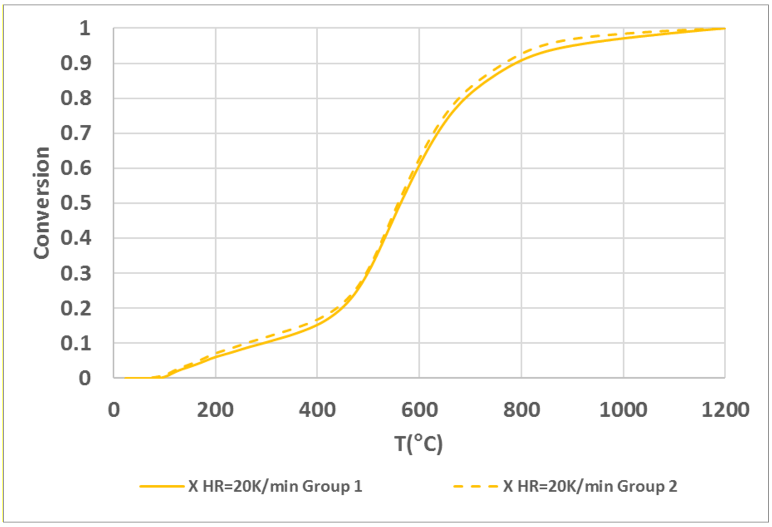

Figure 31. Comparison of two devolatilisation experiments at 20K/min

The charcoal used in our work was an oak charcoal provided by an industrial partner of CEA Grenoble. It was prepared by carbonisation of oak pieces according to the following process. First, temperature was rapidly rised from 100°C to 230°C for drying and starting the carbonisation. Then, a very gradual rise in temperature from 230°C to 390°C was performed over 10 hours. The wood was completely transformed after 10 hours. Finally, the charcoal underwent an extra one-hour stage to homogenise the temperature and to ensure the quality of the product.

This charcoal comes in the form of rough pieces of various sizes. When preparing samples for devolatilisation, the charcoal was crushed to small pieces of about 50 mg to fit the technical requirements of the equipment. Its porosity and density are 0.56 and 600 kg/m^3, respectiveley, based on mercury porosimetry measurements. It consists of 24.45% volatile matter (dry basis) and 74.5% fixed carbon. Before its use for TGA, its humidity was measured at around 4.5%. The ultimate analysis of is given in Table 8.

Sample	C	H	N	S
Oak charcoal	73.11%	3.778%	0.43%	0.167%

Table 8. Ultimate analysis of the oak charcoal samples

III. 3. Results and discussion

In this part, we first analyse the effect of heating rates on the devolatilisation rate. Then the modelling of the reaction is carried out by using single-step global model and multi-step reaction model. Kinetic parameters are obtained by linear regression with Excel or non-linear regression with the curve-fitting package.

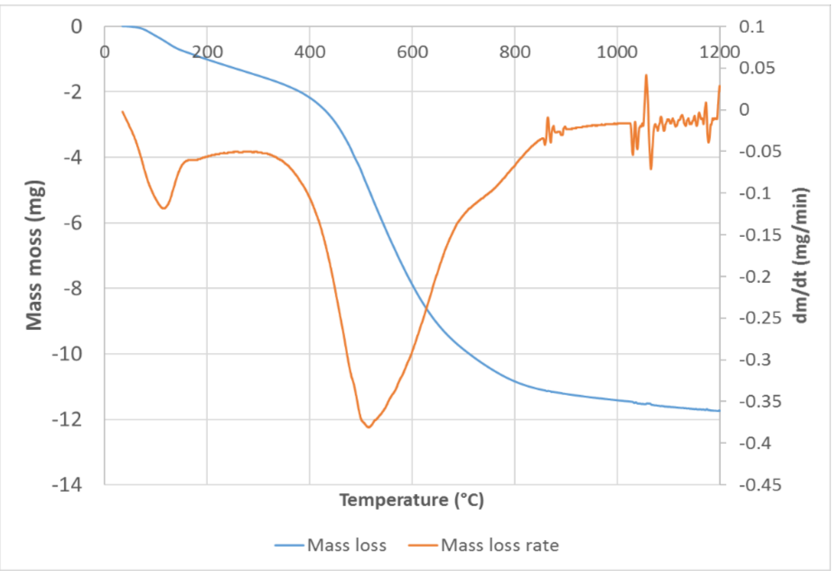

Figure 32. Example of curves of mass loss and mass loss rate at 10 K/min

The solid mass fractions (TG curves) and the time derivative of the thermogravimetry curves (DTG curves) as a function of temperature were recorded to investigate the devolatilisation behaviour of the oak charcoal samples. An example of curves of mass loss and mass loss rate is given in Figure 32. The mass loss took place from 70°C to 1030°C at heating rate of 10 K/min. The mass loss rate witnessed two different stages as can be easily seen in the figure. The total mass loss is about 12 mg for a sample of 50 mg, which means that the volatile matter evolved represents 24% of the charcoal mass, in perfect agreement with the indicated composition.

III. 3.1. Effect of the heating rate

Figure 33 shows the devolatilisation conversion (X) and reaction rate as a function of temperature in TGA tests for different heating rates: 10, 20, 30 and 40 K/min.

First, along with the increase in heating rates, we can notice that the devolatilisation rate slightly shifts to higher temperature. This phenomenon is due to the thermal inertia of the samples and the decrease of the heat transfer effectiveness while increasing the heating rate. Consequently, the heat required for the breakdown of components is achieved at higher temperature, which results in a delay for higher heating rate, commonly called thermal lag. [116]

Figure 34 points out this delay more clearly by the means of the plot of the temperature for which 50% conversion is reached against heating rate. The same phenomenon was also underlined in the work of Lapuerta. [117] However, the curves of different heating rates are close and indeed overlap, which means that the heat transfer did not control the mechanism of the reaction.

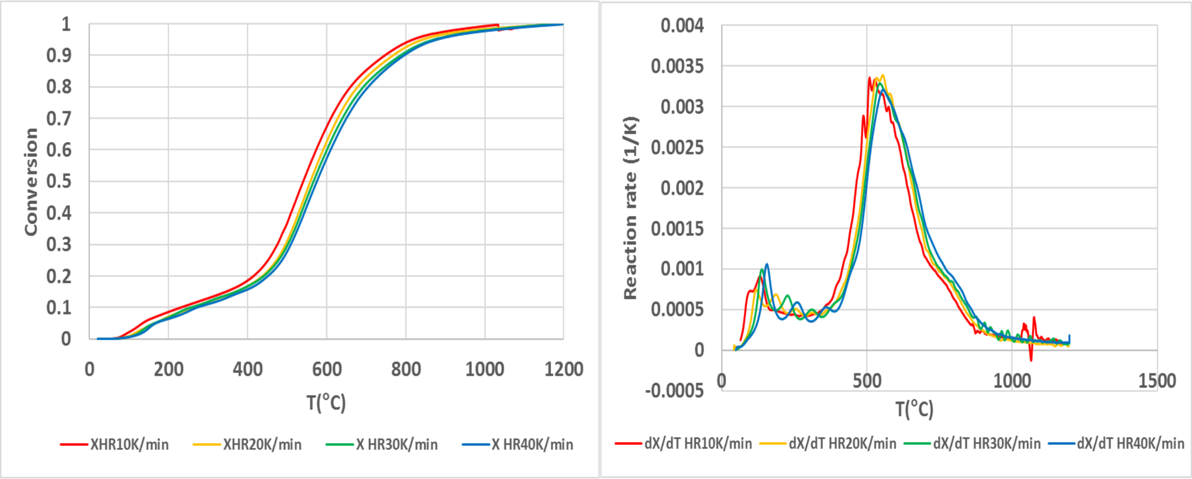

Figure 33. Devolatilisation of oak charcoal at different heating rates

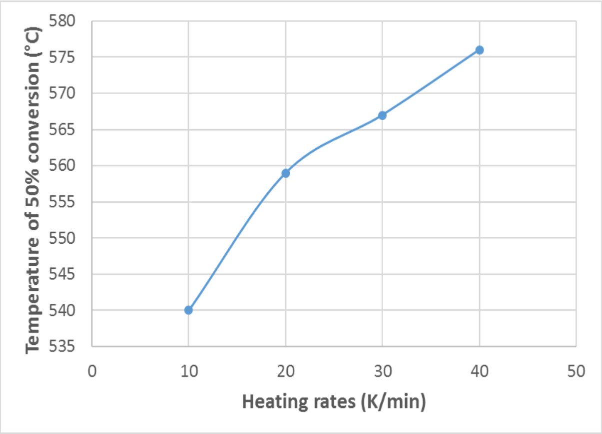

Figure 34. Temperature corresponding to the 50% of the conversion

III. 3.2. Independent parallel reactions modelling

To interpret the experiments, we have tested both the single-step reaction model with isoconversional method and the independent parallel reactions model. The former led to less coherent results with a more complex method. We thus retained the parallel reaction model as Pantoleontos et al., [114] which will be detailed below. Since the heating rate is a factor for determining kinetic parameters, the calculation of the apparent activation energy, frequency factor and mass fraction was carried out by Python curve-fitting package for different heating rates. We used the Trust Region Reflective algorithm (TRF method) for the optimisation of a nonlinear least-squares problem with bounds on the variables.

It is evident that the more reactions are involved, the better fit can be obtained. Many studies have chosen three reactions for the devolatilisation of biomass because it is mainly composed of three major components: hemicellulose, cellulose and lignin. For example, Pantoleontos et al. have modelled the pyrolysis of olive kernel and forest residue at 20 K/min by using three parallel reactions. Besides the lignocellulosic materials in biomass, alcohol–benzene–watersoluble extractives also represents a certain percentage of the mass, which could be up to 20% for the raw oak. [121] The decomposition of extractives usually takes place together with the degradation of the hemicellulose and the lignin. [119] For this reason, the peaks in the DTG curves are not a symbol of a precise component, but rather a pseudocomponent whose devolatilisation is dominant in a particular range of temperature.

As shown in Figure 32 and Figure 35, the decomposition of oak charcoal is mainly divided into two steps according to two distinct peaks in the DTG curve, which is also shown as a noticeable change in the TG curve. For the first step at relatively low temperature, there are several peaks that could refer to the dehydration first and then to the decomposition of hemicellulose and cellulose, which remained in the charcoal sample. When it comes to the second step, it is reported to be the degradation of lignin for a large range of high temperatures as discussed above. [83]

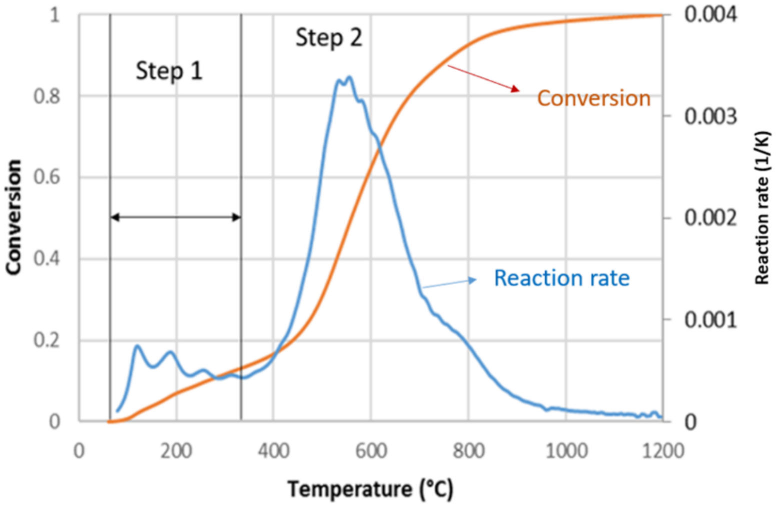

Figure 35. Identification of devolatilisation steps at 20K/min

From Figure 35, the contribution of the first step is within the range of 11–14 wt.% in all cases. The second reaction is dominant in the devolatilisation, accounting for more than 80% of the mass loss. Bearing in mind the nature of the received sample, we chose only two parallel reactions: the dehydration and the decomposition of lignin, because the lowest number of parallel reactions is preferred for the simplification of the model.

Heating rates (K/min)	Pseudocomponent 1			Pseudocomponent 2			Correlation coefficient (R^2)
	E_1 (J/mol)	A_1 (1/min)	C_1	E_2 (J/mol)	A_2 (1/min)	C_2	
10	15029	10	0.136	42465	35	0.864	0.922
20	18711	37	0.133	46024	109	0.867	0.933
30	19861	75	0.131	44675	121	0.869	0.931
40	19794	92	0.116	43787	129	0.884	0.935

Table 9. First-order kinetic parameters of the two parallel reactions

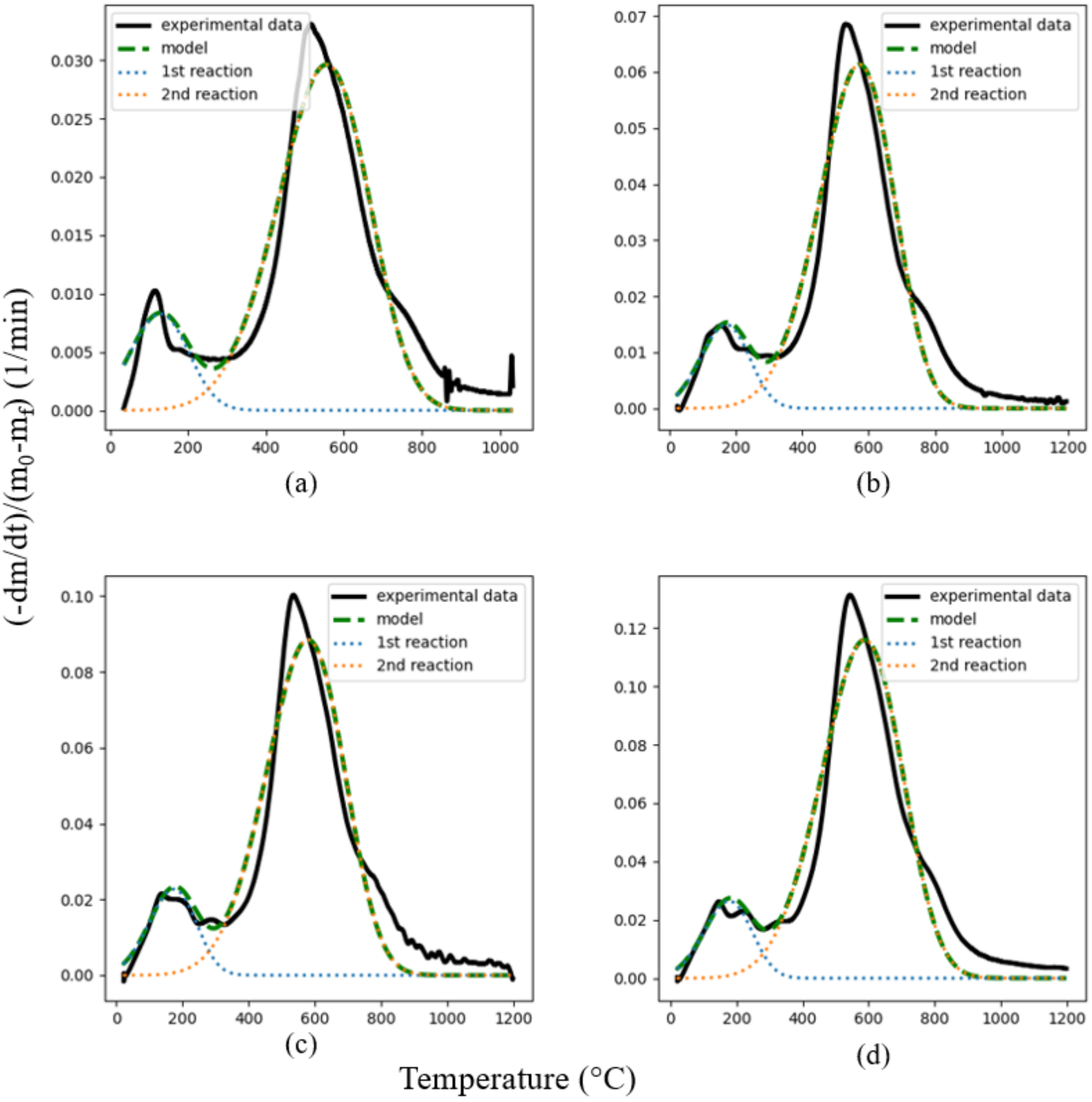

(a) (b) (c) (d)

Figure 36. Modelling the devolatilisation of the oak charcoal at 10(a), 20(b), 30(c) and 40(d) K/min by using two independent parallel reactions

For the determination of kinetic parameters, we chose the heating rate of 20 K/min only since Figure 33 shows relatively similar devolatilisation rates for different heating rates. After the curve-fitting, the kinetic parameters were obtained (See equations III-4 and III-5). The values are given in Table 9. The quality of the modelling is described by the correlation coefficient (>0.92). Figure 36a-d also show the generally good agreement between the experimental and modelled reaction rate curves. The values of apparent activation energy for both reactions remained almost the same for different heating rates and were compared with literature data. For the first devolatilisation step, the apparent activation energy is 18±3 kJ/mol, which is higher than that of olive-waste cake and cotton stalk, but lower than mung beans as listed in Table 10.

Biomass	E_a (kJ/mol)	References
Mung beans	23.28	Li et al. [122]
Olive-waste cake	12.34	Vega-Galvez et al. [123]
Cotton stalk	15.1	Chen et al. [124]
Oak charcoal	18±3	Present study

Table 10. Comparison of apparent activation energy of dehydration in oak charcoal with other biomasses

For the second devolatilisation step, the apparent activation energy of thermal decomposition of lignin is 44±2 kJ/mol and several studies are compared in Table 11. The E_a is perfectly in the range of literature data and corresponds well to those of other oak derived materials.

Biomass	Ea (kJ/mol)	References
Olive kernel	32.8	Pantoleontos et al. [125]
Oak forest residue	49	Alonso et al. [126]
Oak wood	52	Alonso et al. [126]
Oak charcoal	44±2	Present study

Table 11. Comparison of apparent activation energy of thermal decomposition of lignin in parent oak charcoal with other biomasses

III. 4. Conclusion

In this chapter, we introduced the lignocellulosic biomass and the charcoal production by slow pyrolysis. Three components (hemicellulose, cellulose and lignin) are decomposed at different range of temperatures and the lignin turned into charcoal during the pyrolysis process. Three different kinetic models: single-step model, multi-step reaction model (independent parallel reaction schemes) and multi-stage model were presented in detail, the second of which was chosen for the kinetic model.

Thermogravimetry experiments of devolatilisation of oak charcoal samples were carried out at different heating rates. From the experimental data, we analyzed the effect of heating rates and obtained the kinetic parameters of devolatilisation by the independent parallel reactions model.

The charcoal in the BIORED shaft furnace first undergoes devolatilisation and then gasification. The latter reaction is the principal source of the reducing agent CO. In the reactor, the gas mixture is mainly composed of CO and CO_2, while most of the literature are experimental studies under pure CO_2 atmosphere or with particles of extremely small sizes for industrial use (<1 mm). Thus, the next chapter is dedicated to the experimental study of gasification with charcoal particles of industrial size under different composition of CO-CO_2.

IV. Gasification

In our biomass-based shaft furnace, the next transformation undergone by charcoal after the devolatilisation reaction is its gasification. Gasification in general refers to the gas-solid reaction between the solid carbon and CO_2, H_2O and O_2. In our case, the gasification will be that of charcoal by CO_2 according to the reaction $C+CO_2 \leftrightarrow 2CO$ (R7); commonly known as the Boudouard reaction in the field of ironmaking. This reaction is essential in our process as it produces carbon monoxide, which is the reductant required for the reduction of iron oxides. Also important and specific are the operation conditions for this gasification: at temperatures between 850°C and 1100°C and in a gas mixture of 30-40% CO_2 and 60-70% CO, as will be explained in Chapter V.

In the next sections, we will first introduce the kinetic models used for gasification, how the nature of charcoal influences the reactivity and discuss the influence of the experimental conditions according to the literature. Then, the experimental procedure we used to study the charcoal gasification under different CO-CO_2 mixture in the range of 850-1100°C using TGA will be detailed. Those experiments will be used to determine the gasification reaction rates using the n-th order model and Langmuir-Hinshelwood equation. The reactivity function models will be tested to best fit the change in reactivity. Finally, the pore evolution will be analysed by mercury porosimetry and the effect of gas switching time will be discussed.

IV.1. Introduction

IV.1.1. Kinetics

As all typical heterogeneous reactions, gasification involves mass transport of reactants and products, associated with the chemical processes of the reaction itself.

For a gas-solid reaction, which takes place within a porous particle, the general equation takes the following form:

$$aA_{(g)} + bB_{(s)} \leftrightarrow cC_{(g)} + dD_{(s)} \qquad \text{R18}$$

Where, a, b, c and d are the stoichiometric coefficients. The different steps of the reaction are:

1. mass transfer of the reactant gas A in the gas phase from bulk gas to the outer surface of the solid particle,
2. a. diffusion of the reactant gas through the pores of the solid,
    b. adsorption of the reactant gas onto the solid surface,
    c. intrinsic chemical reaction on the solid surface,
    d. desorption of product gas C from the solid surface,

e. diffusion of the gaseous product through the pores of the solid,

3. mass transfer in the gas phase of the gaseous product C from the external surface of the solid to the external gas stream.

One of the processes above, intrinsically slowest, usually controls the overall kinetics and is called the "limiting step". Different regimes like chemical regime (limited by step 2c), diffusional regime (step 2a or 2e), external transfer regime (limiting step 1 or 3), or even mixed regimes are possible for a heterogeneous chemical reactions.

For endothermic or exothermic reactions, the reaction and diffusion steps are accompanied by:

- consumption or release of heat at the reaction sites,
- heat transfer by convection between the gas flow and the surface of the solid particle,
- heat transfer by conduction in the solid.

As a result, the overall kinetic is not only based on the intrinsic reaction rate, but also affected by the mass and heat transfer on the scale of boundary layer, interparticle and intraparticle transport. The intrinsic reaction rate is also called the local heterogeneous reaction rate, which is a function of local gas composition, temperature, and reaction surface area. For this reason, the difference of the overall and intrinsic reaction rates has to be carefully distinguished. The following part contributes to the explanation of the kinetic mechanism of the gasification.

IV.1.1.1. Active sites

Active site theory proposes that reactions occur at favoured sites on the solid-gas surface. According to the Ergun's model, the gasification is divided into three steps: the absorption of CO_2 at an active site C_f to form a carbon-oxygen surface complex and a molecule of CO. [127] [128] The second step is the inhibiting effect of the produced gas CO to the first reaction. Then the complex is decomposed into a new free active site and another CO molecule.

$$C_f + CO_2 \overset{k_1}{\rightarrow} C(O) + CO \qquad \text{R19}$$

$$C(O) + CO \overset{k_2}{\rightarrow} C_f + CO_2 \qquad \text{R20}$$

$$C(O) \overset{k_3}{\rightarrow} C_f + CO \qquad \text{R21}$$

In combination of R19-21, the overall gasification becomes the Boudouard reaction ($C + CO_2 \leftrightarrow 2CO$). In this study, the gasification rate is defined as a function of kinetic parameter in the form of the Arrhenius equation, the partial pressure of CO and CO_2, and the variation of reactivity as a function of the degree of conversion called the reactivity function, $f(X)$.

$$r_X = k(T, P_i) f(X) \qquad \text{(IV-1)}$$

IV.1.1.2. Langmuir-Hinshelwood and n-th order kinetics

Assuming the pseudo-steady-state condition for the C(O) complex in the reactions R19-21, one can obtain the equation of Langmuir-Hinshelwood (L-H) as a function of reaction rates and partial pressures in the equation (IV-2):

$$k(T,P_i)f(X) = \frac{k_1 P_{CO_2}}{1+\frac{k_1}{k_3}P_{CO_2}+\frac{k_2}{k_3}P_{CO}} f(X) \qquad \text{(IV-2)}$$

where k_1, k_2, k_3 are the reaction rate constants for the three reactions and partial pressures are in bars. Assuming that the inhibiting gas CO is negligible amount, a more usual expression is the n-th order model:

$$k(T,P_i)f(X) = Aexp\left(-\frac{E}{RT}\right) P_{CO2}^{n} f(X) \qquad \text{(IV-3)}$$

In fact, the homographic L-H expression does not correspond to a power law but an order between 0 and 1 can reflect it approximately.

IV.1.1.3. Gasification reactivity functions

The reactivity function is also called the conversional function, which depicts the change in reactivity with conversion. Different models have been proposed in the literature with certain assumptions including physical models like volume reaction model, shrinking core model, random pore model, and modified random model; and empirical models like integrated core model (n-order model) and n-z model. Details of some of them are shown below.

Volume reaction model

The Volume Reaction Model (VRM), also known as the homogeneous model, assumes that the reaction takes place at all sites of the solid in parallel, so the reaction rate slows down with the conversion according to a pseudo first order with respect to the solid:

$$\frac{dX}{dt} = k(1-X) \qquad \text{(IV-4)}$$

The VRM has advantage of being simple and generally well adapted to experimental data. Gomez et al. found that the VRM is the best performing model, after removing the effect of switching the reacting gas from N_2 to CO_2 in the TGA. [129]

Shrinking core model and integrated core model

The Shrinking Core Model (SCM) assumes that the particle is a solid sphere or cylinder with the reaction happening only at the outer surface and gradually moving inside. [130] The power m is equal to 2/3 and 1/2 whereas the particles are supposed to be spherical and cylindrical respectively. Since the form of solid may be hard to determine, the adjustable non-negative parameter m is to be determined from the experimental curves. With unspecified value of m, the SCM is sometimes called the Integrated Core Model (ICM).

$$\frac{dX}{dt} = k(1 - X)^m \qquad \text{(IV-5)}$$

Random pore model (RPM)

RPM was developed by Bhatia and Perlmutter as more general than the SCM and able to depict reaction rates that not always decrease with conversion. [131] The initial pore development including pore growth and pore emergence accelerates the reaction rate in the beginning. The following pore reduction such as the collapse of pore walls and overlapping pore surfaces decreases the specific surface area, thus slowing down the reaction rate. As a result, without mass transfer and gas dispersion effects, the change in total pore surface area creates a maximum reaction rate for a particular conversion. This model was often applied to gasification. The gasification rate is expressed as:

$$\frac{dX}{dt} = k(1 - X)\sqrt{1 - \varphi \ln(1 - X)} \qquad \text{(IV-6)}$$

where the values for the reaction rate constant, k, and the pore structure constant, φ, are determined from the experimental data on the rate as a function of conversion by using a curve-fitting method. Higher φ values indicate higher progressive porosity of the sample and implies more reaction occurring in the internal pores of the char. [132] However, if the maximum is a consequence of gas switching stage (See section IV.3.5), it can be considered as a systematic error induced by the procedure to isolate pyrolysis from gasification. [129]

Modified random pore model (MRPM)

Zhang et al. proposed a semi-empirical extension to the original RPM: the MRPM introduces a dimensionless constant, c and a dimensionless power law constant, p into the original RPM as described in equation (IV-6). The additional constants provide the RPM with the extended flexibility to describe the reactivity in the higher conversion range without much alteration of the original assumptions for RPM. [133]

$$\frac{dX}{dt} = k(1 - X)\sqrt{1 - \varphi ln(1 - X)}\,(1 + (cX)^p) \qquad \text{(IV-7)}$$

where c and p are empirical constants.

Apparent activation energy and frequency factor

The reaction rate k is expressed by the Arrhenius equation and two methods have been applied to calculate the frequency factor and apparent activation energy. The first is the curve-fitting method: by using the experimental reaction rates at different temperatures and conversions, a curve-fitting package is able to calculate the kinetic parameters of Arrhenius law and the reactivity function at the same time. The second method is from regression of experimental reaction rates at the same conversion using the linearized Arrhenius equation since it is assumed that the reaction rate k is independent of the conversion.

$$lnk = lnA - \frac{E_a}{RT} \tag{IV-8}$$

IV.1.2. Reactivity of chars

It is clear that not all the biomass exhibits the same kinetic behaviour during gasification. A variable often used is the char reactivity, defined as follows:

$$R = \frac{1}{1-X}\frac{dX}{dt} \tag{IV-9}$$

The char reactivity is dependent on the chemical structure, mineral content and porosity. Chemical structure provides reactive sites with dislocations, crystalline edges and heterocyclic centers. Mineral contents act as catalyzers or inhibiters for further dislocations. Porosity is another important factor for the total surface area and the pores control the local concentration of reactive gas along with the conversion, thus influencing the gasification rate. [134]

The following section will discuss the role of biomass features on the reactivity, such as porosity, specific surface area, mineral content, pyrolysis conditions and carbon source. Furthermore, the experimental conditions like temperature, pressure, partial pressures of gasifying agent, particle size and gas flow rates also have an important effect on reactivity.

IV.1.2.1. Porosity and surface area

The gasification takes place at the interface between the solid and the gas, more specifically, the reaction sites on the surface. The gasification rate is promoted at high temperatures, leading to a more developed pore structure and larger specific surface area in the chars, which greatly increases the number of reaction sites with oxidizing free radicals. [135]

According to the IUPAC classification recommendations, pores are divided into three main size classes: Micropores (0–2 nm), Mesopores (2–50 nm), and Macropores (>50 nm). The pore structure is determined by: (1) the specific internal pore volume, (2) the specific internal surface area, and (3) the distribution of internal pore volume. The first two factors are proportional to the reaction rate roughly speaking, while the distribution of internal pore volume is more complex. The large surface area resulting from the smallest pores like micropores may not be available to a particular reactant unless the reaction enlarges these pores and the reaction time is sufficient for the mass diffusion.

According to Liu et al, the porosity of chars continues to increase until a conversion of 0.9 is reached, and then the structure collapses rapidly at the end of the reaction. Their BET (Brunauer-Emmett-Teller) analysis showed that the gasification occurred where existing pores become larger and new micropores emerge. [136] Kawakami et al. investigated the reaction rate of coke, wood charcoal and graphite with pure CO_2 at 1173 and 1373 K, and concluded that the rise in specific surface area corresponds well to the change in the volume of pores smaller than 10^{-8} m in diameter. Furthermore, they determined that the reaction took place exclusively on the surface of pores between 10^{-8} to 10^{-6} m in diameter. [137]

IV.1.2.2. Mineral contents

The mineral contents of biomass differ from a biomass to another. Alkali and Alkaline Earth Metals (AAEM) were investigated to be catalyser to the gasification and act as active sites. [135] Di Blasi analysed the factors affecting the parameters of the global reaction and reported that mineral matter content is one of the most influential factors; and at the end of the reaction, the effect of mineral matter becomes more noticeable due to the increase in catalytically active sites available. [138] [139]

Zahara et al. established a linear relation between initial catalytic activity and Na, K, Ca, Fe, and Si concentrations for gasification of six types of sugar cane bagasse. [140] Similar work has been carried out to obtain a correlation between initial catalytic activity and (Ca + Na)/Si ratio. [141] For this reason, the Alkali index has been introduced by many researchers to quantify the ratio of AAEM species to silicon and aluminium oxides:

$$Alkali\ Index = Ash \times \frac{CaO+K_2O+MgO+Na_2O+Fe_2O_3}{Al_2O_3+SiO_2} \tag{IV-10}$$

It is reported that the higher the alkali index, the higher the reactivity of chars. [142] [143] Vamvuka et al. studied the gasification of waste paper char between 800°C and 950°C and the performance of the alkali used was in the following order: $Li_2CO_3 > K_2CO_3 > CaCO_3 > Rb_2CO_3 > CaSO_4 > Cs_2CO_3 > Na_2CO_3$. [144] Huang et al. observed that gasification reactivity of fir char was improved through the addition of metal catalysts, in the order K > Na > Ca > Fe > Mg. [145] However, some researchers claimed that there was no clear correlation between the reactivity of biomass and alkali index, but crystalline structure was playing a significant role. [146] [147]

IV.1.2.3. Pyrolysis conditions

Pyrolysis conditions are crucial to the reactivity due to their strong impact on the structure of char. Although most literature works are unconclusive, it is commonly believed that pyrolysis atmosphere, time, temperature, heating rates, pressure and reactors have their effects on the gasification reactivity. Xiao and Yang studied the effect of multiple pyrolysis atmospheres (N_2, H_2 and CO_2) on gasification. [148] The H_2 atmosphere appears to be the best for pyrolysis of straw semi-char while the CO_2 one is the worst, which is confirmed by the pyrolysis study of coal under hydrogen at pressures raging 0.1–3.0 MPa according to Guo et al. [149] Gomez et al. reported that the pyrolysis time for coal char under inert gas atmosphere prior to gasification decreases the char's reactivity due to the reduction of mesopores. [129]

The gasification reactivity is proportional to the temperature until 400°C and decreases with the temperature in the range of 500-1200°C. [148] [150] High pyrolysis temperature causes smaller pores or cavities that are difficult for the CO_2 to enter and for the product gas to escape. However, opposed opinions were argued for the influence of the temperature. Thus, particle size and diffusion effects should also be considered for comparison. [151] [152]

Besides, pressure decreases char reactivity and high heating rates improves gasification rates. [153] [154] Pyrolysis process has also a substantial influence and microwave pyrolysis favours the reactivity compared with the conventional pyrolysis.

IV.1.3. Operating conditions of the gasification

In addition to the nature of char sample, experimental conditions influence significantly the reactivity as well. For this reason, it is important to explain the precise effect of each parameter including temperature, pressure, partial pressure of gasifying agent, particle size and gas flow rate.

IV.1.3.1. Temperature

From a thermodynamic point of view, the Boudouard reaction is highly endothermic with enthalpy change of 172 kJ/mol. This implies that, first, an increase in temperature favours the reaction in the forward way and, second, that bringing heat is necessary to sustain the reaction. From a kinetic point view, the gasification reactivity is promoted by increasing the temperature. Walker et al. have used the temperature as a measure of intrinsic reactivity to discuss the relative importance of each step in the overall reaction scheme. [155] The change in gasification rate depends on the temperature and three ideal regimes are proposed in Figure 37. [155] At low temperature (about 800°C), the reaction is limited by the surface chemical reaction involving the adsorption of the reactant gas and desorption of the product gas on the external and internal surfaces, thus, the reaction is under kinetic control regime (Regime I). As the temperature increases, the reaction rate increases, thus the diffusion effect plays a more important role. At intermediate temperature, limiting factor switches to the diffusion of the reactant gas inside the pore of the particles or intraparticle diffusion control (Regime II). At high temperature

(>1400°C), mass transfer of the reactant gas from the bulk flow to the stagnant gas region turns into the most difficult stage (Regime III). Figure 37 also depicts the values of effectiveness factor and those of apparent activation energy E_a under the different regimes. E_t (intrinsic activation energy) is obtained as E_a and effectiveness factor is equal to 1 under regime I as diffusion is neglectable. With increasing temperature, effectiveness factor decreases and E_a decreases till ½ E_t.

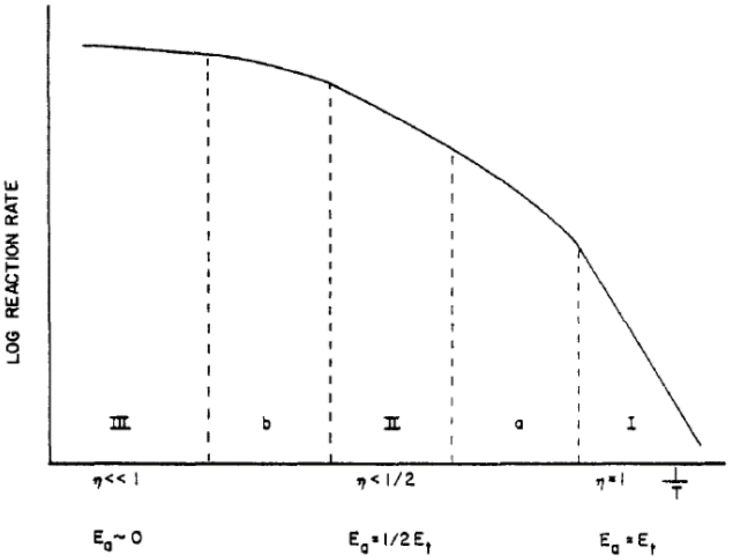

Figure 37. Regimes of apparent reaction rates with temperature [155]

IV.1.3.2. Pressure

Pressure is an important factor for mass and heat transfer of the reaction, and generally the overall gasification rate increases with the pressure. This is not a thermodynamic effect because the reverse would be expected from Le Chatelier rule. Higher pressure and higher temperature reduce the time of intrinsic reaction but increase the time for pore diffusion and external diffusion. Kim et al. have studied the gasification of sub-bituminous coal in a pressurized wire-heating reactor (PWHR) at elevated pressures. [156] At 973K, the experiment was under kinetic control (Regime I), but at 1573K, pore diffusion became the limiting step (Regime II). When the pressure reached higher value, the reaction shifted to the Regime III. It is important to note that since the diffusion is dominant under high pressure, the reactivity of chars decreases with pressure until a maximum value. This behaviour was observed in the iron catalysed gasification of corn stover char, pressure from 1 to 4 atm enhanced the reactivity but further pressure increases lead to similar reaction rate. [157]

IV.1.3.3. Partial pressure of CO_2

The Boudouard reaction is reversible. The driving force for the reaction is $P_{CO_2} - P_{CO_2,eq}$. If CO_2 partial pressure is larger than the equilibrium curve at given temperature and pressure (i.e. over the blue curve in Figure 38), the reactants react to generate products. In a CO_2-CO mixture, increasing the CO partial pressure acts against gasification, this is the thermodynamic effect. But CO has also an inhibitor kinetic effect, so the removal of CO from the active sites is important for the gasification rate as well. Factors like particle size, pore size and particle mass affect the diffusion speed of CO and CO_2. However, when CO concentration is very small, the inhibition effect is insignificant and may be ignored. In our case (BIORED process), the CO concentration is high.

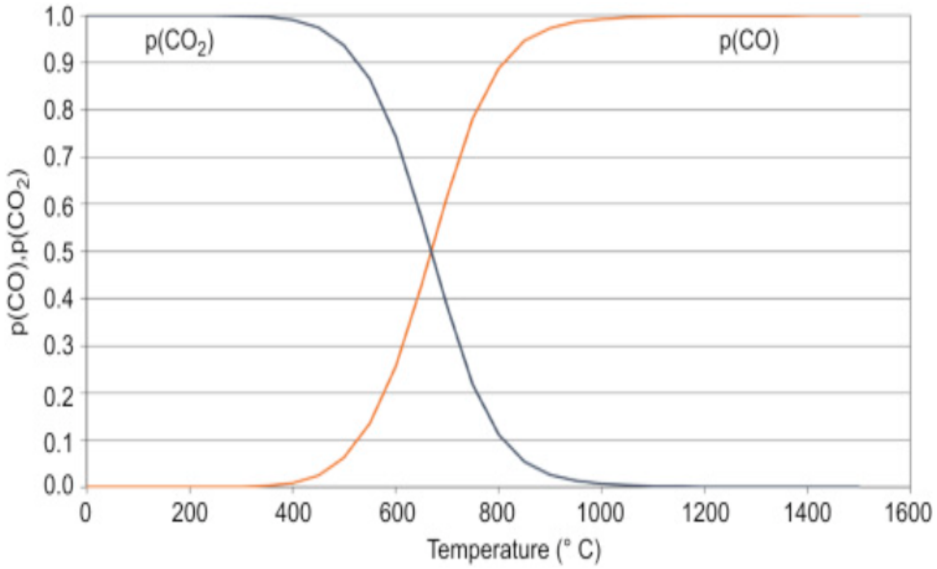

Figure 38. Equilibrium partial pressures for the Boudouard reaction [158]

IV.1.3.4. Particle size

Several studies on the effect of the particle size on the reaction rate were reported in the literature. In [159] for example, charcoal samples ranging from 60 to 900 µm were studied, higher rates were found for the smallest particles and were considered as the intrinsic reaction rates. In this study, a significant role of the particle size in the mass and heat transfer was observed.

However, in another study [133], the effect of particle size in the gasification of a low rank coal with particles ranging 106–1000 µm was found to be negligible. [160] This shows that for samples with low reactivity, the intrinsic reaction is slow enough for neglecting the diffusion even though the particle has relatively large particle size.

IV.1.3.5. Gas flow rate

Gas flow rate plays an important role in the mass transfer around the particles. First, the constraint of external diffusion decreases with higher flow rate. Second, the local concentrations of CO and CO_2 are essential for gasification rate: sufficient gas flow rate is able to remove the product gas and provide fresh reactive gas rapidly to favour the gasification. It is reported that in a TGA equipment the gas flow rate above 60 ml/min increased no longer the reaction rate, thus a gas flow of more than 80ml/min was suggested. [146]

IV.1.4 Conclusion

From the literature review, it appears that charcoal gasification was often studied and many gasification kinetic laws are available. [132] [133] [138] However, testing some of these kinetic laws, we calculated that the reaction rates could vary by orders of magnitude. This is due to the variability in the nature of the samples and in the experimental procedures. Besides, no study were conducted on the gasification of a relatively large sample (1g) by CO-CO_2 mixtures with significant amount of CO. Thus, it was decided to carry out our own experimental study on the gasification of charcoal lumps.

IV.2. Materials and Method

IV.2.1. Samples

The charcoal used in this study was the same oak charcoal, provided by the CEA in Grenoble, than the one used for the study of devolatilisation. This charcoal was prepared by slow pyrolysis at 390°C and consists in 24.45% volatile matter (dry) and 74.5% fixed carbon in the form of rough pieces of various sizes. Pieces of 200-500 mg of cylindrical shape with particle sizes of 5-10 mm were chosen for the gasification study.

IV.2.2. Experimental Setup

Figure 39 shows the diagram of the experimental equipment: SETARAM TG96 thermobalance. The thermobalance, equipped with a 28-mm diameter tube and accepting mass loss up to 3 g, was chosen for the study of gasification. In this equipment, the sample is placed in a crucible in an oven, and reacts with a controlled reactive gas atmosphere. The variation of its mass is recorded during time. From the acquired data, we can derive the gasification rate and interpret the results. The cylindrical wire crucible in platinum (Figure 40) was specially chosen to avoid external mass transfer.

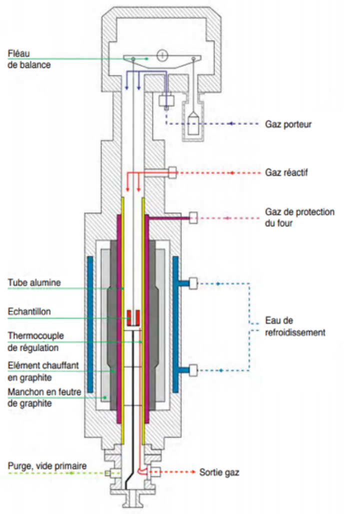

Figure 39. Diagram of the TG96 thermobalance

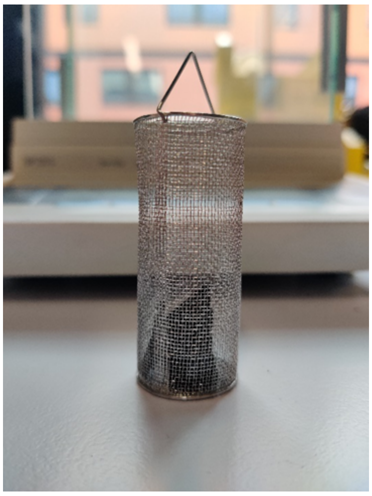

Figure 40. Photo of the mesh crucible with a charcoal lump

IV.2.3. Procedure

The procedure for each experiment in the TGA was as follows:

- About 1 g of oak charcoal containing 2-5 pieces was placed in a wire-mesh crucible into the thermobalance in an inert atmosphere of 100 ml/min of pure argon under atmospheric pressure. Then the furnace was heated at 20 K/min. The atomic mass of Argon (40) is close to that of CO_2 (44), which implies less diffusion differences. The devolatilisation occurred during the heating process.
- When the oven temperature reached the target temperature (850-1100°C), the devolatilisation was complete; we then allowed 10 minutes to stabilize the temperature of the sample.
- The reactive gas was then introduced and gasification began. Three mixtures were tested (100 ml/min CO_2; 75 ml/min CO_2 + 25 ml/min CO; and 50 ml/min CO_2 + 50 ml/min CO). The test continued until that there was no more mass loss. The gasification under 50-50% CO_2-CO at 850°C was cancelled due to its extremely low reactivity.
- The oven was cooled to 25°C under argon.

IV.3. Results and discussion

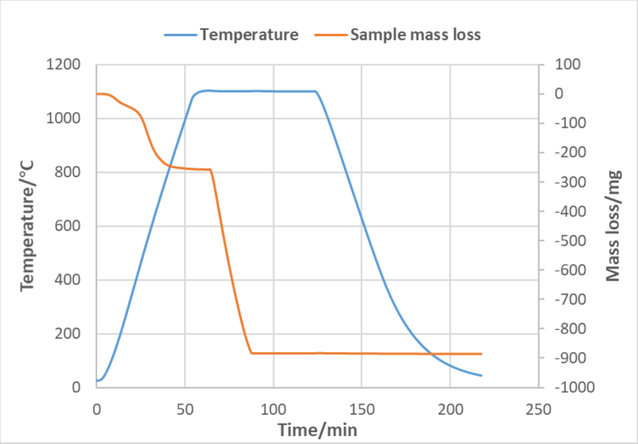

Figure 40. Example of mass loss curve and sample temperature change during gasification

Figure 40 shows the evolution of the sample temperature and its mass loss during the whole gasification test: at first, the mass of the sample started to decrease at about 100℃ because of moisture loss, and then the mass continued to decrease due to the devolatilisation of the remaining lignocellulose. Once the temperature of oven reached the target temperature, the gas was shifted from inert gas Argon to the reactive gas mixture (at 70 min in this experiment). The gasification took place and continued until that there was only ash left in the crucible, which corresponds to a stabilized value of the sample mass.

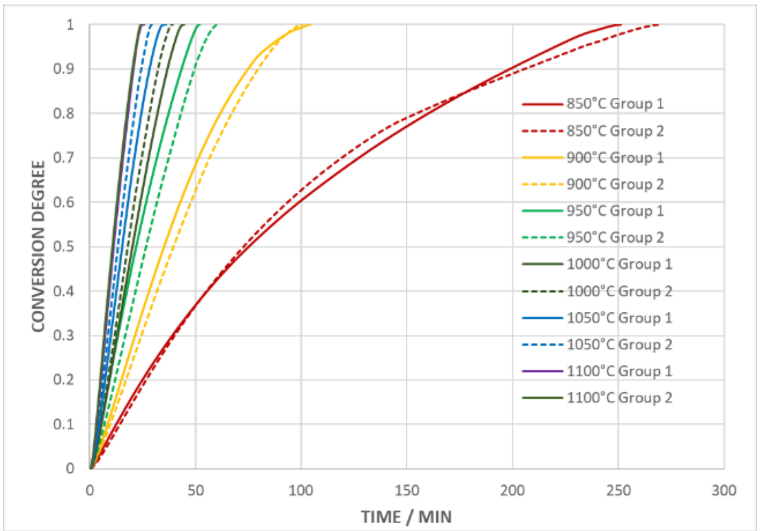

Figure 41. Curves of reproducibility under 100% CO_2 at different temperatures (Solid line: first group; dot line: second group)

The sample was composed of 2-5 pieces of oak charcoal, so the scatter of geometry of the different pieces and the irregular ash index complicated the reproducibility. However, two same groups of gasification experiments generally exhibit the same behavior of conversion. Figure

41 depicts the satisfactory reproducibility of two same sets of experiments. Mermound et al. also found a deviation of about 10% in their experimental conditions and the achieved repeatability was acceptable considering the wood heterogeneity and the large size of the particles. [161]

IV.3.1. Effect of gasification conditions

In this part, we will discuss about the effect of gasification conditions from experimental data. The observation will be compared with literature.

IV.3.1.1. Effect of temperature

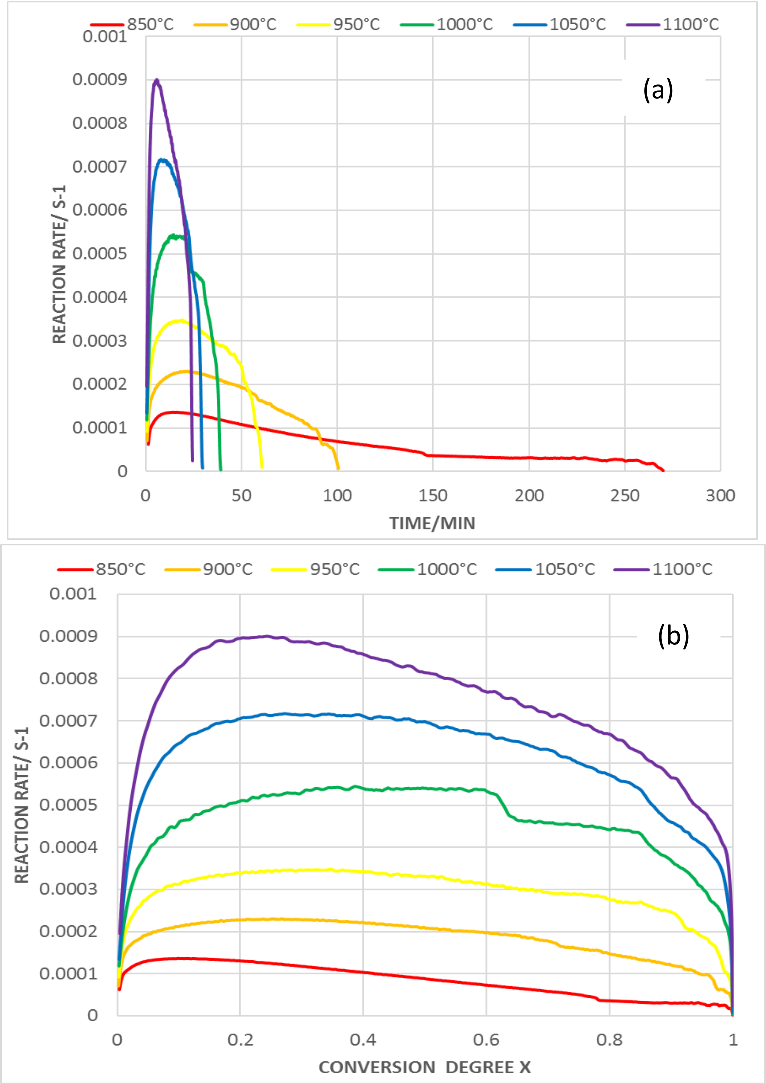

Figure 42. Evolution of the gasification rate with (a) time and (b) conversion at 850-1100°C

Figure 42 shows the evolution of the mass loss rate with time and char conversion for different temperatures in the isothermal runs. The increase in temperature contributed to faster gasification rate and shorter reaction time, especially at relatively low temperatures. For instance, the gasification time declined from 270 minutes to 40 minutes when the temperature rose from 850℃ to 1000°C. This was expected, a temperature rise promotes the charcoal reactivity and the amount of active gasification sites for reaction with CO_2; both of which improve the overall reactivity. [162] At low temperatures, the reaction was under Regime I, where the intrinsic reaction resistance is far higher than the diffusion resistance. However, at high temperatures, the increase in temperature promotes significantly the intrinsic reaction rate and makes the intraparticle diffusion limiting, so the rise in the reaction rate became less important. In Figure 42b, the reaction rate reached its maximum value at low conversion values, $X<0.2$ in most cases, and then decreased at all temperatures, which is consistent with the Random Pore Model.

However, a recent work has suggested that such a maximum rate was not associated with real reaction mechanisms, but was rather a result of replacing the inert gas with the reaction gas during experiments. [129] To study this phenomenon, we changed the position of the gas mixture inlet and compared the sequential results with the original ones. Results of these experiments are discussed in part IV. 3.5.

The reactivity depends on the conversion, on the temperature and on the gas composition as well. For most chars of coal, lignite and peat, reactivity decreases with increasing conversion, whereas the opposite is observed for most chars of biomass. [163] In the literature, the reference value (unity value) of the reactivity, also called reactivity index, was chosen differently according to the authors: X=0.05, 0.2, 0.5, or an average value in a certain range of conversion. In the present study, we considered reactivity index at X=0.05 as the reference value.

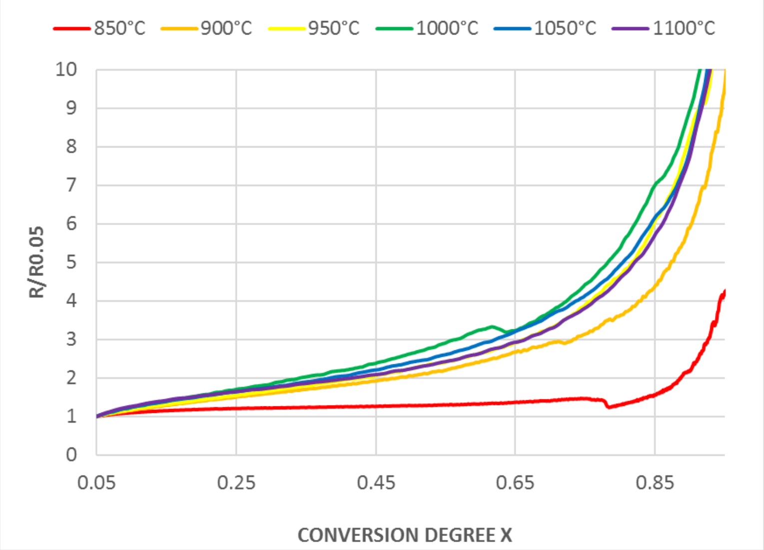

Figure 43. Change in R/R0.05 with conversion under 100% CO_2 at different temperatures

We can see in Figure 43 that the reactivity continuously increases with the conversion for all the temperatures considered (850-1100°C). However, the reactivity for temperature higher than

900°C exhibited the same behavior, while for 850°C the reactivity increased more slowly until 80% conversion, indicating that the reaction regime changed from 850°C to 900°C. Besides, for the reactivity at all temperatures, there are two different regions: the reactivity increased linearly with conversion in the range of 0-0.75, and for higher values of conversion ($X>0.75$) the reactivity evolution is exponential. The first linear stage of increase is attributed to the development of pores volume and specific surface area along with the conversion. The second stage may reflect, as stated by several authors, the catalytic effect of Alkali and Alkaline Earth Metals (AAEM) on reactivity since their concentration in the rest of the solid has increased,[177] however, for the charcoal in our study, the ash concentration is quite low.

IV.3.1.2. Effect of gas composition

Figure 44 shows the influence of gas composition on the gasification rate. The gasification test under 50%CO_2+50%CO at 850°C was too slow for the industrial use hence ignored. We observed that the increase in the CO_2 partial pressure enhanced char gasification rate, thus, the gasification under pure CO_2 finished faster at almost all temperatures. In addition, the switch from 75%CO_2+25%CO to 50%CO_2+50%CO slowed down the gasification rate more significantly than that from 100%CO_2 to 75%CO_2+25%CO, especially at relatively low temperatures (<1050°C). This is due to the more important reduction of the driving force in the equilibrium curve in the former case. Meanwhile, the maximum values of reaction rates decreased with increasing CO partial pressure. At 850°C, this trend was not observed probably because the reaction rate at 100% CO_2 was so slow that the existence of CO had less impact. In addition, the inaccuracy of experimental conditions like geometry of the samples and the irregular ash index may have played a great role. Again, we observed the increase in reaction rate at the early stage of conversion in most cases, which is consistent with the RPM.

Another approach to visualize the effect of CO-CO_2 partial pressure is by the change in the reactivity index. The reactivity index is normally taken as an indicator of the char gasification reactivity, which is defined here when $X=0.05$. Higher reactivity index indicates higher reactivity. Figure 45 shows the $R_{0.05}$ values versus 1000/T. Here we can clearly see the positive effect of increasing the CO_2 partial pressure and the limiting effect of the product gas CO, especially at relatively high temperature.

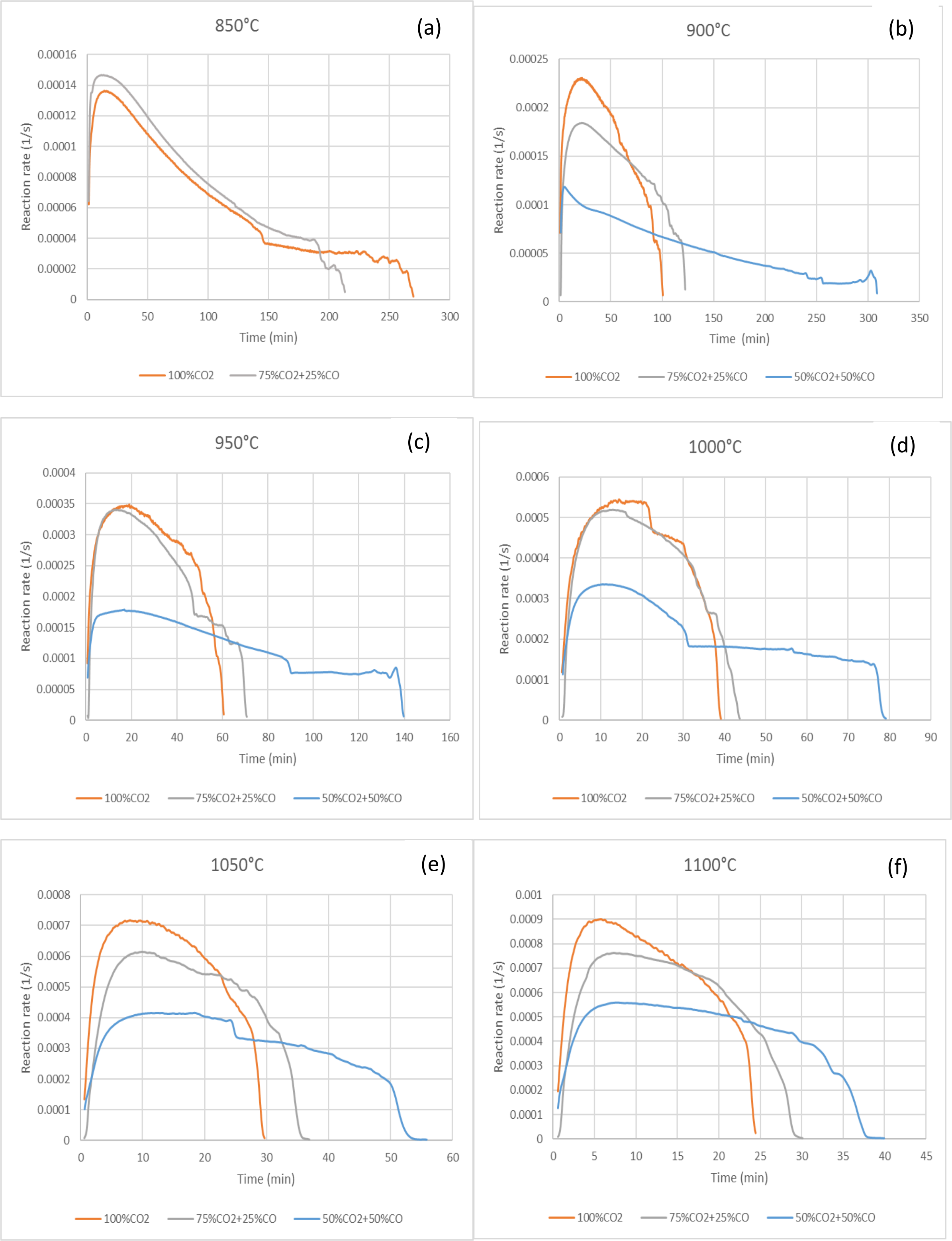

Figure 44. Evolution of the gasification rate with time at 850-1100°C under different atmospheres

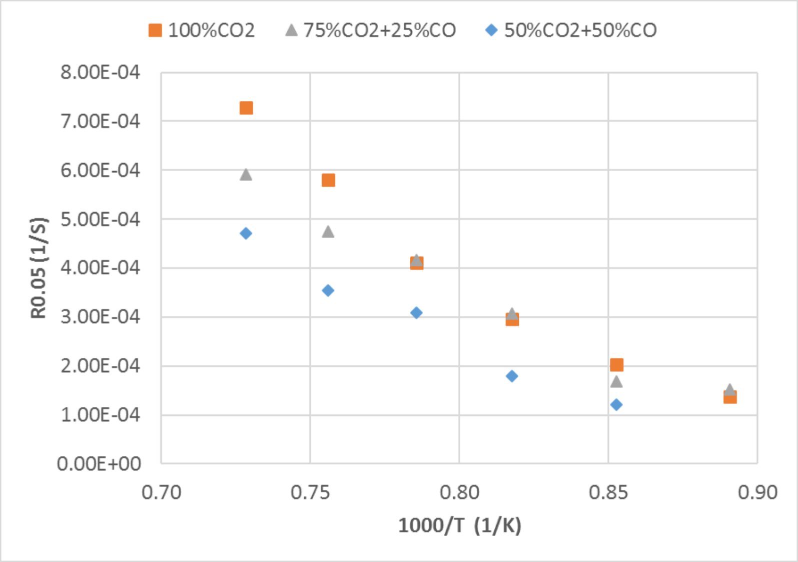

Figure 45. R0.05 values versus 1000/T under different gas mixture at different temperatures

IV.3.2. Kinetic parameters with pure CO_2 gasification

The curve-fitting of the simplified n-th order model was first tested. The partial order of CO_2 was not clear in our experiments because we kept the total pressure of CO and CO_2 equal to atmospheric pressure rather than using an inert gas like Argon, thus the inhibiting effect of CO cannot be eliminated. However, even though the reaction order is not obvious, we were able to compare the calculated apparent activation energy with numerous literature data.

Many authors consider that f(X) is equal to unity when X = 0.05 or X = 0.5. Scott et al. suggested that the initial rate of reaction was preferred, since only the initial properties of char were known and it was less affected by the pore evolution due to the conversion of the char. [164] In our study, we chose X =0.05 as the initial rate and f(X=0.05) = unity.

Consequently, if $\frac{r(X)}{r(X=0.05)}$ is plotted as a function of the conversion X, one should get f(X) and could possibly obtain a single curve or all temperatures if the reaction is in the kinetically controlled regime. Figure 46a shows that it is not the case, there are globally two behaviors, the one at 850°C and the other one for the other temperatures. Thus, the reaction is probably kinetically controlled at 850°C (and under) and in a mixed pore diffusion-controlled regime at the higher temperatures.

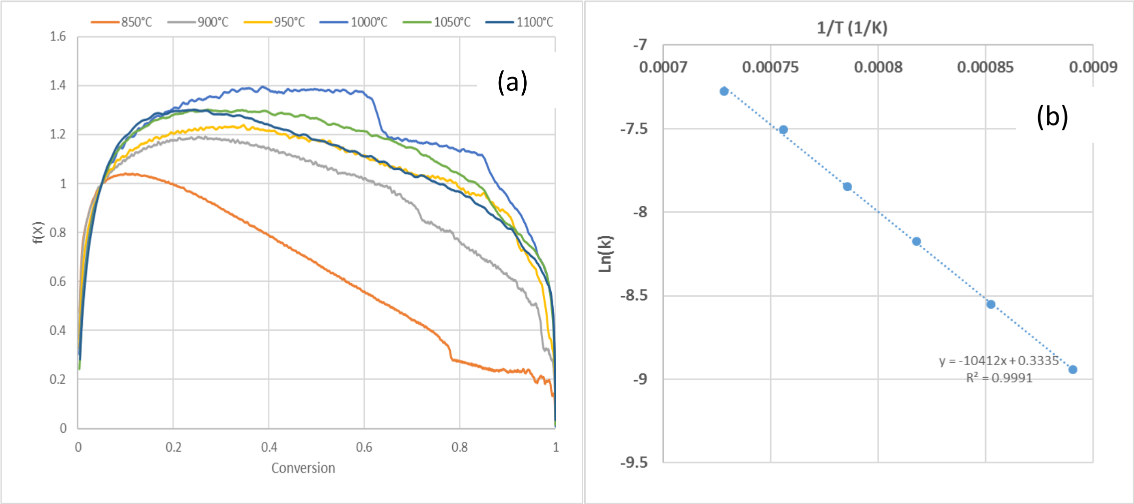

Figure 46. (a) Reactivity function over conversion and (b) Arrhenius plot of gasification rate for oak charcoal under pure CO_2 gas

However, an Arrhenius plot of the initial reaction rates at X=0.05 (Figure 46b) gives a straight line, suggesting an unchanged limiting process in the whole range of temperatures (850-1100°C). The derived apparent activation energy is 86.5 kJ/mol. According to Ollero et al., values for the gasification of biomass chars vary between 99 and 318 kJ/mol. [163] This scatter in literature data reflects non-intrinsic but rather apparent values of the activation energy because the conditions of operation, the reactivity of biomass and the method of analysis were different. The relatively low apparent activation energy value in the present work is probably due to the effect of the pore diffusion associated with the large size of sample we used. Indeed, Bui concluded that large particle size not only enhanced the diffusional resistance of reactive gas into the active sites, but also emphasized the inhibiting effect of the product gas due to the accumulation inside the pore and, last but not least, possible heat transfer limitations. [159] Gomez-Barea et al. found the same phenomena, the importance of the diffusional effects at high temperature and large particle size, i.e., at large Thiele modulus. [166] Vincent et al. have also concluded an increase in the reactivity values, along with an increase in the temperature, and a decrease with an increase in the particle size for torrefied and pyrolyzed chars. [167] In the present study, we chose large samples on purpose, to be representative of the charcoal lumps that could be used in the BIORED process. Consequently, the diffusional resistance in our experimental protocol prevented us to obtain "intrinsic reaction" kinetics. The diffusional effects are here included in the kinetic parameters.

IV.3.3. Kinetic modelling of gasification under mixture of CO and CO_2

As discussed in sector IV-1, the Langmuir-Hinshelwood equation is well adapted to represent the effect of varied partial pressure of CO_2 and CO. We determined its parameters by curve-fitting from a large set of experiments: different temperatures (850°C-1100°C) and gas compositions (CO_2-CO/50-50, 75-25, 100-0). The curve-fitting toolbox in Python with the TRF method for the optimization of a nonlinear least squares allowed us to estimate the kinetic parameters from the initial reaction rates with bounds on the variables. The objective function is as follows:

$$OF = \sum_{i=1}^{n}[\left(\frac{dX}{dt}\right)_{exp} - (\frac{dX}{dt})_{calc}]^2 \qquad \text{(IV-11)}$$

where $\left(\frac{dX}{dt}\right)_{exp}$ and $(\frac{dX}{dt})_{calc}$ are respectively the experimental and simulated reaction rate, and *n* is the number of experimental points. Figure 47 shows that the result of the L-H model is relatively satisfactory to fit the experimental results with CO inhibition.

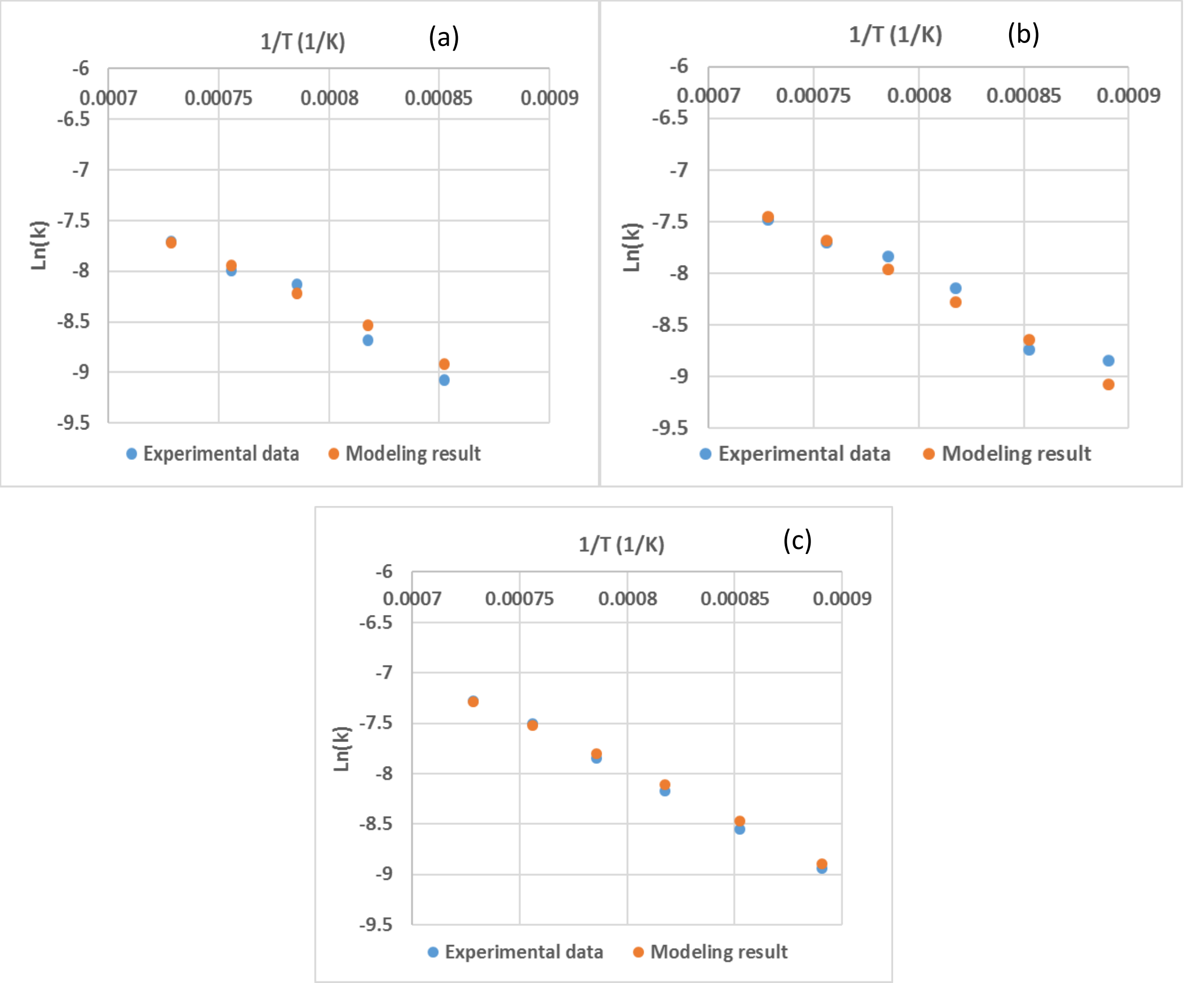

Figure 47. Comparison of L-H model and experimental reaction rate under different CO_2-CO conditions (a) 50-50; (b) 75-25; (c) 100-0

According to equations (R19-R21) plus the Arrhenius law for the constants, six parameters have to be determined: A_1, A_2, A_3, Ea_1, Ea_2, Ea_3.

Char origin	Ea_1(kJ/mol)	Ea_2(kJ/mol)	Ea_3(kJ/mol)	References
Oak charcoal	130	172	57	Present work
Birch	165	21	236	Barrio et al. [168]
Wheat	100	-1	155	Rathmann et al. [169]
Wheat	152	-2	241	Illerup et al. [170]
Coconut	157	243	408	Bandyopadhyay et al. [171]
Olive pits	60	38	167	Ollero et al. [163]

Table 12. Comparison of apparent activation energies for CO_2/CO gasification of char

The calculated activation energies were compared to values from other studies where CO inhibition and the L–H model were considered (Table 12). The apparent activation energy of the first reaction is in the range of literature study (between 100 and 165 kJ/mol in most cases). However, the second reaction exhibits scattered results and even negative values, which could be understood as a zero-activation energy, i.e., the reaction 2 does not depend on temperature. [168] [163] The third apparent activation energy is more important than the first in the literature suggesting that the third reaction is the rate-limiting step for the overall gasification, which contrasts with our work probably because we used much larger sample than other studies. The obtained initial Langmuir-Hinshelwood gasification rate is expressed by Equation (IV-12):

$$k(T,P_i) = \frac{328 * \exp(-\frac{130.795}{RT})P_{CO_2}}{1 + \frac{328 * \exp(-\frac{130.795}{RT})}{0.128 * \exp(-\frac{57.176}{RT})}P_{CO_2} + \frac{5340 * \exp(-\frac{172.316}{RT})}{0.128 * \exp(-\frac{57.176}{RT})}P_{CO}} \; s^{-1} \qquad (\mathrm{IV}-12)$$

IV.3.4. Pore evolution and Reactivity function

IV.3.4.1. Pore size distribution by mercury porosimetry

We used mercury porosimetry to analyse the pore evolution of our charcoal samples. The samples were the charcoal pieces gasified at different degrees of conversion: raw charcoal, devolatilised charcoal, and partially gasified charcoal samples. The principle of mercury porosimetry is to fill the pores of a solid, from the largest to the smallest, by gradually increasing the pressure applied. With the device Micromeritics Autopore 9500, pores between 1 mm and 10 nm can be analysed. Thus, the behaviour of micropores (0-2 nm) is neglected in the present study.

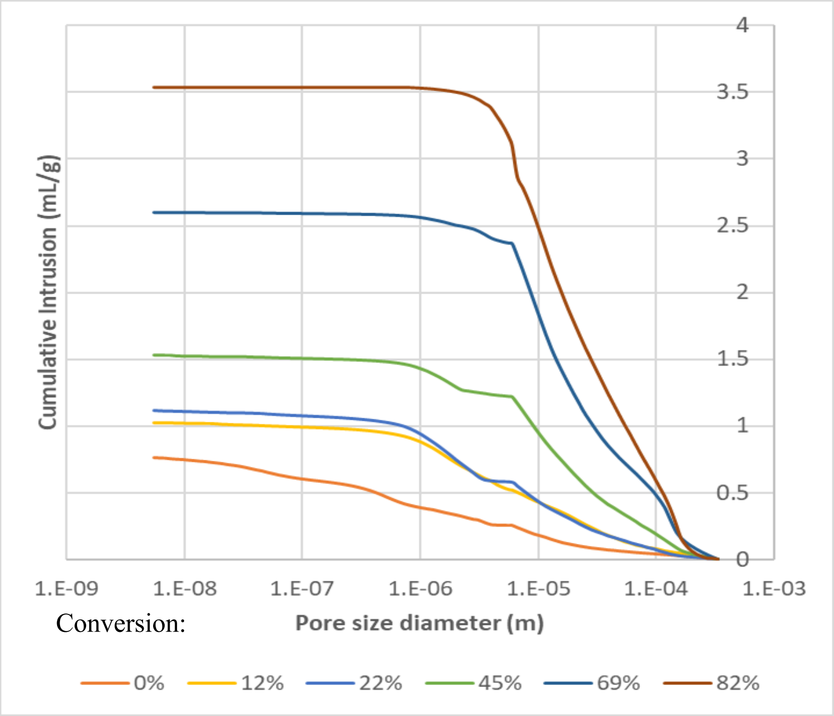

Figure 48. Evolution of the cumulative intrusion volume with the degree of conversion for a gasification at 900°C

Figure 48 presents the cumulative pore volume of charcoal measured at different conversions for a gasification at 900°C. The pore structure analysis at 0% conversion refers to the sample after the devolatilisation in argon atmosphere and it has little difference with that of the raw material. The selection of 12, 22, 45, 69 and 85% conversions aimed at investigating the pore evolution from the beginning to the end of the gasification. The largest pores had a diameter of around $5x10^{-3}$m. The total pore volume showed a relatively slight augmentation at the early stages of gasification from 0% to 22%, and increased more significantly afterwards.

Figure 49 shows the change in the pore size distribution with conversion at 900°C. For the charcoal at 0% conversion, the pore distribution was more or less regularly distributed between $5x10^{-9}$m and $5x10^{-3}$m. Once the gasification began, the volume of pores smaller than $5x10^{-7}$m declined and that of pores larger than $5x10^{-7}$ m increased until 22% conversion. It indicates that the reaction took place in the surface area of the pores smaller than $5x10^{-7}$ m and that these pores turned into larger pores in the early stage of gasification. However, since the smallest pores (smaller than $5x10^{-7}$ m) were almost consumed at 22% conversion, the surface area of pores between $5x10^{-7}$ and 5×10^{-6} m became the new reaction sites. As the gasification continued from 22% conversion to the end of the reaction, these pores became pores larger than 5×10^{-6} m. Therefore, the gasification occurred at the sites where the pores size is smaller than 5×10^{-6} m. Kawakami et al. also studied the gasification of coke, wood charcoal and graphite in the cubic form of 10x10x10 mm, and they concluded that the reaction occurs exclusively on the surface of pore between 10^{-8} to 10^{-6} m in diameter. [137] Another study of Kawakami et al. proved that at temperature lower than 1100°C, the CO_2 molecules could penetrate into the bulk to contribute the reaction. Thus, the reaction occurred on the surface of small pores between 10^{-8} to 10^{-6} m in diameter in their work. [172] Kashiwaya et al. suggested that the gasification should not occur on the surface of pores smaller than 10^{-5} m that are found in the highly graphitized area. [173] Compared with these studies, we observed almost the same phenomenon: the gasification of 1g oak charcoal took place in the mesopores and some macropores at the early stage and then continued in the macropores when mesopores were fully replaced by macropores. In contrast, Komarova et al. using coal char samples of smaller particle size reported that the char gasification occurred only in the micropores and mesopores and the former turned into small size of mesopores (close to 2nm) for the further reaction, but the mesopores did not change into macropores. [174]

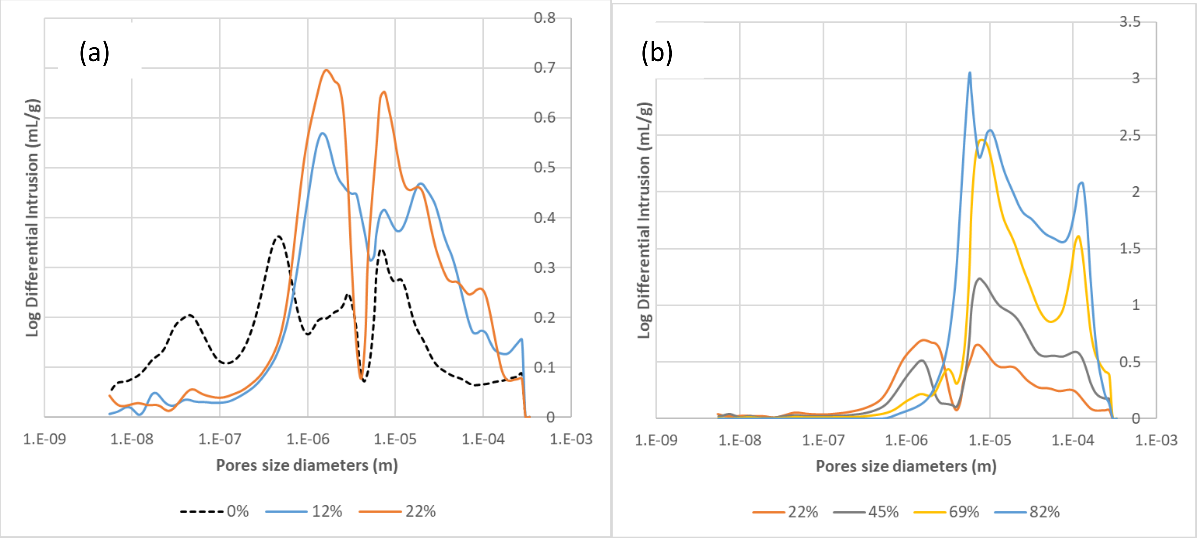

Figure 49. Change in the pore size distribution of the charcoal with the conversion degree (a) at early stages (b) for the rest of gasification at 900°C

The maximum reaction rate was achieved at approximately 22% at 900°C (See Figure 42b) and the reaction kept the same rate then and finally slowed down to the end. It can be inferred that the gasification occurring in the surface area of pores smaller than $5x10^{-7}$ m in the early stage was slower than that on pores between $5x10^{-7}$ and 5×10^{-6} m.

As described in the introduction, the porosity was expected to increase due to the increase in the total volume and simultaneously the apparent density declined. The total porosity ϵ was calculated as follows:

$$\epsilon = \frac{\rho_{true}-\rho_{app}}{\rho_{true}} \quad \text{IV-13}$$

where the true density ρ_{true} is defined as the ratio of char mass and volume of solid after deduction of the void volume, and apparent density ρ_{app} is defined as the same ratio including void volume. Both can be measured with mercury porosimetry.

Figure 50 depicts the change in the porosity and the apparent density at different conversions. The apparent density declined slightly from 600 kg/m^3 in the beginning and then dropped linearly to 200 kg/m^3 at 82% conversion. The porosity increased slowly from 0.55 to 0.6 during char conversion from zero to 0.42 and then was promoted much faster from 45% conversion. The porosity for char of 82% conversion reached 0.8. A similar value was obtained with brown coal char CO_2-gasification in the study of Komarova. [174]

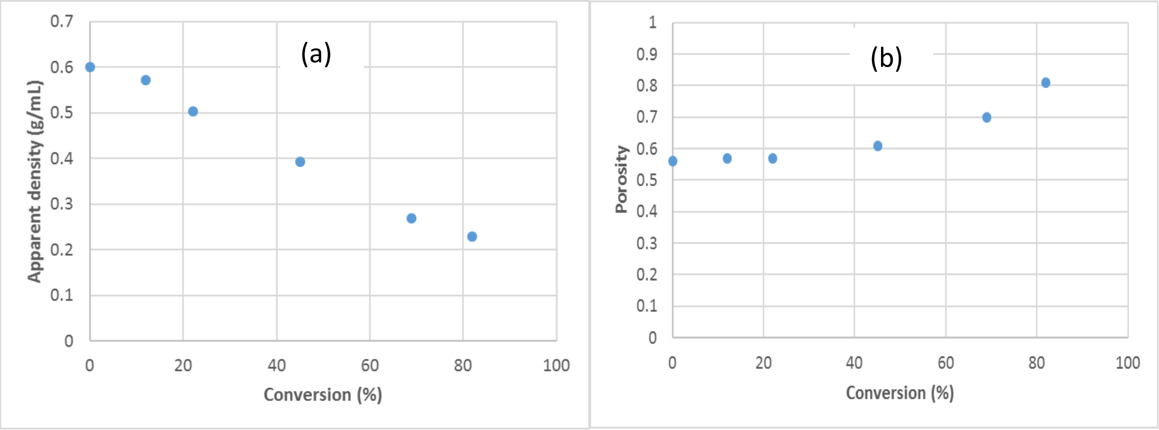

Figure 50. Change in (a) the porosity and (b) the apparent density of the charcoal with conversion at 900°C

Those results, obtained toward the end of this work, give interesting insights on the way the solid charcoal is consumed during gasification. From the experimental knowledge of the evolution of the pore size distribution, it should be possible, through pore models [175] , to calculate the change in reaction rate with conversion via the evolution of the specific surface area. Sbaffo et al. did that in the opposite case of a reaction causing a decrease in porosity. [176] We lacked time to develop a similar approach for gasification.

IV.3.4.2. Reactivity function

Figure 51 depicts the change of reaction rate with conversion for 100-0%, 75-25% and 50-50% CO_2-CO at different temperatures. One can see that reaction rates are showing a peak value at conversion value of approximately 0.2. We tested four models (VRM, ICM, RPM and MRPM) against the experimental curves. The curve-fitting was performed using again the curve-fitting toolbox of Python.

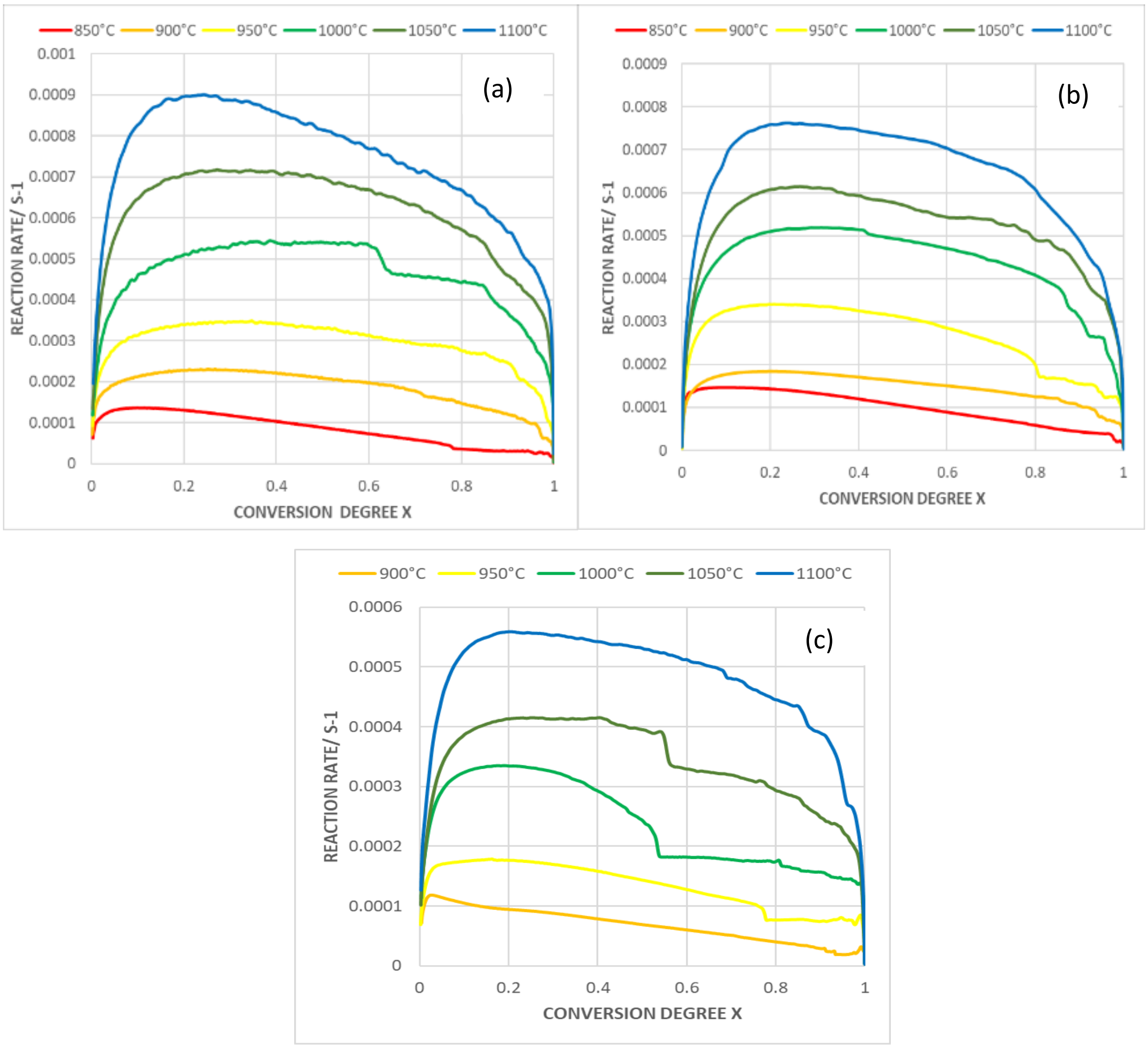

Figure 51. Reaction rate at different temperatures under different CO_2-CO conditions (a) 100-0%; (b) 75-25%; (c) 50-50

As shown by the correlation coefficients (Table 13), VRM and ICM models were unable to predict the reactivity. This was expected as they assume that the reaction rate always slows down with the conversion. The model leading to the best correlation was the MRPM, whose correlation coefficients were always superior to 0.90 except at 1000°C under 50-50% CO_2-CO. Other studies confirmed that the experimental data for biomass chars were better described with the modified random pore model over the entire conversion range. [177] [179] The MPRM parameters are listed in Table 13: the pore structure constant φ, dimensionless constant c and dimensionless power constant p (appendix A shows the comparison of experimental and simulated curves).

Gas mixtures	Temperatures (°C)	Correlation coefficients (R^2)				MRPM parameters		
		VRM	ICM	RPM	MRPM	φ	c	p
100-0% CO_2-CO	850	0.77	0.65	0.95	0.94	0.64	10^{-4}	0.12
	900	-1.65	0.75	0.79	0.98	5.37	1.09	12.48
	950	-4.19	0.45	0.33	0.97	6.18	1.14	8.52
	1000	-5.52	-0.08	0.28	0.93	8.86	1.13	9.40
	1050	-4.58	0.24	0.36	0.92	7.69	1.13	10.28
	1100	-4.78	0.36	0.29	0.91	6.95	1.12	11.87
75-25% CO_2-CO	850	0.54	0.97	0.94	0.99	1.51	1.06	22.14
	900	-2.62	0.81	0.54	0.95	4.39	1.12	9.64
	950	-1.32	0.77	0.82	0.97	5.18	1.07	24.82
	1000	-2.64	0.42	0.67	0.97	7.33	1.11	7.96
	1050	-2.87	0.32	0.53	0.96	7.99	1.14	9.11
	1100	-2.41	0.37	0.67	0.97	8.27	1.12	8.81
50-50% CO_2-CO	900	0.74	0.94	0.91	0.99	0.49	1.08	8.99
	950	-0.67	0.87	0.70	0.97	2.66	1.09	27.05
	1000	-0.72	0.77	0.54	0.55	2.15	10^{-4}	0.12
	1050	-1.60	0.69	0.68	0.97	6.06	1.12	13.35
	1100	-1.87	0.59	0.63	0.97	6.50	1.14	8.87

Table 13. Correlation coefficients for the fitting of CO_2 gasification using VRM, ICM, RPM, MRPM and kinetic parameters of MRPM

However, using different kinetic parameters of the MRPM according to conditions is not appropriate for the the kinetic modelling of gasification in the BIORED shaft furnace. For this reason, a single, average MRPM equation (IV-14) was derived from the curve-fitting of all the reactivity functions at different temperatures under pure CO_2 atmosphere (See Appendix A):

$$f(X) = (1 - X)\sqrt{1 - 4.89 ln(1 - X)}\,(1 + (1.07X)^{21.32}) \quad \text{(IV-14)}$$

In conclusion, the final gasification rate is the combination of equation (IV-12) and (IV-14) and is expressed as follows:

$$\frac{dX}{dt} = \frac{328*\exp\left(-\frac{130.795}{RT}\right)P_{CO_2}}{1+\frac{328*\exp\left(-\frac{130.795}{RT}\right)}{0.128*\exp\left(-\frac{57.176}{RT}\right)}P_{CO_2}+\frac{5340*\exp\left(-\frac{172.316}{RT}\right)}{0.128*\exp\left(-\frac{57.176}{RT}\right)}P_{CO}} \cdot (1 - X)\sqrt{1 - 4.89 ln(1 - X)}\,(1 + (1.07X)^{21.32})\ s^{-1} \quad \text{(IV-15)}$$

IV.3.5 Effect of gas switching time

We also carried out some experiments in which the localization of the gas injection in the thermobalance is changed to investigate the influence of gas switching time on the reaction rate.

Two configurations were used, one with gas introduced through the inlet for the reactive gas near the sample (standard injection), and one with gas introduced through the inlet for the carrier gas at the head of the thermobalance furnace, which results in a significant increase in gas switching time (See Figure 37a). The anticipated time for the reacting gas to flush the inert gas after its introduction was about 20 min for injection at the head and 5 min for injection near the sample. The injection at the head is a usual practice and was first performed before we observed that the injection near the sample was preferable and was thus selected as the standard practice for the rest of the experiments. All the results previously presented were with the latter injection.

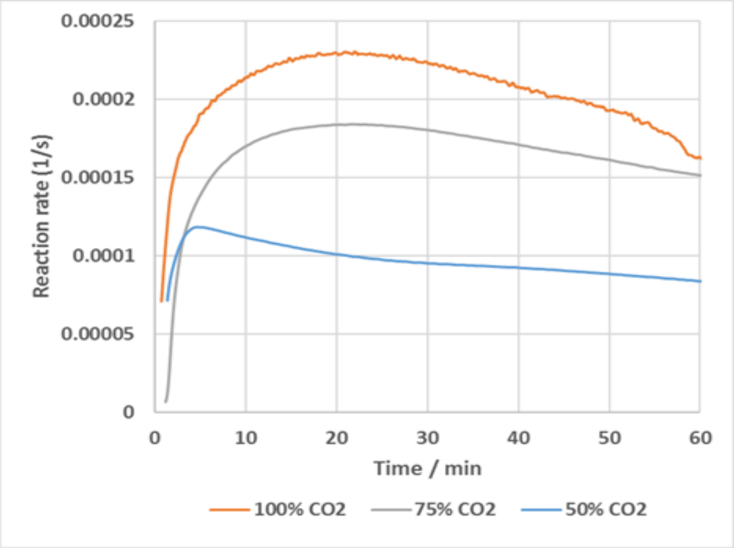

Figure 52. The effect of partial pressure with the reaction rate vs. time at 900°C when switching from Argon to different CO_2-CO conditions (100-0%; 75-25%; 50-50%) for the standard introduction

Gomez et al. has pointed out that the maximum reaction rate is not due to the increase in the reactivity but is the result of gradually increasing CO_2 partial pressure in the gas mixture while the inert gas is shifted to the reactive gas. [129] They proved that the time to observe a maximum reaction rate, after changing the reaction gases remained constant whatever the temperature, thereby confirming the effect of the variable reactive gas concentration on the gasification. However, in the present study, contrary to their conclusion, the time to reach the maximum reaction rate lasted longer than the gas switching time for gasification tests under 75-25% and 100-0% CO_2-CO mixtures (see Figure 52). It indicates that the increase in reactive surface area and porosity does influence reactivity according to the modified random pore model, even after the reactive gas was fully introduced in the reactor.

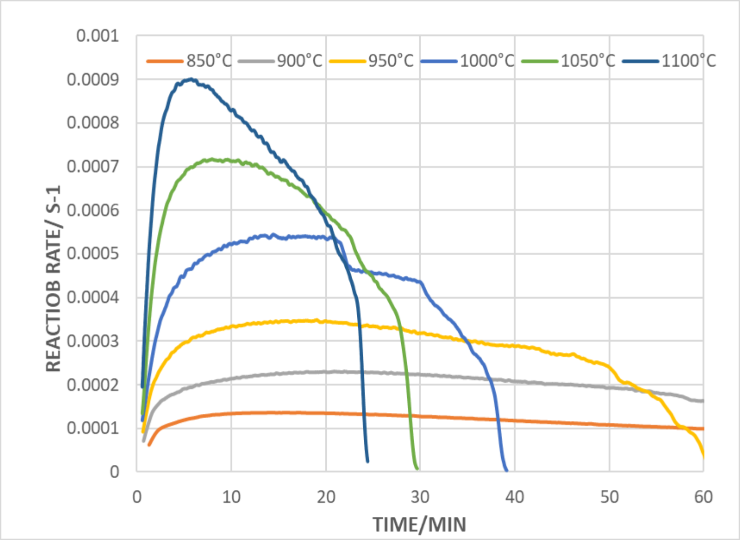

Figure 53. The effect of temperature with the reaction rate vs. time when switching from Argon to 100% CO_2 at 850-1100°C for the standard injection

Figure 53 confirms the same observation, where can see that the time to reach maximum reaction rate at different temperatures was not constant.

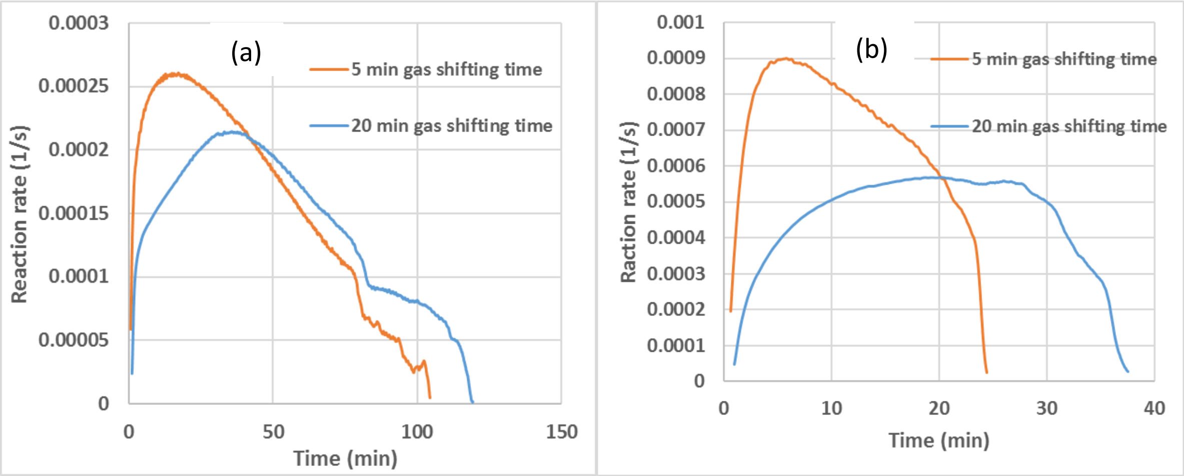

Figure 54. Comparison of reaction rate with different gas switching time under 100% CO_2 gas at 900℃ (a) and 1100℃ (b)

As shown in Figure 54, the maximum reaction rate decreases with gas switching time and was almost twice higher in 5-min gas switching time than that in 20-min gas switching time at 1100°C. This observation is consistent with the work of Gomez et al. They claimed that the char exposure to an inert gas atmosphere prior to gasification decreased the reactivity of the char. This can be explained by a reduction in the char mesopore area, which was induced when pyrolysis and gasification were separated with an isothermal step using an inert gas. [129]

IV.4. Conclusion

The gasification of charcoal is a heterogeneous reaction, which means that not only the intrinsic reaction at the solid surface, but also the mass transfer of reactant and product gas, and possibly heat transfer contribute to the overall transformation. Regarding the reaction mechanism, the Langmuir-Hinshelwood model assumes the gasification starts with the formation of the carbon-oxygen surface complex on the active sites and finishes with the decomposition of the complex to release CO. Different assumptions lead to various physical models in the literature, such as VRM, SCM, RPM and MRPM; and empirical models like n-order model and n-z model. The reactivity is dependent on the porosity and surface area, mineral contents and pyrolysis conditions. Furthermore, the operating conditions including temperature, pressure, gas composition, particle size and gas flow rate, have a strong influence on the reactivity as well.

We studied the gasification of 1-g oak charcoal pieces under different CO-CO_2 mixture at 850-1100°C using thermogravimetry. The experimental results show that an increase in temperature made the gasification faster and the reaction time shorter, especially at relatively low temperatures. The increase in the CO_2 partial pressure enhanced char gasification rate. Taking the reaction rate at $X=0.05$ as the initial rate for the kinetic study, the pre-exponential factor was 1.396 s^{-1} and the calculated apparent activation energy was 86.5 kJ/mol with the n-th order model. The kinetic parameters of the three reactions of the Langmuir-Hinshelwood model were determined and the apparent activation energies were compared with those of other studies. Through mercury porosimetry analysis of partially gasified samples, we showed that the gasification of the charcoal took place in the mesopores and some macropores at the early stage and then continued in the macropores when the mesopores were fully replaced by macropores. The modified Random Pore Model appeared to be the only satisfactory approach to fit the experimental reactivity function. We investigated the effect of the gas switching time in the TG experiments. Contrary to the conclusion of Gomez et al., we found that the increase in reactive surface area and porosity still influenced the reactivity, in agreement with the modified random pore model, even after the reactive gas was fully introduced in the reactor.

V. Modelling of the BIORED shaft furnace

Three different reactor types were introduced earlier to perform gas-based direct reduction: retort, shaft furnace and fluidized bed reactor. Among these, the shaft furnace is preferred thanks to the high heat transfer between the solid and the gas and its relatively simple installation. In this chapter, we will introduce the mathematical model of the shaft furnace for the BIORED process and study the evolution of temperatures, gas composition, charcoal conversion and reduction of iron ore. Then we will perform a sensitivity analysis on the effect of inlet gas temperature, inlet gas composition and charcoal reactivity. At last, since the process does not exist yet at industrial or pilot scale, we will present a specific experimental method by TGA to validate our model.

V.1. Mathematical modelling of shaft furnace: state of the art

The reduction process that takes place inside a direct reduction reactor is complex to model since, in addition to the heat, mass and momentum transfers, it involves a set of both homogenous and heterogeneous chemical reactions. In this context, a great number of models have already been developed to represent the DR process. Models from the pellet scale to the reactor scale exist. We will first introduce the pellet scale.

The reduction of iron oxides at pellet scale by H_2 or CO or the mixture of H_2-CO has been extensively studied. Most of the work combines experimental study and modelling of the kinetics. Some works are based on the unreacted shrinking core model (USCM) with one (iron-hematite interface) or more fronts separating the solid phases (iron-wustite-magnetite-hematite interface, from the outside to the center), others use porous solid approach (grain models, where the pellet is assumed to be composed of a set of spherical grains) or even homogeneous models (the pellet is seen as a continuum). In the present study, we chose a combination of USCM and solid porous model.

On the reactor scale, the first models that were developed aimed at understanding the behaviour of commercial shaft furnaces and the effect of operational parameters. Takenaka et al. and Takahashi et al. developed 1-D models of the Midrex shaft furnace with the three-interface pellet model in 1986. [180] [181] The kinetics of the reduction of the pellets and the side reactions were measured from independent experiments and were incorporated in their models. From the models, they could show the important effects of temperature, pressure, and gas composition on the metallization degree. Parisi et al. in 2004 simulated the reduction zone of the shaft furnace with the USCM. The model satisfactorily fits the data from at least two MIDREX plants

(Siderca SA in Argentina and Gilmore Steel Co. in the U.S.). [182] The proposed model was able to study the relation between metallization and productivity and how the production is affected by the proportion of carbon monoxide in the reducing gas. Alhumaizi et al. in 2011 presented a model of a 1-D DRI plant using the USCM and a homogenous model of the reformer. [183] The modelling of the two major units (shaft furnace and reformer) contributed to a better understanding of the Midrex technology. In 2015, Shams et al. improved the modelling of the shaft furnace by considering the whole reactor, including the transition and cooling zone, which are usually less studied in the literature. [184] Castro et al. in 2018 analysed the shaft furnace as a multiphase and multicomponent reactor by applying a comprehensive mathematical 2-D model. [185] Their model features a packed bed composed of pellets of different diameters and lump ore with the gas flow through the arrangement of particles. Our group in 2017 developed a 2-D model (REDUCTOR) to simulate the whole shaft furnace (Midrex or HYL) including the reduction, transition and cooling zones, on which the present work is based. [187]

Recently, the modelling of the shaft furnace aims to investigate novel propositions on the classical shaft furnace. Ranzani et al. in 2013 developed a model of shaft furnace for hydrogen ironmaking and experimentally validated the feasibility of the reduction of iron ore pellets by H_2. [3] Ghadi et al. in 2017 developed a 2-D mathematical model with the USCM to examine the effect of a dual gas injection system on the behaviour of the Midrex process and energy consumption. [186] The choice of one or two injection of hydrogen leads to different radial and axial distributions of operational parameters including gas and solid temperature, fractional reduction of iron oxides and hydrogen and water vapour concentration. Shao et al. in 2021 modelled a shaft furnace for hydrogen reduction of iron oxide pellets under operation with top gas recycling (TGR). [188] A single-row gas injection system and a new top gas recycling system featuring dual-row injection was also evaluated briefly with the coupled phenomena of gas-solid counter current reactive flow and heat transfer. Rocha et al. in 2019 proposed a combination of the shaft furnace for direct reduction with self-reducing pellet burden. [189] In addition, with the goal of improving the furnace efficiency and reducing the need for reformed gas, the injection of natural gas and oxygen into the bustle region is proposed. The simulation results obtained for a combination of 15% of self-reducing pellets in the burden with 2.5% oxygen and natural gas injection were the best among the scenarios simulated, with a reduction of 10% in the gas consumption. Alencar et al. in 2021 studied the clustering formation by adapting a numerical model of a DR process. [190] The clustering is the sintering of the metallic iron on the surface of the pellets in such a way that they attach to each other, forming clusters that hinder the gas flow through the shaft.

This short review reveals that no model of a shaft furnace fed with a charge containing biomass has been published. Thus, we had to develop our own approach.

V.2. Mathematical model

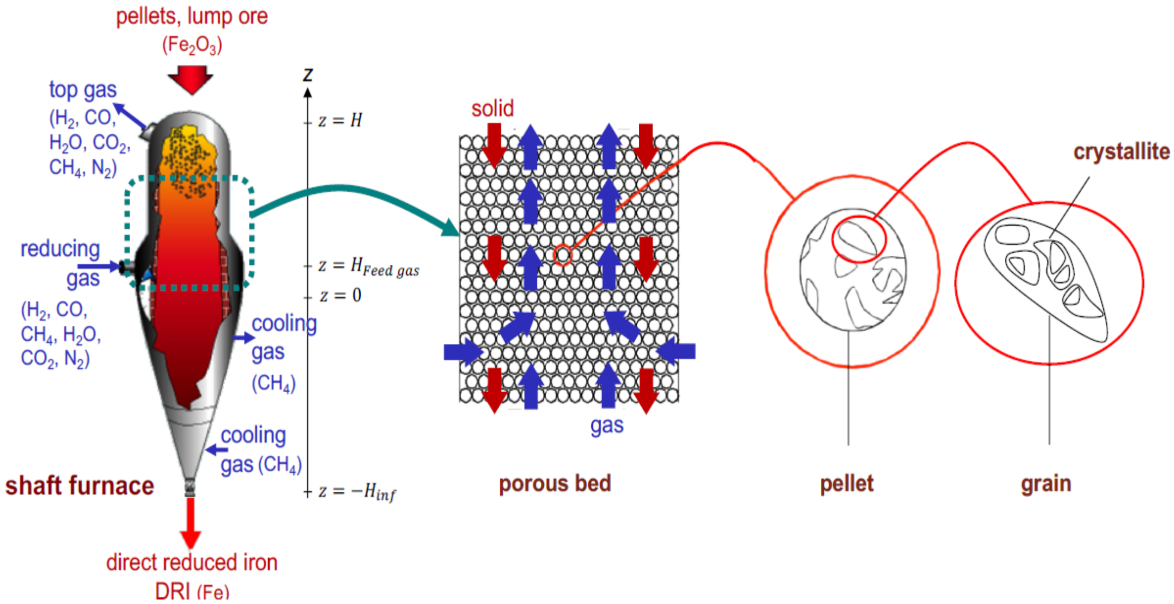

Figure 55. Diagram showing the principle of the standard REDUCTOR model [16]

A mathematical model of the BIORED process was written on the basis of a precious model devised in our laboratory. During the last 20 years, our group has developed the REDUCTOR model, which simulates the operation of a typical gas-based iron ore direct reduction furnace.[3] [187] In this model, the iron ore pellets and reducing gas flow counter-currently. The solid descends by gravity and the hot reducing gas is introduced in the lateral side. The 2-D geometry is considered cylindrical for the reduction and transition zones and conical for the cooling zone. It is a multi-scale model: from reactor to pellets to grains to crystallites (see Figure 55). [3] To model the BIORED process, we decided to focus on the cylindrical reduction zone only. The standard REDUCTOR model was modified to simulate the BIORED shaft furnace, the major adaptation was to take into account two solids (iron ore pellets and charcoal lumps) and the biomass-related reactions (gasification and devolatilisation) as well.

V.2.1. Single pellet model

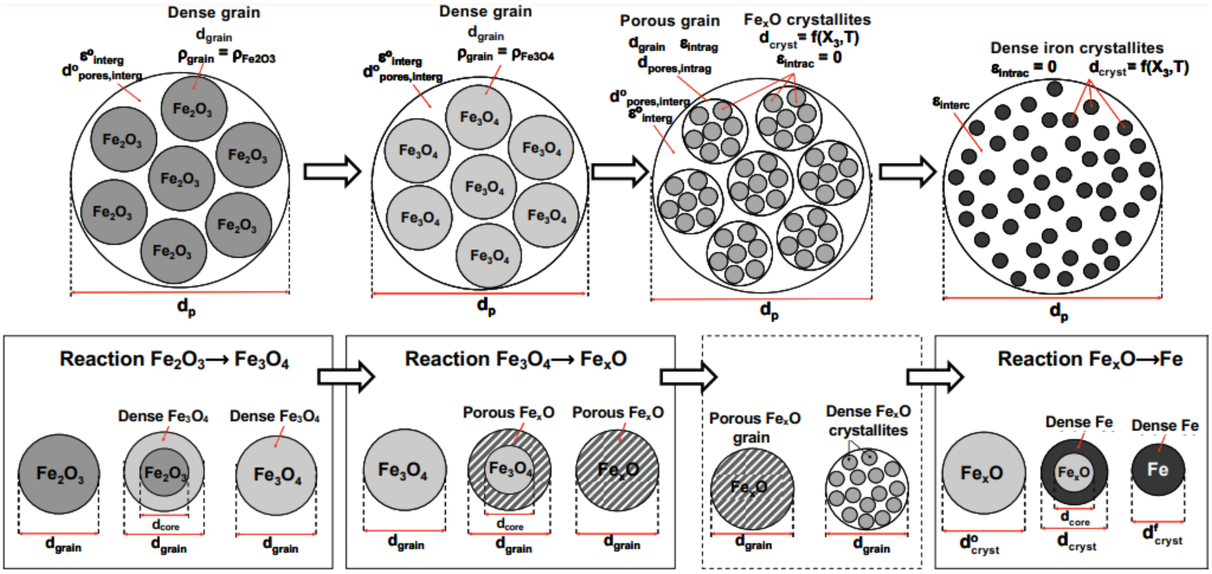

Figure 56. Schematic diagram of the kinetic model of the reduction of hematite pellets by a reducing gas (H_2 and CO). Top row: evolution on the pellet scale. Bottom row: evolution on the grain scale (R1, R2, R4 and R5) and on the crystallite scale (R3 and R6) [16]

Figure 56 shows a schematic representation of the iron ore pellet developed by Ranzani da Costa from a set of experimental observations.[15] The initial pellet is assumed to be composed of dense, spherical grains of hematite. The hematite is reduced to magnetite according to the USCM model on the scale of the grains, and then the magnetite grains are transformed into porous wustite. In the wustite state, the initial grains break up into small wustite crystallites (these were termed crystallites to distinguish them from the initial grains). These wustite crystallites are then reduced into iron according to the USCM model again and the formed layer of iron covers the crystallites. The pores in the grains and crystallites have different sizes and vary with the temperature and the conversion of the reactions. These were measured and an average pore diameter, which could vary with temperature and reaction rate, was derived.[15] Based on this geometrical model, and on the law of addictive reaction times,[197] a kinetic model was built, which enables us to calculate the reaction (R1-R6) rates as a function of the local gas composition and temperature.[3] This model was left unchanged in our work.

V.2.2. Charcoal grain model

The charcoal grains undergo devolatilisation and gasification during their way down in the shaft furnace (See Figure 57).

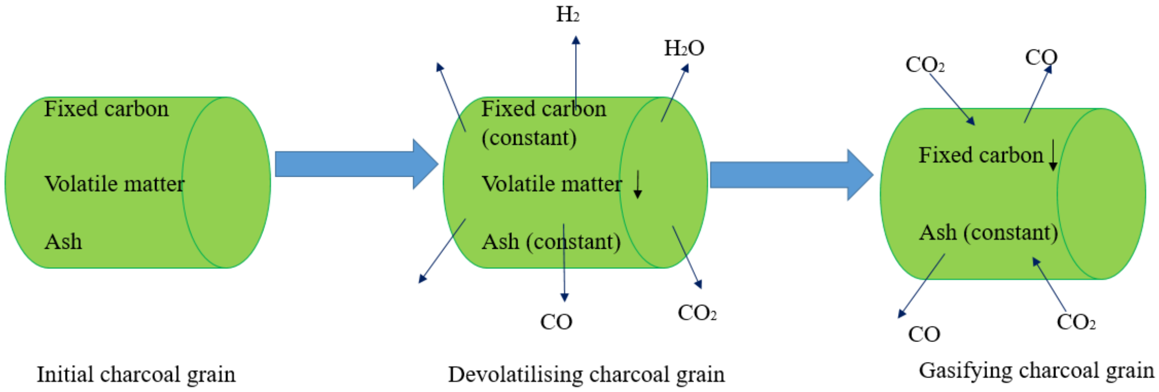

Figure 57. Evolution of a charcoal grain

A cylindrical shape was chosen as more representative of the charcoal grains than spheres. The diameter is assumed to remain constant during devolatilisation, the density being decreasing. During gasification, the volume of grain gets smaller with the conversion degree:

$$V_X = V_{ini} \cdot (1 - X)^m \qquad \text{(V-1)}$$

The value of m was determined as 0.11 from measurements of the volume of partially gasified samples. The devolatilisation and the gasification rates are calculated as a function of the local gas temperature and composition as explained in Chapter III and IV.

V.2.3. Assumptions and boundary conditions

The assumptions below, made in REDUCTOR, were also used for the modelling of the biomass-based shaft furnace. [15]

- The shaft furnace is operated at steady state.
- The model is 2-dimensional with cylindrical coordinates.
- The solid flow is considered in plug flow in the cylindrical zone; the gas flow is calculated through the porous solid bed.
- Gas phase is considered as a compressible Newtonian fluid with density calculated by the ideal gas equation.
- The initial iron ore pellets (diameter 1.5 cm) are made of dense Fe_2O_3 (density 5275 kg/ m^3) grains, the size of which is 19 μm. The pellet porosity is 0.33 and the average pore size is 6 μm.
- The diameter of the pellets is assumed to be constant and the temperature inside is uniform.
- All the heat of reactions is absorbed or released in the solids.

- The porosity of the bed remains constant and equal to 0.5.
- The reactions 1-6 are considered reversible and of first order with respect to each gaseous reactant.
- Wustite is taken as $Fe_{0.95}O$. Thus, the reactions R1-6 are then written with $Fe_{0.95}$ (See Table 14 hereafter).

In a first approach to model the BIORED shaft furnace, we made further simplifying assumptions.

- The furnace is limited to its cylindrical section.
- The physical and chemical direct interactions between charcoal grains and pellets are negligible.
- The initial charcoal grains are cylinders of diameter 10 mm and length 15 mm. Their composition is: fixed carbon 74.5%, volatile matter 25%, ash 0.5%. The initial density of the charcoal grains is 750 kg/m^3.
- The volume fractions of both pellets and charcoal in the bed are constant and also is each of their velocities. This is a consequence of taking the bed porosity constant throughout.
- The carbon deposition due to the reverse Boudouard reaction only happens on the surface of iron ore pellets.

V.2.4. Chemical reactions

Table 14 lists the main reactions that describes the reduction of iron ore pellets and the devolatilisation and gasification of the charcoal lumps. The reduction reactions by CO (R1 to R3’) prevail because the whole reactor is almost full of the mixture of CO and CO_2 except, as the results will reveal, at the very top side where the devolatilisation takes place and produces different kinds of reducing gas (R8). The gasification or the Boudouard reaction (R7 and R7’) has different roles for charcoal and pellets. As we will see, the carbon deposition on the surface of pellets is prevailing at low temperature at the top of the reactor, whereas the direct Boudouard reaction of charcoal is the source of CO at high temperature at the bottom. The reduction reactions by H_2 (R4 to R6') are also considered yet marginal.

R1	$3Fe_2O_{3(s)} + CO_{(g)} \rightarrow 2Fe_3O_{4(s)} + CO_{2(g)}$
R2’	$Fe_3O_{4(s)} + \frac{16}{19}CO_{(g)} \rightarrow \frac{60}{19}Fe_{0.95}O_{(s)} + \frac{16}{19}CO_{2(g)}$
R3’	$Fe_{0.95}O_{(s)} + CO_{(g)} \rightarrow 0.95Fe_{(s)} + CO_{2(g)}$
R4	$3Fe_2O_{3(s)} + H_{2(g)} \rightarrow 2Fe_3O_{4(s)} + H_2O_{(g)}$
R5’	$Fe_3O_{4(s)} + \frac{16}{19}H_{2\,(g)} \rightarrow \frac{60}{19}Fe_{0.95}O_{(s)} + \frac{16}{19}H_2O_{(g)}$
R6’	$Fe_{0.95}O_{(s)} + H_{2(g)} \rightarrow 0.95Fe_{(s)} + H_2O_{(g)}$
R7	$CO_{2(g)} + C_{(s,pellets)} \leftrightarrow 2CO_{(g)}$
R7’	$CO_{2(g)} + C_{(s,charcoal)} \leftrightarrow 2CO_{(g)}$
R8	$C_{0.21}O_{0.51}H_{1.74} \rightarrow 0.56H_{2(g)} + 0.23H_2O_{(g)} + 0.06CO_{(g)} + 0.11CO_{2(g)} + 0.04CH_{4(g)}$

Table 14. Main reactions considered in the model

V.2.5. Chemical reaction rates

The reduction reactions rates are calculated using the law of additive reaction times. The following steps are considered: external mass transfer, diffusion in the pellet pores between the grains, diffusion in the pores of the porous oxide around the grains, solid-state diffusion of O through the dense iron layer around the wustite crystallites, chemical reactions of reduction (R1 to R6’) at the gas-solid interface. This was explained in detail in Ranzani’s and Hamadeh’s work.[15] [16] We just here reproduce the final expression obtained. [16]

	Hematite → Magnetite	Magnetite → Wüstite	Wüstite → Iron
External transfer	$\tau_{ext,i} = \frac{\tilde{\rho}_{Fe_2O_3,ini} d_p}{18 k_g c_t (x_{k,\infty} - x_{k,eq(i)})}$	$\tau_{ext,i} = \frac{8\tilde{\rho}_{Fe_3O_4,ini} d_p}{57 k_g c_t (x_{k,\infty} - x_{k,eq(i)})}$	$\tau_{ext,i} = \frac{\tilde{\rho}_{Fe_{0.95}O} d_p}{6 k_g c_t (x_{k,\infty} - x_{k,eq(i)})}$
Intergranular diffusion	$\tau_{diff,interg(i)} = \frac{\tilde{\rho}_{Fe_2O_3,ini} (d_p)^2}{72 (D_{k,eff})_{interg,i} c_t (x_{k,\infty} - x_{k,eq(i)})}$	$\tau_{diff,interg(i)} = \frac{2\tilde{\rho}_{Fe_3O_4,ini} (d_p)^2}{57 (D_{k,eff})_{interg,i} c_t (x_{k,\infty} - x_{k,eq(i)})}$	/
Intragranular diffusion	/	$\tau_{diff,intrag(i)} = \frac{2\tilde{\rho}_{Fe_3O_4,ini} (d_{grain,ini})^2}{57 (D_{k,eff})_{intrag,i} c_t (x_{k,\infty} - x_{k,eq(i)})}$	/
Inter-crystallite diffusion	/	/	$\tau_{diff,interc(i)} = \frac{\tilde{\rho}_{e_{0.95}O} (d_p)^2}{24 (D_{k,eff})_{interc,i} c_t (x_{k,\infty} - x_{k,eq(i)})}$
Intra-crystallite diffusion (solid phase)	/	/	$\tau_{diff,intrac,(i)} = \frac{\tilde{\rho}_{Fe_{0.95}O} d^2_{cryst,ini}}{24 D_{sol} (c_{ox,eq} - c_{ox,\infty})}$
Chemical reaction	$\tau_{chem,i} = \frac{\tilde{\rho}_{Fe_2O_3} d_{grain,ini}}{6 k_i c_t (x_{k,\infty} - x_{k,eq(i)})}$	$\tau_{chem,i} = \frac{\tilde{\rho}_{Fe_3O_4} d_{grain,ini}}{2 k_i c_t (x_{k,\infty} - x_{k,eq(i)})}$	$\tau_{chem,i} = \frac{\tilde{\rho}_{Fe_{0.95}O} d_{cryst,ini}}{2 k_i c_t (x_{k,\infty} - x_{k,eq(i)})}$

Reaction i	**Reaction Rate mol $\mathbf{m^{-3}\,s^{-1}}$**
$i = 1$ and 4	$v_i = \frac{1}{3}\widetilde{\rho}_{Fe_2O_3,ini}\left\{\tau_{ext,i} + 2\tau_{diff,interg(i)}\left[(1-X_i)^{-\frac{1}{3}} - 1\right] + \frac{\tau_{chem,i}}{3}(1-X_i)^{-\frac{2}{3}}\right\}^{-1}$
$i = 2$ and 5	$v_i =$ $\frac{1}{3}\widetilde{\rho}_{Fe_2O_3,ini}\left\{\tau_{ext,i} + 2\left(\tau_{diff,interg(i)} + \tau_{diff,intrag(i)}\right)\left[(1-X_i)^{-\frac{1}{3}} - 1\right] + \frac{\tau_{chem,i}}{3}(1-X_i)^{-\frac{2}{3}}\right\}^{-1}$
$i = 3$ and 6	$v_i =$ $\frac{1}{3}\widetilde{\rho}_{Fe_2O_3,ini}\left\{\tau_{ext,i} + 2\left(\tau_{diff,interc(i)} + \tau_{diff,intrac,(i)}\right)\left[(1-X_i)^{-\frac{1}{3}} - 1\right] + \frac{\tau_{chem,i}}{3}(1-X_i)^{-\frac{2}{3}}\right\}^{-1}$

Table 15. Kinetic sub-model of a single pellet. Expressions of the characteristic times (first) and the reaction rates (second). i: reaction number, k: H_2 or CO. [16]

These equations were used as such in the BIORED version of the code. The mass transport coefficients k_g and the effective diffusion coefficients $D_{k,eff}$, as well as the grain and pore characteristics vary with the composition and temperature.[16]

The charcoal devolatilisation rate is calculated as introduced in Chapter III. The expression of the reaction rate in $mol_{VM}s^{-1}m^3_{bed}$ is

$$r_8 = \tilde{\rho}_{VM,ini}[0.867 \cdot \frac{108.7}{60}\exp\left(-\frac{46024}{RT}\right) + 0.133 \cdot \frac{36.9}{60}\exp\left(-\frac{18711}{RT}\right)]$$

where $\tilde{\rho}_{VM,ini}$ is the initial molar concentration of charcoal volatile matter per unit volume of bed.

For charcoal gasification, the combination of the Langmuir-Hinshelwood kinetics and the modified random pore model leads to the following relationship:

$$r_{7'} = \tilde{\rho}_{Cfixed,ini} \cdot [left\ hand\ side\ of\ Equation\ (IV-15)]$$

where $\tilde{\rho}_{Cfixed,ini}$ is the initial molar concentration of charcoal fixed carbon per unit volume of bed.

V.2.6. Balance equations

The model involves the numerical solution of the local conservation equations of mass, energy and momentum using the finite volume method. The main equations are listed below. The notation is explained further below.

The solid pellets descend by gravity and the gas moves upwards counter currently. Since the velocity of the gas is much higher than that of the solid, the solid charge can be considered as a porous medium consisting of quasi-stationary spheres. With such assumptions, the Ergun equation (V-3) can be used.

When combining the momentum equation with the equation of continuity:

$$\boldsymbol{\nabla} \cdot \left(\frac{C_t}{K}\boldsymbol{\nabla}\mathrm{P}\right) = r_7 + r_{7'} + r_8 \qquad \text{(V-2)}$$

$$\boldsymbol{u_g} = -\frac{1}{K}\boldsymbol{\nabla P} \quad \text{with } K = \frac{150(1-\varepsilon_s)^2}{\varepsilon_s{}^3 d_p^2}\mu_g + \frac{1.75(1-\varepsilon_s)}{\varepsilon_s{}^3 d_p}\rho_g u_g \qquad \text{(V-3)}$$

The gas species move by convection and diffusion, which gives for the molar balances for gaseous species i:

$$\boldsymbol{\nabla}\cdot\left(C_t \boldsymbol{u_g} x_i\right) = \boldsymbol{\nabla}\cdot\left(C_t \mathrm{D}_g \boldsymbol{\nabla} x_i\right) + S_{g,i} \qquad \text{(V-4)}$$

Table 16 lists the $S_{g,i}$ source terms. Although included in REDUCTOR, CH_4 was not considered here because it is only present at the very top of the furnace and in very low concentrations.

i	$S_{g,i}\ (mol\ s^{-1}\ m_{bed}^{3})$
H_2	$-r_1 - \frac{16}{19}r_2 - r_3 + 0.56r_8$
CO	$-r_4 - \frac{16}{19}r_5 - r_6 + 2r_7 + 2r_{7'} + 0.56r_8$
H_2O	$r_1 + \frac{16}{19}r_2 + r_3 + 0.23r_8$
CO_2	$r_4 + \frac{16}{19}r_5 + r_6 - r_7 - r_{7'} + 0.23r_8$

Table 16. Source terms of the gas species

As the volume of the reactor is filled with a heterogeneous gas/solid mixture, the gaseous phases and the solid phases may not have the same temperature. It is therefore necessary to consider two different temperatures, and heat transfer by convection and conduction takes place between them. Here is the energy balance of the gas phase:

$$\rho_g c_{pg}\left(u_{gr}\frac{\partial T_g}{\partial r} + u_{gz}\frac{\partial T_g}{\partial z}\right) = \frac{1}{r}\frac{\partial}{\partial r}\left(r\lambda_g\frac{\partial T_g}{\partial r}\right) + \frac{\partial}{\partial z}\left(\lambda_g\frac{\partial T_g}{\partial z}\right) + a_b h\left(T_s - T_g\right) + \sum_i S_{g,i}\int_{T_g}^{T_s} c_{p_i} dT \qquad \text{(V-5)}$$

The solid species are only moving down by convection. The mass balances for pellet species are:

$$\boldsymbol{\nabla}\cdot\left(\varepsilon_{s,p}\rho_{s,p}\boldsymbol{u_{s,p}}\omega_{j,p}\right) = S_{s,i} \qquad \text{(V-6)}$$

And the mass balances for charcoal species are:

$$\boldsymbol{\nabla}\cdot\left(\varepsilon_{s,ch}\rho_{s,ch}\boldsymbol{u_{s,ch}}\omega_{j,ch}\right) = S_{s,i} \qquad \text{(V-7)}$$

Where $S_{s,i}$ are listed in Table 17 next page.

The energy balance of the solid phase is written:

$$-\rho_b u_{s,z} c_{ps} \frac{\partial T_s}{\partial z} + \rho_b u_{s,r} c_{ps} \frac{\partial T_s}{\partial r} = \frac{1}{r}\frac{\partial}{\partial r}\left(r\lambda_{eff,r}\frac{\partial T_s}{\partial r}\right) + \frac{\partial}{\partial z}\left(\lambda_{eff,z}\frac{\partial T_s}{\partial z}\right) + a_b h\left(T_g - T_s\right) + \sum_{n=1}^{8}(-v_n \, \Delta_r H_n) \quad \text{(V-7)}$$

Solid phase	Solid species	$S_{s,i}\ (kg\ s^{-1}\ m_{bed}^{3})$
Pellets	Fe_2O_3	$-3M_{Fe2O3}(r_1 + r_4)$
	Fe_3O_4	$M_{Fe2O3}(2r_1 - r_2 + 2r_4 - r_5)$
	$Fe_{0.95}O$	$M_{Fe0.95O}(\frac{60}{19}r_2 - r_3 + \frac{60}{19}r_5 - r_6)$
	Fe	$0.95M_{Fe}(r_3 + r_6)$
	C	$-M_C r_7$
Charcoal	Fixed carbon	$-M_C r_{7'}$
	VM	$-M_{VM} r_8$

Table 17. Source terms of the solid species

In order to involve the different types of energy transfer in the porous medium, the notion of effective conduction is used. The effective conductivity is calculated as the sum of two terms. The first term is a static contribution due to the effects of radiation, gas conduction and interparticle conduction. The second term is a dynamic contribution from gas convection on the effective conduction. [189]

The main notations above are as follows. *i*: a species, *M*: molecular weight (kg mol^{-1}), *r*: reaction rate (mol $s^{-1}m^{-3}$), n_i: stoichiometric coefficient, C_t: gas total concentration (mol m^{-3}), ε: volume fraction (-), *r*: radius (m), *z*: height (m), ρ: density (kg m^{-3}), C_p: specific heat (J $kg^{-1}K^{-1}$), D_g: diffusion coefficient (m^2 s^{-1}), λ: heat conductivity (W $K^{-1}m^{-1}$), ω: mass fraction in a solid phase (-), *u*: phase velocity (m s^{-1}), *T*: temperature (K), *P*: pressure (Pa), *x*: volume fraction in gas phase (-), *d*: diameter (m), *S*: source term (equation-dependent) (mol $s^{-1}m^{-3}$), and *h*: heat transfer coefficient (W $m^{-2}K^{-1}$). The subscripts represent the solid phase (*s*), gas phase (*g*), chemical species (*i*) (gas: CO, CO_2, H_2, H_2O, CH_4, N_2; solid: volatile matter and fixed carbon in charcoal, and Fe_2O_3, Fe_3O_4, $Fe_{0.95}O$, Fe, ash in iron ore pellets), charcoal (*ch*) and pellets (*p*), reaction number (n).

V.3. Results

The part above described in details the governing equations and the kinetic expression of the various reactions. The objective of the model is to simulate the BIORED shaft furnace for an industrial and commercial perspective. For this reason, we chose input data representative for a commercialized Midrex process. For instance, the solid inlet corresponds to about 1Mt/yr of iron ore pellets treated and to 0.72Mt of DRI produced/yr. The main characteristics of the reactor are listed in Figure 58.

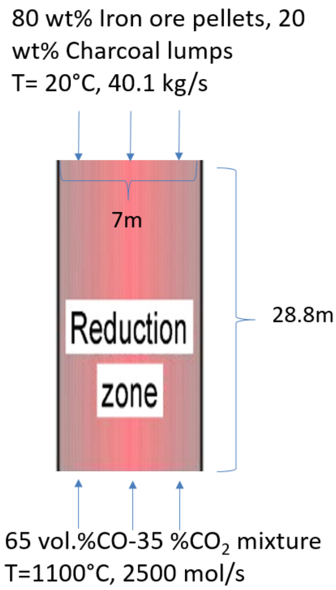

Figure 58. Main parameters of the simulated reactor for the reference case

The simulations considered a mix of iron ore pellets (96.5 wt% Fe_2O_3 and 3.5 wt% gangue) and charcoal grains fed at the top at room temperature and CO-CO_2 gas mixture introduced at 1100°C at the bottom. Although the model is two-dimensional, the situation modelled, with a uniform inlet gas flow introduced at the bottom, leads to a one-dimensional behavior, with uniform values as a function of the radius. The results in the following part aim to show the evolution of temperatures and gas composition along with the reactions of devolatilisation and gasification of charcoal lumps and the reduction of iron ore pellets. For a full understanding of the reactor behaviour, all the results should be considered simultaneously, even if for writing these will be presented successively.

V.3.1. Evolution of temperatures and gas compositions

Figure 59 shows the temperature of the solid and gaseous phases in the reactor. At first sight, the gas and solid temperatures are almost equal as a result of the high heat transfer coefficients. The difference lies only in the upper side because the solid is fed at room temperature and is heated very rapidly at the inlet. The temperatures remains at 700-800°C for most of the reactor. This range of temperature is high enough for the reduction of hematite to wustite. On the other hand, it is "low enough" for the reduction of wustite to iron because the last step of reduction is thermodynamically penalized at high temperature (See Figure 14b, Chapter II). At the bottom of the reactor, the gasification takes place (as will be shown later) thanks to the high temperature from the hot gas. However, as the gasification is very endothermic ($\Delta_r H$=172 kJ/mol at 293K), the temperature of the gas decreased rapidly to 800 degrees within about 3 m even though the reducing gas was fed at 1100°C. The occurrence of a temperature plateau at an intermediate temperature is analogous to what happens in the higher part of a blast furnace: the "thermal reserve zone" which results from a balance between coke gasification and iron ore reduction.

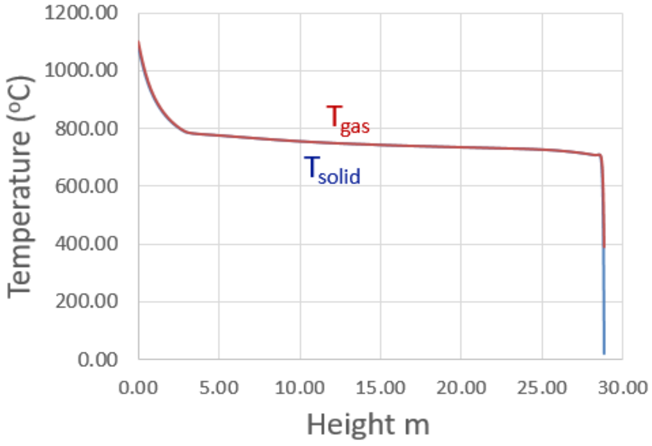

Figure 59. Profile of temperatures along the shaft furnace

In regards to the composition of gases (Figure 60), H_2 and H_2O were not introduced in the reducing gas, but they are produced by the devolatilisation reaction just after the solid inlet, where the cold charcoal is heated by the hot gas. The volatile matter represented 25wt% of charcoal and the release of pyrolysis gas is mainly 56% in volume of H_2 and 23% in volume of H_2O. The reaction of devolatilisation is very fast, so the release of H_2 and H_2O is very rapid. The maximum concentration of H_2 is about 2.6% of the gas. On the other hand, H_2 is oxidized into H_2O in the reduction of hematite to magnetite, so the concentration of H_2 and H_2O are both influenced by the devolatilisation and the reduction reactions.

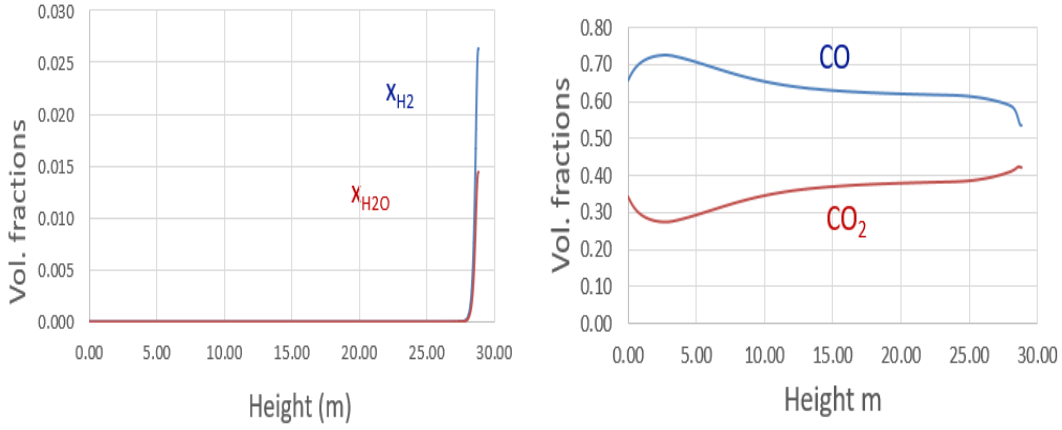

Figure 60. Profile of the gas compositions along the shaft furnace

Concerning the concentration of CO and CO_2, it is worth to note first that the production of CO and CO_2 by devolatilisation is negligible in comparison with the amount produced by the gasification. The CO-CO_2 gaseous mixture composition (accounting for more than 95% of gas in the whole reactor) is mainly influenced by the reduction of the iron ore pellets and the reversible Boudouard reaction. The reducing gas mixture enters at the bottom and the CO first accumulated owing to the gasification reaction rate, there faster than the reduction reaction rate. However, the accumulation rapidly stops because the gasification rate (as we will see) decreases along with temperature so that the reduction of wustite consumes more CO than its production by gasification. Thus after a peak, the CO concentration continues to decrease due to the stepwise reduction. In the upper part, a sharp drop in CO concentration is observed due to the first reduction (hematite to magnetite, shown later). At the top, the exhaust gas still contains a large quantity of CO and CO_2, which indicates a possible recycling of this gas.

V.3.2. Evolution of charcoal lumps

The charcoal lumps used in our simulations were composed of 25% of volatile matter and 75% fixed carbon. In the simulated furnace, the temperature of solid rises up to 700 degrees within about one meter and the release of volatile matter takes place very rapidly once being heated. It can be seen in Figure 61 that the conversion of charcoal reached 25% after full devolatilisation.

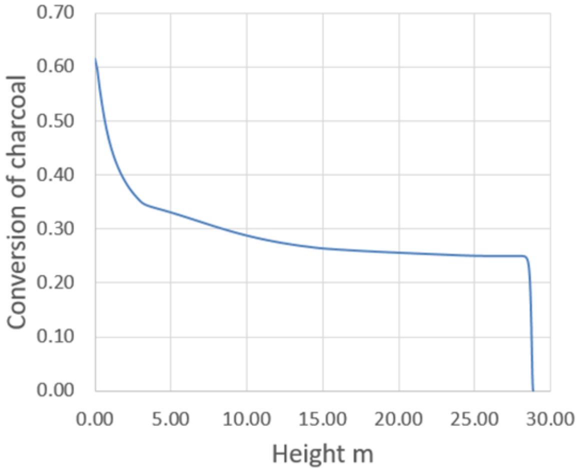

Figure 61. Conversion of charcoals in the shaft furnace

It is also reported by Liu et al. that coal devolatilisation and iron oxides reduction occur simultaneously during the heating of the coal-iron ore mixture. [198] The charcoal was pre-pyrolyzed, so the formation of bio-oil is not supposed to occur. The produced gases are CO_2, CO, H_2, H_2O and CH_4. [101] Methane is in too low concentration to influence the reactor. Nevertheless, the role of H_2 is important for the reduction of iron ore pellets because the production of H_2 is not negligible and because the reduction by H_2 is several times faster than that by CO.

The small amount of CO and CO_2 released via the devolatilisation just join the CO-CO_2 atmosphere. It is worth to note that the gas and the solid being counter-flow, the devolatilisation only has effects on the first one meter of the reactor, and then the gas flows out of the reactor as the exhaust gas.

The gasification of the fixed carbon of the charcoal lumps is the source of the reducing agent CO. According to the results, from top to bottom, the Boudouard reaction effectively starts at about 700 degrees in the middle of the reactor and is slowly accelerated due to the increase in temperature. At the bottom, the gasification rate strongly enhances owing to higher solid temperature. Compared with devolatilisation, it is much slower and lasts for more than ten meters. The conversion is not completed at the bottom. Gasification accounts for 98% of the CO production whereas devolatilisation represents only 2%.

Charcoals properties may strongly change from a product to another because of the nature of the biomass and the pyrolysis conditions. Consequently, they may show different reactivities for gasification. To get a better insight into the effect of the gasification on the reactor behaviour, we have compared our oak charcoal with other biomass charcoals studied in the literature. This point will be discussed in the sensitivity analysis.

V.3.3. Evolution of iron ore pellets

The pellets are very rapidly heated by the hot gas in the first meter of the shaft, which makes the reduction start immediately. The reduction of iron ore pellets occurs in three steps: $Fe_2O_3 \longrightarrow Fe_3O_4 \longrightarrow FeO \longrightarrow Fe$ over the whole height of the shaft (See Figure 62). It is also reported by Liu et al. that the mixture of coal and iron ore undergoes a stepwise reduction. [198]

The hematite is fully converted to magnetite very fast in the first meter because this first step of reduction with CO is thermodynamically favorable even though the temperature is relatively low (about 500°C). In addition, the H_2 produced by the devolatilisation of charcoal lumps accelerates the reduction and is totally consumed by the reduction of hematite. Then the magnetite is reduced to wustite by CO in the next four meters. It is clearly seen that the second step is more difficult than the first one. The last step, wustite to metallic iron, is the slowest. The whole rest of the reactor is needed to reach a satisfactory degree of metallization. This points out that the residence time plays an important role and should be chosen (through the solid flow rate or the dimension of the reactor) to exceed the time necessary for the reduction reactions. Unfortunately, in the last meter close to the exit, the iron is slightly re-oxidised. Indeed the operating conditions shifted from the side of reduction to the side of oxidation at the bottom of the furnace, as can be seen in the diagram of Chaudron (see Figure 60b from 5m to

0m). As a consequence, it is important to control the ratio of CO/(CO+CO_2) so that the re-oxidation is avoided at the end of the reactor.

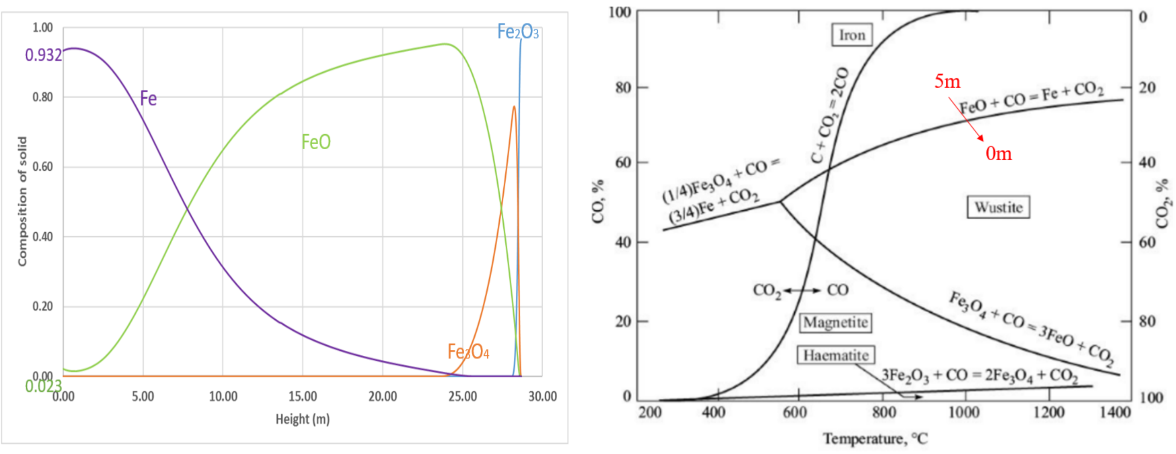

Figure 62. Evolution of the composition of the pellets in the shaft furnace (a) and Chaudron diagram (b)

Not shown in the figure, a carbon deposit on the pellets occurs slightly in the middle of the reactor. Below, this carbon is gasified together with the charcoal lumps when the conditions shifts to the carbon solution loss side.

V.4. Sensitivity analysis

The results presented above correspond to the operation of the furnace in a “reference case” that was determined after many trials. Since such a reactor does not exist, we had first to guess a set of operating conditions, to analysis the results, to test the influence of different parameters, to modify the input data accordingly. The first results rapidly showed that gasification and reduction take place in distinct zones in the reactor with gasification at the bottom, next to the gas inlet. This is because gasification, more than reduction, requires a high temperature to occur at a significant rate and, when occurring, it decreases the temperature due to its endothermicity. Thus, the most influential operating parameters are the gas inlet temperature and composition. We present the effect of these parameters below, together with that of the gasification rate.

V.4.1. Effect of the inlet gas temperature

Figure 63 shows the effect of increasing the gas inlet temperature from 1100°C to 1150°C. First, even though the gas temperature was higher than that of the reference case, the cooling down of the gas by gasification took place similarly and the temperature decreased to about 800°C at the same height. However, as the gasification rate is favoured at high temperature, the CO production at the bottom was promoted and the global CO content is higher than that of the reference case. The complete reduction from hematite to metallic iron (100% metallization degree) is obtained much more efficiently, without re-oxidation and requiring only 15 m of the reactor in comparison to 28 m with little re-oxidation for the reference case. Consequently, a shorter and more compact reactor could be imagined.

It could therefore seem preferable to use an inlet gas temperature higher than 1100°C. In fact, this should not be feasible because of the occurrence of sticking. At high temperatures, the DRI pellets tend to stick to each other, forming clusters that hinder or block the solid flow down. The temperature not to be exceeded is not very clear in the literature. We situated it at 1100°C.

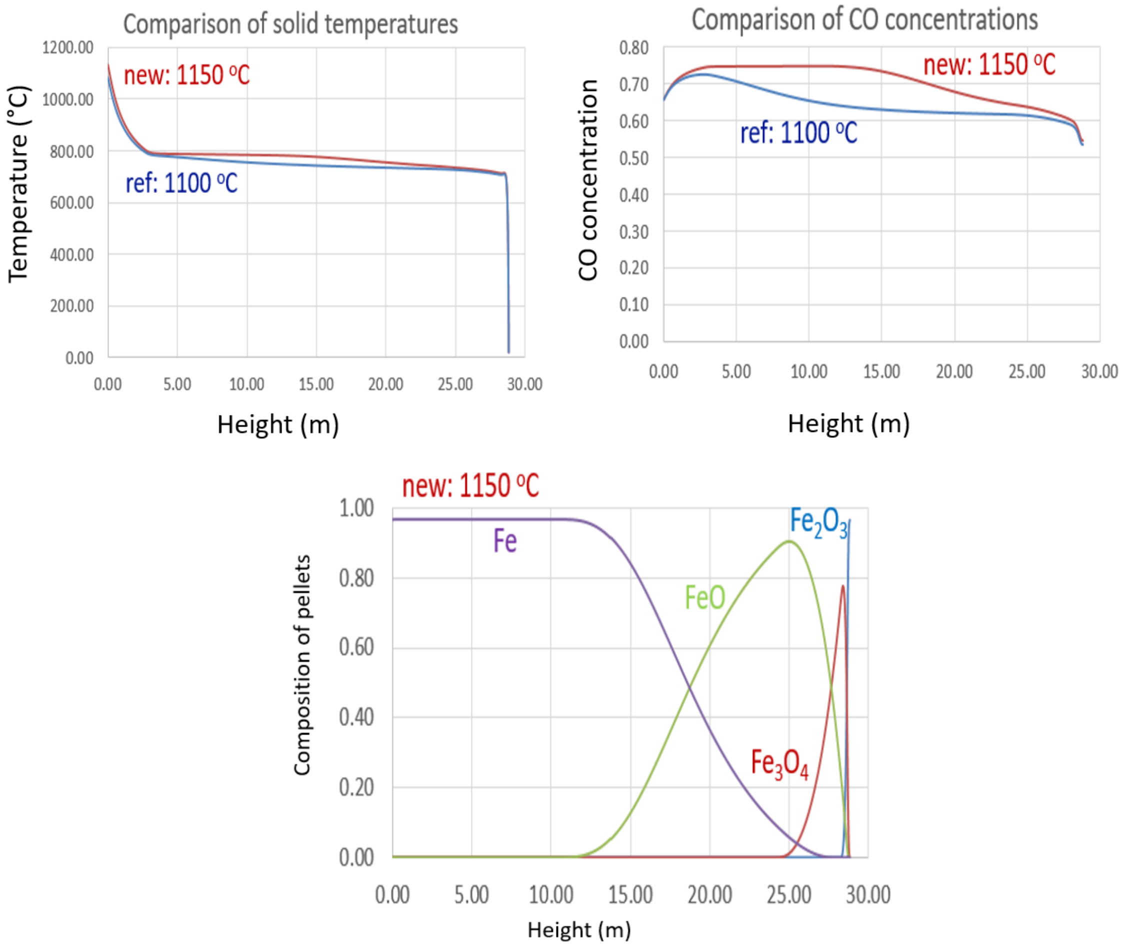

Figure 63. Sensitivity analysis on the effect of inlet gas temperature

V.4.2. Effect of the inlet gas composition

In order to analyse the influence of the concentration of CO at the inlet of the reactor, a simulation with a reduced concentration of CO (e.g. 63% CO-37% CO_2) was carried out. The results are shown in Figure 64.

According to the figure, the solid temperatures remained the same, which means that the gasification rate had not significantly changed. However, since the inlet CO content was lower, the driving force for the last step of reduction was lower than that of the reference case and the reaction was closer to the thermodynamic equilibrium. Consequently, the hematite was reduced to wustite in the same way as for the reference case, but the reduction of wustite to iron was slowed down and the re-oxidation was enhanced due to a lower CO concentration. As a result , the metallization degree did not exceed 85%. From the comparison, conclusion can be driven that a high CO content in the inlet gas is crucial to the metallisation degree.

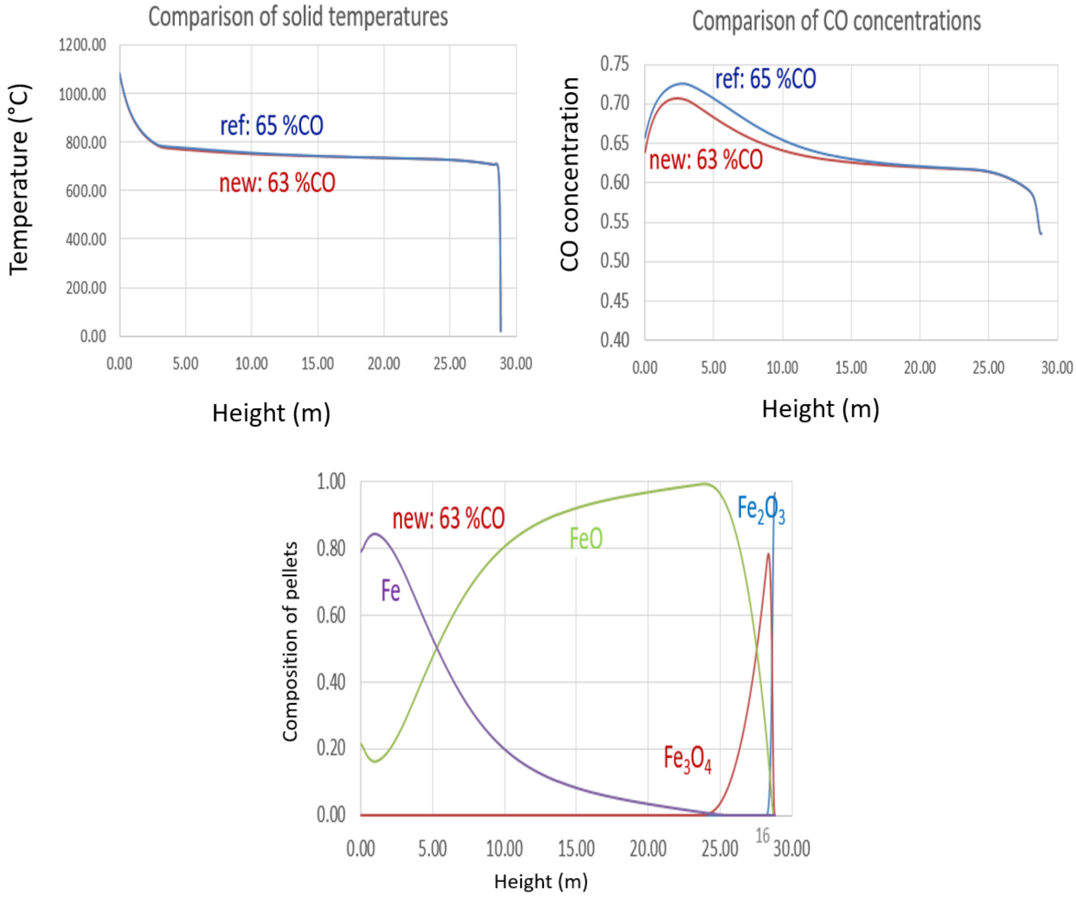

Figure 64. Sensitivity analysis on the effect of inlet gas composition

V.4.3. Effect of the charcoal reactivity

It is clear that not all the biomass exhibits the same reactivity, as mentioned in Chapter IV. To study the influence of the gasification rate, instead of using the gasification kinetics we measured for oak charcoal lumps, we decided to test the gasification kinetics proposed by Klose et al. for beech wood char that are about 10 times faster. [199] The results are shown in Figure 65.

First, the gasification rate was far faster than that of the reference case, which resulted in a more significant production of CO. The gas temperature was cooled down very quick to 800°C at 1 meter high and the gasification stopped. The evolutions of CO and iron ore reduction were similar to the ones presented before for a higher inlet gas temperature. More CO produced greatly increased the reduction rates. A full metallisation was reached 12 m below the solid inlet. According to Bagatini et al., the reactivity of reductants also has strong influence on the morphology of the iron produced in addition to the CO production. [200]

This result about the decisive influence of the charcoal gasification kinetics is very important. The oak charcoal we used was not intended for its use in BIORED nor were its pyrolysis conditions optimised for a gasification at 1100°C under CO-CO_2. This means that it should be possible to select and prepare a charcoal specially for BIORED, which could exhibit a reactivity similar to that given by Klose and load to a shaft furnace efficiency close to that shown in Figure 65.

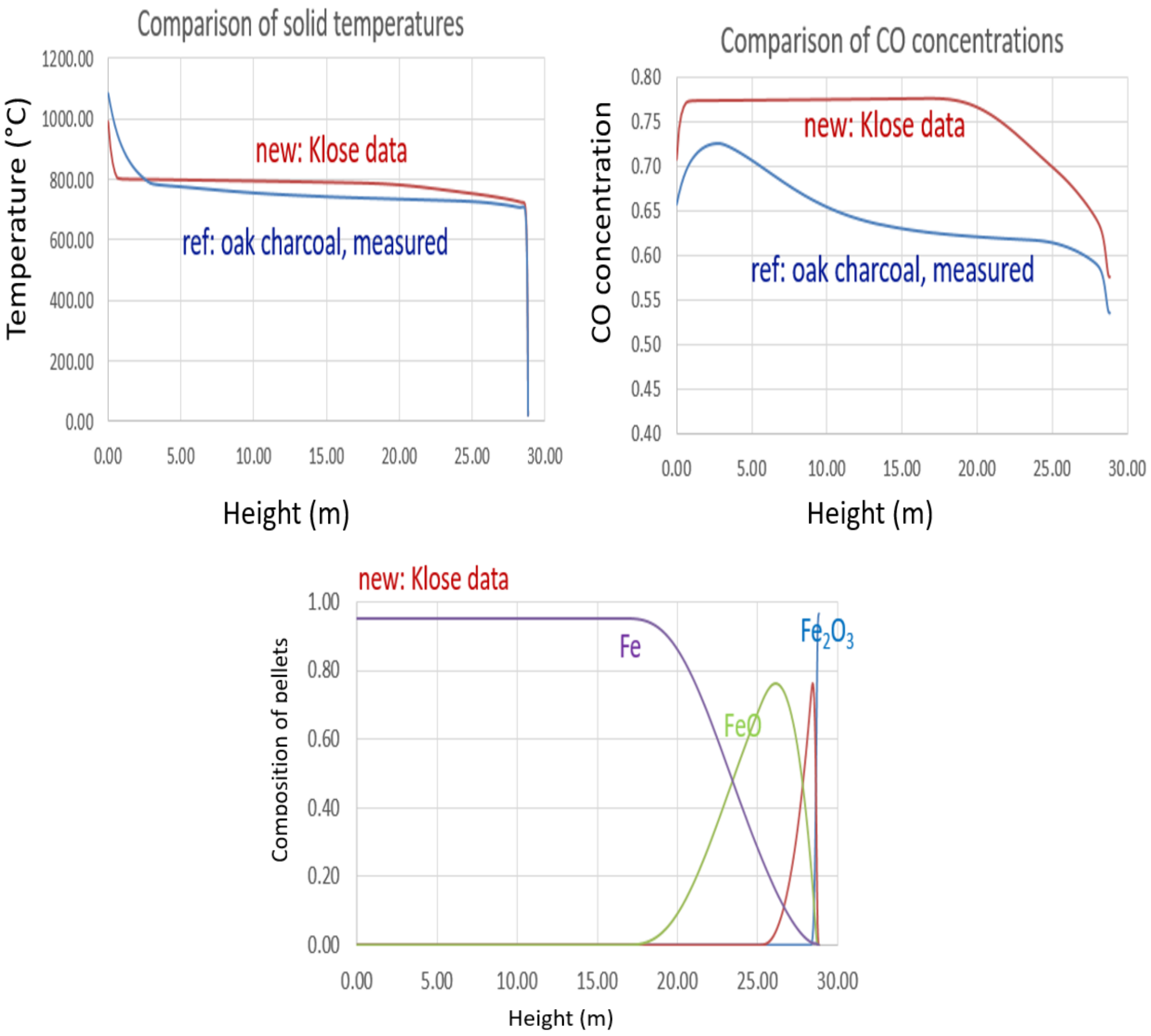

Figure 65. Sensitivity analysis with a more reactive charcoal

V.5. Experimental validation

Without any demonstrator or pilot-scale facility at our disposal to experimentally test the BIORED concept and validate the model results, we opted for an indirect validation using TGA. We equipped the thermobalance with programmable gas flow controllers for CO and CO_2. To validate our model, we decided to reproduce the path of a pellet inside the shaft furnace within the TGA. To do so, the composition and the temperature of the reactive gas, which was sent to the TGA chamber, were varied in conformity with the local conditions seen by the pellets during their simulated descent in the furnace. Doing so, the measured mass loss versus time should correspond to the mass loss of a pellet in the shaft furnace versus its age in the reactor.

V.5.1. Materials

The iron ore pellets for the experiment were from CVRD (Vale) in Brazil and the composition corresponding to the DR grade is presented in Table 18. They are composed of 95% hematite, 0.13% wustite and around 5% inert oxides. In the case of complete reduction, the mass loss is about 28.6%, which is the easiest indicator to determine the degree of metallization in the experimental part. The pellets have somewhat irregular shapes, but we assume a perfectly spherical shape for simplification.

Oxides	Fe_2O_3	CaO	MgO	SiO_2	Al_2O_3	FeO	S	P	Others
Mass %	94.93	2.02	0.8	1.4	0.61	0.13	0.004	0.024	0.08

Table 18. Compositions of CVRD-DR iron ore pellets

The thermobalance used was SETARAM TG 96 (See Chapter IV) and the programmable mass flow controllers could deliver up to 500 cm^3/min (STP) of CO and 360 cm^3/min of CO_2.

V.5.2. Experimental methods

A perfect similarity between calculated industrial shaft conditions and experimental conditions in the thermobalance was not possible. This first experimental limit is the gas flow rate. We retained the maximum experimental flow rate, calculated the corresponding gas velocity and input the gas flow rate for the simulation to get the same gas velocity. This varied between 2 and 9 cm/s. The solid flow rate for the simulation needed also to be reduced, it was adjusted together with the bed height to get a residence time corresponding to the time of the experiment. The main characteristics of the resulting simulated case are given in Table 19. In this simulation, no H_2 nor H_2O were considered.

Height (m)	0.45
Diameter (m)	3.5
Solid flow rate (kg/s)	0.23
Gas flow rate (mol/s)	14.68
Solid temperature (°C)	20
Gas temperature (°C)	1200

Table 19. Inlet data of the simulation for validation via TGA

The gas temperature and composition evolution are shown in Figure 66. On the left, the modelled temperature is also the set point from the experiment, the experimental temperature being that actually measured. On the right, the gas composition shown is both the simulation result and the composition of the inlet gas mixture for the experiment.

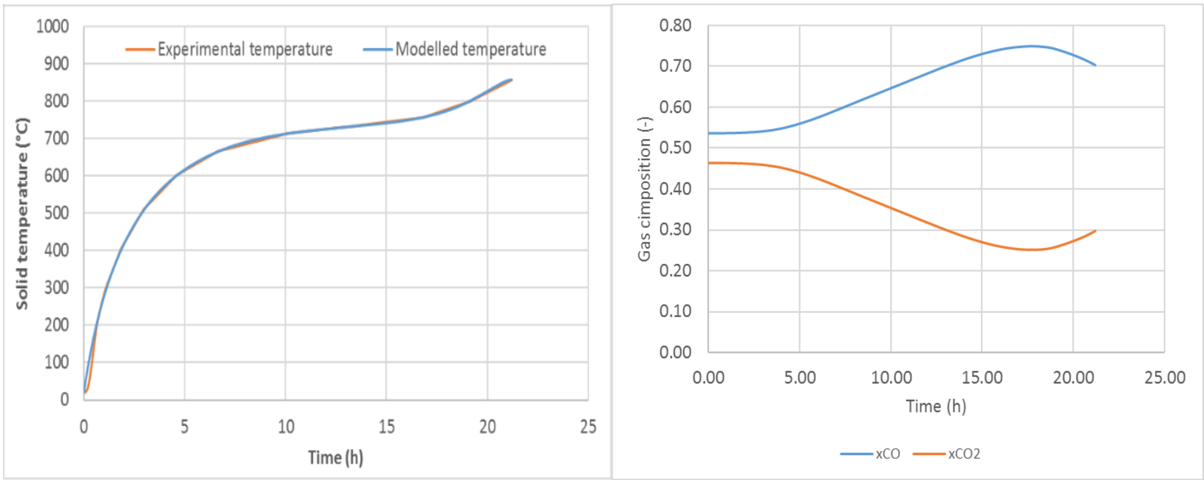

Figure 66. Main experimental conditions of TG

These conditions are thus somewhat different from those of the reference simulation and, as we will see, less favorable to a complete conversion.

The sample was one iron ore pellet, the weight of which was about 7 g. It was put in a wire Platinum crucible. The thermobalance was purged twice to assure the elimination of air and was directly fed by the reactive gas that contains the initial composition of the gas at the top of the simulated shaft. The thermobalance furnace was then heated according to the solid temperature evolution from the model and the feeding gas changed progressively its composition based on the simulated results during the heating (Figure 66). The computer continuously recorded the mass loss.

V.5.3. Experimental results

The mass loss of the pellets recorded by the TGA is shown in Figure 67 together with the calculated mass fraction of the different iron oxides and of metallic iron. The measured mass loss exhibits three major steps, which are associated with the reduction of the three successive iron oxides. The first plateau is representative of the reduction of hematite to magnetite, and the mass loss reached about 3%, which corresponds well to the weight change due to oxygen removal for the reduction of hematite to magnetite. The simulation and experiment both indicate the end of the first step at about 4 hours. The reduction of magnetite to wustite, which corresponds to the second plateau, took more time to attain its completion than the first reaction. The reduction of wustite to metallic iron lasted until the end in the experience and the total mass loss was about 26.08%. This mass loss is slightly less than that of 100% oxygen removal (28.6%), indicating an incomplete reduction of wustite to iron. However, in the simulation, the reduction of wustite to iron finished at 15 hours, which was earlier than the experience. Besides, the composition of iron was only about 90% at 15 hour due to the presence of deposited carbon and gangue, and it increased up to 96% thanks to the gasification of the deposited carbon between 15h and 19h.

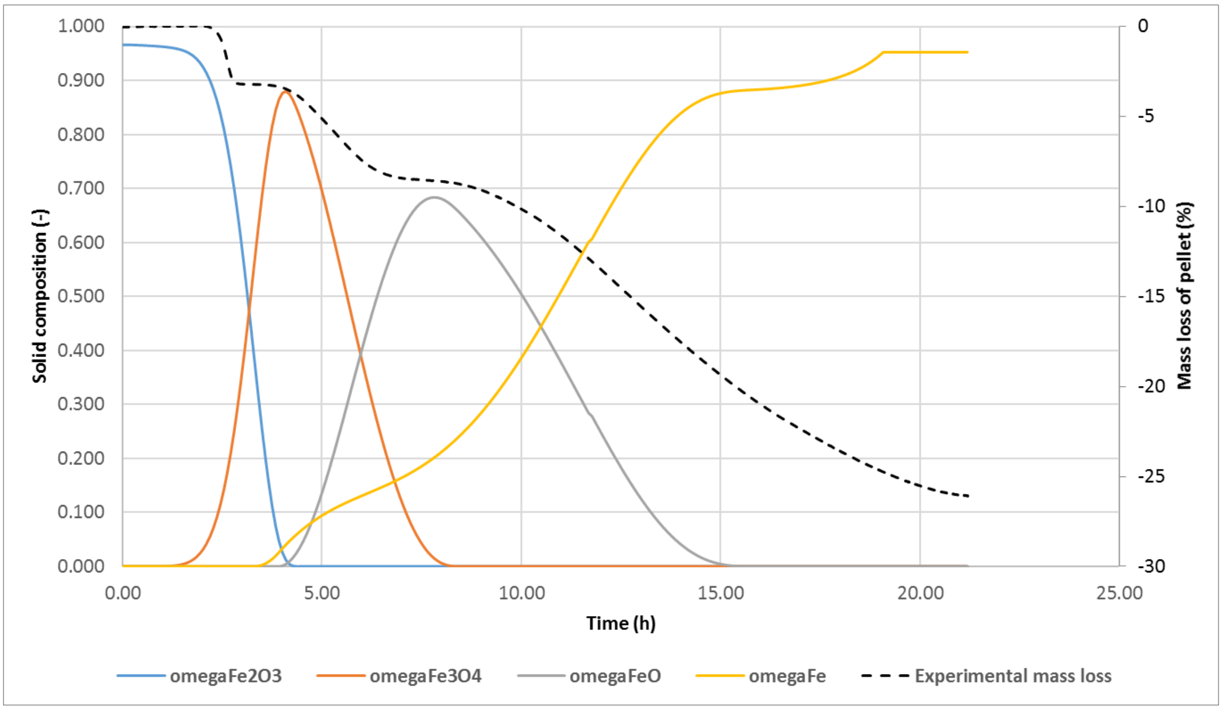

Figure 67. Comparison of experiment mass loss and simulated solid composition

The formation of a dense iron layer around the pellet could explain the difference in the reduction of wustite to iron between the experiment and the simulation. Indeed, the iron layer promoted the closure of pores and hindered the diffusion of reactant and product gases. The phenomenon is described in the single pellet model but at a higher temperature, because this description correspond to the reduction by H_2. The reduction by CO was less studied experimentally by our group and complementary measurements would be welcome.

As a conclusion, despite few differences between the experiment and the simulation, the comparison can be considered as satisfactory and as a first, indirect, validation of the model.

V.6. Conclusion

A mathematical model of the BIORED process was built on the basis of the REDUCTOR model previously developed in the laboratory. This model was adapted to include the charcoal as a second solid and the reactions of devolatilisation and gasification. Several calculations were run and showed the feasibility and the potential of the BIORED process.

Using a high temperature of the inlet gas at the bottom and a gas mixture rich in CO, it is possible to obtain a DRI of high metallisation, which was the main purpose of our study. The set of calculated results reveals how the reduction, devolatilisation and gasification take place in the shaft furnace. Ways to improve the process have been proposed, like looking for a more reactive charcoal.

A specific experiment was designed to reproduce in a thermobalance the thermal and chemical conditions undergone by a pellet in its descent along the shaft furnace. The comparison of the experimental result with the corresponding calculation is satisfactory.

VI. Environmental benefits and potential development of the BIORED process

In this chapter, we will first identify potential sites for the industrial implementation of the BIORED process worldwide, on the basis of local resources of biomass and iron ore. In the following, we focus on the environmental assessment of the BIORED-EAF route by the method of life cycle assessment (LCA). The environmental impacts of this new route will be evaluated and compared with those of the conventional route for a better understanding.

VI.1. Potential for development

At present, the gas-based direct reduction plants are often located in the steel plants, either as a complementary process in a classic integrated steel plant, or as the ironmaking process of the electric steelmaking route (See Figure 3, Chapter 2). We considered another option for BIORED: the implementation of the biomass-based DR plant close to a mining site and/or the pelletising plant, with the idea that the iron ore suppliers could wish to sell DRI instead of iron ore or iron ore pellets, DRI being a more valuable product.

VI.1.1. Potential industrial implementation of the BIORED process

The development potential of the process in existing mines area is possible if a nearby biomass resource is sufficient and well managed. For countries such as Brazil, India, Sweden or South Africa, both criteria are reached, so, we focused on these countries in our study. Many data in this section were obtained with the help of O. Bensouidi, M. Craspsky and T. Rinaldi, students at Mines Nancy, who we thank for their work.

VI.1.1.1 The market of iron ore products and the iron ore mines

The global iron ore production is about 3.3 billion tonnes. It is estimated that the iron ore stocks are around 165 billion tonnes, which could last 70 years. Tensions may rise since 80% of the iron ore in the market comes from only five countries (Australia, Brazil, China, India and Russia). Australia is the world's largest producer with a production of about 930 Mt of iron ore in 2019. [201] Brazil follows Australia with an annual production of 480 Mt in 2019. China takes the third place by 350 Mt in 2019, but it supplies an iron ore of poor quality, forcing itself to reduce its production. In addition, other countries such as Sweden, Algeria, Congo and South Africa are worth investigating as well because the iron ore mining is important in these countries. The following section will be dedicated to the principal mine sites in the world.

In Australia, most of the mines and reserves are located in the west of the country and Tasmania or near Adelaide accounts for the rest. As for Brazil, it has two principal regions for the iron ore production: Minas Gerais and Para. Brazil also has the largest open pit mine in the world: the Carajas mine. In Sweden, more than 27.5 Mt/an iron ore is extracted in the Kiruna mine. In India, the mines of Joda and Vyasanakere in the centre of the country produced less than 1 Mt/an. Finally, several countries are important iron ore producers in Africa: South Africa, Algeria, Congo and Cameroon. The Northern Cape region in South Africa is the most dynamic producer and it contains the Kolomela mine with 13 Mt/an. Algeria has a few iron mines like Gar Djebilet (20 Mt). Cameroon produces 40 Mt/an of iron ore in the east of the country at the Mbalam mine.

Besides the amount of iron ore production, its quality also plays an important role. Based on its iron content, the iron ores are referred as poor (Fe ≤ 30%), medium (30% < Fe ≤ 50%) or rich (Fe > 50%). The evolution of the richness of iron ore is shown in Figure 68. [202] There are several types of ore: magnetite Fe_3O_4 (50% to 67%), hematite Fe_2O_3 (30% to 65%) and limonite (25% to 45%). The first two types are the most consumed in the steelmaking industry.

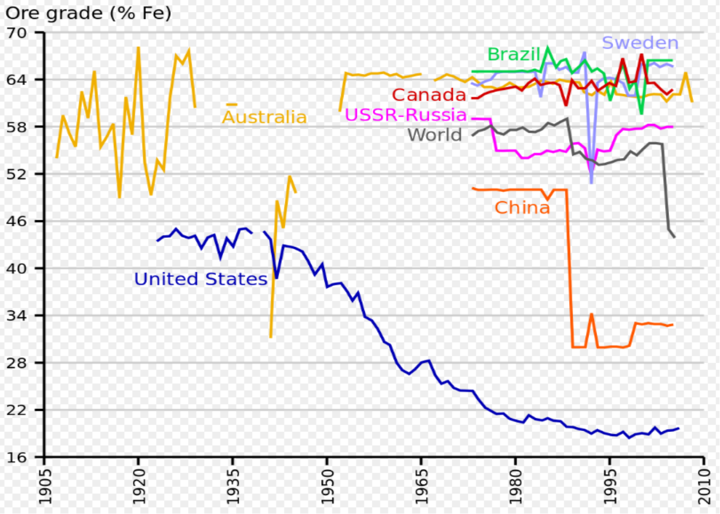

Figure 68. Evolution of the richness of iron ore [202]

The price depends largely on the iron content. A classic index for tracking the price of ore is the IODEX 62. This index is representative of the price of iron ore of 62% concentration. Another index used is the IODEX 65, which reflects the price of 65% Fe mainly found at Carajas in Brazil. For the economic investigation of the BIORED process, we present here the prices of other iron-based products, including the lumps, pellets, DRI, HBI and pig iron as shown in Figure 69.

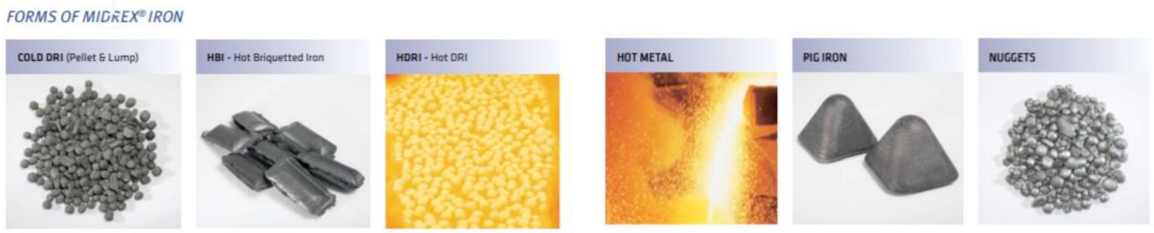

Figure 69. Photos of iron-based products

Apart from the production of iron ore fines, prices of other iron-based products need to be investigated for the economic comparison as shown in Table 20. The price of the Brazilian iron ore (or Fe 65% ore) is higher, with a gap of about \$20/t owing to the better quality. On the other hand, DRI is sold at the same price in the global market since its iron content is close. Furthermore, the price of DRI is similar to that of HBI or Pig Iron. The values in Table 20 are those as of Feb. 2021. However, the volatility corresponds to the variations in the spot price of iron ore; it can be assumed, and this is important for comparison, that the difference between an iron ore product price and the iron ore price remains approximately constant. These prices are highly volatiles.

Types	Global Price (\$/t)
Iron ore fines	170
Iron ore lumps	190
Pellets	220
DRI/HBI/Pig Iron	350

Table 20. Prices of different iron products [203]

VI.1.1.2 Global biomass resources

To determine whether a mine is a potential site for the BIORED process, it is necessary to find sufficient biomass resources nearby. Generally, tropical and subtropical areas are able to provide a large amount of biomass thanks to their favourable climates. Arid regions such as Australia or north of Africa are likely to have difficulty in supply of biomass; the transport of biomass from nearby countries could be a potential but expensive solution. Figure 70 shows the biomass sources in unity of tonnes of carbon per hectare (MgC/ha) in the world. [204]

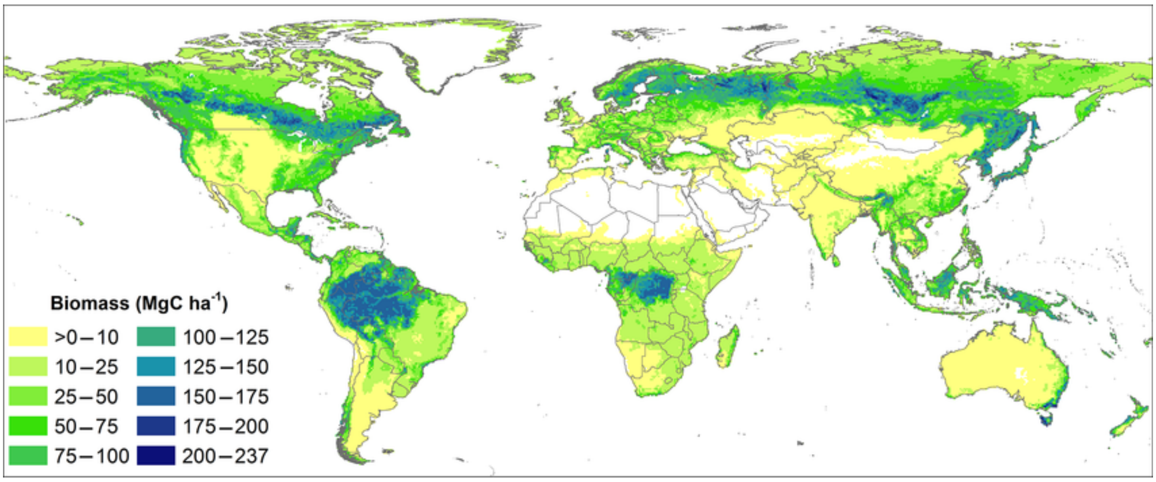

Figure 70. Estimated global carbon biomass [204]

The ULCOS project distinguished three origins of biomass: dedicated plantations, tropical residues and other residues.[205] We decided to consider only the dedicated biomass plantations, which is the most environmentally responsible method, though costly. There are some criteria for the plantation:

- more than 800-1000 mm of rain per year,
- a population density below 80 inhabitants/km^2,
- land is not necessary for other agricultural or ecological use.

As for the choice of planted species, eucalyptus appears to be the most relevant. Indeed, this tree is quite easy and fast to grow and its plantations are spreading more and more around the world. Concerning the management of eucalyptus plantations, 7-year rotations are set up and three cuts are possible on the same tree over its entire life. However, the productivity is not the same from one region to another. Schematically, we can consider that 20 tonnes of dry materials can be harvested per year and per hectare in Brazil, while only 10 tonnes in Congo.

From the results of the reference simulation (Chapter 5), we can determine that 184.4 kg of charcoal are required to produce 1 t of DRI. Assuming a good mass yield for the carbonisation (35%), 527 kg of dry wood are needed for producing 1 t of DRI with the BIORED process. For a forest production of 10 t/ha/yr, 527 km^2 of forest would be needed to produce 1 Mt/DRI/yr. This is a rather high figure but which remains viable in woody countries. It also means that the amount of available biomass in the region will be a crucial factor for the output of the plant and, more globally, for the development of the BIORED process.

VI.1.1.3. Case calculations for the Kiruna Mine

For the following of our study, we decided to carry out a cost calculation for a possible implantation near the mine of Kiruna, Sweden.

The Kiruna mine is located near the town of Kiruna in Norrbotten, north of the polar circle. It is the largest underground mine in the world and its annual production is 27.5 million tonnes. The port of Narvik in Norway is located 200 km away and is accessible by train for the selling of iron ore products. The iron ore mined in Kiruna is about 62% concentration. After extraction, about half of iron ore is converted into pellets. The location of the Kiruna mine is not possible to perform eucalyptus plantations because the dominant forest is taiga trees (pines, spruces and larches). Therefore, the chosen biomass to feed the process will be charcoal produced locally in Sweden.

Based on the calculation reported in Appendix B, we compared the economic benefits of three scenarios:

- direct selling of iron ore pellets,
- selling of DRI produced with the conventional Midrex process,
- selling of DRI produced with the new BIORED process.

The cost consists mainly in the investment of factory in the first year, the production of the DRI, the purchase of the charcoal lumps, the transport of goods, the electricity and CO_2 emissions during the whole process. The main results of our calculation are reported in Table 21 and more details are reported in Appendix B.

Scenarios	Pellets	DRI (Midrex)	DRI (BIORED)
Profits with installation (first year)	1225 M$	163 M$	714 M$
Profits without installation	1225 M$	963 M$	1114 M$

Table 21. Comparison of profits for the Swedish case study

Among different scenarios, the direct selling of pellets appears to be the most profitable because it avoids the costly construction of the shaft furnace and gas reformer. The profit generated by the new process is unfortunately less than that of pellets, but more than that of the Midrex process, especially in the first year, thanks to the avoidance of the gas reformer. These results should be considered as a first analysis, that would need further refinement, but which indicates a possible profitability of the new process.

VI.2. LCA introduction

Since biomass is used in BIORED, plus electricity for EAF steelmaking, a good score of the new route regarding the global warming is expected. To calculate it precisely, and also to quantify the other environmental impacts, we carried out a Life Cycle Assessment (LCA). For their help in this study, we are grateful to C. Sitz, M. Tronet and A. Villa, students in Mines Nancy.

VI.2.1. LCA framework

A schematic representation of the life cycle is shown in Figure 71. [206] According to ISO, [207] Life cycle assessment is best known for quantitative analysis of environmental aspects of a product over all its life cycle stages (raw material extraction, manufacturing, transportation and distribution, use and recycling). An LCA is a systematic tool that enables the analysis of environmental loads of a product throughout its entire life cycle and the potential impacts of these loads on the environment.

- "Products" in this context include both products, processes, and services.
- Emissions to the air, water, and soil (such as CO_2, solid wastes) and resource consumption, constitute "environmental loads".
- "Environmental impacts" in the LCA context, refer to adverse impacts on areas that should be safeguarded, such as ecosystem, human health, and natural resources.

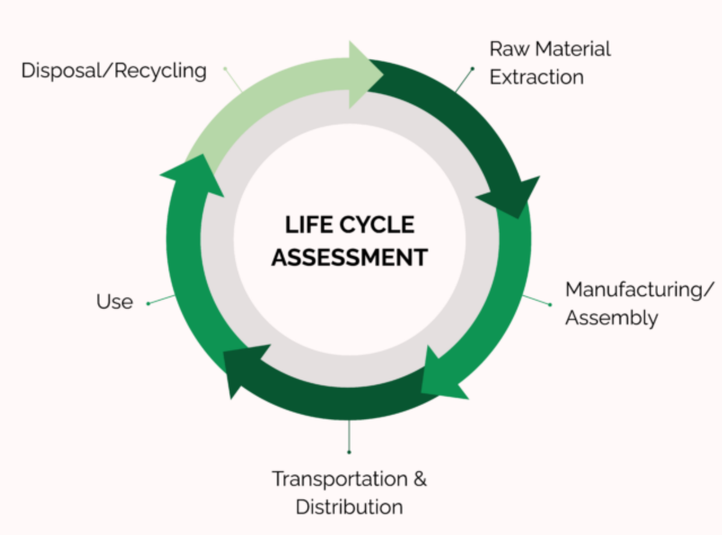

Figure 71. Schematic representation of the life cycle of a generic product [206]

Based on the defined life cycle, the LCA evaluates the potential impacts of a product or system to the environment. Such a holistic approach has many strengths: [207]

- identifying opportunities to improve the environmental performance of products at various points in their life cycle,
- informing decision-makers in industry, government or non-government organizations (e.g. for the purpose of strategic planning, priority setting, product or process design or redesign),
- providing relevant indicators of environmental performance, and

- marketing (e.g. implementing an ecolabelling scheme, making an environmental claim, or producing an environmental product declaration).

The LCA consists of four stages: goal and scope definition, inventory analysis, life cycle impact assessment (LCIA) and interpretation (See Figure 72). [208]

The goal and scope definition is the first and fundamental stage, which consists in specifying the problematic, objectives and scopes of the study. In order to establish a great framework of the study, it is important to well define the functional unit (FU) and system boundaries. The FU defines the reference service to be investigated and allows different systems supplying this defined service to be compared. [206]

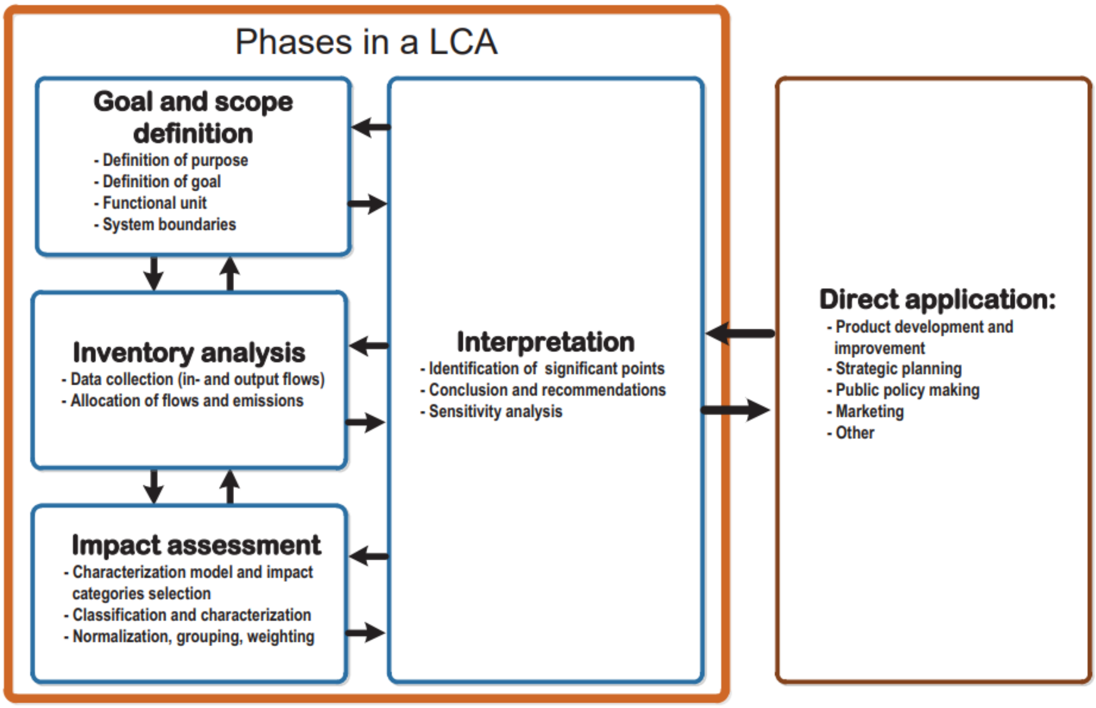

Figure 72. LCA framework (ISO 14040:2006) [208]

The inventory analysis consists in an exhaustive listing of all the inputs and the outputs of the system all along the life cycle. The inputs and outputs refer to the energy and raw material flows, products and co–products, waste and emissions to air, water, and soil. Commercial databases are generally used to build the inventory. [209]

Once the inventory is built, it can be turned into potential impacts on the ecosphere. This step is called Life Cycle Impact Assessment (LCIA). Several methods of LCIA have been developed by different expert groups. The European Commission (European Commission, Joint Research Centre, & Institute for Environment and Sustainability, 2010) edited a guideline for these methods in 2010. In the guideline, the strengths, particularities, methodology used and impact categories were analysed. Table 22 lists the most used methods. For our study, we chose the ReCiPe method. [210]

		Impact modelling depth			
Methodology	**Developed by**	Midpoint	Endpoint	Normalisation	**Source**
CML 2002	CML (Netherlands)	X		X	(Guinée et al., 2002)
Eco-indicator 99	PRé (Netherlands)		X	X	(M. Goedkoop & Spriensma, 2001)
IMPACT 2002+	Ecole Polytechnique Fédérale de Lausanne (Switzerland)	X	X	X	(Jolliet et al., 2003)
ReCiPe	Radboud University Nijmegen + PRé + CML + RIVM (Netherlands)	X	X	X	(Mark Goedkoop et al., 2009)

Table 22. Methods for LCIA [210]

The interpretation of the LCIA is the last stage where analysis is realized with the results of LCIA for the defined objective and scope. Conclusion is drawn to localize the problems for improvements or alternative solutions. The interpretation follows three steps: identify major issues, determinate the influence of major issues and develop conclusions and suggestions. [211]

VI.3. Life cycle assessment of the BIORED-EAF process

VI.3.1. Method

VI.3.1.1 Goal and scope

The goal of the study is to assess the potential environmental benefits of using biomass as a substituent of fossil-carbon in the steelmaking. To do so, we carried out an LCA of the studied steelmaking process (ironmaking with BIORED and steelmaking with EAF) using the software GaBi with the Ecoinvent database 7.1., and we compared it with LCA of other steelmaking scenarios in order to confirm the environmental benefits of the BIORED-EAF process. Here again, we selected the case of a plant located near Kiruna mine, in Sweden.

VI.3.1.2 Function and functional unit

The function of the process is to produce steel from iron ore pellets and charcoal lumps. We chose to define the functional unit as producing one tonne of liquid steel (LS) because steelworkers frequently use a tonne of liquid steel as a reference and the following steel rolling process does not affect the comparison results, because it is the same in all the scenarios.

VI.3.1.3 System boundaries

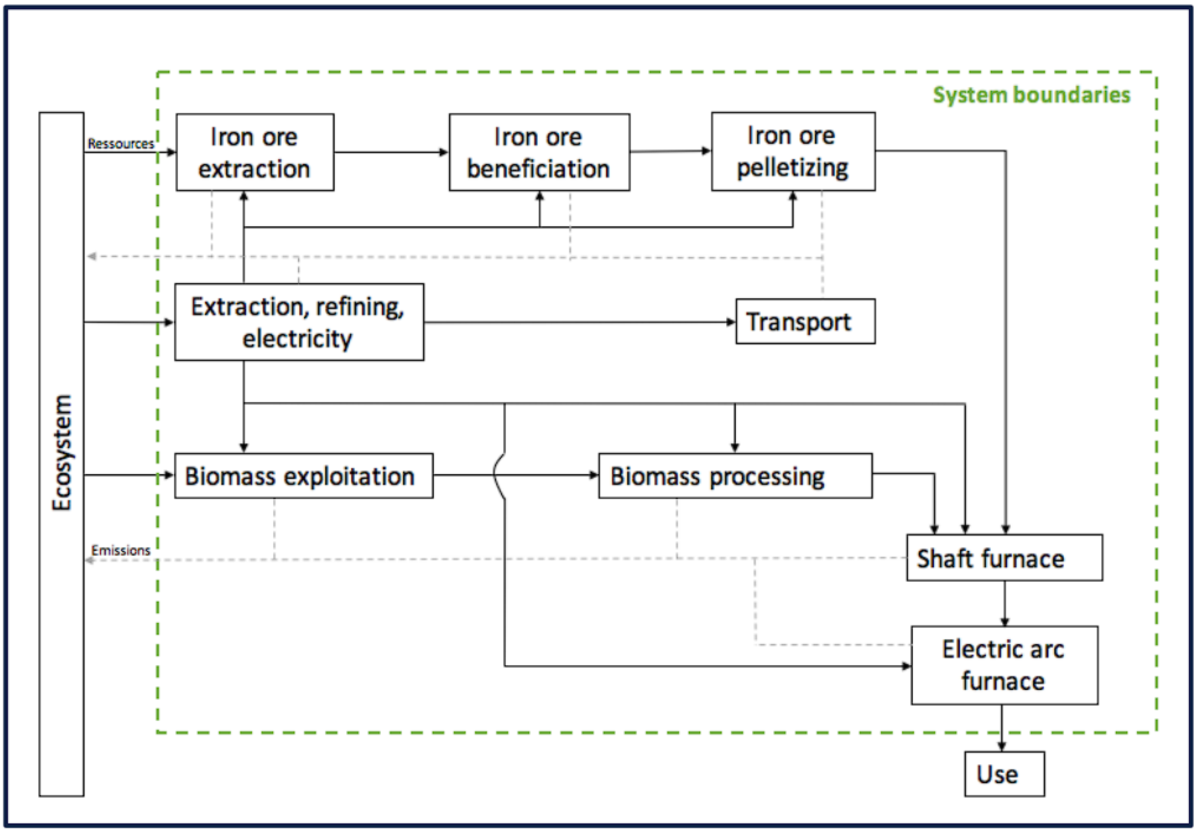

Figure 73. Schematic diagram of system boundaries

Since our study anticipates the plantation of biomass (namely the cradle), we considered "cradle-to-gate" life cycle from the extraction of raw materials to the production of the liquid steel as it is shown in Figure 73. Besides, we did not take into account the construction of the infrastructures, such as the shaft furnace and the EAF, which is assumed to be negligible considering the high annual production.

Literature study usually only focuses on the "gate to gate" life cycle, which means the life cycle starts from the reception of iron ore fines or pellets, coal, etc. It aims to study specifically the impacts of iron and steelmaking routes rather than mining processes; for example, the value of 1.8 $t_{CO2\text{-}eq}/t_{HRC}$ is generally retained for the BF-BOF route. However, Tanzer et al. considered the whole life cycle of steel ("cradle to grave" life cycle) rather than only the "gate to gate" life cycle, which results in higher values. Furthermore, they have recently compared the carbon emissions of introducing bioenergy with carbon capture and storage (BECCS) in multiple steelmaking routes, including blast furnace and HIsarna smelting reduction, and Midrex and ULCORED direct reduction. [212] For this reason, we will cite their work for the comparison.

VI.3.1.4 Evaluation methodology

Before carrying out the LCA, we had to define the impacts we wanted to assess and the evaluation methods. The impacts on climate change are prioritized, but the impacts on other categories may be useful. For these reasons, we decided to consider all the intermediate impact categories. We chose the evaluation method ReCiPe 2016 as it is one of the most recent ones and often used in the LCA of steelmaking. Furthermore, unlike CML 2001, ReCiPe takes into account the land use, which is particularly relevant here, as we need a plantation for charcoal production. Thus, ReCiPe method evaluates the following impacts on the intermediate categories: climate change (including and excluding biogenic CO_2), fine particulate matter formation, fossil depletion, freshwater consumption, ecotoxicity and eutrophication, human toxicity (cancer and non-cancer), ionizing radiation, land use, marine ecotoxicity and eutrophication, metal depletion, photochemical ozone formation (ecosystems and human health), stratospheric ozone depletion and terrestrial acidification and ecotoxicity.

VI.3.2. Process description

VI.3.2.1. Charcoal production

We consider that charcoal is produced from the plantation and harvesting of taiga trees in Sweden. It is worth to note that reasonable plantation management and sustainable harvesting can protect the biomass from deforestation. The plantation and management of woods are considered negligible considering their low impacts on environment. The collected woods are transported to the carbonization plant for the pyrolysis and production of charcoals.[213] Regarding the transportation to the charcoal plant, we considered an average transport distance of 90 km between the forest and the plant and a logging truck over 32 tonnes based on the description of the Swedish road network and Sweden logging trucks dimensions according to Svenson. [214]

VI.3.2.2. Pellet production

Extraction

The extraction is divided into different steps according to the Kiruna mining operator LKAB:

- Drifting: digging transport routes in the rock
- Drilling and blasting: drilling holes to insert explosives through the ore body
- Loading and haulage: using underground trucks, then electric trains and finally electric conveyor to carry up the ore to the surface
- Crushing: breaking the ore into ten-centimetre pieces

- Screening and separations: sorting the ore in order to increase the iron concentration from around 45% to 62%.

Concentration

This stage consists of purifying (through a physical treatment called “flotation”) and separating the iron ore to convert it into a highly concentrated and pure iron ore powder. Some additives such as olivine, quartzite, limestone and dolomite are blended with the powder. Iron ore is beneficiated to reach a 99% rate of metallic ore (LKAB).

Pelletizing

The pelletizing process is an agglomeration method that converts the iron ore concentrate to pellets. Pelletizing requires two main inputs: bentonite as a binder, and the iron ore concentrate. Four steps are necessary to create the pellets: [216]

- Grinding the bentonite with the iron ore concentrate for homogenization
- Mixing and balling with water
- Preheating and induration
- Cooling the pellets

Germany is known to be a big bentonite producer and we assumed that bentonite was imported from the Hamburg port. The commercial distance between Hamburg and Lulea ports was taken from the Searates website. [215]

VI.3.2.3. Shaft furnace (Figure 20, Chapter II)

The iron ore pellets are reduced under the atmosphere of CO and CO_2 with a co-charge of charcoals. Considering the stoichiometry of the reaction and the production of CO and CO_2 simultaneously, there will be a net increase in gas flow and only 85% of the output flow is recirculated. The rest 15% will be sent to a burner in order to oxidise the carbon monoxide. The heat produced is recovered through a heat exchanger, which reheat the 85% of the exhaust gas. Finally, the heated gas goes through an over-heater with addition of oxygen to increase the temperature up to 1100°C before the inlet of the shaft furnace.

VI.3.2.4. EAF

After obtaining the DRI, the goal is to melt it into liquid steel by adding some elements to respect the chemical composition of steel and to discard impurities. This step is performed in an electric arc furnace, which is composed of a shallow depth and large furnace with a removable cover. [217] Three graphite electrodes, inserted through holes in the cover, are required for the electric arc. Several openings are operated to add some chemical products, remove the liquid steel and the slag. A 100% DRI-EAF load without scrap is chosen in this study. The chemical composition of the DRI is presented in Table 23. Some necessary elements like coal and lime (Table 24) are added since the DRI produced in the BIORED shaft furnace lacks some elements.

Composition	Gangue	FeO	Fe	C
Mass fraction	0.047	0.022	0.928	negligible

Table 23. Chemical composition of the DRI with 95% of metallization

VI.3.3. Data inventory

NB: when data for the Swedish case were lacking, equivalent process data for Switzerland or or average Europe were taken.

VI.3.3.1 Data of electricity production in Sweden

The electricity generation, based on the IEA data (2020), and the emission factors, given by the IPCC (2014), by source of production in Sweden show that the Swedish electric mix is mainly decarbonated (See Figure 74). [218] [219] Most of Sweden's electricity supply comes from hydro and nuclear power plants, along with a growing contribution from wind. These three methods are almost carbon-free, which is a significant advantage in reducing CO_2 emissions of the whole DRI-EAF process.

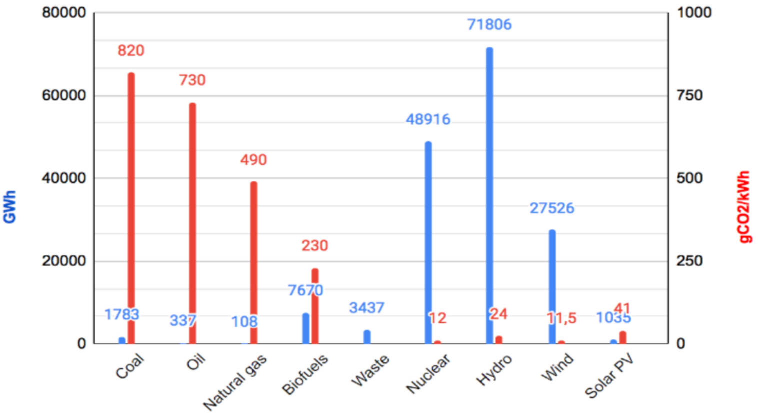

Figure 74. The sources of electricity generation in Sweden and their emission factors [218]

VI.3.3.2 LCA inventory of charcoal production

We used the data from Wu et al. for the harvesting and transportation to the charcoal plant of Mallee biomass. [220] The energy consumption is assumed to be a mix of 58% of diesel (LHV= 41 MJ/kg) and 42% of green Swedish electricity. For the transformation of the trees into woodchips, we considered a diesel energy consumption of 7.4 L per tonne of wood. [221] The received woodchips in the charcoal plant are then carbonized and the carbonization follows the data of Fick et al. [87]

VI.3.3.3 LCA inventory of iron ore extraction and preparation

This part involves different sources of literature data because individual articles contain only part of the iron ore preparation. Data of open pit mining operations by Haque were rearranged with data from an iron ore underground mining extraction process of Bauxite. [193] [194] In fact, surface mining requires less energy than underground mining due to lower requirements for hauling, water pumping and ventilation. As for the concentration step, we used figures from Ferreira and Garcia. [224]

VI.3.3.4 LCA inventory of pellets production

Regarding pelletizing, we based our inventory on the article by Lv and al., whose production is carried out in China. [225] They used the BF gas and anthracite to heat the pellets. However, we considered that there was no BF near the unit of pellet production. Meanwhile, with the proximity of natural gas from Denmark, the pellets are heated by the natural gas. Considering LHV (BF gas) = 3.35 MJ/m^3 and LHV (anthracite) = 30 MJ/kg, 195 kWh are necessary to heat the pellets which corresponds to 20.3 m^3 of natural gas (LHV (NG) = 9.6 kWh/m^3). A green pelletising process is that of the Hybrit project [40] , using biomass as fuel, but data lacked to consider it.

VI.3.3.5 LCA inventory of direct reduction furnace and auxiliary system

Direct reduction furnace

The shaft furnace is in a steady state fed by the solid input containing the charcoal lumps and the pellets and the gas input containing CO and CO_2. The exhaust gas is recycled and treated before reuse by the auxiliary system. The solid charge is composed of 80 wt% of pellets and 20 wt% of charcoal lumps, and we considered a metallization efficiency of 95 % for our reactor.

Gas burner and heat exchanger

After the treatment of exhaust gas, 15% of it then goes to the gas burner in order to heat the 85% of the remaining gas thanks to the heat exchanger. In the gas burner and then in the over-heater, an incoming flow of O_2 (4.48 Nm^3/s) enables a combustion with the gas, which we consider as a total reaction. Per functional unit, the combustion results in the production of 530 kg_{CO2}/t_{LS}, which is considered as a biogenic CO_2 since the CO used for the reaction comes from the gasification of charcoal.

Compressor

The circulation of gas requires a compressor for obtaining three bar at the entrance. An electricity consumption is anticipated but considered to be negligible in the present study.

Elevator

Per functional unit, the elevator has to carry up to 1100 kg of iron ore pellets and 285 kg of charcoal up to the height of the top (25 m). The mechanical energy required is $E_m = mgz = 3.4$ MJ. Considering an electro-mechanic efficiency of 90%, the electrical energy required is E_e=3.8MJ.

	Process	Inputs	Unit	Quantity	Outputs	Unit	Quantity
Charcoal	Harvesting	Diesel	kg/FU	2.03			
		Electricity	MJ/FU	20.9	Biomass	kg/FU	921
	Transport	Mass per distance	tkm/FU	82.9			
	Wood chipping	Biomass	kg/FU	921	Woodchips	kg/FU	921
	Carbonisation	Wood chips	kg/FU	921	Charcoal	kg/FU	193
		Air	kg/FU	2390	Dust	kg/FU	0.07
		Water	kg/FU	92.1	Used water	kg/FU	92.1
		Electricity	MJ/FU	930	CO_2	kg/FU	503
					CH_4	kg/FU	0.006
					VOC (without CH_4)	kg/FU	0.77
Iron ore pellets	Iron ore extraction	Iron ore	kg/FU	2720	Iron ore	kg/FU	2460
		Water	kg/FU	516			
		Explosives	kg/FU	1.23	Waste rock	kg/FU	737
		Diesel	kg/FU	0.98			
		Electricity	MJ/FU	124			
	Iron ore concentration	Iron ore	kg/FU	2460	Iron ore concentrate	kg/FU	1453
		Water	kg/FU	0.928			
		Amines	kg/FU	0.128			
		Flocculant	kg/FU	0.033			
		Starch	kg/FU	1.24			
		Calcium	kg/FU	0.725			
		Sodium	kg/FU	0.99			
		Electricity	MJ/FU	3770			
	Transport bentonite	Mass per distance	tkm/FU	60.40			
	Pelletizing	Iron ore concentrate	kg/FU	1453	Pellets	kg/FU	1467
		Bentonite	kg/FU	27.3	Grinding dust	kg/FU	0.01
		Tap water	kg/FU	220	Dust	kg/FU	0.01
		Natural gas	m^3/FU	29.8	Hydrogen fluoride	kg/FU	0.01
		Electricity	kWh/FU	75	Nitrogen oxides	kg/FU	0.03
					Sulfur dioxide	kg/FU	0.02
	Transport iron pellets	Mass per distance	tkm/FU	484			
Reactor and auxiliaries	Reactor	Charcoal	kg/FU	193	DRI	kg/FU	1047
		Pellets	kg/FU	1467	CO_{2b}	kg/FU	708
					Ashes	kg/FU	0.36
	Gas burner, heat exchanger and warmer	Liquid oxygen	kg/FU	45.8	CO_{2b}	kg/FU	598
	Pump	Electricity	MJ/FU	1			
	Elevator	Electricity	MJ/FU	3.8			
EAF	Electric Arc Furnace	DRI	kg/FU	1047	Liquid steel	kg/FU	1000
		Lime	kg/FU	39	Slag	kg/FU	109
		Coal	kg/FU	17.2	CO_2	kg/FU	80
		Graphite	kg/FU	1.9			
		Oxygen	kg/FU	4.29			
		Refractory bricks	kg/FU	4			
		Dolomite	kg/FU	16			
		Natural gas	m^3/FU	4.34			

Table 24. Life cycle inventory of the biomass-based steelmaking

VI.3.3.6 LCA inventory of EAF

Considering the chemical composition of the DRI, necessary elements listed in Table 24 are added into the EAF, besides the need of electricity. We represented our EAF using data of a virtual steel electric furnace according to Patisson. [226] The original data referred to DRI produced with hydrogen; therefore, the additions for the EAF were adapted to our case to satisfy the composition of the steel.

VI.4. Results and discussion

VI.4.1. Environmental assessment of the process

After the introduction of each flow into the LCA software *GaBi*, we obtained the results for each midpoint impact categories of the *ReCiPe* method. These are shown in Figure 75, with the usual convention of plotting the total of each impact as 100%. There is no interest to consider the emissions of the biogenic carbon in our study because it will be involved in the carbon cycle by the growth of plants. However, we will present its emissions for understanding its scale.

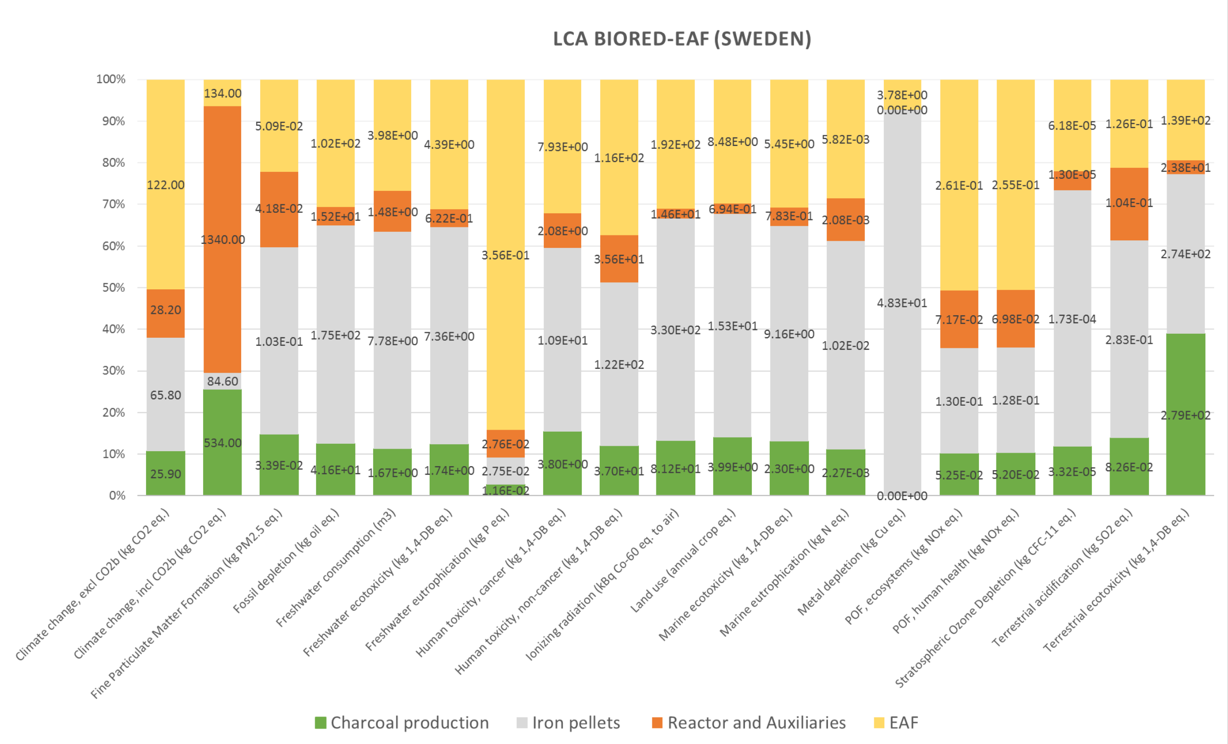

Figure 75. ReCiPe midpoints for the new DRI-EAF route

Considering the impacts on climate change, the process results in emissions of about 2092.6 $kg_{CO2\text{-}eq}$ per FU, of which about 1850 $kg_{CO2\text{-}eq}$ is from the biogenic carbon. As a result, the emissions of non-biogenic carbon, of 242 $kg_{CO2\text{-}eq}$ per FU are low, significantly lower than that of other existent processes, as will be shown later, thanks to the replacement of fossil carbon by the charcoal. Tanzer et al. reported in their LCA study that the high use of bioenergy in Midrex-EAF could decrease the CO_2 emissions from 1500 to 900 $kg_{CO2\text{-}eq}/t_{HRC}$ (HRC = Hot Rolled Coil, the standard steel product). [212] An important reduction of 600 $kg_{CO2\text{-}eq}/t_{HRC}$ in their work could be reached by using the DRI reduced by 100% bio-syngas from woods and mainly woods for fuel. We have to mention here that their CO_2 emissions of 900 $kg_{CO2\text{-}eq}/t_{HRC}$ are much higher than ours because first, their electricity consumption emitted about 500 $kg_{CO2\text{-}eq}/t_{HRC}$ due to the generation of electricity with high carbon footprint (400 gCO_2/kWh). In addition, they assumed that the loaded solid in the EAF contained 17% of scrap, which needs further 121 kg_{CO2}/t_{scrap}. Eventually, they used a “cradle to grave” life cycle (not the same FU): the production of 1 tonne of HRC required 1024 kg liquid steel and emitted about 70 $kg_{CO2\text{-}eq}/t_{HRC}$ due to the electricity consumption in the steel finishing and rolling.

Without emissions of biogenic carbon, the EAF represents 42% of the GHG emissions (122 $kg_{CO2\text{-}eq}$ per FU). The emissions of the EAF are less important than the value of 240 $kg_{CO2\text{-}eq}$ per FU in Table 1 thanks to the fact that the power consumption is from relatively clean electricity in Sweden. The emissions are mostly due to the energy consumption and the fossil additives in the EAF. Regarding other midpoint impacts, we can see that the EAF has important contributions for most of the impacts due to the large amount of electricity consumption. Even though the source of Swedish electricity is relatively “clean” in Europe, the generation of electricity still has important impacts on the environment. For example, for the impact of land use, the electricity generation from hydro and wind requires large space for installation of these plants. The production of iron pellets plays an important role in the environmental impacts mostly due to its large electricity consumption, and particularly leads to full metal depletion. The charcoal production and the shaft furnace are relatively less harmful, which consists with our expectations. In terms of the land use, it is important to note that it refers to the species loss of the land rather than the occupation of the surface. For this reason, the forest in our case is very eco-friendly, so land use of charcoal production is not important.

VI.4.2. Processes comparisons

VI.4.2.1. Scenario BF-BOF (100% coke)

In order to compare the impacts of our process to existing processes, we carried out a complete LCA of a blast furnace using 100% of coke. We used as a basis the work of Fick et al. who considered the elementary processes of resources extraction, transportation, electricity production, the coke oven, the agglomerate unit and the blast furnace. [87] We implemented them on the Gabi software with only some changes in the transportation and the electricity for a process located in Sweden. Then the pig iron is transformed into liquid steel in the basic oxygen furnace.

The CO_2 emissions of this process is about 1928 $kg_{CO2\text{-}eq}$ per FU, without the biotic carbon. Those emissions are slightly lower than the results of Tanzer because the Swedish electricity is more decarbonated as mentioned before. According to them, the reduction of electricity's carbon intensity from 400 to 0 gCO_2/kWh results in 100–200 $t_{CO2\text{-}eq}/t_{HRC}$ less CO_2 for BF-BOF steelmaking route. [212]

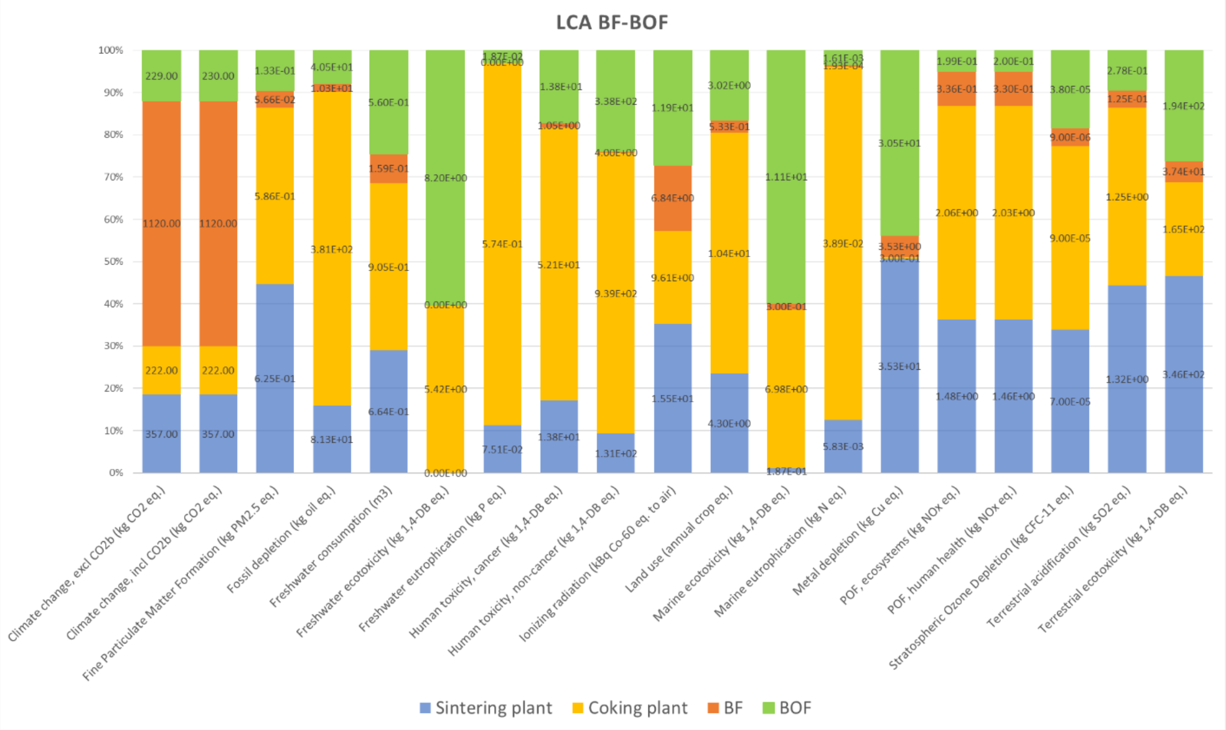

Figure 76. ReCiPe midpoints for the BF-BOF route

The results in Figure 76 show that the blast furnace is the main contributor to the climate change as expected. The blast furnace is a great emitter because the fossil carbon is the reducing agent for the reduction of iron oxides. Besides, the cowpers in the auxiliary system are combustors, where the blast furnace gas is burned to produce the heat and electricity for the system; thus, the CO_2 production is significant. Other impacts are not important because the energy of BF is almost only provided by fossil carbon and the operation does not need plenty of other inlets. The coking process is the most significant contributor to many other midpoints, such as fossil depletion, freshwater eutrophication and POF. For this reason, many alternative ironmaking routes to the BF-BOF have been studied to avoid the coking process. The sintering process and BOF are responsible for many midpoints as well, although slightly lower than that of the coking process.

Finally, we decided to compare the ReCiPe midpoints of this blast furnace scenario with the studied process in Figure 77. It is important to note that the ordinate of Figure 77 and Figure 78 is in the logarithmic scale. The graphic shows that we reduce significantly the GHG emissions from 1928 to 242 $kg_{CO2\text{-}eq}$ per FU if we exclude the biogenic CO_2 emissions. Most of the midpoint impacts are much less important for the biomass-based steelmaking process except freshwater consumption, ionizing radiation, land use and stratospheric ozone depletion. The freshwater consumption, ionizing radiation, land use are mainly from the electricity mix from nuclear, hydro and wind.

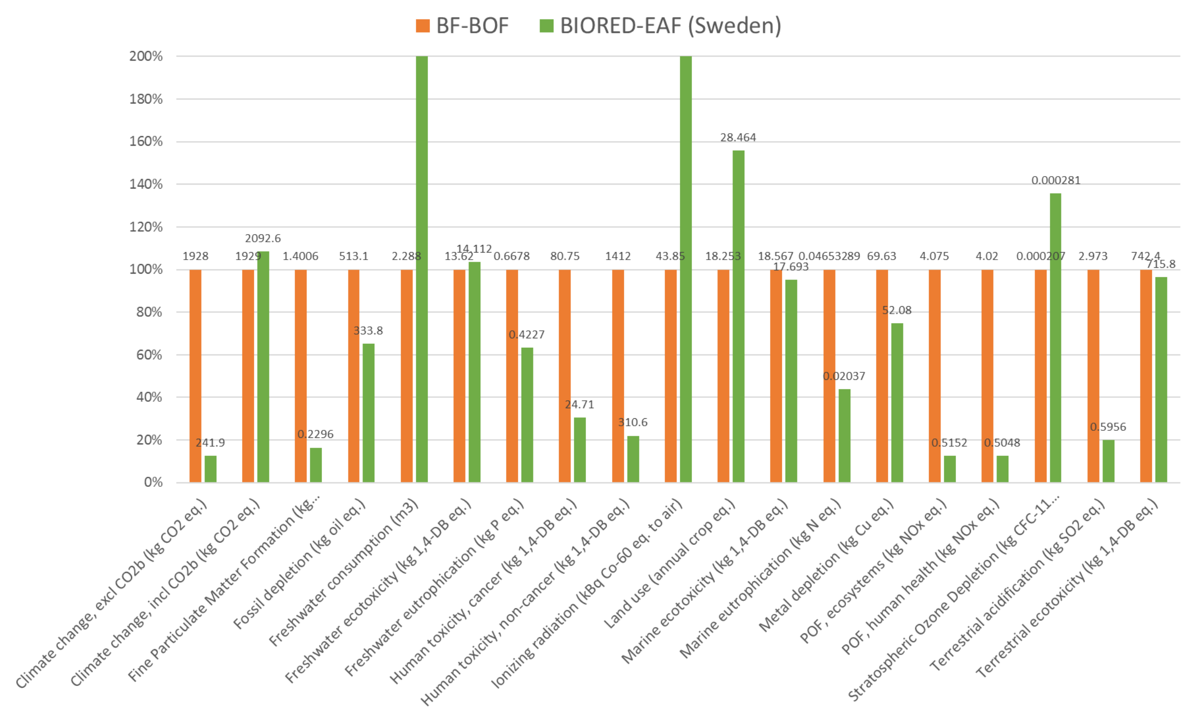

Figure 77. Comparison between new BIORED-EAF (green) and BF-BOF (orange) routes

VI.4.2.2. Electricity sensitivity analysis

This BIORED-EAF route uses more electricity than the blast furnace route, mostly due to the electric arc furnace. However, the Swedish electric system presents one of the lowest carbon intensity in the world, with 46 gCO_2/kWh in 2016, compared to the European Union average one of 397 gCO_2/kWh in 2016. Therefore, the following section is dedicated to a sensitivity analysis to the electricity mix. We chose to use the Spanish electricity mix (359 gCO_2/kWh in 2016) because it is very representative to the European Union average one.[227] Figure 78 compares the ReCipe midpoints between these two scenarios. The Spanish scenario results in the scenario of 936.7 $kg_{CO2\text{-}eq}$ per FU. Tanzer et al. also reported that the typical Midrex-DRI route could emit 900 kg $t_{CO2\text{-}eq}/t_{HRC}$ (almost the same value as the present scenario) with an electricity of 400 gCO_2/kWh if 100% replacement of DRI fuel with wood bio-syngas, 50%

replacement of agglomeration fuel with charcoal, and 100% replacement of steam boiler natural gas with wood chips. [212] In conclusion, their calculations for a "Biomass-Midrex" process with a European mix are very consistent with our results.

Besides, except for ionizing radiation, land use and freshwater consumption, all the other midpoints present worst results in the Spanish scenario.

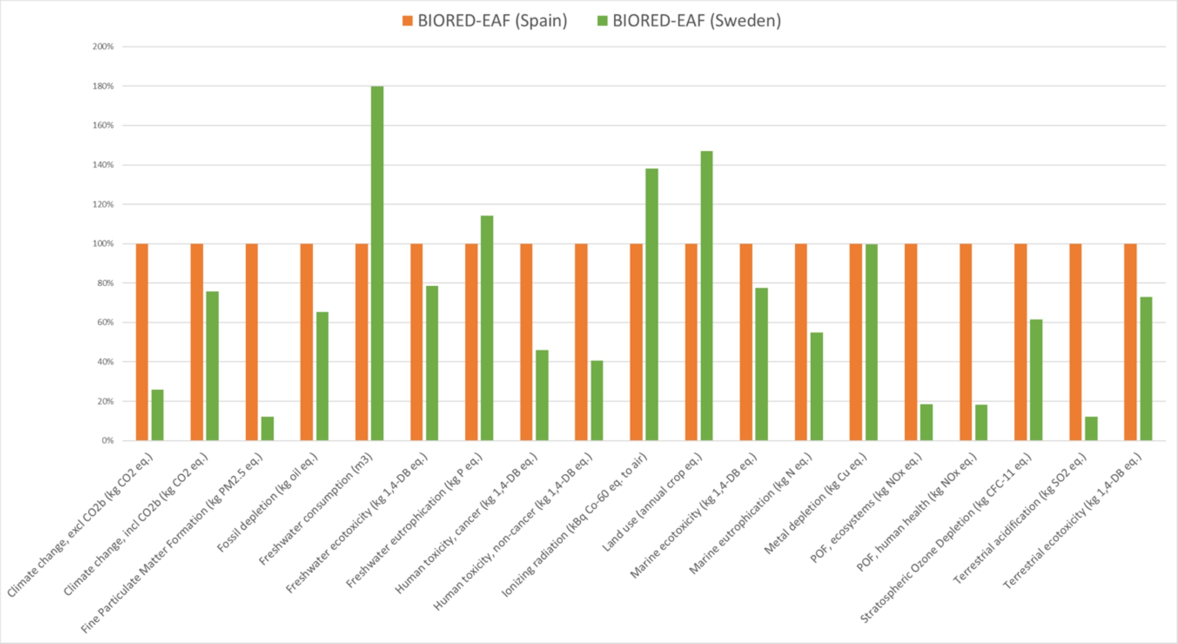

Figure 78. Compared ReCiPe midpoints between Swedish (green) and Spanish (orange) Scenarios

VI.4.3. Limits and improvement

This LCA presents several limits. Some procedures are neglected, especially the installation of the reactors. The by-products of biomass carbonisation were not taken into account, which could reduce the energy consumption via their valorisation like combustion for heat recovery. Furthermore, the end of life of the solid waste after the shaft furnace was also not considered, which could bring about more ecotoxicity. Regarding the BIORED-EAF LCA, we realised on the time of checking this manuscript that the carbonisation yield was taken as 35%, a value around the most efficient ones in the industry. Actually, even if a lower value could change the gaps between scenarios, it would not change the conclusions of the comparison.

During the implementation of the EAF, we noticed that the energy consumption of this stage decreases when scrap is added to the DRI. Consequently, a potential way of improving our study case would be by adding scrap in the EAF. Tanzer et al charged 18% scrap and 82% DRI in the EAF for steelmaking. [212] Furthermore, the reusing of used steel (i.e., scrap recycling) appears as a solid alternative to its production, especially as the world steel stock is increasing.

VI.5. Conclusion

In this chapter, the potential implementation in some woody mining areas was proposed and the financial benefits were estimated. An important feature is that the availability of biomass in the region of setting up has to be ascertained. A life cycle assessment of the BIORED-EAF process in Sweden was conducted as well. The determination of several midpoint impact categories using ReCiPe 2016 showed the great environmental benefits of this process. Moreover, several comparisons were done and results showed that the biomass-derived DRI-EAF process was the most environmentally friendly with an emission of only 242 $kg_{CO2\text{-}eq}$ per FU and great benefits in most of the intermediate impacts. The low CO_2 emissions are explained by the use of the carbon-neutral reducing agent and low-carbon electricity. Indeed, by locating our process in Sweden, we chose an electricity mix strongly decarbonized, which brings about better results. Switching the Swedish electric mix to the Spanish one resulted in an important increase in the CO_2 emissions, but keeps BIORED process highly competitive compared to standard process. Eventually, we list here the CO_2 emissions of the processes previously mentioned:

Scenarios	CO_2 emissions	Electricity emission factors
BIORED-EAF Sweden	242 $kg_{CO2\text{-}eq}/t_{LS}$	46 gCO_2/kWh
BF-BOF Sweden	1928 $kg_{CO2\text{-}eq}/t_{LS}$	46 gCO_2/kWh
BIORED-EAF Spain	937 $kg_{CO2\text{-}eq}/t_{LS}$	359 gCO_2/kWh
Midrex-EAF (Tanzer et al.)	1500 $kg_{CO2\text{-}eq}/t_{HRC}$	400 gCO_2/kWh

Table 25. Comparison of CO_2 emissions for different scenarios

VII. Conclusion and perspectives

The objective of our study was to evaluate an innovative alternative for the reduction of CO_2 emissions in the DRI-EAF route for the ironmaking. This alternative consists in substituting the carbon-neutral biomass for fossil carbon. Our assessment was based on technical feasibility and then environmental impacts. The first aspect was investigated by experimentation at laboratory scale and mathematical modelling associated with numerical simulations. Regarding environmental impacts, a LCA was conducted.

In a first part, the operation of the conventional route of the iron and steelmaking was presented. Then the alternative route DRI-EAF became our hot topic besides the improvement of the conventional route. The DRI-EAF route has been a fierce competitor to the BF-BOF route for the last decades thanks to its reduced energy consumption and CO_2 emissions (from 1.8 t_{CO2-eq}/t_{HRC} to 970 kg_{CO2-eq}/t_{HRC}). Several typical gas-based processes for the production of DRI were presented. Among those, the Midrex and HYL processes are dominant in the present market and the shaft furnace shows greater advantages than the retort reactor and fluidized bed reactor. For some ironmaking processes, biomass was identified as a potential carbon-neutral alternative to fossil fuels. In this context, we investigated a breakthrough option, that we called the BIORED process, which combines direct reduction of iron ore by CO with in-situ charcoal gasification, inside a typical shaft furnace reactor with gas recycling.

In a second part, the biomass-related reactions were experimentally investigated by TGA. Experiments of devolatilisation of oak charcoal samples were carried out at different heating rates. From the experimental data, we analyzed the effect of heating rates and obtained the kinetic parameters of devolatilisation by the independent parallel reactions model. An overall kinetic law of rate of the dehydration and decomposition of the lignin as a function of temperature was obtained. Afterwards, the gasification of charcoal particles of industrial size under different composition of CO-CO_2 at 850-1100°C was studied because it is the principal source of the reducing agent CO in the BIORED process. The increase in temperature contributes to faster gasification rate and shorter reaction time, especially at relatively low temperatures. The increase in the CO_2 partial pressure enhances the char gasification rate. Taking reaction rate at $X=0.05$ as the initial rate for the kinetic study, the pre-exponential factor was 1.396 s^{-1} and the calculated apparent activation energy was 86.5 kJ/mol by the n-th order model. The kinetic parameters of the three reactions of the Langmuir-Hinshelwood model were obtained and the apparent activation energies were compared with other studies. Through the analysis of the mercury porosimetry, it was shown that the gasification of the oak charcoal pieces took place in the mesopores and some macropores at the early stage and then continued in the macropores when mesopores were fully replaced by macropores. The Modified Random Pore Model appeared to best fit the experimental reactivity function. Investigating the effect of the gas switching time between the inert and reactive gas mixture, were found that, contrary to the conclusion of Gomez et al., the increase in reactive surface area and porosity still influenced reactivity according to the Modified Random Pore Model even after the reactive gas was fully introduced in the reactor.

The next part was the modelling of the novel process. In the literature, a great number of models have already been developed to simulate the DR process. We used the 2-D model REDUCTOR developed by D. Wagner, A. Ranzani da Costa and H. Hamadeh at the IJL, which simulates the direct reduction of iron ore by hydrogen and CO in the reduction zone, transition zone and cooling zone of the shaft furnace. The pellet reduction model is based on the law of characteristic times, describing six reduction reactions and taking into account the transport by diffusion in the granular structure (grains and crystallites) of the pellet. The model was upgraded introducing a second granular solid phase, the charcoal grains, and the chemical reactions associated. The kinetics of devolatilisation and gasification obtained from the experimentation were included. The new model can simulate the evolution of temperatures, gas and solid composition along the shaft, as well as the rates of the reactions (devolatilisation and gasification of charcoal lumps and reduction of iron ore pellets). The model reveals the inside behaviour of the shaft furnace. The gasification takes place at the bottom, the devolatilisation at the top, whereas the reduction occurs stepwise along the furnace. Using a high gas inlet temperature and a CO-CO_2 mixture rich in CO, it is possible to make DRI with high metallisation in a shaft furnace fed with iron ore pellets and charcoal. A sensitivity analysis was performed to investigate the effect of inlet gas temperature, inlet CO content and charcoal reactivity.

Since no experimental, pilot, or plant data were available to validate our model, a new idea was brought out for the validation of the mathematic model. In a thermobalance, we submitted a pellet to the same temperature, gas flow rate and gas composition as seen by a pellet along its path inside the simulated shaft to investigate its reduction behaviour. The experiment showed a nearly complete reduction of hematite and the expected stepwise reduction reactions; however, the exact time or reaction rate did not fully correspond to the simulated results.

In the last part of our study, the potential implementation of the BIORED process in some areas was proposed and the financial benefits were estimated. A life cycle assessment of the BIORED DRI-EAF process assumed located in Sweden was conducted for the determination of the environmental impacts. Results by using the ReCiPe 2016 method showed the great environmental benefits of this process. In particular, when compared to the blast furnace route, the results showed that the DRI-EAF process from biomass was the most environmentally friendly with an emission of 242 $kg_{CO2\text{-}eq}$ per tonne of liquid steel (8 times lower) and better scores in most intermediate impacts categories. The low CO_2 emissions are due to the use of a carbon-neutral reducing agent and low-carbon electricity. Indeed, by locating our process in Sweden, we have chosen a decarbonised electricity mix, which leads to better results. However, switching from the Swedish to the Spanish electricity mix showed a significant increase in CO_2 emissions, but still better than the Midrex process. In conclusion, the process may also be the competitor of the shaft furnace by using H_2 as both are very "clean" regarding the climate change.

As for perspectives, it would be of particular interest in the future to study the reduction of iron ore with wood directly, rather than with the pre-treated charcoal. Wood exhibits better gasification reactivity than charcoal, which is favourable to the formation of CO. Wood is more mechanically resistant than charcoal, thus promoting the moving behaviour of the solid loads. Finally, yet importantly, the direct use of wood may only require a drying process, which is more cost-effective. However, wood has high volatile content and generates large quantities of tar when heated at the top of the reactor, which could probably harm the reactor and auxiliary tubes. Besides, wood with low carbon content and high bulk volume needs more amounts to provide the same volume of CO than charcoal. In conclusion, the use of wood directly seems a promising alternative to charcoal in our biomass-based shaft furnace if we could ensure the technical feasibility.

The validation of the model was based on an iron ore pellet at laboratory scale; we could study the behaviour of the charcoal lumps according to the same methodology. In the future, one could also realize the reduction of iron ore pellets with charcoal lumps in a pilot shaft furnace in the laboratory for better validation.

Furthermore, the environmental impacts of the process were well determined by the method of LCA, but the economic aspects were not clear for us. This last part could be improved in a next study.

The operating conditions of the process could also be further optimised once the best suited biomass agent has been selected. If charcoal, the reactivity to gasification under $CO\text{-}CO_2$ at high temperature could be improved with a proper choice of the resource and of the carbonisation conditions, which, in turn, would improve the performance and compactness of the shaft furnace.

Finally, regarding the development potential of the process itself, the results of more detailed cost calculations and resource availability on case studies would be welcome.

VIII. List of Figures

IX. List of Tables

X. References

[1] GIEC, Changements climatiques 2001. Rapport de synthèse du GIEC (IPCC) - Genève, 2001.

[2] https://ec.europa.eu/clima/eu-action/international-action-climate-change/climate-negotiations/paris-agreement_en

[3] A. Ranzani Da Costa, D. Wagner, F. Patisson, Modelling a new, low CO_2 emissions, hydrogen steelmaking process, J. Clean. Prod.46 (2013) 27–35.

[4] http://www.worldsteel.org

[5] Ragauskas, A. J. et al. The Path Forward for Biofuels and Biomaterials. Sci. 311 (5760), 484–489 (2006).

[6] https://www.statistiques.developpement-durable.gouv.fr

[7] Midrex Technologies, 2017a. 2015 World Direct Reduction Statistics. www.midrex.com/assets/user/news/MidrexStatsBook2015.pdf (Accessed 4 July 2017).

[8] Vyazovkin, S.;Wight, C.A. Kinetics in solids. Annu. Rev. Phys. Chem. 1997, 48, 125–149.

[9] Slopiecka, K.; Bartocci, P.; Fantozzi, F. Thermogravimetric analysis and kinetic study of poplar wood pyrolysis. Appl. Energy 2012, 97, 491–497.

[10] Antal, Jr., M.J., Varhegyi, G., Jakab, E.: Cellulose pyrolysis kinetics: revisited. Ind. Eng. Chem. Res. 37, 1267-1275 (1998).

[11] G. Pantoleontos, P. Basinas, G. Skodras, P. Grammelis, J.D. Pintér, S. Topis, G.P. Sakellaropoulos, A global optimization study on the devolatilisation kinetics of coal, biomass and waste fuels, Fuel Processing Technology 90 (2009) 762–769.

[12] G. Skodras, P. Grammelis, P. Basinas, E. Kakaras, G.P. Sakellaropoulos, Pyrolysis and combustion characteristics of biomass and waste-derived feedstock, Ind. Eng. Chem. Res. 45 (2006) 3791–3799.

[13] María Zabalo Alonso, A thermogravimetric and kinetic study on devolatilization of woody biomass, Phd thesis, Norwegian University of Science and Technology, July 2016 Page 11.

[14] Emami Taba, L., Irfan, M.F., Wan Daud, W.A.M., Chakrabarti, M.H.: The effect of temperature on various parameters in coal, biomass and CO-gasification: a review, Renew. Sustain. Energy Rev. 16 (8), 5584–5596 (2012).

[15] A. Ranzani da Costa, La réduction du minerai de fer par l'hydrogène : étude cinétique, phénomène de collage et modélisation. PhD thesis, Université de Lorraine, Nancy, France, 2011.

[16] H. Hamadeh, Modélisation mathématique détaillée du procédé de réduction directe du minerai de fer. PhD thesis, Université de Lorraine, Nancy, France, 2017.

[17] https://www.ipcc.ch/site/assets/uploads/sites/2/2019/06/SR15_Full_Report_Low_Res.pdf. GIEC, Changements climatiques 2019 Intergovernmental Panel on Climate Change.

[18] https://www.britannica.com/science/global-warming/Global-warming-and-public-policy

[19] https://ec.europa.eu/clima/eu-action/international-action-climate-change/climate-negotiations/paris-agreement_en

[20] IEA: Iron and Steel Technology Roadmap: Towards more sustainable steelmaking. Paris, 20 November 2017.

[21] Duarte, P.E., Becerra, J.: Reducing greenhouse gas emissions with Energiron nonselective carbon-free emissions scheme. Stahl Und Eisen, 131, 85 (2011).

[22] EVRAZ Canadian Steel: Low Carbon Footprint. November 2016.

[23] The Steel Eco-Cycle, Scientific Report 2004-2012, D853. Jernkontoret Research; 2012.

[24] J.P. Birat, J. Borlée, B. Korthas, J. van der Stel, K. Meijer, C. Günther, M. Halin, T. Bürgler, H. Lavelaine, C. Treadgold, I. Millar, D. Sert, T. Torp, F. Patisson, B. Paya, E. Burstrom “Breakthrough solutions to the CO_2 challenge explored by the European steel industry: the ULCOS program. A progress report in the Spring of 2008.” SCANMET III Conference, 3rd International Conference on Process Development in Iron and Steelmaking, 8-11 June 2008, Luleå, Sweden, Proceedings edited by Swerea Mefos, Luleå, 1-15.

[25] Hutson, M.: The Promise of Carbon-Neutral Steel, The New Yorker, Annals of a Warming Planet, September 18, 2021.

[26] Émissions de CO_2: ArcelorMittal va remplacer en France trois de ses hauts-fourneaux à charbon par des fours électriques et à hydrogène, Le Monde, 4 Février 2022. https://www.lemonde.fr/planete/article/2022/02/04/emissions-de-co2-arcelormittal-va-remplacer-en-france-trois-de-ses-hauts-fourneaux-a-charbon-par-des-fours-electriques-et-a-hydrogene_6112249_3244.html

[27] International Energy Agency, « Energy Technology Perspectives 2020 », Energy Technology, Perspectives, p.400 (2020).

[28] https://www.bhp.com/news/prospects/2020/11/pathways-to-decarbonisation-episode-two-steelmaking-technology

[29] Lu, L.: Chemistry structure and quality of iron ore sinter. In: Proceeding of The Iron and Steel Technology Conference and Exposition, AISTech 2015. Cleveland, Ohio, USA; 2015.

[30] Pardo, N., Moya, J.A: Prospective scenarios on energy efficiency and CO_2 emissions in the European iron and steel industry. Energy 54, 113–28 (2013).

[31] Dutta, S. K., Sah., R.: Direct Reduced Iron: Production. In Encyclopedia of Iron, Steel, and Their Alloys. Taylor and Francis: New York, 1082-1108 (2016).

[32] Lu, Y., Wei, Z., Wang, Y., Zhang, J., Li, G., Zhang, Y.: Research on the characteristics and kinetics of direct reduction of limonite ore fines under CO atmosphere in a rotary drum reactor. Powder Technology 352, 240–250 (2019).

[33] Chatterjee, A., Sponge iron production by direct reduction of iron oxide, 2014.

[34] Morales, J., ENERGIRON. The Innovative Direct Reduction Technology, (2015). www.energiron.com.

[35] World direct reduction statistics, (2016). www.Midrex.com.

[36] Atsushi, M., Uemura, H., Sakaguchi, T.: Midrex process. Kobelco technology review No. 29 Dec. 2010.

[37] Brent, A., Mayfield, P., Honeyands T.: Fluidised bed production of high quality hot briquetted iron for steelmaking, September 1997, Conference: AusIMM International Conference on Alternative Routes of Iron and Steelmaking (ICARISM ’99) At: Perth.

[38] http://www.iipinetwork.org/wp-content/Ietd/content/circored.html

[39] Patisson, F., Mirgaux O., Birat, J.P.: Hydrogen steelmaking. Part 1: Physical chemistry and process metallurgy. Matériaux & Techniques 109, 303 (2021).

[40] Patisson, F., Mirgaux O.: Hydrogen Ironmaking: How It Works. Metals 10, 922 (2020).

[41] Astier, J. : Réduction directe. Techniques de l'ingénieur, 2005. M7 580v2: p. 1-22.

[42] Devisme, O.: Contribution à l'étude de la réduction des oxydes de fer par l'hydrogène : mécanisme et cinétique de la réaction. Mémoire présenté en vue d'obtenir le diplôme d'ingénieur du Conservatoire National des Arts et Métiers. 2005.

[43] Gaballah, I., Bert, P., Dufour, L.C., Gleitzer, C.: Kinetics of the reduction of wustite by hydrogen and carbon monoxide+hydrogen mixture. Observation of trichites. Mém. Sci. Rev. Mét., 69, 523-530 (1972).

[44] Mondal, K., Lorethova, H., Hippo, E., Wiltowski, T., Lalvani, S.B., Reduction of iron oxide in carbon monoxide atmosphere - reaction controlled kinetics. Fuel Processing Technology 86, 33-47 (2004).

[45] Jenkins, B.M., Baxter, L.L., Miles Jr., T.R., Miles, T.R: Combustion properties of biomass, Fuel Processing Technology 54, 17–46 (1998).

[46] Fritsche, U.R., Kampman, B., Bergsma G.: Better Use of Biomass for Energy. Position Paper of IEA RETD and IEA Bioenergy, December 2009.

[47] Mandova, H., Gale, W.F., Williams, A., Heyes, A.L., Hodgson, P., Miah, K.H.: Global assessment of biomass suitability for ironmaking – Opportunities for co-location of sustainable biomass, iron and steel production and supportive policies. Sustainable Energy Technologies and Assessments 27, 23-39 (2018).

[48] Mousa, E., Wang, C., Riesbeck, J., Larsson, M.: Biomass applications in iron and steel industry: An overview of challenges and opportunities. Renewable and Sustainable Energy Reviews 65, 1247-1266 (2016).

[49] Basu, P.: Handbook of Biomass gasification, pyrolysis and torrefaction; Practical design and theory. UK Elsevier's Science and Technology (2013).

[50] Venderbosch, R.H., Prins W. Fast pyrolysis technology development. Biofuels Bioproducts Biorefining 4,178–208 (2010).

[51] Chen, W., Farooq, W., Shahbaz, M., Naqvi, S.R., Ali, I., Al-Ansari, T.: Current status of biohydrogen production from lignocellulosic biomass, technical challenges and commercial potential through pyrolysis process. Energy, 226, 120433 (2021).

[52] Goyal, H.B., Seal, D., Saxena, R.C.: Bio-fuels from thermochemical conversion of renewable resources: a review. Renew Sustain Energy Rev 12, 504–17 (2008).

[53] Bertero, M., Sedran, U.: Coprocessing of bio-oil in fluid catalytic cracking. Recent advances in thermo-chemical conversion of biomass. Elsevier, 355–81 (2015).

[54] Strahan, G.D., Mullen, C.A., Boateng, A.A.: Characterizing biomass fast pyrolysis oils by 13C NMR and chemometric analysis. Energy Fuels 25, 5452–61 (2011).

[55] Al-Rumaihi, A., Shahbaz, M., Mckay, G., Mackey, H., Al-Ansari, T.: A review of pyrolysis technologies and feedstock: A blending approach for plastic and biomass towards optimum biochar yield. Renewable and Sustainable Energy Reviews 167, 112715 (2022).

[56] Bridgwater, A.V., Meier, D., Radlein, D.: An overview of fast pyrolysis of biomass. Org Geochem 30, 1479–93 (1999).

[57] Tezer, Ö., Karabağ, N., Öngenb, A., Çolpan, C. Ö., Ayole A.: Biomass gasification for sustainable energy production: A review. International Journal of Hydrogen Energy Volume 47, 15419-15433 (2022).

[58] Elliott, D.C., Biller, P., Ross, A.B., Schmidt, A.J., Jones, S.B.: Hydrothermal liquefaction of biomass: Developments from batch to continuous process, Bioreource Technology 178, 147–156 (2015).

[59] Babich, A., Arnsfeld, S., Senk, D., Gudenau H.W.: Biomass Use in the Iron and Steel Metallurgy, Proc. 54th Committee Meeting of the Japan Society for the Promotion of Science, Tokyo 8-9 December 2011. pp. 1.1-14.

[60] Babich, A., Arnsfeld, S., Senk, D., Gudenau H.W.: Investigation of Usage of Biomass in Steelmaking; Research Activities at the IEHK in Aachen, Proc. International Workshop on Utilisation of Biomass for Mitigation of CO_2 Emissions, Sendai, 12 December 2011, pp. 2.1-17.

[61] Mühlböck, M., Naderer, G., Fehringer E: SWGR- Selective waste gas recirculation-next generation. In: Proceeding of METEC & 2nd ESTAD. Düssel- dorf, Germany; 2015.

[62] Mousa, E.A., Babich, A., Senk D.: Iron ore sintering process with biomass utilization. In: Proceeding. METEC & 2nd ESTAD. Düsseldorf, (Germany); 2015.

[63] Wang, C., Mellin, P., Lövgren, J., Yang, W., Salman, H., Hultgren, A., Larsson M: Biomass as blast furnace injectant-considering availability, pretreatment and deployment in Swedish steel industry. Energy Convers Manag 102, 217–26 (2015).

[64] Mathieson, J.G., Somerville, M.A., Deev, A., Jahanshahi, S.: 19 - Utilization of biomass as an alternative fuel in ironmaking. Iron Ore Mineralogy, Processing and Environmental Sustainability, 581-613 (2015).

[65] Wei, R., Zhang, L., Cang, D., Li, J., Li, X., Xu, C.: Current status and potential of biomass utilization in ferrous metallurgical industry. Renewable and Sustainable Energy Reviews 68, 511-524 (2017).

[66] Kaewpanha, M., Guan, G., Hao, X., Wang, Z., Kasai, Y., Kusakabe, K., Abudula A.: Steam co-gasification of brown seaweed and land-based biomass. Fuel Processing Technology 120, 106-112 (2014).

[67] Guo, D., Zhu, L., Guo, S., Cui, B., Luo, S., Laghari, M., Chen, Z., Ma, C., Zhou, Y., Chen, J., Xiao, B., Hu, M., S. Luo: Direct reduction of oxidized iron ore pellets using biomass syngas as the reducer. Fuel Processing Technology 148, 276-281 (2016).

[68] Bagatini, M.C., Zymla, V., Osório, E., Vilela, A.C.F.: Carbon Gasification in Self-reducing Mixtures. J-STAGE, ISIJ, International 54 Issue 12 (2014).

[69] Liu, G., Strezov, V., Lucas, J.A., JWibberley L.: Thermal investigations of direct iron ore reduction with coal. Thermochimica Acta 410, 133-140 (2004).

[70] Strezov, V.: Iron ore reduction using sawdust: Experimental analysis and kinetic modelling. Renewable Energy 31, 1892-1905 (2006).

[71] Li, J., Wei, R., Long, H., Wang, P., Cang, D.: Sticking behaviour of iron ore–coal pellets and its inhibition. Powder Technol 262,30–5 (2014).

[72] Long, H., Li, J., Wang, P., Shi, S.: Reduction kinetics of carbon containing pellets made from metallurgical dust. J Iron Steel Res 39, 585–92 (2012).

[73] Guo, D., Hu, M., Pu, C., Xiao, B., Hu, Z., Liu, S., Wang, X., Zhu, X.: Kinetics and mechanisms of direct reduction of iron ore-biomass composite pellets with hydrogen gas. International Journal of Hydrogen Energy 40, 4733-4740 (2015).

[74] Hu, Q., Yao, D., Xie, Y., Zhu, Y., Yang, H., Chen, Y., Chen, H.: Study on intrinsic reaction behavior and kinetics during reduction of iron ore pellets by utilization of biochar. Energy Conversion and Management 158, 1-8 (2018).

[75] International Energy Agency, « Energy Technology Perspectives 2020 », Energy Technology,Perspectives, p.400 (2020).

[76] https://en.wikipedia.org/wiki/Bloomery

[77] Diebold, J., Scahill, J.: Biomass to gasoline. In: Soltes, E.J., Milne, T.A. (Eds.), Pyrolysis Oils from Biomass, 264–276 (1988).

[78] Deglise, X., Donnot, A.: "Bois énergie." Techniques de l'Ingénieur BE 8 535. (2004).

[79] Santhoshkumar, A., Ramanathan, A.: Energy and life cycle assessment of solar assisted microwave pyrolysis of waste biomass. 2019 IOP Conf. Ser.: Earth Environ. Sci. 312 012017.

[80] Sarma V. Pisupati, Vijayaragavan Krishnamoorthy, in Integrated Gasification Combined Cycle (IGCC) Technologies, 2017.

[81] A.F. Bush, J.J. Leonard, W.H. Yundt, Gas Analyses in Large Fire Experiments, 1969, in Project Flambeau, US Dept Agriculture, vol. 3. app. C, p.55.

[82] Xavier Déglise. Les conversions thermochimiques du bois. Revue forestière française, 1982, 34 (4), pp.249-270. doi: 10.4267/2042/21577.

[83] El-Sayed, S.A., Mostafa, M.E.: Kinetic parameters determination of biomass pyrolysis fuels using TGA and DTA techniques. Waste Biomass Valor 6, 401-415 (2015).

[84] Suriapparao, D.V., Tejasvia, R.: A review on role of process parameters on pyrolysis of biomass and plastics: Present scope and future opportunities in conventional and microwave-assisted pyrolysis technologies. Process Safety and Environmental Protection 162, 435–462 (2022).

[85] Grønli, M. Industrial production of charcoal, INTEF Energy Research. (2002).

[86] Antal, M.J., Croiset, E., Dai, X., DeAlmeida, C., Mok, W.S., Norberg, N.: "High-Yield Biomass Charcoal." Energy & Fuels 10, 652-658 (1996).

[87] Fick, G.: thesis: Analyse environnementale de l'utilisation de biomasse pour la production de tuyeau en fonte, 2013.

[88] Pelaez-Samaniegoa, M.R., Cortez, L.B., Garcia-Perez, L.B., Rosillo-Calle, F., Mesa, J.: "Improvements of Brazilian carbonization industry as part of the creation of a global biomass economy." Renewable and Sustainable Energy Reviews 12, 1063–1086 (2008).

[89] Sun, Y., Jiang, J., Zhao, S.: Biomass carbonization industrial process. 2011 International Conference on Materials for Renewable Energy & Environment.

[90] Branca, C., Di Blasi, C., Elefante R.: "Devolatilisation and Heterogeneous Combustion of Wood Fast Pyrolysis Oils." Industrial and Engineering Chemistry Research 44(4), 799-810 (2005).

[91] BTG-BTL (2009). "2009 - Brochure BTG-BTL Pyrolysis oil.

[92] Mohan, D., Pittman Jr., C.U., Steele, P.H.: "Pyrolysis of Wood/Biomass for Bio-oil: A Critical Review." Energy & Fuels 20, 848-889 (2006).

[93] Dynamotive (2009). Dynamotive Bio-Oil - Information Booklet 2009.

[94] Akom, M., Martin, A., Oti-Boateng, C., Otoo, E., Dawoe, E.: Yield and cost of charcoal produced by a locally fabricated reactor. J. Agric. Environ. Sci 9, 2334–2412 (2020).

[95] Czajczy´nska, D., Anguilano, L., Ghazal, H., Krzy˙ zy´nska, R., Reynolds, A.J., Spencer, N., Jouhara, H.: Potential of pyrolysis processes in the waste management sector. Therm. Sci. Eng. Prog 3, 171–197 (2017).

[96] Maschio, G.: "Pyrolysis, a promising route for biomass utilization." Bioresource Technology 42, 219-231 (1992).

[97] Horne, P.A., Williams, P.T.: "Influence of temperature on the products from the flash pyrolysis of biomass." Fuel 9, 1051-1059 (1996).

[98] Dufoura, A., Girods, P., Masson, E., Rogaume, Y., Zoulalian, A.: Synthesis gas production by biomass pyrolysis: Effect of reactor temperature on product distribution. international journal of hy drogen energy 34, 1726–1734 (2009).

[99] Di Blasi, C., Signorelli, G., Di Russo, C., Rea, G.: "Product Distribution from Pyrolysis of Wood and Agricultural Residues." Industrial & Engineering Chemistry Research 38, 2216-2224 (1999).

[100] Di Blasi, C.: "Modeling chemical and physical processes of wood and biomass pyrolysis." Progress in Energy and Combustion Science 34, 47-90 (2008).

[101] Khasraw, D., Spooner, S., Hage, H., Meijer, K., Li Z.: Devolatilisation characteristics of coal and biomass with respect to temperature and heating rate for HIsarna alternative ironmaking process. Fuel 284, 119101 (2021).

[102] Sbirrazzuoli, N.: Determination of pre-exponential factors and of the mathematical functions f(a) or G(a) that describe the reaction mechanism in a model-free way. Thermochim. Acta 564, 59–69 (2013).

[103] Friedman, H.L.: Kinetics of thermal degradation of char-forming plastics from thermogravimetry. Application to a phenolic plastic, J. Polym. Sci. Part C Polym. Symp. 6 (1), 183–195 (1964).

[104] Vyazovkin, S.; Burnham, A.K.; Criado, J.M.; Pérez-Maqueda, L.A.; Popescu, C.; Sbirrazzuoli, N.: ICTAC Kinetics Committee recommendations for performing kinetic computations on thermal analysis data. Thermochim. Acta 520, 1–19 (2011).

[105] Coats, A., Redfern, J.P.: Kinetic parameters from thermogravimetric data. II, J. Polym. Sci. Part B Polym. Lett. 3 (11), 917–920 (1965).

[106] Kissinger, H.E.: Reaction kinetics in differential thermal analysis, Anal. Chem. 29 (11), 1702–1706 (1957).

[107] Flynn, J.H., Wall, L.A.: A quick, direct method for the determination of activation energy from thermogravimetric data, J. Polym. Sci. Part B Polym. Lett. 4 (5), 323–328 (1966).

[108] Starink, M.: The determination of activation energy from linear heating rate experiments: a comparison of the accuracy of isoconversion methods, Thermochim. Acta 404 (1-2), 163–176 (2003).

[109] Akahira, T., Sunose, T., Method of determining activation deterioration constant of electrical insulating materials, Res. Rep. Chiba Inst. Technol. (Sci Technol) 16, 22–31 (1971).

[110] Ali, I., Bahaitham, H., Naebulharam, R.: A comprehensive kinetics study of coconut shell waste pyrolysis, Bioreour.Technol. 235, 1–11 (2017).

[111] Zou, S., Wu, T., Yang, M., Li, C., Tong J.: Pyrolysis charactristics and kinetics of the marine mricroalgae Dunaliella tertiolecta using thermogravimetric analyzer. Biosurce Technology 101, 359-365 (2010).

[112] Starink, M.J.: The determination of activation energy from linear heating rate experiments: a comparison of the accuracy of isoconversional methods. Thermochimica Acta 404, 163-176 (2003).

[113] Orfao, J.J.M., Antunes, F.J.A., Figueiredo, J.L.: Pyrolysis kinetics of lignocellulosic materials—three independent reactions model, Fuel 78, 349–358 (1999).

[114] Pantoleontos, G., Basinas, P., Skodras, G., Grammelis, P., Pintér, J.D., Topis, S., Sakellaropoulos, G.P.: A global optimization study on the devolatilisation kinetics of coal, biomass and waste fuels. Fuel Processing Technology 90, 762–769 (2009).

[115] Willner, T., Brunner, G.: Pyrolysis kinetics of wood and wood components. Chem. Eng. Technol. 28, 1212-1225 (2005).

[116] Antal, Jr., M.J., Varhegyi, G., Jakab, E.: Cellulose pyrolysis kinetics: revisited. Ind. Eng. Chem. Res. 37, 1267-1275 (1998).

[117] Lapuerta, M., Hernandez, J.J., Rodriguez, J.: Kinetics of devolatilisation of foretry wastes from thermogravimetric analysis. Biomass and Bioenergy 27, 385–391 (2004).

[118] 88Sonobe, T, Worasuwannarak, N.: Kinetic analyses of biomass pyrolysis using the distributed activation energy model. Fuel 87, 414–21 (2008).

[119] Aboyade, A.O., Hugo, T.J., Carrier, M., Meyer, E.L., Stahl R., Knoetze J.H., Görgens J.F.: Non-isothermal kinetic analysis of the devolatilisation of corn cobs and sugar cane bagasse in an inert atmosphere. Thermochimica Acta 517, 81–89 (2011).

[120] Biagini, E., Fantei, A., Tognotti, L.: Effect of the heating rate on the devolatilisation of biomass residues, Thermochimica Acta 472, 55–63 (2008).

[121] Hamilton, J.R., Knauss, S.J.: Wood Factors Affecting the Variation in Specific Gravity of Northern Red Oak (Quercus rubra) Associated with Soil Origin. Foret Ecology and Management 17, 129-136 (1986).

[122] Li, Z., Kobayashi, N.: Determination of moisture diffusivity by thermogravimetric analysis under non-isothermal condition. Drying technology 23 (6), 1331-1342 (2005).

[123] Vega-Gálveza, A., Mirandaa, M., Puente Díaz, L., Lopeza, L., Rodrigueza, K., Di Scalab, K.: Effective moisture diffusivity determination and mathematical modelling of the drying curves of the olive-waste cake. Bioresource Technology 19 (101), 7265-7270 (2010).

[124] Chen, D., Li, K., Zhu, X.: Determination of effective moisture diffusivity and activation energy for drying of powdered peanut shell under isothermal conditions. Bioreource 7(3), 3670-3678 (2012).

[125] Pantoleontos, G., Basinas, P., Skodras, G., Grammelis, P., Pintér, J.D., Topis, S., Sakellaropoulos, G.P.: A global optimization study on the devolatilisation kinetics of coal, biomass and waste fuels. Fuel processing technology 90, 762-769 (2009).

[126] Alonso, M., Tran, K., Wang, L., Skreiberg, O.: A kinetic study on simutaneously boosting the mass and fixed-carbon yield of charcoal production via atmospheric carbonisation. Energy Procedia (2017) 120, 333-340.

[127] Ergun, S.: Kinetics of the reaction of carbon dioxide with carbon. J Phys Chem 60, 480–5 (1956).

[128] Jing, X., Wang, Z., Zhang, Q., Yu, Z., Li, C., Huang, J., Fang, Y.: Evaluation of CO_2 gasification reactivity of different coal rank chars by physicochemical properties. Energy Fuels 27, 7287–93 (2013).

[129] Gomez, A., Silbermann, R., Mahinpey, N.: A comprehensive experimental procedure for CO_2 coal gasification: Is there really a maximum reaction rate? Appl Energy 124, 73–81 (2014).

[130] Szekely, J., Evans, J.: A structural model for gas–solid reactions with a moving boundary. Chem Eng Sci 25, 1091–1107 (1970).

[131] Bhatia, S.K., Perlmutter, D.D.: A random pore model for fluid-solid reactions: Isothermal, kinetic control. AIChE J. 26 (3), 379–386(1980).

[132] Ahmed, I.I., Gupta, A.K.: Kinetics of woodchips char gasification with steam and carbon dioxide. Applied Energy 88, 1613–1619 (2011).

[133] Zhang, Y., Ashizawa, M., Kajitani, S., Miura, K.: Proposal of a semi-empirical kinetic model to reconcile with gasification reactivity profiles of biomass chars. Fuel 87 (4–5), 475–481(2008).

[134] Laurendeal, N.M.: Heterogeneous kinetics of coal char gasification and combustion. Progress in energy and combustion science 4, 221-270 (1978).

[135] Roncancio, R., Gore, J. P.: CO_2 char gasification: A systematic review from 2014 to 2020. Energy Conversion and Management: X 10, 100060 (2021).

[136] Liu, L., Cao, Y., Liu, Q.: Kinetics studies and structure characteristics of coal char under pressurized CO_2 gasification conditions. Fuel 146, 103–10 (2015).

[137] Kawakami, M., Taga, H., Takenaka, T., Yokoyama, S.: Micro pore structure and reaction rate of coke, wood charcoal and graphite with CO_2. ISIJ International, 44, 2018–2022 (2004).

[138] Di Blasi, C.: Combustion and gasification rates of lignocellulosic chars Prog. Energy Combust. Sci. 35, 121−140 (2009).

[139] López-González, D., Fernandez-Lopez, M. Valverde, J.L., Sanchez-Silva, L.: Gasification of lignocellulosic biomass char obtained from pyrolysis: Kinetic and evolved gas analyses. Energy 71, 456-467 (2014).

[140] Zahara, Z.F., Kudo, S., Daniyanto, Ashik, U.P., Norinaga, K., Budiman, A., Hayashi, J.I.: CO_2 Gasification of sugar cane bagasse: quantitative understanding of kinetic and catalytic roles of inherent metallic species. Energy Fuels 32, 4255–68 (2018).

[141] Byambajav, E., Hachiyama, Y., Kudo, S., Norinaga, K., Hayashi, J.I.: Kinetics and mechanism of CO_2 gasification of chars from 11 mongolian lignites. Energy Fuels 30, 1636–46 (2016).

[142] Zhang, L., Huang, J., Fang, Y., Wang, Y.: Gasification reactivity and kinetics of typical Chinese anthracite chars with steam and CO_2. Energy Fuels 20, 1201–10 (2006).

[143] Zuo, H.B., Zhang, P.C., Zhang, J.L., Bi, X.T., Geng, W.W., Wang, G.W.: Isothermal CO_2 gasification reactivity and kinetic models of biomass char/anthracite char. Bioresources 10, 5233–41 (2015).

[144] Vamvuka, D., Karouki, E., Sfakiotakis, S., Salatino, P.: Gasification of Waste Biomass Chars by Carbon Dioxide via Thermogravimetry—Effect of Catalysts. Combustion Science and Technology 184:1, 64-77 (2012).

[145] Huang, Y., Yin, X., Wu, C., Wang, C., Xie, J., Zhou, Z., Ma, L., Li, H.: Effects of metal catalysts on CO_2 gasification reactivity of biomass char, Biotechnology Advances 27, 568–572 (2009).

[146] Huo, W., Zhou, Z., Chen, X., Dai, Z., Yu, G.: Study on CO_2 gasification reactivity and physical characteristics of biomass, petroleum coke and coal chars. Bioreour Technol 159, 143–9 (2014).

[147] Wang, G., Zhang, J., Shao, J., Liu, Z., Wang, H., Li, X., Zhang, P., Geng, W., Zhang, G.: Experimental and modeling studies on CO 2 gasification of biomass chars. Energy 114, 143–54 (2016).

[148] Xiao, R., Yang, W.: Kinetics characteristics of straw semi-char gasification with carbon dioxide. Bioresource Technol 207, 180–7 (2016).

[149] Guo, W., Wang, Y., Lin, X., Wang, G., Zheng, P., Yang, Y., Mochida, I.: Structure and CO_2 gasification reactivity of char derived through pressured hydropyrolysis from low-rank coal. Energy Fuels 33, 8032–9 (2019).

[150] Zhu, S., Bai, Y., Hao, C., Li, F., Bao, W.: Investigation into the structural features and gasification reactivity of coal chars formed in CO_2 and N2 atmospheres. Journal of CO_2 Utilization 19, 9–15 (2017).

[151] Wang, L., Alsaker, N., Skreiberg, O., Hovd, B.: Effect of carbonization conditions on CO_2 gasification reactivity of biocarbon. Energy Proc 142, 932–7 (2017).

[152] Wang, L., Maziarka, P., Skreiberg, O., Løvås, T., Wadrzyk, M., Sevault, A.: Study of CO_2 gasification reactivity of biocarbon produced at different conditions. Energy Proc 142, 991–6 (2017).

[153] Jayaraman, K., Gokalp, I.: Effect of char generation method on steam, CO_2 and blended mixture gasification of high ash Turkish coals. Fuel 153, 320–7 (2015).

[154] Noumi, E.S., Blin, J., Valette, J., Rousset, P.: Combined effect of pyrolysis pressure and temperature on the yield and CO_2 gasification reactivity of acacia wood in macro- TG. Energy Fuels 29, 7301–8 (2015).

[155] Walker, P., Rusinko, F., Austin, L.: Gas reactions of carbon, Advances in catalysis 11, 133–221 (1959).

[156] Kim, R.G., Hwang, C.W., Jeon, C.H.: Kinetics of coal char gasification with CO_2: impact of internal/external diffusion at high temperature and elevated pressure. Appl Energy 129, 299–307 (2014).

[157] Roncancio, R., Ulcay, M.S., Arango, J.E., Gore, J.P.: Experimental study of CO_2 corn stover char gasification using iron nitrate as a catalyst under a high-pressure environment. Fuel 267, 117237 (2020).

[158] Tangstad, M., PaulBeukes, J., Steenkamp, J., Ringdalen, E.: Coal-based reducing agents in ferroalloys and silicon production. New Trends in Coal Conversion. (Combustion, Gasification, Emissions, and Coking), 405-438 (2019).

[159] Bui, H.H., Wang, L., Tran, K.Q., Skreiberg Ø.: CO_2 gasification of charcoals produced at various pressures. Fuel Process Technol 152, 207–14 (2016).

[160] Skodras, G., Nenes, G., Zafeiriou, N.: Low rank coal – CO_2 gasification: experimental study, analysis of the kinetic parameters by Weibull distribution and compensation effect. Appl Therm Eng 74, 111–8 (2015).

[161] Mermoud, F., Salvador, S., Van de Steene, L., Golfier, F.: Influence of the pyrolysis heating rate on the steam gasification rate of large wood char particles. Fuel Elsevier 85 (n° 10-11), 1473-1482 (2006).

[162] Emami Taba, L., Irfan, M.F., Wan Daud, W.A.M., Chakrabarti, M.H.: The effect of temperature on various parameters in coal, biomass and CO-gasification: a review, Renew. Sustain. Energy Rev. 16 (8), 5584–5596 (2012).

[163] Ollero, P., Serrera, A., Arjona, R., Alcantarilla, S.: The CO_2 gasification kinetics of olive residue. Biomass and Bioenergy 24, 151-161 (2003).

[164] Scott, S.A., Davidson, J.F., Dennis, J.S., Fennell, P.S., Hayhurst, A.N.: The rate of gasification by CO_2 of chars from waste. Proceedings of the Combustion Institute 30, 2151–2159 (2005).

[165] Zheng, Y., Marek, E., Scott, S.A.: The effect of CO on CO 2 -char gasification. Proceedings of the Combustion Institute 38, 4261–4269 (2021).

[166] Gómez-Barea, A., Ollero, P., Fernández C.: Diffusional Effects in CO_2 Gasification Experiments with Single Biomass Char Particles. 1. Experimental Investigation, Energy & Fuels 20, 2202-2210 (2006).

[167] Vincent, S.S., Mahinpey, N., Aqsha, A.: Mass transfer studies during CO_2 gasification of torrefied and pyrolyzed chars, Energy 67, 319-327 (2014).

[168] Barrio, M., Hustad, J.E.: CO_2 gasification of birch char and the effect of CO inhibition on the calculation of chemical kinetics. Progress in Thermochemical Biomass, Conversion, Volume 1 (2001).

[169] Rathmann, O., Hald, P., Bak, J., Boll Illerup, J., Gjernes, E., Fjellerup, J., Olsen, A.: Com-bustion and gasification of coal and straw under pressurized conditions.

Task 2: Determination of kinetic parameters in PTGA. Roskilde: Risø National Laboratory, Risø-R-819 (EN), Denmark.

[170] Illerup, J.B., Rathmann, O.: CO_2 gasification of Wheat straw, barley straw, willow and giganteous. Department of Combustion Research, RISØ National Laboratory, 12 December (1995).

[171] Bandyopadhyay, D., Ghosh, A.: Validity of rate equation based on Langmuir-Hinshelwood mechanism for gasification of carbon - a reappraisal. Steel research 73, 79-86 (1996).

[172] Kawakami M., Mizutani Y., Ohyabu T., Murayama K., Takenaka T., Yokoyama S.: Reaction Kinetics of Coke and some Carbonaceous Materials with C02 and Coke Strength after Reaction. Steel research int. 75 NO.2 (2004).

[173] Kashiwaya, Y., Takamaru, H., Ishii, K.: Coke Degradation Mechanism in Raceway of Blast Furnace and Less Degradation Properties. Tetsu-to-Hagané 89, 819 (2003).

[174] Komarova, E., Guhl, S., Meyer, B.: Brown coal char CO_2-gasification kinetics with respect to the char structure. Part I: Char structure development. Fuel 152, 38–47 (2015).

[175] Bhatia, S.K.: Analysis of Distributed Pore Closure in Gas-Solid Reactions. AlChE Journal (Vol. 31, No. 4), 648 (1985).

[176] Sbaffo, F., Patisson, F., Houzelot, J.L., Ablitzer, D.: Modélisation d’une réaction gaz-solide poreux avec évolution de la porosité. La Revue de Métallurgie-CIT/Science et Génie des Matériaux Décembre 2000.

[177] Alvarez, J., Lopez, G., Amutio, M., Bilbao, J., Olazar, M.: Kinetic Study of Carbon Dioxide Gasification of Rice Husk Fast Pyrolysis Char. Energy Fuels 29, 3198−3207 (2015).

[178] Jiuan Jing Chew et al.: Isothermal kinetic study of CO2 gasification of torrefied oil palm biomass, Biomass and Bioenergy 134 (2020).

[179] Duman, G., Azhar Uddin, M.d., Yanik J.: The effect of char properties on gasification reac-tivity. Fuel Processing Technology 118, 75–81 (2014).

[180] Takenaka, Y., Kimura, Y.: Mathematical model of direct reduction shaft furnace and its application to actual operations of a model plant. Computers and Chemical Engineering 10, 61-13 (1986).

[181] Takahashi, R., Takahashi, Y., Yagi, J., Omori, Y.: Operation and Simulation of Pressurized Shaft Furnace for Direct Reduction. Transactions ISI1 26, 765-774 (1986).

[182] Parisi, D.R., Laborde, M.A.: Modeling of counter current moving bed gas-solid reactor used in direct reduction of iron ore. Chemical Engineering Journal 104, 35–43 (2004).

[183] Alhumaizi, K., Ajbar, A., Soliman, M.: Modelling the complex interactions between reformer and reduction furnace in a Midrex-based iron plant. The canadian journal of chemical engineering 90, 1120-1141 (2011).

[184] Shams, A., Moazeni, F.: Modelling and simulation of the Midrex shaft furnace: reduction, transition and cooling zones. 2015. The journal of the minerals, metals & materials society 67, 2681-2689 (2015).

[185] Castro, J.A., Rocha, E.P., Oliveira, E.M., Campos, M.F.: Mathematical modeling of the shaft furnace process for producing DRI based on the multiphase theory. REM, Int. Eng. J., Ouro Preto, 71(1), 81-87 (2018).

[186] Ghadi, A.Z., Valipour, M.S., Biglari, M.: CFD simulation of two-phase gas-particle flow in the Midrex shaft furnace: The effect of twin gas injection system on

the performance of the reactor. International journal of hydrogen energy 42, 103-118 (2017).

[187] Hamadeh, H., Mirgaux, O., Patisson, F.: Detailed modeling of the direct reduction of iron ore in a shaft furnace. Materials 11, 1-16 (2018).

[188] Shao, L., Zhang, X., Zhao, C., Qu, Y., Saxen, H., Zou, Z.: Computational analysis of hydrogen reduction of iron oxide pellets in a shaft furnace process. Renewable Energy 179, 1537-1547 (2021).

[189] Rochaa, E.P., Castro, J.A., Silva, L., Caldas, R.S.: Computational Analysis of The Performance of Shaft Furnaces with Partial Replacement of the Burden with Self-Reducing Pellets Containing Biomass. Materials Research 22(6), e20190533 (2019).

[190] Alencar J.P.S.G., Pereira, B.A., Castro, J.A., Resende, V.G., Vasconcelos, W.L.: Evaluation of the impact of cluster formation in a direct reduction shaft furnace through numerical simulation. Metallurgy and materials 74 (2021).

[191] Chatterjee A.: Sponge iron production by direct reduction of iron oxide, 2010.

[192] Patisson, F., Mirgaux, O.: Hydrogen ironmaking: how it works. Metals 10, 922 (2020).

[193] Elshishini, S., Elnashaie, S.: Modeling, simulation and optimization of industrial fixed bed catalytic reactors. Gordon & Breach, London, 1994.

[194] Froment, G.F., Bischoff, K.B.: Chemical reactor analysis and design, second edition, New York: Wiley, 1990.

[195] Knudsen, J.G., State, O., Hottel, H.C., Sarofim, A.F., Wankat, P.C.: Heat and Mass Transfer, 1999.

[196] Wilke, C.R.: A Viscosity Equation for Gas Mixtures, J. Chem. Phys. 18, 517 (1950).

[197] Sohn, H.Y.: The law of additive reaction times in fluid-solid reactions, Metall. Trans. 9B, 89–96 (1978).

[198] Liu, G., Strezov, V., Lucas, T.A., Wibberley, L.J.: Thermal investigations of direct iron ore reduction with coal. Thermochimica Acta 410, 133–140 (2004).

[199] Klose, W., Wolki, M.: On the intrinsic reaction rate of biomass char gasification with carbon dioxide and steam. Fuel 84, 885–892 (2005).

[200] Bagatini, M.C., Zymla, V., Osório, E., Vilela, A.C.F.: Carbon Gasification in Self-reducing Mixtures. ISIJ International 54, 2687–2696 (2014).

[201] U.S. Geological Survey: Mineral Commodity Summaries 2020. Retrieved 2020-07-30.

[202] Mudd, G.M.: The "Limits to Growth" and Finite Mineral Resources, P5.

[203] Bensouidi, O., Craspsky, M., Rinaldi, T.: “Carthographie mondiale de potential d’un nouveau procédé”, Rapport de Projet Mines Nancy, février 2021.

[204] Pettinari, M.L., Chuvieco, E.: Generation of a global fuel data set using the Fuel Characteristic Classification System. Biogeosciences 13, 2061–2076 (2016).

[205] Jiesewetter, J., Hoppesteyn, P.D.J.: Biomass-based steel production. Final report of ULCOS SP7, Feb, 2006.

[206] https://stich.culturalheritage.org/life-cycle-assessment-explained/

[207] ISO 14040:2006.

[208] https://www.iso.org/standard/37456.html

[209] Ecoinvent Center, 2010.

[210] European Commission et al., 2010

[211] Perez-Gallardo, J.R.: Eco-design of large-scale photovoltaic (PV) systems with multi-objective optimization and Life-Cycle Assessment. 2013.

[212] Tanzer, S.E., Blok, K., Ramírez, A.: Can bioenergy with carbon capture and storage result in carbon negative steel? International Journal of Greenhouse Gas Control 100, 1031-1042 (2020).

[213] Norgate, T., Langberg, D.: Environmental and Economic Aspects of Charcoal Use in Steelmaking. ISIJ International 49, 463-469 (2009).

[214] Svenson, G.: Thesis: Optimized route selection for logging trucks, 2017.

[215] https://www.searates.com/services/distances-time/

[216] Lv, W., Sun, Z., Su, Z.: Life cycle energy consumption and greenhouse gas emissions of iron pelletizing process in China, a case study. J of cleaner production 233, 1314-1321 (2019).

[217] Dressel G. L.: "Use of DRI in EAF's", 2010.

[218] https://www.iea.org/countries/sweden

[219] https://www.ipcc.ch/site/assets/uploads/2018/02/ipcc_wg3_ar5_annex-iii.pdf

[220] Wu, Fu, Q., Giles, R., Bartle, J.: Energy Balance of Mallee Biomass Production in Western Australia. Bioenergy Australia 2005—Biomass for Energy, the Environment and Society. Bioenergy Australia, Melbourne 19, (2005).

[221] Pelletier, C.: Analyse environnementale et économique des filières bois-énergie. HAL open science, 2018.

[222] Haque, N., Norgate, T.:Life cycle assessment of iron ore mining and processing, 2015. Iron ore, Mineralogy, processing, and environmental sustainability,1st edition, 615-630 (2015).

[223] Grbes, A., Galic, I., Farkas, B., Budes, I.: Modelling-friendly life cycle inventory of underground mining of bauxite: A case study from Jajce mines in Bosnia and Herzegovina. 2021.

[224] Ferreira, H., Leite, M.G.P.: "A Life Cycle Assessment study of iron ore mining", J of cleaner production 108, 1081-1091 (2015).

[225] Lv, W., Sun, Z., Su, Z.: Life cycle energy consumption and greenhouse gas emissions of iron pelletizing process in China, a case study. J of cleaner production 233, 1314-1321 (2019).

[226] Patisson, F.: personal communication, 2021.

[227] Sphera, GaBi Databases 2020 Edition Upgrades & Improvements. 2020.

XI. Appendixes

Appendix A

In the part IV.3.4.2, we discussed the simulation of experimental reactivity functions and MRPM was the most appropriate. The curve-fitting was determined from the experimental data of the reactivity function, f(X) versus conversion, X. Figure 79 illustrates the comparison of reactivity functions between the experimental curves (lines in black) and simulated curves with MRPM models (line in blue) under100-0%, 75-25% and 50-50% CO_2-CO at different temperatures. These two curves are close except at 1000°C under 50-50% CO_2-CO.

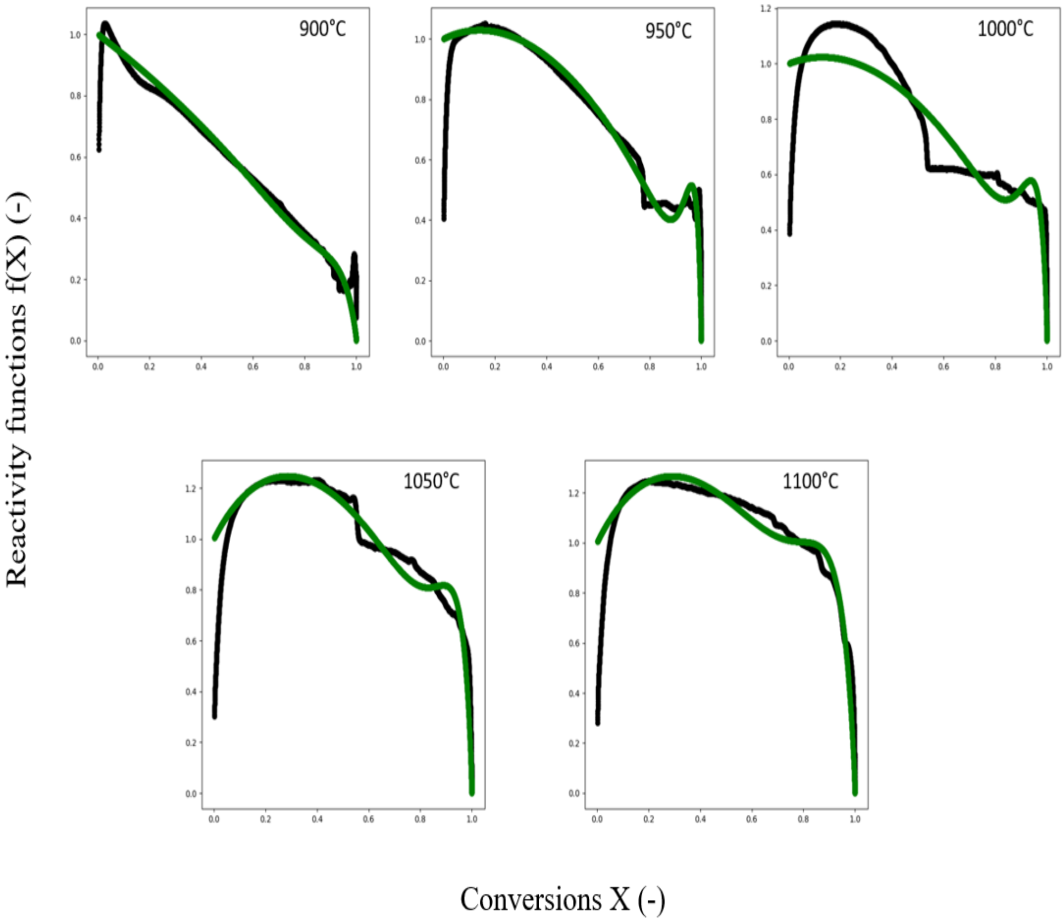

(a) Comparison under 50-50% CO_2-CO

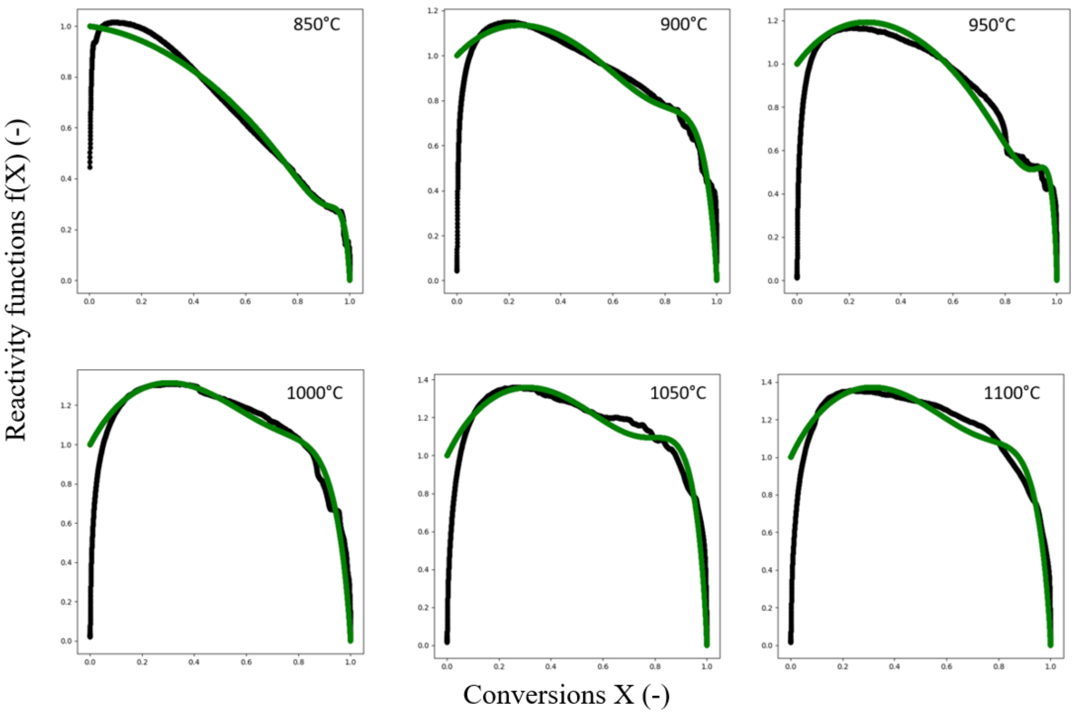

(b) Comparison under 75-25% CO_2-CO

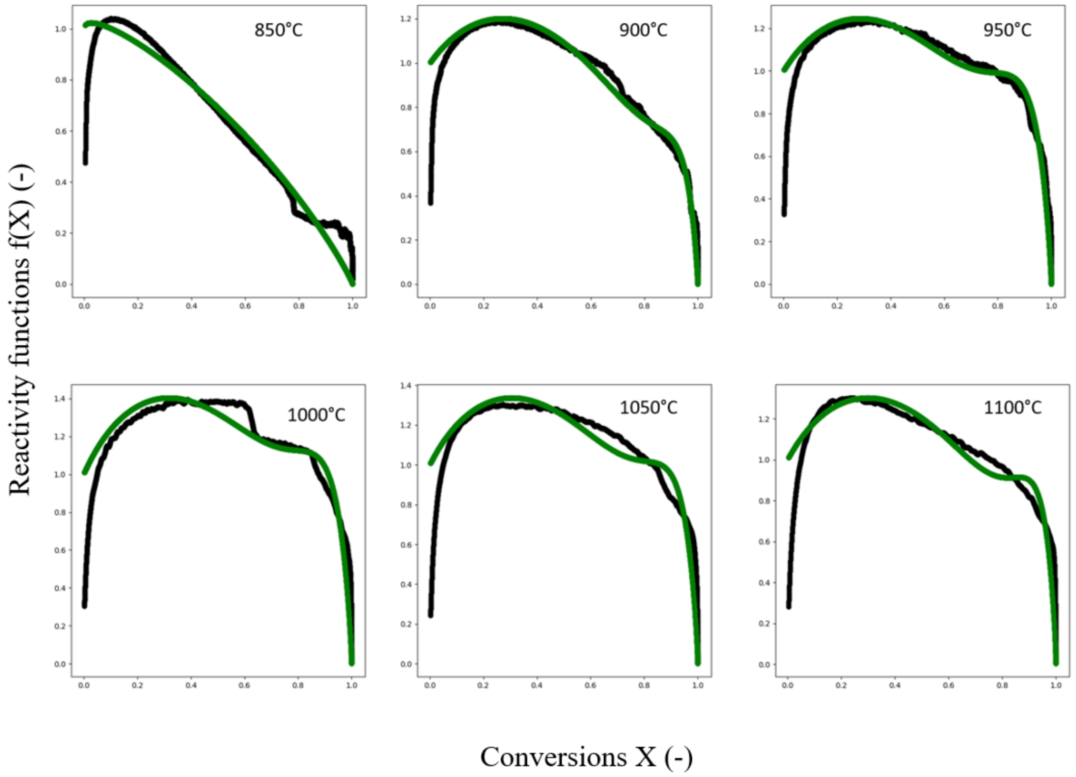

(c) Comparison under 100-0% CO_2-CO

Figure 79. Comparison of reactivity functions between the experimental curves and simulated curves with MRPM models

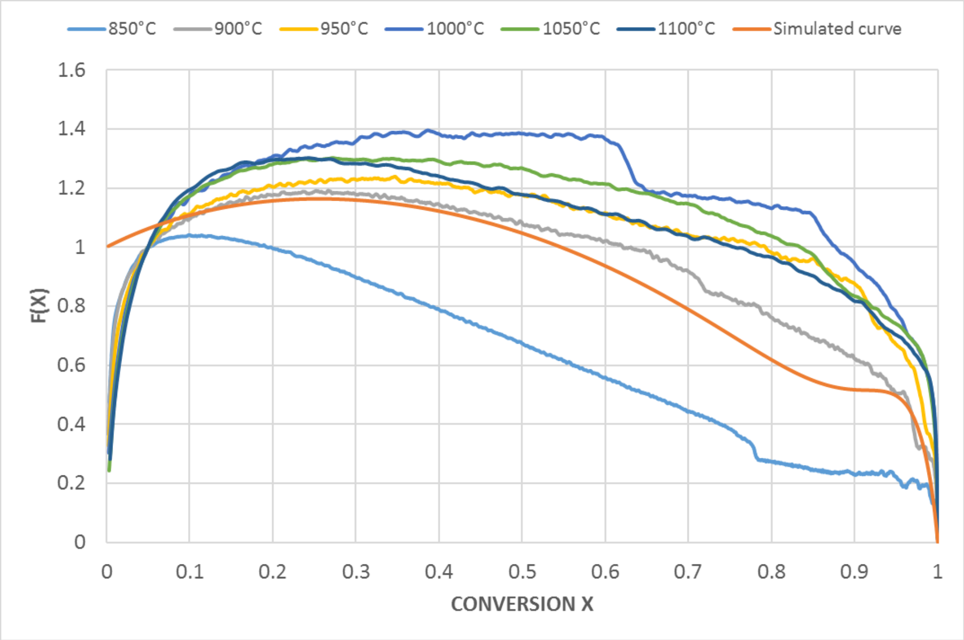

Figure 80. Comparison of reactivity functions between the experimental curves and simulated curves with MRPM models under pure CO_2 atmosphere

Appendix B: Cost evaluation of a BIORED process plant in Kiruna, Sweden

First, to unify the prices in the form of euros, it is important to define the exchange rate between US dollars and euros (1 € = 1.22 $ at the time of writing).

The Kiruna mine is located in Norrbotten County in the north of Sweden. It is the largest underground mine in the world and has an annual production of 27.5 Mt iron ore. The port of Narvik in Norway is 200 km away and can be reached by train. This is the place where the finished products are sold. The iron ore mined in Kiruna has the index 62. After extraction, about half of the iron ore is processed into pellets.

Figure 81. Location of Kiruna and Narvik

The production is assumed 4 Mt DRI/an and the solid change is consequently 0.912 Mt of charcoals and 5.72 Mt of pellets. As mentioned above in VI.1.3, the supply of charcoal is assumed to be locally produced at 150 $/t.

The economic profits of three scenarios will be compared in the following scenarios: direct selling of pellets, selling of DRI from the Midrex process and selling of DRI from the biomass-based process.

Reference scenario 0: Direct selling of pellets

Typically, the price of pellets is 220 $/t at the port of Kiruna. The annual turnover will therefore be 1258 M$. However, the pellets have to be transported to the port, which results in additional costs and emissions.

- Transport costs: The fixed costs of transport by train are equal to 1.7 €/t and the variable costs are 0.015 €/t.km. The transport of one tonne of pellets to the port therefore costs 4.7 €. Over a year, these costs will be 26.9 M€ or 32.8 M$.
- CO_2 emissions: The electricity consumption of the train is 0.0415 kWh/t.km. In Sweden, the emission factor for electricity is 0.03 kg_{CO2}/kWh. Thus,

transporting one tonne of pellets over 200 km emits 0.249 kg of CO_2. Over the year, the emissions are 1.42 kt_{CO2}. The carbon tax in Sweden is 123 $/t of CO_2 emitted so the cost due to the carbon tax is then 174.7 k$.

In summary, the transportation of pellets costs the company 33 M$ per year, producing a profit of 1225 M$.

Alternative scenario 1: Selling of DRI from the Midrex process

Investments in the first year:

Firstly, a Midrex production unit has to be built. Its Capex (Capital expenditure) is estimated at 200 $/$t_{DRI}$ per year. It is assumed that the GHG emissions during construction are negligible.

Period of operation:

- Costs: According to the difference between the price of iron ore and that of pellets, we assume that the overall Opex (operating expenditure) of the process is 50$$/t_{DRI}. Thus, it will be necessary to spend 200 M$ per year in Opex.
- CO_2 emissions: The Midrex process itself emits 436 $kg_{CO2\text{-}eq}/t_{DRI}$, thus1.74 Mt of CO_2 per year. Based on the carbon tax in Sweden, 214 M$ must be paid each year.

Transport and selling of DRI:

The price of DRI is 350 $/t. Thus, the turnover will be 1400 M$ each year.

The costs of transportation and related GHG emissions are then considered:

- Transport costs: The fixed costs of transport by train are equal to 1.7 €/t and the variable costs are 0.015 €/t.km. The transport of one tonne of DRI to the port therefore costs 4.7 €. Over a year, these costs will be 18.8 M€ or 22.9 M$.
- CO_2 emissions: The electricity consumption of the train is 0.0415 kWh/t.km. In Sweden, the emission factor for electricity is 0.03 $kg_{CO2\text{-}eq}$/kWh. Thus, the transport of one tonne of DRI over 200 km emits 0.249 kg CO_2. Over the year, the emissions are 996 $t_{CO2\text{-}eq}$. The cost due to the carbon tax is then 122.5 k$.

The total costs are therefore 23 M$.

Profits:

Revenues: 1400 M$ per year

Expenses:

- First year: 1237 M$
- Each year: 437 M$

Therefore, the profits will be 163 M$ in the first year and 963 M$ later.

Alternative scenario 2: Selling of DRI from the BIORED process

Investments in the first year:

Firstly, a direct reduction plant needs to be built. Its Capex is estimated at 100 $/t$_{DRI}$ produced per year. 400 M$ is therefore invested in the first year. It is also assumed that the GHG emissions during construction are negligible.

Period of operation:

- Costs: 25$/t$_{DRI}$ is needed to pay for maintenance and labor. 60 kWh of electricity is required to produce 1 tonne of DRI and the price of electricity in Sweden is 0.089 $/kWh, so 5.34 $/t$_{DRI}$ must be spent. For one year, 121.4 M$.
- CO_2 emissions: The only CO_2 emissions come from electricity consumption. The emission factor in Sweden is 0.03 kg$_{CO2}$/kWh, so one tonne of DRI is responsible for the emission of 1.8 kg CO_2. Over the year, these emissions are therefore 7.2 kt$_{CO2}$. The annual cost is 0.89M$.

In total, the process requires an investment of 122.3 M$.

Charcoal purchase and transport:

The 0.912 Mt of charcoal costs 136.8 M$. The cost of the transport and carbon tax should be considered. For this reason, it is assumed that charcoal is purchased within a 90 km radius.

- Transport costs: The transport costs are then 3.2 €/t. Over the year, this represents an investment of 2.9 M€ or 3.5 M$.
- CO_2 emissions: The electricity consumption of the train is 0.0415 kWh/t.km. In Sweden, the emission factor for electricity is 0.03 kg$_{CO2}$/kWh. Thus, transporting one tonne of charcoal over 90 km emits 0.112 kg CO_2. Over the year, the emissions are 102 tonnes of CO_2. The cost due to the carbon tax is then 12.6 k$.

The total costs are therefore 3.5 M$.

Transport and sale of DRI:

The costs of transport and related GHG emissions are then taken into account:

- Transport costs: The fixed costs of transport by train are equal to 1.7 €/t and the variable costs are 0.015 €/t.km. The transport of one tonne of DRI to the port therefore costs 4.7 €. Over a year, these costs will be 18.8 M€ or 22.9 M$.
- CO_2 emissions: The electricity consumption of the train is 0.0415 kWh/t.km. In Sweden, the emission factor for electricity is 0.03 kg_{CO2}/kWh. Thus, the transport of one tonne of DRI over 200 km emits 0.249 kg CO_2. Over the year, the emissions are 996 $t_{CO2\text{-}eq}$. The cost due to the carbon tax is then 122.5 k$.

The total costs are therefore 23 M$.

Profits:

Revenues: 1400 M$

Expenses:

- First year: 686 M$
- Each year: 286 M$

Scenarios	Pellets	DRI (Midrex)	DRI (BIORED)
Profits with installation (first year)	1225 M$	163 M$	714 M$
Profits without installation	1225 M$	963 M$	1114 M$

Table 26. Comparison of profits for the Swedish case study

Résumé

La substitution du carbone fossile par du carbone biogénique issu de la biomasse pourrait réduire considérablement la contribution de l'industrie sidérurgique au réchauffement climatique. L'objectif de ce travail de thèse était de poser les bases et d'analyser un procédé innovant d'élaboration du fer, dénommé BIORED (*biomass-based iron ore reduction*). Dans celui-ci, des boulettes de minerai de fer et de la biomasse granulaire sont chargées au sommet d'un four à cuve vertical. Le minerai est réduit par CO issu de la gazéification in-situ de la biomasse (réaction de Boudouard). Nous avons déterminé les cinétiques de dévolatilisation et de gazéification de la biomasse choisie, du charbon de bois, par thermogravimétrie. Ces cinétiques ont été modélisées par le schéma des réactions indépendantes en parallèle et l'équation de Langmuir-Hinshelwood, respectivement. Nous avons transformé un modèle existant de simulation du procédé de réduction directe du minerai de fer par les gaz pour tenir compte des deux solides et des réactions associées à la biomasse. Les résultats du nouveau modèle montrent que dans le réacteur BIORED, la gazéification prend place en bas du four, tandis que la réduction du minerai de fer s'étage, la réduction de la wustite en fer métallique étant l'étape la plus longue. Le degré de métallisation obtenu est satisfaisant et le mélange de gaz de tête (CO-CO_2) pourrait être recyclé pour réutiliser CO et économiser l'énergie. Nous avons développé un protocole expérimental spécifique pour la validation du modèle et les résultats de l'expérience correspondent relativement bien aux résultats numériques. Enfin, les possibilités de développement potentiel du procédé BIORED dans certaines régions du monde ont été quantifiées, et une analyse du cycle de vie de la fabrication d'acier sur la base de ce procédé a montré une diminution considérable des émissions de CO_2 (divisées par 8) et de la plupart des autres impacts sur l'environnement, par rapport à la filière usuelle haut fourneau et convertisseur.

Mots clés : réduction directe, minerai de fer, biomasse, sidérurgie, émissions de CO_2, thermogravimétrie, gazéification, four à cuve, modélisation mathématique.

Abstract

Substituting fossil carbon with biogenic carbon from biomass could considerably reduce the contribution of the steel industry to global warming. The objective of this thesis was to introduce and analyse an innovative ironmaking process, called BIORED (biomass-based iron ore reduction). In this process, iron ore pellets and granular biomass are loaded together at the top of a vertical shaft furnace. The ore is reduced by CO produced from the in-situ gasification of the biomass (Boudouard reaction). The devolatilisation and gasification kinetics of the selected biomass, charcoal, were determined from thermogravimetry experiments. These kinetics were modelled by the scheme of independent parallel reactions and the Langmuir-Hinshelwood equation, respectively. We used an existing numerical model of a gas-based direct reduction process to create a new one that considers two solids and the biomass-related reactions. The model results show that the gasification takes place at the bottom of the BIORED reactor, while the reduction of the iron ore occurs step-wisely, with the reduction of wustite to metallic iron being the slowest. The degree of metallisation is satisfactory and the top gas (CO-CO_2 mixture) could be recycled to reuse CO and save energy. We developed a specific experimental protocol for the validation of the model. The experimental results satisfactorily agree with the numerical ones. Eventually, the potential industrial development of the BIORED process in different regions of the world was assessed, and a life cycle assessment of a new steelmaking route based on BIORED process showed a considerable reduction in CO_2 emissions (divided by 8) and most other environmental impacts, compared to the conventional Blast Furnace-Basic Oxygen Furnace route.

Keywords: direct reduction, iron ore, biomass, ironmaking, steelmaking, CO_2 emissions, thermogravimetry, gasification, shaft furnace, mathematical modelling.